An investigation into the synthesis, structural characterisation, thermal and polymorphic behaviour of organic crystalline materials

By

Adam Cowell

A thesis submitted to

The University of Birmingham

For the examination of

DOCTOR OF PHILOSOPHY

This thesis and the work described in it are entirely my own, except where I have acknowledged either help from a named person or a reference is given to a published source or a thesis. Text taken from another source will be enclosed in quotation marks and a reference will be given.

27th Spetember 2010

Abstract

The organic solid state appears in a complex number of forms. The design, synthesis and application of solid state organic materials have a big impact upon society, e.g. pharmaceuticals. Traditionally, the process of selecting active pharmaceutical ingredients (APIs) was limited to free drug or accepted salt formulations. The cocrystallisation of APIs with a former molecule significantly increases the developmental options for APIs. Many pharmaceutical solids are prepared as polycrystalline materials in order to deliver favourable physical properties, i.e. solubility, bioavailability and stability. In such cases, the development and application of structure solution techniques via powder X-ray diffraction (pxrd) has played an ever increasing pivotal role. In this thesis a number of new multi-component materials; oxamic acid:nicotinamide, oxamic acid:isonicotinamide, fumaric acid:nicotinamide, maleic acid:nicotinamide and maleic acid:isonicotinamide, will be synthesised, via a number of synthetic methods, and fully structurally characterised. A direct comparison of structures solved by powder and single crystal diffraction, have been made in order to evaluate the reliability of structure solution from pxrd in these types of materials. The thermal behaviour of molecular materials will be presented as significant structural information can be extracted from the anisotropic expansion of molecular materials. In conjunction with the research into new multi-component materials, the structure solution of oxamic acid via pxrd, single X-ray diffraction and neutron diffraction will be investigated. Small organic molecular materials like oxamic acid provide a challenge to the crystallographer due to the similarities in the electron density surrounding each functional group in the molecule.

Acknowledgements

The past four years or so would not have been as enjoyable an experience if it wasn't for the people who I have shared my time with. Firstly, I would like to thank my supervisor Dr Maryjane Tremayne for allowing me the opportunity to study a PhD and for her vital guidance and input into the project. I will be ever in debt to Dr Sam Chong whose expertise and professionalism at the start of my PhD was vital to putting me on the right track to crystallographic happiness, and also an excellent drinking partner on conferences. I would like to extend my acknowledgements to both Dr Louise Male and Dr Benson Kariuki for their insight and single crystal diffraction knowledge. I would like to thank past and present members of Team Tremayne, Liana, Duncan, Raja and Laura (especially for printing the thesis) for their help, guidance and general good-natured chitchat.

I would also like to acknowledge the wider structural, theoretical and physical chemist community living on the second floor of the Haworth building including; Dr Dan Binks, Dr Tom Penfold, Dr Andy Bennett, Dr Oliver Borbon, Dr Emma Chapman, Loggy, Jan, Jon, Professor Johnston, Dr Britton and may others that I am sure I have missed.

I would like to acknowledge my grandad and nan, Richard and Olive Hasson. If it wasn't for their help during my undergraduate studies I wouldn't be in this position now, both of whom sadly passed away during my PhD. Finally, I would like to thank my wife Nicola, and thank her again and again, just for being ace.

Contents

1.0	**Introduction**	**1**
1.1	The fundamentals of crystalline state	2
1.2	Space groups	5
1.3	X-ray diffraction from crystalline solids	5
1.4	The crystallographic phase problem	7
1.5	Single crystal vs. powder diffraction	8
1.6	Preferred orientation	11
1.7	Structure prediction	12
1.7.1	Indexing	14
1.7.2	Space group assignment	14
1.7.3	Pattern decomposition	15
1.7.4	Structure solution	16
1.7.5	Differential evolution	17
1.7.6	Rietveld refinement	19
1.8	Polymorphism	20
1.9	Structure prediction	22
1.10	Thermal behaviour	24
1.11	Forms of organic solids	26
1.11.1	Cocrystals vs. Salts	27
1.11.2	Cocrystals applications	30
1.11.3	Cocrystal synthesis	32
1.11.4	Reduced solvent methods for cocrystallisation synthesis	34
1.11.5	Cocrystal design	35

1.12 Aims.....38

2 Methodology..... 47

2.1 Variable temperature x-ray diffraction..... 47

2.1.1 Software and data handling..... 47

2.2 Structure solution from X-ray powder diffraction..... 47

3 Experimental..... 56

3.1 Instrumentation..... 56

3.1.1 Bruker AXS D5000 high-resolution X-ray powder Diffractometer..... 56

3.1.2 Bruker AXS D5005 high-resolution X-ray powder Diffractometer..... 56

3.1.3 Sample effects using the Bruker AXS D5005 high-resolution X-ray powder diffractometer.....57

3.1.4 Bruker AXS D5000 high-resolution X-ray powder diffractometer fitted with Oxford Cryostream and capillary stage..... 59

3.1.5 Bruker APEXII CCD Single Crystal diffractometer..... 60

3.1.6 Perkin Elmer Pyris 1 DSC (differential scanning calorimeter).60

3.1.7 Solid state NMR (nuclear magnetic resonance)..... 61

3.1.8 Solution NMR (nuclear magnetic resonance) 61

3.1.9 Solid state Infra-red..... 61

3.1.10 High pressure liquid chromatography (HPLC).....62

3.2 Synthetic technique for cocrystal/salt synthesis..... 62

3.2.1 Solvent mediated crystallsation 62

3.2.2 Incubator controlled solvent-mediated crystallisation.....62
3.2.3 Liquid assisted grinding..... 63
3.2.4 Slurry sonication..... 63
3.2.5 Dry grinding..... 63
3.3 Preparation and characterisation of system under investigation...63
3.3.1 Oxamic acid:isonicotinamide..... 63
3.3.2 Synthesis..... 63
3.3.3 NMR analysis..... 64
3.3.4 HPLC results..... 65
3.3.5 DSC analysis..... 65
3.3.6 Preparation of sample for single crystal diffraction..... 65
3.3.7 Stoichiometric diversity..... 66
3.4 Oxamic acid:nicotinamide..... 66
3.4.1 Synthesis..... 66
3.4.2 NMR analysis..... 67
3.4.3 HPLC result..... 68
3.4.4 DSC analysis..... 68
3.4.5 Preparation of sample for single crystal diffraction..... 68
3.5 Fumaric acid:nicotinamide..... 68
3.5.1 Synthesis..... 68
3.5.2 NMR analysis..... 69
3.5.3 Melting point analysis 70
3.5.4 Preparation of sample for single crystal..... 70
3.5.5 Stoichiometric diversity..... 70
3.6 Maleic acid:nicotinamide..... 70
3.6.1 Synthesis (product A) 70

3.6.2 NMR analysis (product A)..... 71

3.6.3 DSC analysis (product A)..... 72

3.6.4 Preparation of sample for single crystal diffraction (product)..... 72

3.6.5 Synthesis (product B)..... 72

3.6.6 NMR analysis (product B)..... 73

3.6.7 DSC analysis (product B)..... 73

3.6.8 Preparation of sample (product B) for single crystal diffraction..... 74

3.7 Maleic acid:isonicotinamide..... 74

3.7.1 Synthesis..... 75

3.7.2 NMR analysis..... 75

3.7.3 Preparation of sample for single crystal diffraction..... 75

3.8 Succinic acid:nicotinamide..... 75

3.8.1 Synthesis.....75

3.9 Adipic acid:nicotinamide.....76

3.9.1 Synthesis..... 76

3.10 Oxamic acid..... 76

3.10.1 Solvent mediated recrystallisation.....76

3.10.2 Neutron powder diffraction..... 76

4.0 Crystal structure determination of Oxamic acid:isonicotinamide and oxamic acid:nicotinamide.....78

4.1 Characterisation of oxamic acid and isonicotinamide..... 80

4.2 Structure solution and refinement from laboratory pxrd data. .84

4.3 Rietveld refinement..... 86

4.4 Oxamic acid isonicotinamide: structure.....91

4.5 Comparison of the Single crystal vs. Powder structure 95

4.6 The efficiency of the DE algorithm..... 98

4.7 Thermal behaviour of oxamic acid:isonicotinamide.....102

4.8 Characterisation of oxamic acid:nicotinamide..... 107

4.9 Structure solution and refinement from laboratory pxrd data...111

4.10 Rietveld refinement..... 113

4.11 Oxamic acid:nicotinamide structure..... 116

4.12 Single crystal vs. Powder structure..... 122

4.13 The efficiency of the DE algorithm..... 128

4.14 Thermal behaviour of oxamic acid:nicotinamide.....129

5.0 Crystal structure determination of Fumaric acid:nicotinamide and maleic acid:nicotinamide and maleic acid:isonicotinamide.....136

5.1 Characterisation of fumaric acid and nicotinamide 137

5.2 Structure solution and refinement from laboratory pxrd data....141

5.3 Rietveld refinement.....143

5.4 Fumaric acid:nicotinamide structure.....146

5.5 Comparison of the single crystal vs. Powder structure.....150

5.6 Efficiency of the DE algorithm.....151

5.7 Thermal behaviour of fumaric acid:nicotinamide.....154

5.8 Cocrystallisation of maleic acid:nicotinamide..... 158

5.9 Characterisation of maleic acid:nicotinamide.....159

5.10 Structure solution of maleic acid:nicotinamide product A.....165

5.11 Describing the structure of maleic acid:nicotinamide.....170

5.12 Thermal behaviour of maleic acid:nicotinamide product A.....170

5.13 Cocrystallisation of maleic acid:isonicotinamide.....173
5.14 Characterisation of maleic acid:isonicotinamide.....177
5.15 Maleic acid:isonicotinamide structure.....177

6.0 **Polymorphism of oxamic acid**.....186
6.1 Oxamic acid.....186
6.2 Polymorph screen.....187
6.3 Liquid assisted grinding.....190
6.4 DSC results.....191
6.5 Solution ^{1}H NMR results.....192
6.6 Solid-state NMR result.....192
6.7 Structure prediction results.....193
6.8 Structure solution of oxamic acid form I from pxrd.....195
6.9 Rietveld refinement.....197
6.10 Oxamic acid form I powder structure.....200
6.11 Single crystal vs. Powder structure of oxamic acid form I.....201
6.12 The attempted structure solution of oxamic acid form II from pxrd.....205
6.13 Neutron diffraction data.....206
6.14 Hydrogenated neutron data.....207
6.14.1 Model A results.....208
6.14.2 Model B results.....209
6.14.3 Model C results.....209
6.15 Thermal behaviour of oxamic acid.....210

7.0 Conclusion **213**

8.0 Appendices A-X.....216-267

List of figures

1.1 Unit cell parallelepiped.

1.2 Lattice types, i) Body centred (I), ii) Primitive (P), iii) C centred and iv) F centred.

1.3 The geometric conditions required for Bragg diffraction.

1.4 Diffraction from an oriented single crystal.

1.5 Diffraction cones of scattered X-rays, diffracted from a powder sample.

1.6 A flow diagram outlining the processes involved in structure solution from pxrd.

1.7 A symmetric vibronic harmonic oscillator.

1.8 The classification of organic solids.

1.9 Classification of a cocrystal (left) and a salt (right).

1.10 Frequency of occurrence of organic molecular co-crystals in the Cambridge Structural Database from 1988 to 2007. For the purposes of this graph, co-crystals are distinct from solvates, hydrates, and simple salts.

1.11 Schematic representations of isothermal ternary phase diagrams with (A) showing similar solubilities between starting components 1 and 2 in solvent S and (B) showing a system with a difference between solubilities of the starting components 1 and 2 in solvent S. Region **A** represents component 1 and solvent, **B** represents component 1 and cocrystal, **C** represents cocrystal, **D** represents component 2 and cocrystal, **E** represents component 2 and cocrystal and finally **F** represents solution.

1.12 Potential synthons found in acid-amides cocrystals.

2.1 An example of local minimum and the global minimum on an energy hypersurface

2.2 Production of an offspring trial structure using a combination of variables of the parent (P) and randomly selected individuals (R1, R2 and R3)

2.3 Flow diagram of the DE calculation process

2.4 Evolutionary progress plot for the successful solution of oxamic acid:nicotinamide showing the best R_{wp} (blue) and the mean R_{wp} (pink) for each generation.

3.1 Diagram showing the techniques used to mount the sample onto the sample holder for collection of low-temperature data on D5005.

3.2 ^{1}H NMR of oxamic acid:isonicotinamide product (from 1:1 starting ratio) using DMSO as solvent. ^{1}H NMR 300MHz (DMSO-d_6): δ = 8.90 ppm (dd, 2H), 8.4 ppm (s, 1H), 8.21 ppm (s, 1H), 7.8 ppm (d, 4H)

3.3 ^{1}H NMR of oxamic acid:nicotinamide multi-component crystal (from 1:1 starting ratio) using DMSO as solvent. ^{1}H NMR 300MHz (DMSO-d_6): δ = 9.10 ppm (dd, 1H), 8.7 ppm (d, 1H), 8.21 ppm (dt, 3H), 7.8 ppm (d, 1H) 7.7 (d, 1H), 7.5 (d, 1H).

3.4 NMR of fumaric acid:nicotinamide product (from 1:1 starting ratio) using DMSO as solvent. ^{1}H NMR 300MHz (DMSO-d_6): δ = 13.2 ppm (s, 2H), 9.10 ppm (dd, 1H), 8.7 ppm (d, 1H), 8.21 ppm (dt, 1H), 8.19 ppm (s, 1H) 7.8 ppm (d, 1H) 7.6 (d, 1H), 6.6 (d, 2H).

3.5 ^{1}H NMR of maleic acid and nicotinamide product A multi-component crystal (from 1:1 starting ratio) using DMSO as solvent. 1H NMR 300MHz (DMSO-d_6): δ = 9.10 ppm (dd, 1H), 8.7 ppm (dd, 1H), 8.21 ppm (dt, 2H), 7.8 ppm (d, 1H) 7.6 (d, 1H), 6.2 (d, 2H).

3.6 ^{1}H NMR of maleic acid and nicotinamide product B (from 1:1 starting ratio) using DMSO as solvent. ^{1}H NMR 300MHz (DMSO-d_6): δ = 13.2 (s, 2H), 9.10 ppm (dd, 1H), 8.7 ppm (dd, 1H), 8.21 ppm (dt, 2H), 7.8 ppm (d, 1H) 7.6 (d, 1H), 6.2 (d, 2H).

3.7 ^{1}H NMR of oxamic acid and isonicotinamide multi-component crystal (from 1:1 starting ratio) using DMSO as solvent. ^{1}H NMR 300MHz (DMSO-d_6): δ = 8.90 ppm (dd, 2H), 8.4 ppm (s, 1H), 8.21 ppm (s, 1H), 6.2 ppm (d, 2H).

4.1 Molecular diagrams of (i) oxamic acid, (ii) isonicotinamide and (iii) nicotinamide

4.2 Potential dimeric synthons for the oxamate unit.

4.3 Powder X-ray diffraction patterns of starting materials, oxamic acid (orange) and isonicotinamide (red) and the oxamic acid:isonicotinamide multi-component material (black)

4.4 Solid state IR spectra of the oxamic acid and isonicotinamide mix (red) and the new multi-component crystal (blue)

4.5 Powder X-ray diffraction data of the starting materials oxamic acid (orange) and isonicotinamide (red). Oxamic acid:isonicotinamide crystallised from solution mediated crystallisation (black), oxamic acid:isonicotinamide ground for 5 minutes(purple), oxamic acid:isonicotinamide ground for 15 minutes (blue), oxamic acid: isonicotinamide ground for 20 minutes (green) and oxamic acid:isonicotinamide from sonic slurry(dark red).

4.6 Molecular structures used in the DE structure solution, torsion angles are indicated by arrows, excluded hydrogen atoms are shown in brackets.

4.7 Differential evolution progress plot for the successful structure solution of oxamic acid:isonicotinamide showing the R_{wp} of the best individual in blue and the mean % R_{wp} of the population in pink.

4.8 The final Rietveld profile for oxamic acid:isonicotinamide. The experimental diffraction pattern is shown by red circles, the calculated diffraction pattern is shown by a solid green line, and the difference plot as a solid pink line. Reflection positions are marked by black dots.

4.9 The molecular structure of oxamic acid:isonicotinamide. Showing the atom numbering scheme and the hard intermolecular hydrogen bonds within the asymmetric unit (dashed lines). Displacement ellipsoids are drawn at the 50% probability level and H atoms are shown as small spheres of arbitrary radii.

4.10 A view along the a axis showing an infinitely hydrogen bonded sheet in the (105) plane. Hydrogen bonds are shown by a dotted green line

4.11 A view of the hydrogen-bonded crystal structure of oxamic acid:isonicotinamide shown in projection down the a-axis. All six intermolecular hydrogen bonds are indicated as dashed lines; five interactions within a sheet (green) and one between sheets (black). The intramolecular hydrogen bond within the oxamate ion is not shown and H atoms not involved in hydrogen bonding have been omitted for clarity.

4.12 A section of the hydrogen bonded sheet of oxamic acid:isonicotinamide. From single crystal data (left) and from pxrd data (right).

4.13 Isonicotinamide molecule from oxamic acid: isonicotinamide. The green molecule represent single crystal positions, red molecule represent DE solution 20.53 and the blue molecule represents final refined positions.

4.14 Oxamic acid molecule from oxamic acid:isonicotinamide. The green molecule represents single crystal positions, red molecule represent atoms from DE solution 20.53 and the blue molecule represents the final refined atom positions.

4.15 Variation of mutation rate *F* with constant population size. *F* = 0.3, 0.4 and 0.5 are shown by green, orange and blue lines respectively. Dotted lines represent the best R_{wp} of the population with the corresponding solid line representing the mean R_{wp} of the population.

4.16 Two diffraction peaks of oxamate:isonicotinamide over the temperature range investigated, 295 K(blue), 250 K (pink), 200 K (orange), 150 K (sky blue) and 100 K(purple).

4.17 The fractional variation of lattice parameters obtained from the LeBail refinement, plotted against temperature; Unit cell volume (purple spots), a (blue line), b (pink line), c (orange line) and β (sky blue dashed line).

4.18 The fractional variation of lattice parameters obtained from Rietveld refinement, plotted against temperature; Unit cell volume (purple spots), a (blue line), b (pink line), c (orange line) and β (sky blue dashed line).

4.19 Powder X-ray diffraction patterns of the starting materials, oxamic acid (orange), nicotinamide (red) and oxamic acid:nicotinamide multi-component material (black).

4.20 Solid state IR spectra of oxamic acid:nicotinamide mix (black) and the new multi-component crystal (blue).

4.21 Powder X-ray diffraction data of the starting materials oxamic acid (orange) and nicotinamide (red). Oxamic acid:nicotinamide crystallised from solution mediated crystallisation (black), oxamic acid:nicotinamide ground for 5 minutes (green), for 15 minutes (purple), for 20 minutes (blue) and oxamic acid:nicotinamide from sonic slurry (dark red).

4.22 Molecular structures used in the DE structure solution, torsion angles are indicated by arrows. Hydrogen atoms excluded from the calculation are shown in brackets.

4.23 Evolutionary progress plot for the successful solution of oxamic acid:nicotinamide showing the best R_{wp} (blue) and the mean R_{wp} (pink) for each generation.

4.24 The final Rietveld profile for oxamic acid:nicotinamide. The experimental diffraction pattern is shown by red circles, the calculated diffraction pattern by a solid green line and the difference plot as a solid pink line. Reflection positions are marked by black dots.

4.25 ORTEP diagram of the two asymmetric molecules in the multi-component crystal

4.26 The tetrameric unit formed in the crystal structure oxamic acid:nicotinamide. Hydrogen bonds are indicated as dashed lines.

4.27 The plannar oxamate acid sheet as viewed along the *a* axis. Hydrogen bonds are shown by the dotted green line.

4.28 The nicotinamide sheet, viewed along the *a* axis

4.29 View along the *b* axis showing the layered structure of oxamic acid and nicotinamide co-crystal adduct.

4.30 Nicotinamide layer from the single crystal structure of oxamate:nicotinamide.

4.31 Nicotinamide layer from the DE solution (R_{wp} = 10.38%) of oxamate: nicotinamide.

4.32 Oxamate layer from the single crystal structure of oxamate:nicotinamide

4.33 Oxamate layer from the DE solution (R_{wp} = 10.38 %) of oxamate acid:nicotinamide.

4.34 The *cis* (left) and *trans* nicotinamide molecule configuration(right)

4.35 Oxamate ion molecule from oxamate: nicotinamide. The green molecule represents single crystal positions, the red molecule represents atoms from the DE solution (10.38) and the blue molecule represents the final refined atomic positions.

4.36 The nicotinamide molecule from oxamate acid: nicotinamide. The green molecule represents single crystal positions, the red molecule represents atom positions from the DE solution (10.38) and the blue molecule represents final refined positions.

4.37 Two diffraction peaks of oxamic acid:nicotinamide over the temperature range investigated, 295 K(blue), 250 K (pink), 200 K(orange), 150 K(sky blue) and 100 K(purple).

4.38 The fractional variation of lattice parameters obtained from LeBail refinement, plotted against temperature; Unit cell volume (purple spots), *a* (blue line), *b* (pink line), *c* (orange line) and β (sky blue dashed line).

4.39 The fractional variation of lattice parameters obtained from Rietveld refinement, plotted against temperature; Unit cell volume (purple spots), *a* (blue line), *b* (pink line), *c* (orange line) and β (sky blue dashed line)

5.1 Molecular diagrams of fumaric acid (i), (ii) maleic acid , (iii) nicotinamide and iv) isonicotinamide

5.2 Powder X-ray diffraction patterns of the starting materials, fumaric acid (orange), nicotinamide (red) and the fumaric acid:nicotinamide multi-component material (black).

5.3 Solid state IR spectra of the fumaric acid and nicotinamide mix (dashed line) and fumaric acid:nicotinamide multi-component crystal (solid)

5.4 Powder X-ray diffraction data of the starting materials fumaric acid (orange) and nicotinamide (red). The fumaric acid:nicotinamide multi-component from solvent mediated recrystallisation (black), fumaric acid:nicotinamide from 10 minutes of LAG (green), from 15 minutes of LAG (purple), from 20 minutes of LAG (blue) and fumaric acid:nicotinamide from sonic slurry (dark red).

5.5 Molecular structures used in the DE structure solution, torsion angles are indicated by arrows. Hydrogen atoms excluded from the calculation are shown in brackets.

5.6 Evolutionary progress plot for the successful solution of fumaric acid:nicotinamide showing the best R_{wp} (blue) and the mean R_{wp} (pink) for each generation.

5.7 The final Rietveld plot for fumaric acid:nicotinamide. The experimental diffraction data is shown by red circles, the calculated diffraction pattern by solid green line and reflection positions are marked by black dots. The difference between the experimental and calculated diffraction pattern is shown by the pink line.

5.8 The molecular structure of fumaric acid:nicotinamide. Showing the atom numbering scheme. Displacement ellipsoids are drawn at the 50 % probability level and H atoms are shown as small spheres of arbitrary radii.

5.9 Fumaric acid and nicotinamide looking down the *a* axis. Carbon, nitrogen, oxygen and hydrogen atoms are shown in black, blue, red and white respectively

5.10 A view along the *b* axis, showing the hydrogen bonded sheets in the (010) plane. Carbon, nitrogen, oxygen and hydrogen atoms are shown in black, blue, red and white respectively.

5.11 Nicotinamide molecule from fuamric acid:nicotinamide. The green molecule represents single crystal positions and the blue molecule represents final refined powder positions (non-hydrogen atoms only).

5.12 Fumaric acid molecule from fumaric acid:nicotinamide. The green molecule represents single crystal positions and the blue molecule represents final refined powder positions (non-hydrogen atoms only)

5.13 Diffraction peak of fumaric acid:nicotinamide over the temperature range investigated, 295 K (blue), 250 K (pink), 200 K (green), 150 K (sky blue) and 100 K (purple).

5.14 The fractional variation of lattice parameters obtained from LeBail refinement, plotted against temperature; Unit cell volume (purple spots), a (blue line), b (pink line), c (orange line) and β (sky blue dashed line).

5.15 The fractional variation of lattice parameters obtained from Rietveld refinement, plotted against temperature. Unit cell volume (purple dashes), *a* (blue), *b* (pink), *c* (orange) and *β* (sky blue dashes).

5.16 Powder X-ray diffraction patterns of the starting materials, maleic acid (orange) and nicotinamide (red). The maleic acid:nicotinamide multi-component material product A (black) and product B (purple)

5.17 Solid state IR spectra of maleic acid and nicotinamide mix (dashed line) and the new multi-component crystal product A (solid line).

5.18 Proposed mechanism for the isomerisation of maleic acid when cocrystallised with nicotinamide

5.19 The powder X-ray diffraction patterns of product A (blue) and product B (red).

5.20 The powder X-ray diffraction patterns of fumaric acid:nicotinamide (black) and maleic acid:nicotinamide product B (purple).

5.21 Powder X-ray diffraction patterns of the starting materials, maleic acid (orange), nicotinamide (red). The maleic acid:nicotinamide multi-component material product A from solvent mediated crystallisation (balck), sonic slurry (green) and mechanochemical grinding (purple).

5.22 Molecular structures used in the DE structure solution, torsion angles are indicated by arrows. Excluded hydrogen atoms are shown in brackets.

5.23 Maleic acid molecule from maleic acid:nicotinamide. The red molecule represents single crystal positions and the blue molecule from the DE solution 16.43. (non-hydrogen atoms only).

5.24 Nicotinamide molecule from maleic acid:nicotinamide. The red molecule represents single crystal positions and the blue molecule from the DE solution 16.43. (non-hydrogen atoms only)

5.25 The molecular structure of maleate:nicotinamide. Showing the atom numbering scheme and the hard intermolecular hydrogen bonds within the asymmetric unit (dashed lines). Displacement ellipsoids are drawn at the 50 % probability level and H atoms are shown as small spheres of arbitrary radii.

5.26 Packing of maleate ions and nicotinamide molecules, viewed along the *a* axis.

5.27 A Hydrogen bonding network running in maleate:nicotinamide.

5.28 X-ray powder diffraction peaks of maleate:nicotinamide over the temperature range investigated, 295 K (blue), 250 K (pink), 200 K (green), 150 K (sky blue) and 100 K (purple).

5.29 The fractional variation of lattice parameters obtained from the LeBail refinement against temperature, Unit cell volume (purple spots), *a* (blue line), *b (*pink line)*, c* (orange line).

5.30 The fractional variation of lattice parameters obtained from the Rietveld refinement against temperature. Unit cell volume (purple spots), *a* (blue line), *b (*pink line)*, c* (orange line).

5.31 Powder X-ray diffraction patterns of the starting materials, maleic acid (orange) and isonicotinamide (red) and the maleic acid:isonicotinamide multi-component material (black).

5.32 Powder X-ray diffraction patterns of the starting materials, maleic acid (orange) and isonicotinamide (red). The maleic acid:isonicotinamide solvent mediated multi-component material (black), sonic slurry (purple) and mechanochemically ground (orange).

5.33 The molecular structure of maleate:isonicotinamide. Showing the atom numbering scheme and the hard intermolecular hydrogen bonds within the asymmetric unit (dashed lines). Displacement ellipsoids are drawn at the 50 % probability level and H atoms are shown as small spheres of arbitrary radii.

5.34 Maleate ions and isonicotinamide molecules ribbons running in the (011) plane.

5.35 Sheets of meleate ions and isonicotinamide molecules

6.1 Molecular structure of oxamic acid

6.2 *Cis* and *trans* isomers of oxamic acid

6.3 The powder diffraction pattern of oxamic acid Form I (red) and Form II (blue)

6.4 Diffraction pattern of oxamic acid ground for 10 minutes in ethyl acetate (pink) and methanol (blue)

6.5 High temperature DSC trace of oxamic acid form II

6.6 A dendogram produced by a PolySNAP, comparing simulated and experimental powder diffraction patterns for oxamic acid. Codes 1 and 2 represent forms I and II of oxamic acid, 3 (ciscis_ai50), 4 (ciscis_ak61), 5 (transcis_ai48), 6 (transcis_aj74), 7 (transcis_ak35), 8 (transcis_am52), 9 (transtrans_de50), 10 (transcis_fc58), 11 (transtrans_am58), 12 (transtrans_am62), 13 (transtrans_da59), 14 (transtrans_am56), 15 (transtrans_af42).

6.7 The molecular structure of oxamic acid and torsion angle

6.8 Differential evolution progress plot for the successful solution of oxamic acid, showing the best % R_{wp} (blue) and the mean % R_{wp} (pink).

6.9 The final Rietveld plot for oxamic acid. Experimental diffraction data is shown by red circles. The calculated diffraction pattern is shown by the solid green line. The difference is shown below in pink. Reflection positions are marked black dots.

6.10 Projection down the *a* axis showing the infinitely hydrogen bonded sheet of oxamic acid form I

6.11 A view along the *b* axis of oxamic acid. Infinitely hydrogen sheets running along the b axis.

6.12 Overlay of single crystal structure and *cis* DE solution of oxamic acid

6.13 Hydrogen bonding network in *cis(trans)*-oxamic acid conformer.

6.14 Hydrogen bonding network in *cis(cis)*-oxamic acid conformer

6.15 Model A, B and C, of oxamic acid

6.16 The fractional variation of lattice parameters obtained from LeBail refinement, plotted against temperature. Unit cell volume (purple dashes), a (blue) , b (pink), c (orange) and β (green) .

List of tables

1.1 The seven crystal systems

4.1 Initial lattice parameters, DE structure solution parameters, refined lattice parameters from Rietveld refinement and single crystal determination and Rietveld agreement factors.

4.2 Hydrogen bond geometry in oxamic acid:isonicotinamide, (Å and °).

4.3 The results from a number of DE calculations with variation in *F* (mutation rate) and NP (population size). For each epoch the final R_{wp} (in %) is given and figures within brackets indicate at which generation convergence was achieved. Runs giving the correct structure solution are indicated by green; the gold cell indicates the lowest R_{wp} achieved and the starting point for the successful structure refinement. Runs that have not converged by the maximum allowed number of generations are shaded grey.

4.4 MDE results for each epoch from five runs. For each epoch the final R_{wp} (in %) is given and figures within brackets indicate at which generation convergence was achieved. Runs giving the correct structure solution are indicated by green; the gold cell indicates the lowest R_{wp} achieved and the starting point for the successful structure refinement.

4.5 Lattice parameters from the LeBail fitting of oxamate:isonicotinamide. ΔL/L0 values are given in square brackets.

4.6 Lattice parameters from the Rietveld refinement of oxamate acid:isonicotinamide. ΔL/L0 values are given in square brackets.

4.7 Linear thermal expansion co-efficients of the lattice parameters of oxamate:isonicotinamide.

4.8 Initial lattice parameters, DE structure solution parameters, refined lattice parameters from Rietveld refinement and single crystal determination and Rietveld agreement factors.

4.9 Intermolecular parameters for the oxamic aicd:nicotinamide co-crystal adduct (Å)

4.10 The results from a number of DE calculations with variation in *F* (mutation rate). For each epoch the final R_{wp} (in %) is given and figures within brackets indicate at which generation convergence was achieved. Runs giving the correct structure solution are indicated by green; the gold cell indicates the lowest R_{wp} achieved and the starting point for the successful structure refinement. Runs that have not converged by the maximum allowed number of generations are shaded grey.

4.11 Lattice parameters from the LeBail fitting of oxamate:nicotinamide. ΔL/L0 values are given in square brackets.

4.12 Rietveld lattice parameters of oxamate:nicotinamide ΔL/L0 values are given in square brackets.

4.13 Linear thermal expansion co-efficients of the lattice parameters of oxamic acid:nicotinamide salt.

5.1 Initial lattice parameters, DE structure solution parameters, refined lattice parameters from Rietveld refinement and single crystal determination and Rietveld agreement factors.

5.2 Hydrogen bonds geometry in fumaric acid:nicotinamide (Å and °).

5.3 The results from a number of DE calculations with variation in *F* (mutation rate) and NP (population size). For each epoch the final R_{wp} (in %) is given and figures within brackets indicate at which generation convergence was achieved. The gold cell indicates the lowest R_{wp} achieved and the starting point for the successful structure refinement. Runs that have not converged by the maximum allowed number of generations are shaded grey.

5.4 Lattice parameters from the LeBail fitting of fumaric acid:nicotinamide. ΔL/L0 values are given in square brackets.

5.5 Rietveld lattice parameters of fumaric acid:nicotinamide

5.6 Linear thermal expansion co-efficients of the lattice parameters of fumaric acid:nicotinamide.

5.7 Initial lattice parameters, DE structure solution parameters and single crystal determination.

5.7 Hydrogen bonds geometry in maleic acid:nicotinamide (Å and °).

5.8 The results from a number of DE calculations with variation in F (mutation rate) and NP (population size). For each epoch the final R_{wp} (in %) is given and figures within brackets indicate at which generation convergence was achieved. Runs that have not converged by the maximum allowed number of generations are shaded grey. Runs 6-9 the preferred orientation was set to 1.64575 in the [001] direction.

5.9 Hydrogen bonds geometry in maleic acid:nicotinamide (Å and °).

5.10 Lattice parameters from the LeBail fitting of maleate:nicotinamide product A. ΔL/L0 are given in square brackets

5.11 Lattice parameters from the Rietveld fitting of maleate:nicotinamide product A. ΔL/L0 are given in square brackets

5.12 Linear thermal expansion co-efficients of maleate:nicotinamide

5.13 Single crystal parameters of maleate:isonicotinamide

5.14 Hydrogen bonds geometry in maleate:isonicotinamide (Å and °).

6.1 Solvent screen of oxamic acid

6.2 Initial lattice parameters, DE structure solution parameters, refined lattice parameters from Rietveld refinement and single crystal determination and Rietveld agreement factors

6.3 Hydrogen bond geometry in oxamic acid, Å and °

6.4 Indexed lattice parameters of oxamic acid form II

6.5 The results from a number of DE calculations with variation in *F* (mutation rate) and NP (population size). For each epoch the final R_{wp} (in %) is given and figures within brackets indicate at which generation convergence was achieved. Each run has been classed as either *cis* or *trans*.

6.6 The results from a number of DE calculations with variation in *F* (mutation rate) and NP (population size). For each epoch the final R_{wp} (in %) is given and figures within brackets indicate at which generation convergence was achieved.

6.7 The results from a number of DE calculations with variation in *F* (mutation rate) and NP (population size). For each epoch the final R_{wp} (in %) is given and figures within brackets indicate at which generation convergence was achieved

6.8 Linear thermal expansion co-efficients of the lattice parameters of oxamic acid

List of Equations

1.1 Bragg's law

1.2 Reverse Fourier transform of the diffraction pattern

1.3 % R_{wp}, y_{iobs} is the experimentally observed intensity at a value of 2θ and y_{icalc} is the calculated intensity at 2θ.

1.4 The creation of a trial structure from members of the preceding population. *K* is the recombination factor and *F* is the mutation factor

1.5 Gibbs free energy of a system

1.6 Where C_v is equal to the heat capacity, R (ideal gas constant), h (planck constant), k (Boltzmann constant), T (temperature in K), υ (frequency)

1.7 Lennard Jones empirical function

1.8 a) Linear thermal expansion of a material where L_0 and is the original length, ΔL is the change in the length and α is the thermal expansion co-efficient

b) Linear thermal expansion of a material where V_0 is the original volume, ΔV is the change in the volume and α is the thermal expansion co-efficient

2.1 y_i(calc) calculation used to in the calculation of % R_{wp}

2.2 Contribution of the m^{th} Bragg peak to the intensity at point i

3.1 Transparency shift error

4.1 Linear thermal expansion at constant pressure L0, is the shortest length recorded dL and δT are the change in length and temperature respectively over the temperature range

1.0 Introduction

Crystallography is defined in the Oxford English dictionary as the branch of physical science which treats the structure of crystals and their systematic classification. The etymology of the word crystallography derives from the Greek, Κρύσταλλος (crystal) and γραφίά (writing). The modern day field of crystallography celebrates its centenary in 2012, after the work of Max von Laue demonstrated that X-rays were electromagnetic in nature and were diffracted by crystalline materials. However, the interest in crystals and their properties has long preceded the mathematical approach developed by Laue, as crystals have long been admired for their ascetically pleasing nature and their debatable mystical power.

The field of crystallography is ever expanding, mainly due to the rapid development of technology that complements the field; whether it is that of more sensitive instrumentation or greater computer power, aiding with the running of structure solution algorithms. The field can truly be considered to be multidisciplinary as it crosses many scientific interfaces, illustrated by the award of the Nobel Prize for chemistry in 2009 to Ramakrishnan, Steitz and Yonath for the studies of the structure and function of the ribosome [1, 2] using protein crystallography.

The Nobel Prize for physics in 2009 was awarded to the inventors of the charge-coupled device (CCD), Willard Sterling Boyle and George Smith[3]; a discovery that has vastly improved the detection of diffracted X-rays.

Crystallography has shaped many scientific advances in the 20th century, as it enables us to position atoms in three dimensions. In the context of molecular materials, the arrangement and packing of molecules within the crystal structure controls the macroscopic properties of the molecular crystalline solid. Armed with this vital structural information, chemists can aim to manipulate the crystalline structure in

order to deliver molecular solids with preferential physical and chemical properties; in effect "crystal engineering".

Molecular crystallography is the central approach encompassing the research contained within this thesis. Crystal engineering approaches are employed in the design of the materials covered here and both powder and single-crystal diffraction used to investigate the resulting materials. The solution of crystalline structure from powder X-ray diffraction still remains a non-trivial task and hence a comparison of the two techniques is used. The ability to use pxrd effectively in these cases allows the solid state chemist to probe systems potentially inaccessible via traditional single crystal approaches.

1.1 The fundamentals of crystalline solids

A crystalline solid contains a three dimensional periodic long-range order. The smallest repeating unit of a crystalline solid is known as a *unit cell*. The *unit cell* is defined by three vectors *a*, *b* and *c*, which form a parallelepiped (figure 1.1). The three vectors are intercepted by three angles α, β, and γ. The whole extended crystalline structure can be reproduced by translational symmetry of the unit cell in all directions. If each molecule was to be represented by a single point, the resulting regular array of points, repeating in nature, connected by translational symmetry, would be known as the *lattice* of the structure.

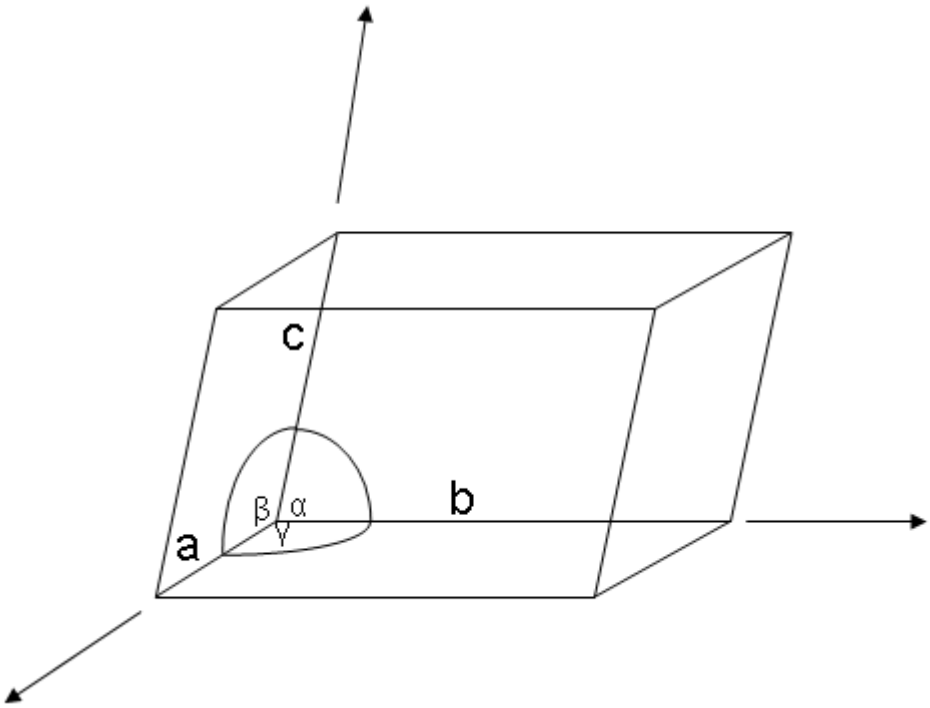

Figure 1.1: Unit cell parallelepiped

Within the unit cell there is a sub-unit known as the *asymmetric unit*. The *asymmetric unit* often describes the structural motif within a unit cell, which after the application of the symmetry operations (i.e. rotation, reflection, inversion and translation) allowed by the space group, generates the complete crystal structure. The asymmetric unit may contain one or more molecules, or even a fraction of a molecule if the molecule contains symmetry within itself.

The combination of both reflection and rotation symmetry implies restrictions onto the lattice parameters of the unit cell. The result of these restrictions is that crystalline solids can broadly be sub-divided into seven crystal systems (Table 1.1). In addition to the seven crystal systems there are four lattice types known as primitive (P), body centred (I), face-centred (F) or C-centred (A, B, C), as shown in figure 1.2.

Table 1.1: The seven crystal systems

Crystal System	Unit cell dimensions	Bravais lattices	Essential symmetry
Cubic	$a = b = c$ $\alpha = \beta = \gamma = 90^\circ$	P, I, F	Four C_3 axes
Hexagonal	$a = b \neq c$ $\alpha = \beta = 90^\circ, \gamma = 120^\circ$	P	One C_6 axis
Trigonal	a = b = c $\alpha = \beta = \gamma \neq 90^\circ$	P (R)	One C_3 axis
Tetragonal	a = b ≠ c $\alpha = \beta = \gamma = 90^\circ$	P, I	One C_4 axis
Orthorhombic	$a \neq b \neq c$ $\alpha = \beta = \gamma = 90^\circ$	P, C, (A), I, F	Three C_2 axis and/or mirror planes
Monoclinic	$a \neq b \neq c$ $\alpha = \beta = 90^\circ \neq \beta$	P C (I)	One C_2 axes and/or mirror plane
Triclinic	$a \neq b \neq c$ $\alpha \neq \beta \neq \gamma$	P	None

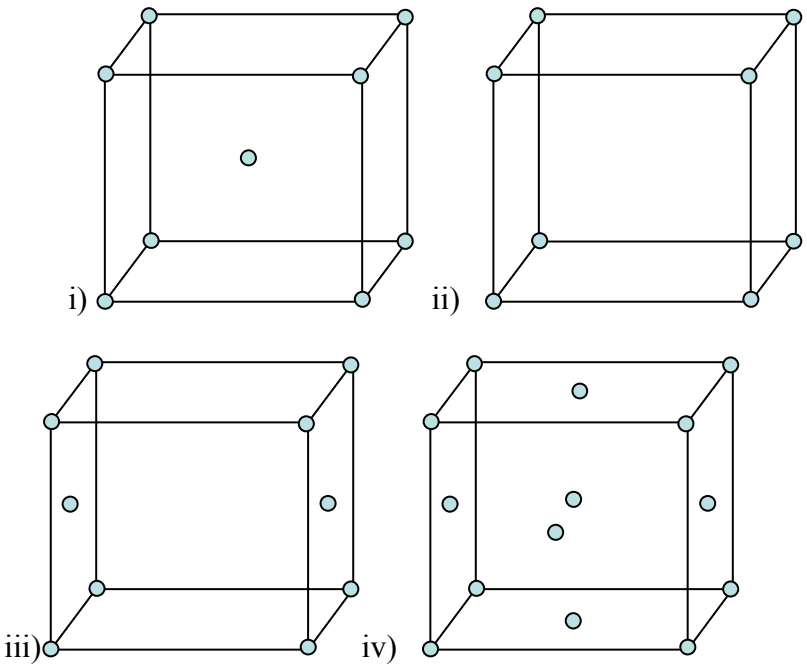

Figure 1.2: Lattice types, i) Body centred (I), ii) Primitive (P), iii) C centred, iv) F centred

1.2 Space groups

Whereas a point group is the complete collection of all symmetry points passing through a central point describing the symmetry of a single individual object, a space group is the complete collection of all symmetry elements that describe an infinitely repeating pattern. By combination of the 7 crystal systems, 14 Bravais lattices and the 32 point groups, we are able to define 230 unique space groups.

1.3 X-ray diffraction from crystalline solids

X-ray diffraction from crystalline solids is an established phenomenon discovered by a German physicist, Max von Laue in 1912, who was interested in the way light and crystals interacted with one another. Von Laue demonstrated mathematically that X-rays were diffracted by crystalline materials and established that X-rays are electromagnetic in nature. He received the Nobel Prize in physics in 1914 for this work. Subsequent work allowed Sir William Bragg and his son Sir Lawrence Bragg to establish a new area of science which led to the analysis of crystal structure by the means of X-ray diffraction. The use of X-rays as a device for discovering the precise three dimensional crystal structure of molecular solids was entirely due to the Braggs and their work was recognised by the award of the Nobel Prize, jointly to father and son, in 1915.

It was shown that electromagnetic radiation (X-rays) with a wavelength similar to that of interplanar distances (d) in crystal planes (of the order 1Å) incident on planes of atoms, results in X-rays being scattered both constructively and deconstructively.

Bragg's law (equation 1.1) is the central to diffraction as it gives the geometric conditions under which a diffracted beam can be observed. The Bragg model as

shown in figure 1.3, can be seen as the reflection of the incident radiation by parallel planes of atoms. The planes which are defined by Miller indices (*hkl*) will only give rise to constructive interference when the second beam, which has travelled the extra distance of AB + BC, is an integral (n) multiple of the wavelength (λ).

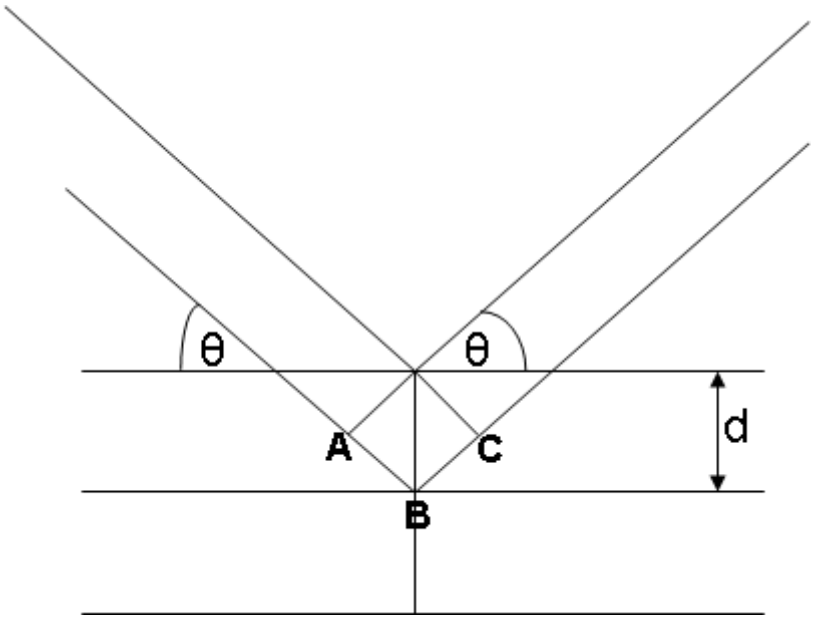

Figure 1.3 The geometric conditions required for Bragg diffraction

$$n\lambda = 2d\sin\theta$$

Equation 1.1: Bragg's law

The standard source of laboratory X-rays is the X-ray tube. X-rays are produced when electrons decelerate as a consequence of hitting a metal target in an evacuated enclosure (most commonly copper or molybdenum). Electrons are drawn to the target as a highly positive charge is kept on the target/anode. Most of the kinetic energy is converted into heat but a small amount of the kinetic energy causes an electron in a core atomic orbital to be ejected. An electron from a higher orbital fills the core hole

and the resulting drop in energy results in emission of radiation of a definite wavelength. Several transitions are possible producing a broad spectrum of background radiation, with a series of intense maxima. In the case of a Cu anode, $CuK\alpha_{1,2}$, transitions produce a maxima at wavelengths(λ) equal to 1.54433 and 1.54051 Å respectively. Metal filters or monochromators can be used to select the required wavelength.

More intense X-rays can be produced from a synchrotron storage ring in which electrons moving at relativistic speed are contained by magnetic fields. The radiation, which is emitted tangentially at numerous stations situated just off the storage ring, from which X-rays that are produced are both tuneable and of a higher flux[4].

X-rays interact with electrons in a solid and hence X-ray diffraction gives a measurement of electron density within a unit cell of a crystalline system. The X-rays are scattered from the electron cloud surrounding an atom at the same frequency as the primary beam, known as Thomson scattering, and are collected on a detector. In the forward direction ($2\theta = 0^{\circ}$) all the electrons scatter X-rays in the same phase, but as 2θ increases, the intensity of the scattered X-rays decreases due to destructive interference. The value of the scattering factor is therefore proportional to the number of electrons in the atom, and therefore small organic molecular materials are not good X-ray scatterers.

1.4 The crystallographic phase problem

A diffraction pattern is related to the Fourier transform of the electron density (see equation 1.2). Thus it should be straightforward to obtain the electron density from the diffraction pattern, and hence solve the crystal structure.

$$\rho(xyz) = \frac{1}{V}\sum_{h,k,l} F(hkl)\cdot \exp\left[-2\pi i(hx+ky+lz)\right]$$

Equation 1.2: Reverse Fourier transform of the diffraction pattern

The image of electron density, $\rho(xyz)$ is obtained by adding all of the diffracted beams with their correct amplitudes and phases. The intensity of the scattered radiation (X-rays) is directly proportional to the square modulus of the structure factor. The diffraction pattern gives only information on intensities and no information on the associated phases of the intensities, thus eluding to the crystallographic phase problem, where it is not possible to calculate the reverse Fourier Transform from the diffraction pattern. In traditional crystallographic approaches the phase problem is solved using 'direct methods'[5] in which statistics and probability are employed to compute the values of the phases. In a centrosymmetric system the phase choice is 0 or π, whereas for a non-centrosymmstric system may lie anywhere between 0 and 2π.

1.5 Single crystal vs. powder diffraction

Single crystal X-ray diffraction experiments require a crystal of a certain quality and size in order to successfully obtain diffraction data that will lead to an accurate structure solution. A preliminary rotational image is often taken before the collection of intensities to assess the quality of the crystal. This preliminary data may also be used to index the crystal system which in turn deciphers the orientation matrix selected for the collection of further data. To record the intensity of individual reflections from lattice planes (hkl) the crystal is systematically moved in three dimensions (Φ, Ω, 2θ) with respect to the beam. The resulting diffraction data are

resolved into three dimensional reciprocal space, with the relative positions of the diffraction maxima used to determine the lattice parameters of the unit cell. The intensities of the diffraction maxima are determined by the structure factor modulus $|F(s)|$. After data collection, corrections concerning instrumental factors, polarization effects, X-ray absorption and potential crystal decomposition, are applied to the entire structure. A simple schematic of single crystal diffraction is shown by figure 1.4.

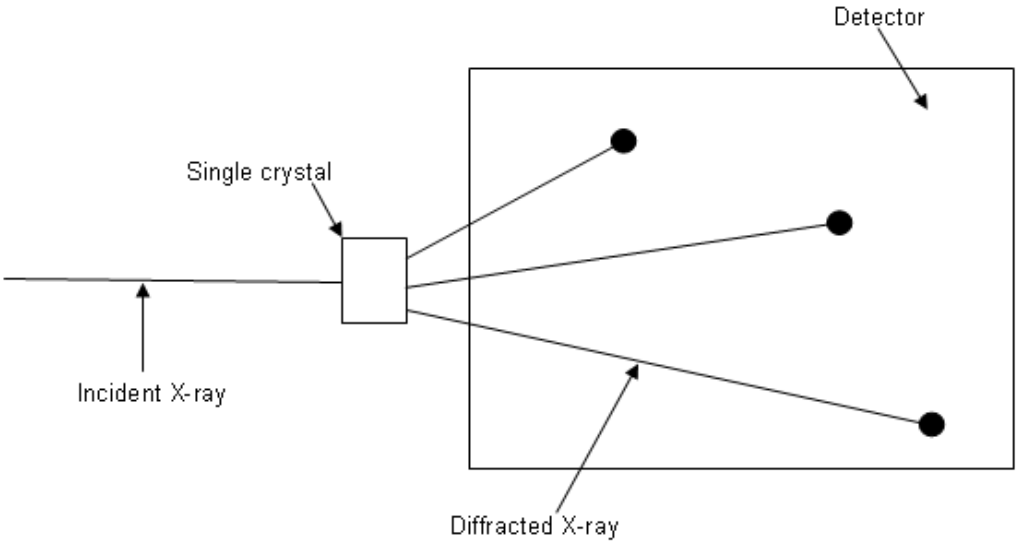

Figure 1.4: Diffraction from an oriented single crystal

In powder X-ray diffraction (pxrd) there are many crystallites that satisfy the Bragg criterion for diffraction from planes (*hkl*). Hence, unlike single crystal X-ray diffraction in which the diffraction maxima are resolved into three dimensions, cone-shaped Debye rings are formed (Figure 1.5). The diffraction data is collected by taking a slice through the Debye ring along 2θ. This process compresses three dimensional data into one dimension (2θ) and results in the inherent problems associated with pxrd data, peak overlap. This can be a particular problem when probing molecular materials with large unit cells and low symmetry, as this

combination leads to a high density of peaks. The inability to extract accurate integrated peak intensities I(s) and accurate peak positions from pxrd results in the structure solution process being challenging and more limited in terms of the complexity of analysis possible in comparison to single crystal diffraction.

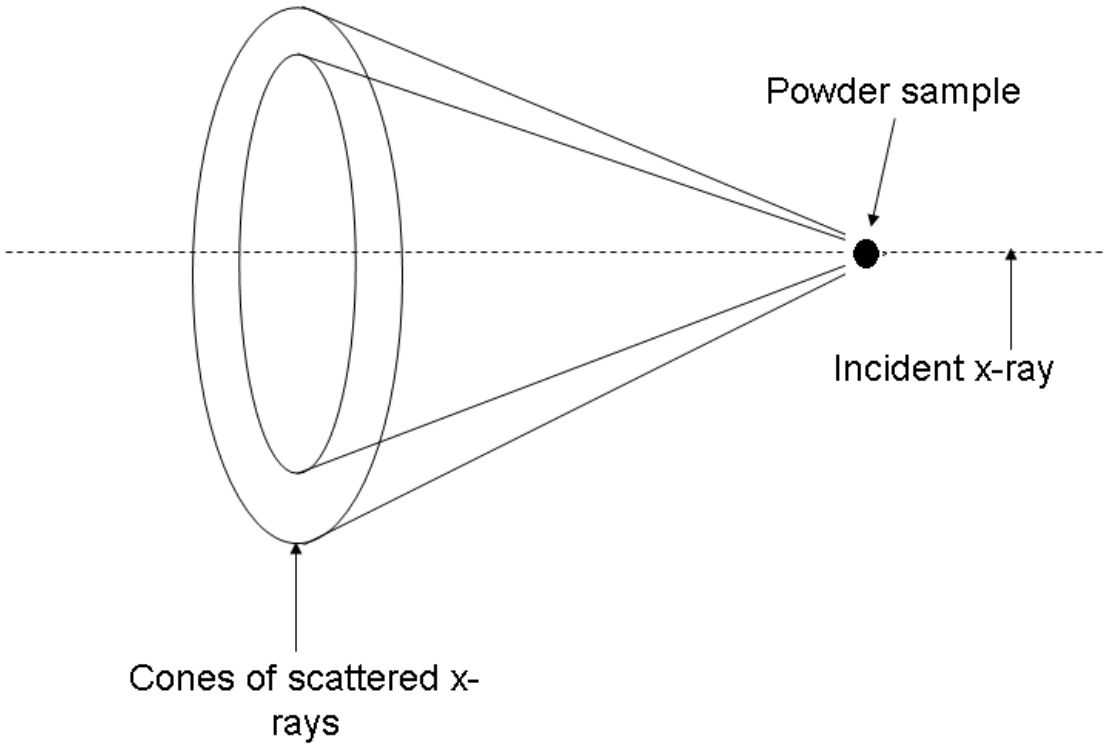

Figure 1.5: Diffraction cones of scattered X-rays, diffracted from a powder sample.

Structures solved via this route are often less precise and of lower accuracy to that of single crystal structures. However, pxrd data is a vital source of information if good quality crystals of the system under investigation cannot be grown, or the method of synthesis is not conducive to the production of good-quality crystals, i.e. when using mechanochemical synthesis (section 1.18). Powder diffraction is often used in cases where there are problems in crystal growth, twinning, or where extreme experimental conditions are required.

1.6 Preferred orientation

There are however problems that can arise with the powder sample itself. An ideal powder sample contains crystallites in random orientations ensuring that not one orientation is artificially more likely to satisfy the Bragg diffraction criterion than other. Preferred orientation occurs when some orientations are favoured and occur more in the sample. This phenomenon is more likely to occur with certain crystallite morphologies, e.g. anisotropic crystallites (long needles or flat platelets). If preferred orientation does occur, certain reflections related by a particular set of Miller indices within the diffraction pattern, will be distorted in terms of intensity. This compounds the problems encountered when extracting intensity information needed in the structure solution process as the intensities do not arise purely from atomic positions. The powder structure solution approach based on the traditional process of extracting intensities from the diffraction pattern is affected more by the presence of preferred orientation than with direct space approaches (section 1.13) as the inclusion of a structural model can restrict the impact of preferred orientation in subsequent refinement.

In order to avoid preferred orientation, sample preparation is very important. Commonly, the occurrence of preferred orientation can be minimised (or better detected) using a capillary in the packing of the powder sample. This geometry is favourable over a flat disc in the case of plate-like crystals which tend to align themselves parallel to the surface of the disc. In a capillary, more random packing of the crystallites leads to more ideal sample. Other experimental approaches include mixing the sample with an amorphous material, grinding to reduce the anisotropic nature of the crystals, and spray drying[6].

However, powder samples containing a high amount of preferred orientation can still be fully structurally characterised using pxrd data, as illustrated in the structure solution of oxamate:nicotinamide (section 4.2). This is often done through the use of Rietveld refinement which can be used to model the effect of preferred orientation effectively with the March-Dollase function[7].

1.7 Structure solution from powder diffraction

Structure solution from pxrd is intrinsically a difficult problem as discussed in section 1.5. The motivation behind the advancement and development of full structural solution of organic molecular materials from pxrd is that many small organic molecular materials cannot be prepared as good-quality crystals.

A pxrd experiment contains the same information as a single crystal experiment but the data is compressed into one dimension (2-theta) resulting in peak overlap. This problem is further compounded as many organic molecular materials often contain a large unit cell and low space group symmetry which results in a higher number of unique peaks with distorted intensities.

Traditionally, pxrd it most commonly used as a qualitative method of phase identification, e.g. fingerprinting of materials or analysis of mixtures. However, due to the rapid development in the power of X-ray sources (e.g. synchrotron radiation), detectors e.g. imaging plates and charged coupled devices and computational structure determination methods, pxrd has been used to determine an ever growing number of increasingly complex crystal structures. Single crystal X-ray diffraction remains the technique of choice, but powder methods have advanced significantly over the last decade[6, 8].

The overall process of structure determination from pxrd can be sub-divided into three distinct sections (figure 1.6):

1) Indexing of the unit cell from peak positions in the diffraction data and space group assignment from systematic absences.
2) Structure solution; location of approximate atomic positions from peak intensity data.
3) Structure refinement, most commonly using the Rietveld profile-fitting method[9].

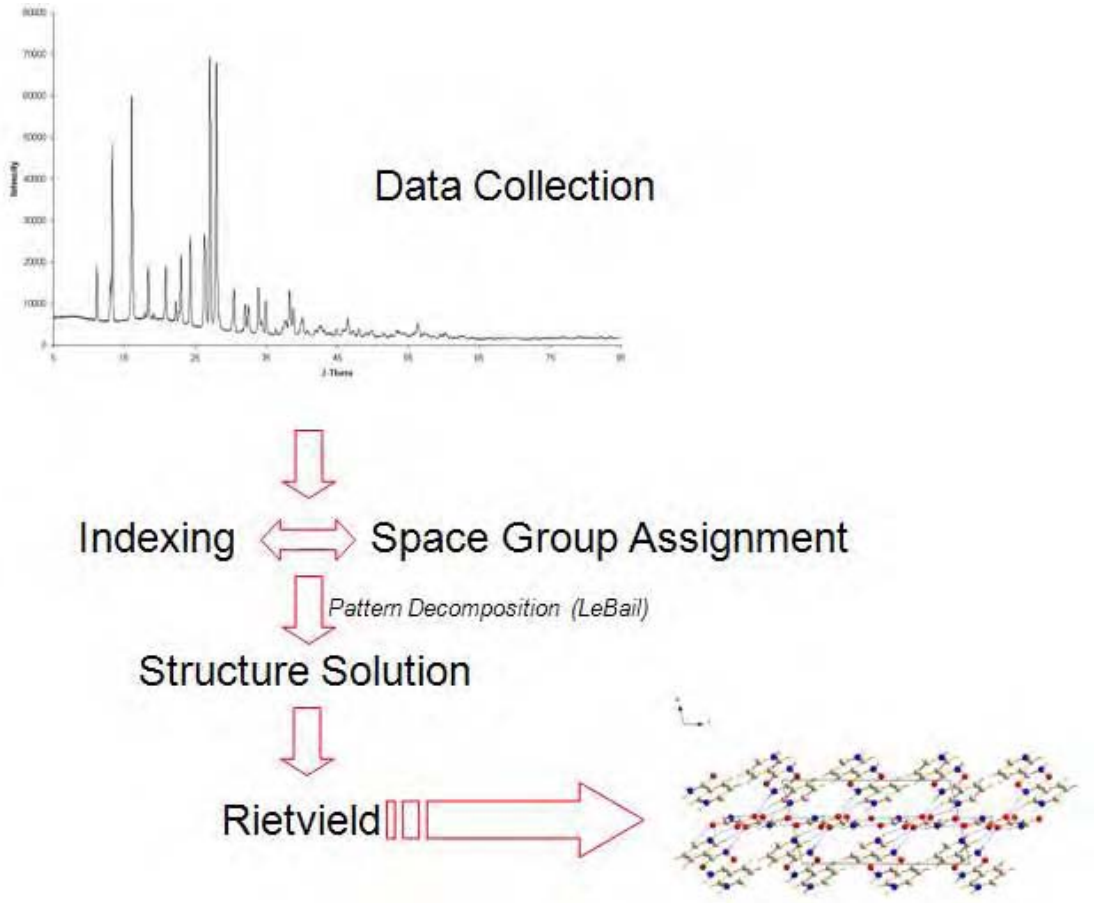

Figure 1.6: A flow diagram outlining the processes involved in structure solution from pxrd.

1.7.1 Indexing

Indexing a powder diffraction pattern successfully aims to determine the correct unit cell parameters and crystal class of a sample. The process of indexing can often be the defining step in the overall process of crystal structure solution from pxrd. If a unit cell cannot be determined, the rest of the structure determination process cannot continue. Many indexing algorithms have been developed including TREOR90[10], ITO[11] and DIVCOL91[12]. These reproduce peak positions generated from possible sets of lattice parameters. A figure-of-merit such as M_{20}[13] is used to rank the generated lattice parameters. In this thesis, a suite of indexing algorithms, CRYSFIRE[14] has been used.

Peak overlap can make the selection of precise positions of reflections difficult in a diffraction pattern, but there are other factors which can prevent fast and reliable indexing. The presence of an impurity phase will lead to problems as the peaks used for indexing are not indicative or reliable. A common source of error is also introduced by the zero-point correction of the diffractometer, where the position of the sample in real terms is different to the calibrated position. This error may be estimated and corrected for by the use of internal and external standards.

Due to the nature of some solid-state molecular synthesis approaches, for example liquid assisted grinding, poor quality powder samples may be produced, resulting in peak broadening, further exaggerating the issue of peak overlap in the diffraction pattern.

1.7.2 Space group assignment

A space group may be assigned to a crystal system by methodically assessing the systematic absences in the diffraction pattern. Due to the symmetry restraints related to specific space groups, some reflections (hkl) will be systematically absent from the diffraction pattern, regardless of unit cell contents. To allow unambiguous space group assignment, peaks need to distinguishable from one another in the case of conventional laboratory data (at least 0.05˚ in 2θ).

If systematic absences are not explicit in defining a space group the structure solution step may be run with a selection of possible space groups. Complementary solid state techniques, such as solid state NMR (nuclear magnetic resonance) [15], aid in space group assignment as the number of molecules present in the asymmetric group of the unit cell can be determined.

1.7.3 Pattern decomposition

When the correct unit cell has been identified through indexing, a 'structureless' refinement (LeBail[16] or Pawley[17]), known as pattern decomposition is used to achieve a more accurate description of the lattice parameters, zero-point and pseudo-voigt peak shape. Diffraction maxima are established along with instrumental settings that account for zero point error through a series of least squares refinement cycles. Unlike a Rietveld refinement, the peak intensities are also treated as refinable variables. If the pattern decomposition step is completed satisfactorily, the information is then used in the structure solution step and will allow for the final model to be more stable in the final refinement. The process of pattern decomposition produces a "target" agreement factor (% R_{wp}) which the structure solution (and refinement) steps are aiming towards.

The pattern decomposition also extracts integrated intensities from the pattern that could be used in a direct methods structure solution or a chi-squared based direct space approach.

1.7.4 Structure solution

Two distinct approaches are taken towards structure solution from pxrd; traditional methods and the direct space approach. The traditional approach is based on methods used in structure solution from single crystal X-ray diffraction, where individual intensities (I(hkl)) are extracted from individual reflections directly from the powder diffraction pattern. One problem with this approach is that of peak overlap (refer to section 1.9) and the inability to extract reliable intensities. However, the approach has been successful in the structure solution of molecular materials from pxrd[18-20].

The second and more recently developed approach to solving crystal structure from pxrd is a 'direct space' approach. In this technique a "trial" structure is produced in isolation to that of the experimental powder diffraction pattern. A suitable figure-of-merit indicator (in our case % R_{wp}) is used to compare the similarity of the trial structure and the experimental diffraction pattern. The R-factor is taken from the Rietveld program[9] and compares the whole digital diffraction profile (equation 1.3).

$$R_{wp} = 100 \times \sqrt{\frac{\sum_i w_i \left(y_{i\,obs} - y_{i\,calc}\right)^2}{\sum_i w_i \left(y_{i\,obs}\right)^2}}$$

Equation 1.3: % R_{wp}, y_{iobs} is the experimentally observed intensity at a value of 2θ and y_{icalc} is the calculated intensity at 2θ, w_i is the weight assigned to the intensity associated with data point *i*.

A term quoted throughout chapters 4, 5 and 6 is χ^2 (equation 1.4 & 1.5), which describes the goodness of fit of an observed distribution (experimental diffraction pattern) against a theoretical one (model produced diffraction pattern).

$$R_e = 'R - \exp ected' = \left[(N-P)/\sum w_i y_i\right]^{1/2} \quad \text{[Equation 1.4]}$$

$$\chi^2 = R_{wp} / R_e \quad \text{[Equation 1.5]}$$

Equation 1.4: R_e, P is the number of parameters adjusted, N is the number of observations, w_i is the weight assigned to the intensity associated with data point *I*, y_i is the experimentally observed intensity at a value of 2θ

Equation 1.5: χ^2 is equal to the square of the ratio of R_{wp} over R_e

Reliable peak shape parameters and accurate lattice parameters are calculated in the pattern decomposition process is performed by LeBail[16] or Pawley[17] approaches) and this information is key to the calculation of a reliable R_{wp} indicator.

The measure of structural complexity also differs in both approaches; in the traditional approach the number of atoms in the asymmetric unit defines the difficulty of the problem, whereas in the direct space approach it is the number of variables involved in the problem that sets the complexity. The variables required to define a structure in a direct space solution can be grouped into three sections; the position of the molecule in the unit cell (*x,y,z*), the orientation of the molecule (θ,Φ,Ψ), and the molecular conformation where freely rotating sections of the molecule are taken into account. The hypersurface of R_{wp} is defined by the set of variables described above and hence incorporates prior crystallographic and chemical knowledge. This acts to reduce the dimensionality of the hypersurface (rather than treating individual atoms) making the structure solution more efficient.

This study concentrates on the differential evolution direct space approach to solving crystal structures using pxrd. There are several other types of direct space approaches that can be found in the literature that use various optimisation techniques to search the hypersurface, such as Monte Carlo[21-26], simulated annealing[27-31], genetic algorithms[32-35] and grid searches[36-40]. All of these approaches have been successful in correctly solving crystal structures from pxrd data, but vary widely in terms of computational efficiency.

1.7.5 Differential evolution

Differential evolution (DE) is an evolutionary algorithm that is widely used in the optimisation of real space parameters[41, 42]. It is a population based optimisation technique that uses a concept of fitness (% R_{wp}) to find a global minimum. DE maintains a population of trial structures by producing offspring from trial structures through a combination of mutation and recombination (equation 1.6).

$$\text{Offspring} = \text{Parent} + K\,(\text{Random}_1 - \text{Parent}) + F\,(\text{Random}_2 - \text{Random}_3)$$

Equation 1.6: The creation of a trial structure from members of the preceding population. *K* is the recombination factor and *F* is the mutation factor.

At the start of the calculation, the trial structures are spread across the hypersurface, as structural parameters for each trial structure are chosen at random. This will lead to the production of distinct and diverse offspring as the initial vectors between members of the population are likely to be large. As the calculation progresses the population will become more alike and less diverse, leading to the shortening of vectors and resulting in convergence of the calculation.

In the DE, each member of the population produces a trial (or offspring) structure which is assessed for its fitness using % R_{wp} (equation 1.3) as the experimental powder diffraction pattern is compared with that simulated from the trial structure. Each member of the population produces an offspring using equation 1.4. If the offspring is fitter than its parent, then the offspring replaces the parent in the population, the opposite is true if the parent is fitter than its offspring. This deterministic approach gives efficient convergence. After each generation is completed, both mean and best % R_{wp} are calculated and the next generation commences in which the process is repeated. Convergence is achieved when the mean and best % R_{wp} are equal, i.e. when the population of structures are the same. The DE technique produces a structure which is only the starting point for Rietveld refinement[9]; in which more flexible structural features are often introduced. More details of the DE and its implementation are given in chapter 2.

1.7.6 Rietveld refinement

As mentioned above, the starting point for a Rietveld refinement[9] is a crystal structure which has been generated by structure solution, in this case from the DE. In order for a refinement to be successful, the crystal structure generated from the DE will have to be close to, or a good description of, the final structure. The refinement considers every point in the powder diffraction pattern as an individual intensity, and then compares it to the diffraction pattern simulated by the model, using % R_{wp} as a figure of merit (equation 1.3). Individual parameters that define the structure (e.g. atomic coordinates) are adjusted by a series of least-square refinements in order to achieve the optimal fit between the two diffraction patterns. Geometric restraints are typically used in a refinement and are 0.01 (tight restraints) on bonds to hydrogen atoms and

0.05 (soft restraints) on bonds between non-hydrogen atoms. The restraints are based on standard molecular geometries derived from prior chemical knowledge[43]; this bias will ensure that the final refined model will be chemically acceptable. Refinements which contain soft restraints generally allow a more stable refinement in the case of molecular structures than those without.

Rietveld refinement can be carried out using a number of different programs; GSAS[44], TOPAS[45], FULLPROF[46] and RIETAN[47] are amongst the most popular in the crystallographic community. For a refinement to be deemed successful it must satisfy three criteria; (i) the model must produce a pattern which is in good visual agreement with that of the experimentally produced diffraction pattern, (ii) the agreement factor (% R_{wp}) must be close to that of the agreement factor produced from the pattern decomposition step (Lebail[16] or Pawley) and (iii) the crystal structure must make both visual and structural sense. In the case of the structures considered in this thesis, this latter check is often judged on expected or predictable hydrogen bond network (chapters 4 and 5). Refinements are often unsuccessful and unstable but this may not always indicate an incorrect model. This may instead be due to poor quality data or sample effects such as preferred orientation which interferes with reflection intensity (see experimental section 3). However, it is important the input model from the structure solution is of sufficient quality or the refinement will fail.

1.8 Polymorphism

Crystalline polymorphism (Greek: poly = many, morph = form) is a comparatively established area of solid state chemistry that continues to attract considerable academic and industrial attention. As with most areas of science, an all encompassing definition is often hard to assert, but a working definition was given by McCrone[48] “a

solid crystalline phase of a given compound resulting from the possibility of at least two different arrangements of the molecule of that compound in the solid state". This phenomenon challenges the field of the organic solid state and our understanding of crystal packing, intermolecular interactions and crystal growth.

The explosion in the volume of research into the phenomenon of polymorphism has followed the rapid development of solid state research techniques, e.g. faster data acquisition in X-ray crystallography in conjunction with the advancements in other solid state techniques such as infra-red spectroscopy, NMR and Raman spectroscopy. The occurrence of polymorphism is significant both academically and industrially as the ability of a molecule to adopt more than one crystal structure often leads to significant variation in physical properties such as melting points, bioavailability, chemical stability and solubility.

The stability of polymorphic forms is dependent on relative free energy; the most stable system having the lower free energy. The most prominent polymorphic form experimentally may not be the most thermodynamically stable, as kinetic factors may also play a role. The thermodynamic relationship between polymorphic forms may be represented by the equation 1.7 below;

$$G = H - TS$$

Equation 1.7: Gibbs free energy of a system

At 0 K the 'TS' term disappears, at which, the most stable polymorphic form has the lowest energy.[49]

In a review by McCrone it was proposed[48], that "the number of forms known for a given compound is proportional to the time and money spent in research on that compound". This is probably still true as there remains a lack of control of polymorphic behaviour and only limited understanding of polymorphic systems. Despite much research still to be done in this area, polymorphism is not a rare occurrence, as confirmed by the incidence of polymorphism reported in the Cambridge Structural Database (CSD) where one third of APIs (active pharmaceutical ingredients) display polymorphic behaviour[50]. Even though there are many recorded instances of polymorphism in the CSD, the control and prediction of the occurrence of multiple crystal forms for an API is still a goal for pharmaceutical manufacture; i.e. the selection of the most thermodynamically stable polymorph and the ability to manufacture it consistently[51]. "Disappearing polymorphism" is an interesting and well documented phenomenon[52, 53] in which polymorphic forms of materials are isolated and characterised. These forms subsequently disappear and are unable to be isolated, even when exhaustive polymorphic screens are conducted. This phenomenon has served only to increase the 'mystique' around polymorphic behaviour and is obviously of great concern industrially, however, with modern research techniques some cases of disappearing polymorphism are being resolved[54].

The discovery of a new polymorph of an API may not need to be a problem; it allows pharmaceutical companies to patent new intellectual property. In the UK, the inventor needs to establish that the new crystal modification offers considerable difference in physical and biological properties[49]. There have been many well documented cases of polymorphism which have transcended chemistry to the legal world.

1.9 Structure prediction

In 1985, Maddox stated, "One of the continuing scandals in the physical sciences is that it remains impossible to predict the structure of even the simplest crystalline solids from knowledge of their composition[55]. "

Even though this quote is over twenty years old, the field of crystal structure prediction remains a challenging prospect. The goal of crystal structure prediction is to be able to predict the full crystal structure given only the structure of the molecule. The ability to do this, in a reliable and robust fashion, would circumvent any need for expensive experimental exhaustive polymorph screening of new materials. The successful prediction of the most thermodynamically stable crystal structure of a material and any potential polymorphs will ensure pharmaceutical companies avoid the problem of a product converting to a different polymorphic form which happens to be thermodynamically more stable. This would avoid potential costly patent challenges and product recalls such as Ritonovair[53]. Crystal structure prediction may also be used as a tool to design systems which possess desired crystal habits or properties[56] based on their relationship with intermolecular interactions and crystal growth.

The quote from Maddox still remains unsatisfied, as crystal structures still remain unpredictable on the whole, however, blind tests[57-60] organised by the Cambridge Crystallographic Data Centre (CCDC) have shown some measured success and developments in the field.

An example where experimental and crystal structure prediction have complimented each other is given by Hulme[61]. Before this study only one polymorphic form of 5-fluorouracil (used in chemotherapy) was known. Through crystal structure prediction calculations it was shown that another polymorph had the potential to be accessed

experimentally as it was close, energetically, to the known form. A second polymorph was subsequently successfully isolated experimentally and structurally characterised corresponding to the predicted second form.

Unfortunately, the global minimum of an energy landscape does not always reliably indicate the experimentally obtained polymorph of the material. Crystal structure prediction approaches consider only thermodynamic factors, neglecting experimentally based considerations such as crystal growth and solvent effects. The crystal structure prediction calculations are traditionally run at 0 K and hence no thermal effects are taken into account. This difference in temperature affects the relative stability of the polymorph observed but it also has to be considered when analysing any predicted structure. Typically, the unit cell volume expands with increasing temperature, although movement in molecular orientations often dictated by steric considerations can lead to small decreases in lattice parameters. The lattice parameters of predicted structures can be parameterised to room temperature by applying thermal expansion coefficients, but many crystal structures behave anisotropically. This also leads to problems when comparing powder diffraction patterns from an experimental structure and that simulated from predicted structures when validating or rationalising prediction results.

1.10 Thermal behaviour

The study of intermolecular forces and the crystal packing of molecules in the crystalline state are of fundamental importance in the design and understanding of the bulk behaviour of small organic molecules. A significant amount of qualitative information on these intermolecular interactions can potentially be determined from investigation of the thermal behaviour of a material.

The heat capacity of a molecular solid signifies the energy absorbed by the crystal during heating. A theoretical approach developed by Einstein in 1907 (equation 1.8), assumed that each atom vibrates about its equilibrium position at a certain frequency (υ). By employing Plancks quantisation assumption, Einstein was able to predict observed experimental trends.

$$C_v = 3 \cdot R \cdot \left(\frac{h.v}{k.T} \right)^2$$

Equation 1.8: Where C_v is equal to the heat capacity, R (ideal gas constant), h (planck constant), k (Boltzmann constant), T (temperature in K), υ (frequency)

Traditionally, atoms are thought to vibrate from their equilibrium position in a crystal structure in a harmonic fashion. If this description were to be true, then the equilibrium atomic position will be invariant of temperature.

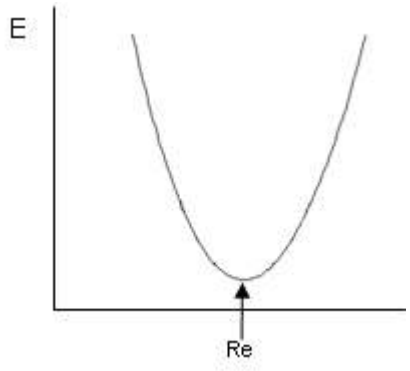

Figure 1.7: A symmetric vibronic harmonic oscillator

However, as most materials expand on heating, this indicates that the model of a simple harmonic oscillator moving in a classical symmetric potential (figure 1.7) is not a good portrayal of intermolecular interactions and distances. This model is

invariant of temperature and hence an asymmetrical description of the potential is used e.g: Lennard-Jones (equation 1.9);

$$V(r) = 4\varepsilon\left[\left(\frac{\sigma}{r}\right)^{12} - \left(\frac{\sigma}{r}\right)^{6}\right]$$

Equation 1.9: Lennard Jones empirical function

The r^{-12} term represents the repulsive component and the r^{-6} term the attractive part of the function, σ is the collision diameter and ε is the well depth.

When the temperature of a substance changes, the energy that is stored in the interactions between atoms changes. When this increases, so does the length of the molecular bond. Hence, solids typically expand upon heating and contract upon cooling, although, there are many reported cases of negative thermal expansion[62, 63]. The response of the material to temperature change is expressed as its co-efficient of thermal expansion, which can be represented as both a linear or volumetric co-efficient (equation 1.10a and 1.10b);

a) $$\frac{\Delta L}{L_0} = \alpha_L \Delta T$$

b) $$\frac{\Delta V}{V_0} = \alpha_v \Delta T$$

Equations 1.10a: Linear thermal expansion of a material where L_0 and is the original length, ΔL is the change in the length and α is the thermal expansion co-efficient.

Equations 1.10b: Linear thermal expansion of a material where V_0 is the original volume, ΔV is the change in the volume and α is the thermal expansion co-efficient

Anistropic thermal expansion is most common in molecular materials with low symmetry as the thermal behaviour is distributed unequally across the three axes with

the angles between these axes (e.g. in monoclinic or triclinic systems) subject to thermal changes. Newman's principle[64] states that the symmetry elements of any physical property of a crystal must include the symmetry elements of the point group of that material. The relationship between thermal behaviour, structure and intermolecular interactions will be investigated in this thesis by powder diffraction. A similar qualitative study has discussed this relationship in the structure of glipizide.[65]

1.11 Forms of organic solids

The classification and definition of organic solid state form is an important process that has promoted much debate[66-70]. The dendogram shown in figure 1.8, illustrates the level of complexity associated with this classification and indeed the variation of properties that are available for a particular molecular component. In addition to these shown below there are hydrates and solvates of varying stoichiometry both for the form itself and any cocrystal of that form. Although all these variants of solid form may display consistent solution chemistry, in terms of solid-state chemistry they must be treated as an independent or new material. As the results in this thesis are focussed on cocrystal and salt formation the subsequent discussion will be limited to these types of material.

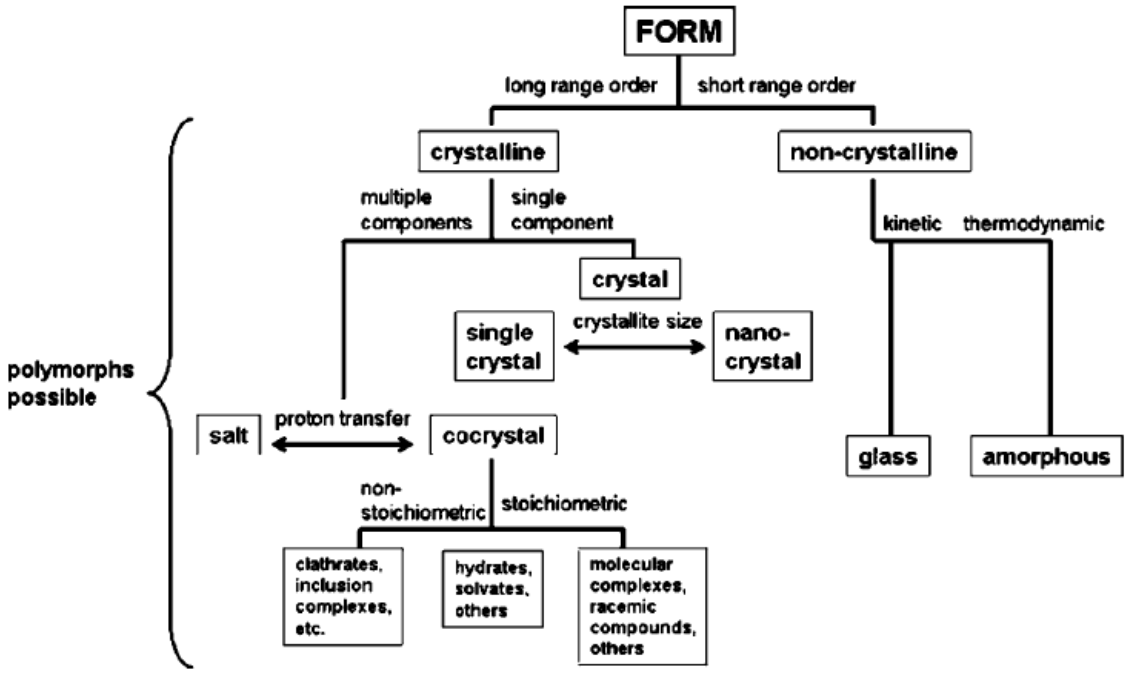

Figure 1.8: The classification of organic solids[71].

1.11.1 Cocrystals vs. Salts

Salt formation and more recently co-crystallisation of APIs represent alternative solid forms that provide a route to physical properties that can deliver more desirable therapeutic capabilities. The cocrystal in particular represents an approach in which the physical properties can be enhanced whilst retaining the chemical properties of the individual components within the cocrystal.

There has been a lively discussion in the literature[70, 72, 73] regarding a definition that gratifies all areas of crystallography and solid state pharmaceutical chemistry. A widely excepted definition was given by A.B. Aakeröy[74] in which he defines co-crystalline materials as "materials that are constructed from homogenous crystalline materials that contain two or more neutral building blocks that are present in definable stoichiometric amounts". This serves to make a clear distinction between cocrystals

and the ideology behind co-crystallisation, however, is not a new one, the first mention of the term "co-crystal" was in 1963[75].

A key aspect to the definition used above, is the consideration of two or more neutral building blocks in which case the material is a cocrystal. If the proton has transferred from the acid to the base as shown in figure 1.9, the resulting complex is termed a salt.

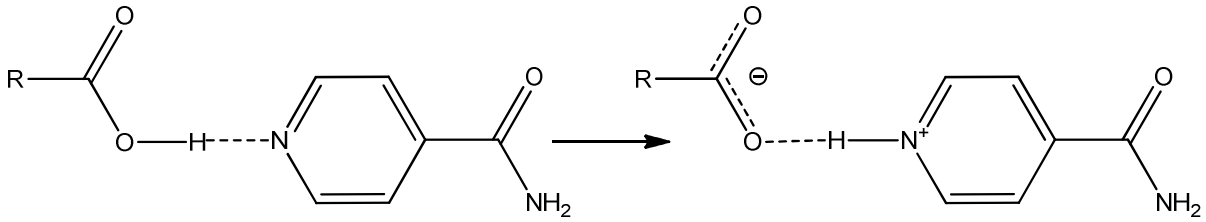

Figure 1.9: Classification of a cocrystal (left) and a salt (right)

Does the position of the hydrogen atom within these materials affect its physical properties? Initial work by Aakeröy[74] has shown that it does, hence the importance of the definition and the distinction between a cocrystal and a salt in the crystallographic community. This study was based on a statistical analysis of over 80 salts and cocrystals, with the aim of being able to prepare multi-component molecular materials with expected stoichiometries and thus promoting particular heterosythons which could control the physico-chemical properties. When a salt had been formed, 45% had unexpected stoichiometry and/or chemical composition (solvate) compared to that of cocrystal formation which had only 5% with unexpected stoichiometry. Even though the statistical pool of structures analysed was small, this general trend demonstrates one advantage of using cocrystals rather than salts in pharmaceutical formulation.

It is widely accepted that reaction between an acid and a base with a ΔpKa (ΔpKa = pKa (base) – pKa (acid)) greater than 3 a is likely to produce a salt[76]. As with all general rules, great care must be taken if using ΔpKa as a predictive tool for the

propensity of a proton transfer between the acid and the base, as pKa is the negative logarithm of the acid dissociation in solution and not the solid state. Based upon experimental evidence [76, 77], if the system is in the range $0 < \Delta pKa < 3$ crystallisation can produce a salt, cocrystal or a disordered material, with the precise location of the proton highly dependent upon the packing and local steric environment. For example the pKa of oxamic acid, isonicotinamide and nicotinamide (chapter 4) are 2.5, 3.4 and 3.6 respectively. This places both the oxamic acid:nicotinamide and oxamic acid:isonicotinamide multi-component materials in the $0 < \Delta pKa < 3$ range. Based on ΔpKa the outcome is uncertain, whether salts, cocrystals or a disordered materials.

Physical effects such as temperature, stoichoimetric ratio of the starting materials and the choice of solvent of crystallisation can have a substantial effect on the salt cocrystal continuum. A variable temperature neutron study of a pentachlorophenol/4-methlypyridine complex[78] showed that the proton moved closer to the oxygen and hence became more neutral in character with increasing temperature. This behaviour was also observed with a urea:phosphoric acid 1:1 salt, in which the proton migrated toward to the phosphate oxygen, becoming centred between the base and the acid at elevated temperatures[79]. It is also reported that more polar the solvent selected for the crystallisation medium, the higher the probability of a salt being formed.[80] In acid-base pairs with a small ΔpKa, it is possible to observe different stoichoimetric ratios giving different ionization states.[81] As pKa, solvent, temperature and stoichiometric ratio of the starting materials all play a role in determining the position of the acidic proton in the salt cocrystal continuum, manipulation of these variables can lead to an intuitive synthetic strategy in the production of a salt or cocrystal, but the unique molecular environment of each material will affect the amount of proton transfer observed.

It is clear that the ability to locate the precise position of the proton in these materials is important. The lack of resolution afforded by conventional pxrd experiments means that this technique alone is not sufficient to fully classify a new multi-component material as a salt or cocrystal. Complementary techniques will be employed within this project in order to achieve full structural classification. In previous studies, the extent of proton transfer has been determined from single crystal X-ray and neutron diffraction[82] and by the consideration of bond lengths and angles of atoms involved[83]. Infra-red spectroscopy is also used to aid classification of organic molecular materials, based on the observation of O-H, N-H and COOH signals[83]. Disorder can often lead to ambiguous solid state classification, as the proton has partial occupancy on both the acid and the base; within these types of adduct a continuum exists between the extremes of the salt and the cocrystal.[84]

1.11.2 Cocrystal applications

Figure 1.10 clearly illustrates the increased awareness interest and research into organic molecular co-crystals over the last decade. The increase in number of structures submitted to the CSD may also be attributed to the advances made in crystallographic techniques.

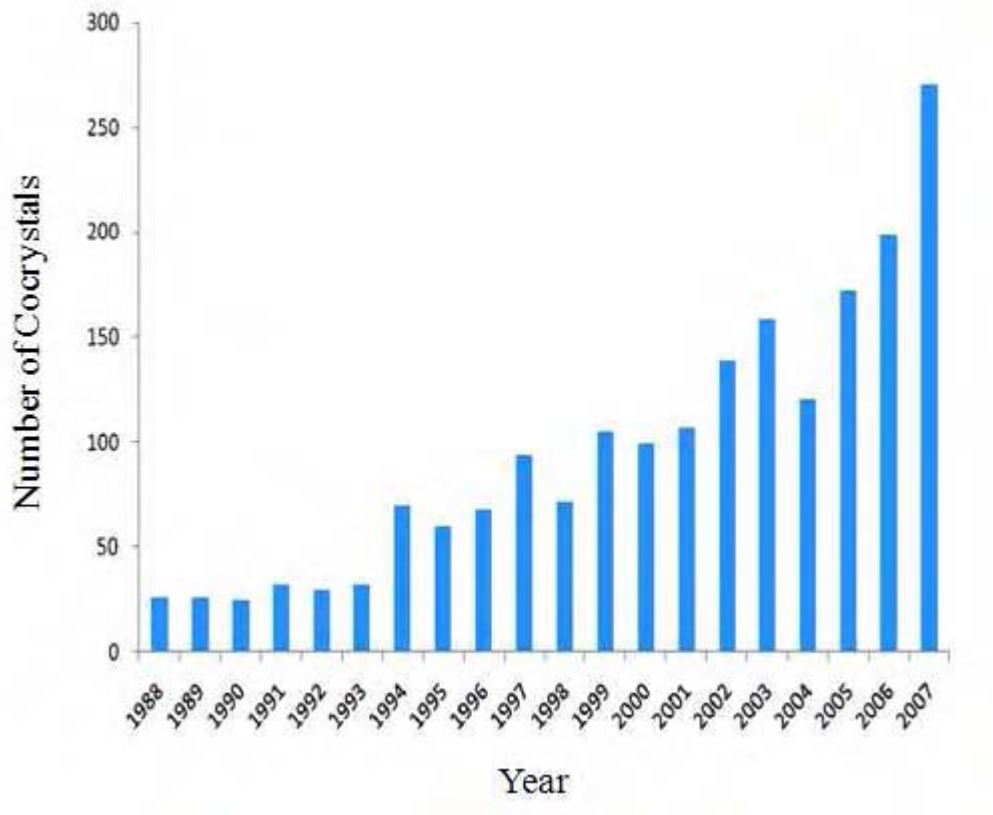

Figure 1.10: Frequency of occurrence of organic molecular co-crystals in the Cambridge Structural Database from 1988 to 2007. For the purposes of this graph, co-crystals are distinct from solvates, hydrates, and simple salts.[85]

In recent studies, molecular cocrystals have been shown to make improvements in bioavailability[86-88], humidity resistance[89] and mechanical stability[90] of APIs. A demonstration of the enhancement of physical properties is shown via the co-crystallisation of three new pharmaceutical co-crystals of the API fluoxetine (the active ingredient in the antidepressant drug Prozac) with three organic acids, this approach highlights the viability of crystal engineering, as all three organic acids use a hydrogen bond to a chloride ion to form a more stable molecular species which have different solubility and dissolution rates to that of the API fluoxetine[91].

Regardless of the enhancement of physical properties, there remains no marketed drug products that manipulate the advantages of co-crystallisation[92] (although there are

products close to release)[93]. This may be due to the production of a metastable form which could manifest itself in the product lifecycle, which in turn could have detrimental effects on bioavailability or manufacturing processes for example or simply due to the many years to get a new pharmaceutical to market or the potential hesitancy for the pharmaceutical industry to develop a new class of form with their APIs. The need for both academic and industrial research into the ever developing area of co-crystallisation, therefore, remains valid.

1.11.3 Cocrystal synthesis

A number of synthetic methods have been successfully used in the synthesis of co-crystalline materials including; solution recrystallisation, sonic slurry and mechanochemical techniques (check section 1.18). However, this search for co-crystals and the scaling up of their production in an industrial setting is a non-trivial task. Solution recrystallisation is a well established purification technique, whereas cocrystallisation via the same route involves the introduction of two or more materials in to solution and the production of a crystalline phase containing both components, rather than two phases each of a single component. Regardless of the method of synthesis, the potential conformers or starting materials must contain both strong hydrogen bond donors and acceptors of which a compatible combination is preferable, in order to form intermolecular interactions.

For solution mediated cocrystallisation to be a success, the solubilities of the starting materials need to be comparable to prevent the crystallisation of one cocrystal former before cocrystallisation can take place[94]. A ternary phase diagram illustrates the complexity of a solvent mediated co-crystallisation of a binary system. The solubilities of the starting materials are integral to these phase diagrams, as

differences alter the morphology of the phase space region in which the formation of a co-crystal formation is thermodynamically favourable.

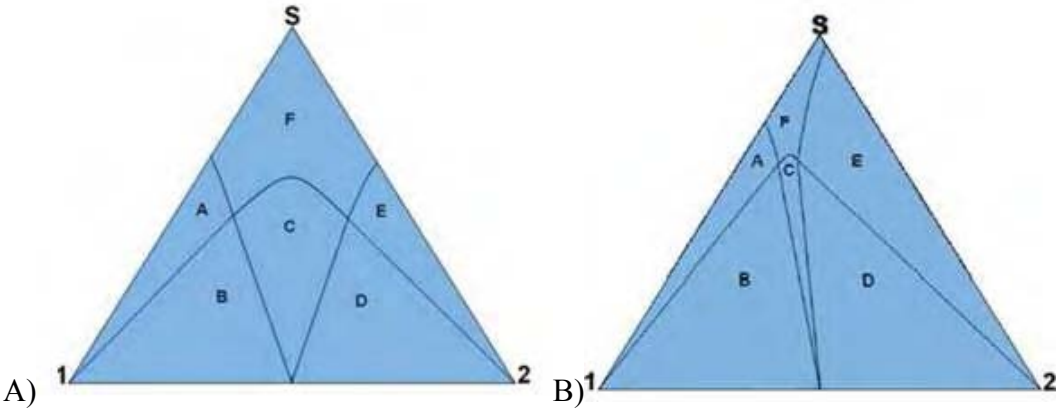

Figure 1.11: Schematic representations of isothermal ternary phase diagrams with (A) showing similar solubilities between starting components 1 and 2 in solvent S and (B) showing a system with a difference between solubilities of the starting components 1 and 2 in solvent S. Region **A** represents component 1 and solvent, **B** represents component 1 and cocrystal, **C** represents cocrystal, **D** represents component 2 and cocrystal, **E** represents component 2 and cocrystal and finally **F** represents solution.[94]

The ternary phase diagrams shown in figure 1.11 are derived from a limited number of experimentally derived phase diagrams.[95, 96] Alternative synthetic methods have been developed to circumvent this problem of non-comparable solubilities, including liquid (or solvent) assisted grinding (1.11.4) and sonic slurry (1.11.4) as viable and intuitive synthetic routes.

1.11.4 Reduced solvent methods for cocrystallisation synthesis

Cocrystals and salts are traditionally produced by cold recrystallisation through solvent evaporation. This technique is favoured as it is the simplest method to scale up to industrial sized experiments[97]. However an alternative method, "solvent drop grinding"[98] has many advantages over the traditional solvent-based method, these include the drastic reduction in the amount of solvent needed for a co-crystallisation experiment, leading to a greener route for production. The treatment and reduction of organic solvents is an important issue in the chemical industry as a large amount accrue annually.

The mechanochemical approach to the formation of co-crystals was reported as early as 1893[99] through the formation of the quinhydrone co-crystal. This field remained undeveloped until work by Etter[100] developed the technique in the field of supramolecular chemistry.

Solvent drop grinding is an intuitively simple technique in which two starting materials, in stoichiometric ratios, are ground together in the presence of a minimal amount of solvent. Neat or dry grinding of starting materials preceded the use of liquid assisted grinding or solvent drop grinding, either using a pestle and mortar or a ball mill. Even though many successful co-crystallisations have been carried out this way[100], it was shown that a small amount of a solvent could act with physical effects (e.g. lubrication) or via the chemical properties of the solvent (e.g. formation of intermediates such as solvates), leading to enhanced polymorphic control, higher quality of crystallisation and higher yield, allowing the range of systems to be studied to widened[101]. The improved efficiency of the mechanochemical approach over that of

solvent recrystallisation can be attributed to the reduction in solvent competition and the solubilities of the starting materials. As discussed earlier, the variation in kinetics between a mechanochemical approach and solvent recrystallisation can also produce different cocrystal form such as stoichiometry or solvation.

In conjunction with liquid assisted grinding a "sonic slurry" method has also been incorporated as a method of producing molecular cocrystals. The use of ultrasound to form co-crystals, with the starting material suspended in a minimum amount of solvent, avoids the inherent differences in the solubilities of the starting materials because the formation of the new co-crystalline phase is due to the growth and collapse of bubbles of micrometer-sized dimensions associated with intense, short lived heating and pressure[102]. The process of crystallising, co-crystallising and screening for solid pharmaceutical forms was patented in 2007 by Childs[103].

1.11.5 Cocrystal Design

To aid intensive cocrystal screening, the development of robust supramolecular strategies and computational techniques to predict the formation of cocrystals is also increasingly important. Overall, it appears that computational energy landscapes can predict that the majority of cocrystals are more stable than their components. However, cocrystallisation does not show a dramatic increase in stabilisation on a lattice energy scale, with the increase in stabilisation only being comparable to a polymorphic energy difference. Current investigations[104, 105] raise the concern with the approximations used in the evaluation of relative energies and the kinetic factors involved in the formation of cocrystals. Our understanding of the factors that govern the formation of hydrogen bonding motifs and direct packing motifs are also still evolving. The most common self assembly approach is that postulated by Etter[100, 106]

and establishes a hierarchy or ranking of potential supramolecular synthons based on the best donor group bonding to the best acceptor group. The aim of 'crystal engineers' is to manipulate and develop strategies (such as Etters Rules) to select systems which display robust preferential synthons.

The successful synthesis of multi-component systems relies on the preferential formation of heteromeric synthons rather than the formation of strong interactions within the individual components of the cocrystal formers. Carboxylic acids and amides are two commonly used functional groups in crystal engineering because they from robust hydrogen bond networks via both O—H---O and N—H---O dimers[107] and are therefore good candidates for the formation of multi-component molecular networks.

Both isonicotinamide and nicotinamide have demonstrated the propensity for cocrystal formation with a range of carboxylic acids [108-112], showing a preference for the formation of a heteromeric acid-pyridine hydrogen bond (**A** in figure 1.12). The formation of synthon **A** was correctly proposed by Aakeroy[112] using the self assembly rules formulated by Etter for a carboxylic acid:isonicotinamide cocrystal. The guidlines proposed by Etter[106] are:

1) All good proton donors and acceptors are used in hydrogen bonding
2) Six-membered-ring intramolecular hydrogen bonds form in preference to intermolecular hydrogen bonds
3) The best proton donors and acceptors remaining after intramolecular hydrogen-bond formation form intermolecular hydrogen bonds to one another.

A synthon energy calculation conducted by Vishweshwar [108] also illustrated the preference for formation of synthon **A** over an acid-amide bond and homomeric hydrogen bonding. The stoichiometry of the starting materials has also been shown to

have an effect on other hydrogen bonding networks observed in these acid-amide systems. Those formed with a monocarboxylic acid in 1:1 or a dicarboxylic acid in a 2:1 ratio show a preference for the formation of synthon **B**, whereas cocrystals with the dicarboxylic acid in a 1:1 ratio tend to form synthon **C**. Synthons **D** and **E** are both homomeric, with **D** being an acid-acid synthon and **E** an amide-pyridine synthon. All these synthons are shown below in figure 1.12 and form the basis of many of the materials covered in this thesis.

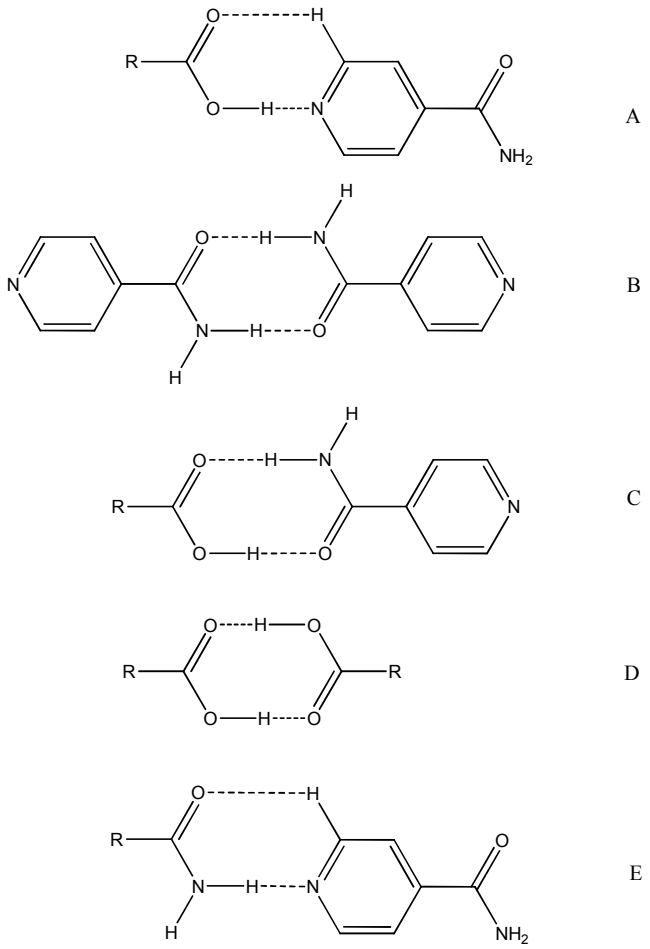

Figure 1.12: Potential synthons found in acid-amides cocrystals

1.12 Aims

The aim of the work reported in this thesis is to investigate many areas of organic molecular crystallography; from the development of solvent free synthetic methods on both binary and multi-component molecular systems, to the full structural characterisation of these materials by both single and powder X-ray diffraction. Spectroscopic techniques will be used to complement the classification of the materials under investigation. Further structural insight will be probed by a study of the thermal behaviour of each material over the range 100-295 K. Research into areas of both industrial and academic importance are presented here, as the materials studied address important aspects of polymorphic and cocrystalline behaviour. The work reported in this thesis aims to;

- To synthesise a number of new multi-component materials; oxamic acid:nicotinamide, oxamic acid:isonicotinamide, fumaric acid:nicotinamide, maleic acid:nicotinamide and maleic acid:isonicotinamide.
- Investigate the use of "reduced solvent" synthetic methods for these multi-component and binary structures.
- Use pxrd to solve the crystal structure of these a number of multi-component systems, using complementary techniques to aid in the classification (salt or cocrystal) of the system.
- Make a direct comparison of structures solved by powder and single crystal diffraction to evaluate the reliability of structure solution from pxrd in this type of material.
- Assessment of the DE algorithm in application to multi-component systems and optimisation of the control parameters and efficiency of the algorithm.

- Comparison of structures formed by isomers isonicotinamide and nicotinamide.
- Investigate the thermal behaviour of these systems over the range 100-295 K and relate the anisotropic expansion to the crystal packing of the material.
- Investigate the polymorphic behaviour of oxamic acid, using neutron, single and powder diffraction, and relate these results to predication.

References:

1. V. Ramakrishnan, *Angewandte Chemie-International Edition*, 2010, **49**, 4355-4380.

2. M. Sprinzl and V. A. Erdmann, *Chembiochem*, 2009, **10**, 2851-2853.

3. W. S. Boyle and G. E. Smith, *Ieee Spectrum*, 1971, **8**, 18-27.

4. *www.**diamond**.ac.uk*.

5. V. Pecharsky and P. Zavalij, in *Fundamentals of powder diffraction and structural characterization of materials*, Editon edn., 2003, pp. 243-244.

6. K. D. M. Harris, M. Tremayne and B. M. Kariuki, *Angewandte Chemie-International Edition*, 2001, **40**, 1626-1651.

7. W. A. Dollase, *J. Appl. Crystallogr.*, 1986, **19**, 267-272.

8. V. K. Pecharsky and P. Y. Zavalij, *Fundamentals of Powder Diffraction and Structural Characterization of Materials*, Kluwer Academic Publishers Group., 2003.

9. H. M. Rietveld, *Journal of Applied Crystallography*, 1969, **2**, 65-71.

10. P. E. Werner, L. Eriksson and M. Westdahl, *Journal of Applied Crystallography*, 1985, **18**, 367-370.

11. J. Visser, *J. Appl. Crystallogr.*, 1969, **2**, 89-95.

12. A. Boultif and D. Louer, *Journal of Applied Crystallography*, 1991, **24**, 987-993.

13. P. M. D. Wolff, *Journal of Applied Crystallography*, 1972, **5**, 243.

14. R. Shirley, *The Crysfire 2002 System for Automatic Powder Indexing: User's Manual, 41 Guildford Park Avenue, Guildford, Surry, GU2 7NL, England, 2002.*, 2002.

15. S. Meejoo, B. M. Kariuki, S. J. Kitchin, E. Y. Cheung, D. Albesa-Jove and K. D. M. Harris, *Helvetica Chimica Acta*, 2003, **86**, 1467-1477.

16. A. Lebail, H. Duroy and J. L. Fourquet, *Materials Research Bulletin*, 1988, **23**, 447-452.

17. G. S. Pawley, *Journal of Applied Crystallography*, 1981, **14**, 357-361.

18. R. J. Cernik, A. K. Cheetham, C. K. Prout, D. J. Watkin, A. P. Wilkinson and B. T. M. Willis, *Journal of Applied Crystallography*, 1991, **24**, 222-226.

19. K. D. Knudsen, P. Pattison, A. N. Fitch and R. J. Cernik, *Angewandte Chemie-International Edition*, 1998, **37**, 2340-2343.

20. P. Lightfoot, M. Tremayne, K. D. M. Harris and P. G. Bruce, *Journal of the Chemical Society-Chemical Communications*, 1992, 1012-1013.

21. K. D. M. Harris, M. Tremayne, P. Lightfoot and P. G. Bruce, *Journal of the American Chemical Society*, 1994, **116**, 3543-3547.

22. M. Tremayne, B. M. Kariuki and K. D. M. Harris, *Journal of Applied Crystallography*, 1996, **29**, 211-214.

23. B. M. Kariuki, D. M. S. Zin, M. Tremayne and K. D. M. Harris, *Chemistry of Materials*, 1996, **8**, 565-569.

24. M. Tremayne, B. M. Kariuki, K. D. M. Harris, K. Shankland and K. S. Knight, *Journal of Applied Crystallography*, 1997, **30**, 968-974.

25. M. Tremayne, B. M. Kariuki and K. D. M. Harris, *Angewandte Chemie-International Edition in English*, 1997, **36**, 770-772.

26. M. Tremayne, E. J. MacLean, C. C. Tang and C. Glidewell, *Acta Crystallographica Section B-Structural Science*, 1999, **55**, 1068-1074.

27. M. Rajeswaran, T. N. Blanton, N. Zumbulyadis, D. J. Giesen, C. Conesa-Moratilla, S. T. Misture, P. W. Stephens and A. Huq, *Journal of the American Chemical Society*, 2002, **124**, 14450-14459.

28. A. Huq and P. W. Stephens, *Journal of Pharmaceutical Sciences*, 2003, **92**, 244-249.

29. N. Shankland, W. I. F. David, K. Shankland, A. R. Kennedy, C. S. Frampton and A. J. Florence, *Chemical Communications*, 2001, 2204-2205.

30. H. Nowell, J. P. Attfield, J. C. Cole, P. J. Cox, K. Shankland, S. J. Maginn and W. D. S. Motherwell, *New Journal of Chemistry*, 2002, **26**, 469-472.

31. A. J. Florence, N. Shankland, K. Shankland, W. I. F. David, E. Pidcock, X. L. Xu, A. Johnston, A. R. Kennedy, P. J. Cox, J. S. O. Evans, G. Steele, S. D. Cosgrove and C. S. Frampton, *Journal of Applied Crystallography*, 2005, **38**, 249-259.

32. B. M. Kariuki, P. Calcagno, K. D. M. Harris, D. Philp and R. L. Johnston, *Angewandte Chemie-International Edition*, 1999, **38**, 831-835.

33. B. M. Kariuki, G. L. Bauer, K. D. M. Harris and S. J. Teat, *Angewandte Chemie-International Edition*, 2000, **39**, 4485-4488.

34. E. Tedesco, B. M. Kariuki, K. D. M. Harris, R. L. Johnston, O. Pudova, G. Barbarella, E. A. Marseglia, G. Gigli and R. Cingolani, *Journal of Solid State Chemistry*, 2001, **161**, 121-128.

35. D. Albesa-Jove, B. M. Kariuki, S. J. Kitchin, L. Grice, E. Y. Cheung and K. D. M. Harris, *Chemphyschem*, 2004, **5**, 414-418.

36. S. Y. Ryabova, N. A. Rastorgueva, E. J. Sonneveld, R. Peschar, H. Schenk, V. A. Tafeenko, L. A. Aslanov and V. V. Chernyshev, *Acta Crystallogr. Sect. B-Struct. Sci.*, 2005, **61**, 192-199.

37. V. V. Chernyshev, A. V. Yatsenko, A. M. Kuvshinov and S. A. Shevelev, *Journal of Applied Crystallography*, 2002, **35**, 669-673.

38. V. V. Chernyshev, K. A. Paseshnichenko, V. A. Makarov, E. J. Sonneveld and H. Schenk, *Acta Crystallographica Section C-Crystal Structure Communications*, 2001, **57**, 72-75.

39. G. Reck, R. G. Kretschmer, L. Kutschabsky and W. Pritzkow, *Acta Crystallographica Section A*, 1988, **44**, 417-421.

40. N. Masciocchi, R. Bianchi, P. Cairati, G. Mezza, T. Pilati and A. Sironi, *Journal of Applied Crystallography*, 1994, **27**, 426-429.

41. B. V. a. S. Babu, K.K.N., *Compt Chem Eng*, 1999, **23**, 327-339.

42. B. V. a. A. Babu, A., *Compt Chem Eng*, 2006, **30**, 989-1002.

43. F. H. Allen, O. Kennard, D. G. Watson, L. Brammer, A. G. Orpen and R. Taylor, *Journal of the Chemical Society-Perkin Transactions 2*, 1987, S1-S19.

44. A. C. Larson and R. B. Von Dreele, *GSAS. General Structure Analysis System, Report No. LAUR 86-748, Los Alamos National Laboratory, Los Alamos, New Mexico, USA*, 1994.

45. A. A. Coelho, *Journal of Applied Crystallography*, 2000, **33**, 899-908.

46. R.-C. J., *Abstracts of the Satellite Meeting on Powder Diffraction of the XV Congress of the IUCr, Toulouse, France, 1990, p.127*.

47. F. Izumi and T. Ikeda, 6th European Powder Diffraction Conference, Budapest, Hungary, 1998.

48. W.C. McCrone, *Polymorphism in physics and chemistry of the organic solid state, Vol2*, 1965, **2**, 725-767.

49. J. Bernstein, Polymorphism in molecular crystals, 2002.

50. A. L. Grzesiak, M. D. Lang, K. Kim and A. J. Matzger, *Journal of Pharmaceutical Sciences*, 2003, **92**, 2260-2271.

51. P. H. Karpinski, *Chemical Engineering & Technology*, 2006, **29**, 233-237.

52. J. D. Dunitz and J. Bernstein, *Accounts of Chemical Research*, 1995, **28**, 193-200.

53. S. R. Chemburkar, J. Bauer, K. Deming, H. Spiwek, K. Patel, J. Morris, R. Henry, S. Spanton, W. Dziki, W. Porter, J. Quick, P. Bauer, J. Donaubauer, B. A. Narayanan, M. Soldani, D. Riley and K. McFarland, *Organic Process Research & Development*, 2000, **4**, 413-417.

54. R. W. Lancaster, P. G. Karamertzanis, A. T. Hulme, D. A. Tocher, T. C. Lewis and S. L. Price, *Journal of Pharmaceutical Sciences*, 2007, **96**, 3419-3431.

55. J. Maddox, *Nature*, 1988, **335**, 201-201.

56. M. Jansen, *Angewandte Chemie-International Edition*, 2002, **41**, 3747-3766.

57. J. P. M. Lommerse, W. D. S. Motherwell, H. L. Ammon, J. D. Dunitz, A. Gavezzotti, D. W. M. Hofmann, F. J. J. Leusen, W. T. M. Mooij, S. L. Price, B. Schweizer, M. U. Schmidt, B. P. van Eijck, P. Verwer and D. E. Williams, *Acta Crystallographica Section B-Structural Science*, 2000, **56**, 697-714.

58. W. D. S. Motherwell, H. L. Ammon, J. D. Dunitz, A. Dzyabchenko, P. Erk, A. Gavezzotti, D. W. M. Hofmann, F. J. J. Leusen, J. P. M. Lommerse, W. T. M. Mooij, S. L. Price, H. Scheraga, B. Schweizer, M. U. Schmidt, B. P. van Eijck, P. Verwer and D. E. Williams, *Acta Crystallographica Section B-Structural Science*, 2002, **58**, 647-661.

59. G. M. Day, W. D. S. Motherwell, H. L. Ammon, S. X. M. Boerrigter, R. G. Della Valle, E. Venuti, A. Dzyabchenko, J. D. Dunitz, B. Schweizer, B. P. van Eijck, P. Erk, J. C. Facelli, V. E. Bazterra, M. B. Ferraro, D. W. M. Hofmann, F. J. J. Leusen, C. Liang, C. C. Pantelides, P. G. Karamertzanis, S. L. Price, T. C. Lewis, H. Nowell, A. Torrisi, H. A. Scheraga, Y. A. Arnautova, M. U. Schmidt and P. Verwer, *Acta Crystallographica Section B-Structural Science*, 2005, **61**, 511-527.

60. G. M. Day, T. G. Cooper, A. J. Cruz-Cabeza, K. E. Hejczyk, H. L. Ammon, S. X. M. Boerrigter, J. S. Tan, R. G. Della Valle, E. Venuti, J. Jose, S. R. Gadre, G. R. Desiraju, T. S. Thakur, B. P. van Eijck, J. C. Facelli, V. E. Bazterra, M. B. Ferraro, D. W. M. Hofmann, M. A. Neumann, F. J. J. Leusen, J. Kendrick, S. L. Price, A. J. Misquitta, P. G. Karamertzanis, G. W. A. Welch, H. A. Scheraga, Y. A. Arnautova, M. U. Schmidt, J. van de Streek, A. K. Wolf and B. Schweizer, *Acta Crystallographica Section B-Structural Science*, 2009, **65**, 107-125.

61. A. T. Hulme, S. L. Price and D. A. Tocher, *Journal of the American Chemical Society*, 2005, **127**, 1116-1117.

62. W. Miller, C. W. Smith, D. S. Mackenzie and K. E. Evans, *Journal of Materials Science*, 2009, **44**, 5441-5451.

63. J. S. O. Evans, T. A. Mary, T. Vogt, M. A. Subramanian and A. W. Sleight, *Chemistry of Materials*, 1996, **8**, 2809-2823.

64. R. E. Newnham, *Properties of Materials: Anisotropy, Symmetry and Structure*, Oxford press, 2005.

65. J. C. Burley, *Acta Crystallographica Section B-Structural Science*, 2005, **61**, 710-716.

66. A. L. Bingham, D. S. Hughes, M. B. Hursthouse, R. W. Lancaster, S. Tavener and T. L. Threlfall, *Chemical Communications*, 2001, 603-604.

67. K. R. Seddon, *Crystal Growth & Design*, 2004, **4**, 1087-1087.

68. J. Bernstein, *Crystal Growth & Design*, 2005, **5**, 1661-1662.

69. G. R. Desiraju, *Crystal Growth & Design*, 2004, **4**, 1089-1090.

70. J. D. Dunitz, *Crystengcomm*, 2003, **5**, 506-506.

71. G. P. Stahly, *Crystal Growth & Design*, 2007, **7**, 1007-1026.

72. G. R. Desiraju, *Crystengcomm*, 2003, **5**, 466-467.

73. A. D. Bond, *Crystengcomm*, 2007, **9**, 833-834.

74. C. B. Aakeroy, M. E. Fasulo and J. Desper, *Molecular Pharmaceutics*, 2007, **4**, 317-322.

75. K. Hoogsteen, *Acta Crystallogr. Sect. B-Struct. Sci.*, 1963, 16. 28-38.

76. S. L. Childs, G. P. Stahly and A. Park, *Molecular Pharmaceutics*, 2007, **4**, 323-338.

77. B. R. Bhogala, S. Basavoju and A. Nangia, *Crystengcomm*, 2005, **7**, 551-562.

78. I. Majerz, Z. Malarski and L. Sobczyk, *Chemical Physics Letters*, 1997, **274**, 361-364.

79. C. C. Wilson, *Acta Crystallographica Section B-Structural Science*, 2001, **57**, 435-439.

80. J. H. Clark and C. W. Jones, *Journal of the Chemical Society-Chemical Communications*, 1990, 1786-1787.

81. D. Wiechert and D. Mootz, *Angewandte Chemie-International Edition*, 1999, **38**, 1974-1976.

82. T. Steiner, *Angewandte Chemie-International Edition*, 2002, **41**, 48-76.

83. C. B. Aakeroy, I. Hussain and J. Desper, *Crystal Growth & Design*, 2006, **6**, 474-480.

84. Z. J. Li, Y. Abramov, J. Bordner, J. Leonard, A. Medek and A. V. Trask, *Journal of the American Chemical Society*, 2006, **128**, 8199-8210.

85. S. L. Childs and M. J. Zaworotko, *Crystal Growth & Design*, 2009, **9**, 4208-4211.

86. O. Almarsson and M. J. Zaworotko, *Chemical Communications*, 2004, 1889-1896.

87. J. F. Remenar, S. L. Morissette, M. L. Peterson, B. Moulton, J. M. MacPhee, H. R. Guzman and O. Almarsson, *Journal of the American Chemical Society*, 2003, **125**, 8456-8457.

88. N. Blagden, M. de Matas, P. T. Gavan and P. York, *Advanced Drug Delivery Reviews*, 2007, **59**, 617-630.

89. A. V. Trask, W. D. S. Motherwell and W. Jones, *Crystal Growth & Design*, 2005, **5**, 1013-1021.

90. C. C. Sun and H. Hou, *Crystal Growth & Design*, 2008, **8**, 1575-1579.

91. S. L. Childs, L. J. Chyall, J. T. Dunlap, V. N. Smolenskaya, B. C. Stahly and G. P. Stahly, *Journal of the American Chemical Society*, 2004, **126**, 13335-13342.

92. R. R. Schartman, *International Journal of Pharmaceutics*, 2009, **365**, 77-80.

93. M. Zaworotko, Personal communication., 2010.

94. N. Blagden, D. J. Berry, A. Parkin, H. Javed, A. Ibrahim, P. T. Gavan, L. L. De Matos and C. C. Seaton, *New Journal of Chemistry*, 2008, **32**, 1659-1672.

95. J. Linol, T. Morelli, M. N. Petit and G. Coquerel, *Crystal Growth & Design*, 2007, **7**, 1608-1611.

96. K. Ito and Sekiguch.K, *Chemical & Pharmaceutical Bulletin*, 1966, **14**, 255-262.

97. A. M. Thayer, *Chemical & Engineering News*, 2007, **85**, 11-19.

98. N. Shan, F. Toda and W. Jones, *Chemical Communications*, 2002, 2372-2373.

99. A. Ling and Baker. J, *Journal Chem Soc*, 1893, **63**, 1314.

100. M. C. Etter, *Journal of Physical Chemistry*, 1991, **95**, 4601-4610.

101. T. Friscic and W. Jones, *Faraday Discussions*, 2007, **136**, 167-178.

102. D. K. Bucar and L. R. MacGillivray, *Journal of the American Chemical Society*, 2007, **129**, 32-33.

103. T. Friscic, S. L. Childs, S. A. A. Rizvi and W. Jones, *Crystengcomm*, 2009, **11**, 418-426.

104. N. Issa, P. G. Karamertzanis, G. W. A. Welch and S. L. Price, *Crystal Growth & Design*, 2009, **9**, 442-453.

105. P. G. Karamertzanis, A. V. Kazantsev, N. Issa, G. W. A. Welch, C. S. Adjiman, C. C. Pantelides and S. L. Price, *Journal of Chemical Theory and Computation*, 2009, **5**, 1432-1448.

106. M. C. Etter, *Accounts of Chemical Research*, 1990, **23**, 120-126.

107. R. K. R. Jetti, F. Xue, T. C. W. Mak and A. Nangia, *Journal of the Chemical Society-Perkin Transactions 2*, 2000, **6**, 1223-1232.

108. P. Vishweshwar, A. Nangia and V. M. Lynch, *Crystal Growth & Design*, 2003, **3**, 783-790.

109. M. Schmidtmann, M. J. Gutmann, D. S. Middlemiss and C. C. Wilson, *Crystengcomm*, 2007, **9**, 743-745.

110. L. Orola and M. V. Veidis, *Crystengcomm*, 2009, **11**, 415-417.

111. S. Karki, T. Friscic and W. Jones, *Crystengcomm*, 2009, **11**, 470-481.

112. C. B. Aakeroy, A. M. Beatty and B. A. Helfrich, *Journal of the American Chemical Society*, 2002, **124**, 14425-14432.

2. Methodology

2.1 Variable temperature X-ray diffraction

2.1.1 Software and data handling

X-ray powder diffraction data collected as a RAW file was converted to a UXD format using Diffract file exchange [XCH] and an in-house Perl-based converter used to create data files (GSA, XDD) that are required for input into other crystallographic software.

Information about previously published crystal structures (as in the case of 5-fluorouracil) was downloaded from the Cambridge Structural Database (CSD) in the form of crystallographic information files (CIF) format[1]. The CIF was opened in Mercury[2] for the generation of a powder diffraction pattern and to be used as a diagnostic test to confirm that the experimental pattern contained no chemical or physical impurity and was of the same phase as that previously reported. The unit cell parameters from the CIF were then used as a starting point for the LeBail profile fitting procedure in GSAS[3]. In cases where the previously published crystal structure had been determined at room temperature, this set of lattice parameters was used as a starting point for the LeBail fit. The lattice parameters produced from the room temperature LeBail fit were in turn used as a starting point for 250 K data and the process repeated sequentially down the temperature range.

2.2 Structure solution from X-ray powder diffraction

As discussed in the introduction, the determination of crystal structures from pxrd is an intrinsically difficult task, predominately due to the problem of peak overlap. The

approach taken in this thesis was to fully structurally characterise materials from powder X-ray diffraction using a direct space evolutionary algorithm approach based on DE (differential evolution).

Prior to the direct space calculation, unit cell indexing (1.7.1) space group assignment and pattern decomposition (i.e. LeBail) (1.7.3), are completed in order to fully describe the unit cell parameters and peak profile characteristics that remain constant throughout the calculation. Any errors introduced to the structure solution process at this stage will be transmitted into the direct space search, alluding to a false solution.

An XDD file was created via the in-house Perl-based converter and opened in XFIT[4]. The XFIT[4] program was used to determine the positions of the peaks required for indexing, and this information was used in the CRYSFIRE[5] program. CRYSFIRE[5] is used to run a suite of indexing programs, the results are collated in a summary file. All possible unit cells are then listed in order of merit. To verify that the lines selected in XFIT[4] are generated by a specific unit cell, Chekcell[6] was used. The space group was then determined by examining the systematic absences in the diffraction pattern and then verifying the space group by international crystallographic tables and Chekcell[6]. The GSA file was read into GSAS[3] via the EXPGUI platform. Background points in the diffraction pattern were also identified via the EXPGUI.

% R_{wp} (equation 1.3) is the driving force behind the DE calculation, but a disadvantage of this is that it is a computationally expensive cost function. One of the main advantages of DE as an experimental optimisation technique is that the cost function is derived from a physical experiment, in this case a powder diffraction pattern. The calculation for % R_{wp} in this work is the same as that used in the Rietveld refinement (which follows the direct space calculation). This is one advantage of using % R_{wp} as the cost function, as direct comparisons can be made in "fitness"

between the refined crystal structure and the direct space solution. Equation 2.1 is used to calculate $y_i(calc)$ in a % R_{wp} calculation.

$$y_i(calc) = y_i(bg) + s\sum_m \phi_{i,m}\left|Fm\right|^2$$

Equation 2.1: $y_i(calc)$ calculation used to in the calculation of % R_{wp}

Where $y_i(bg)$ is the background intensity at the i^{th} data point, s is the scale factor, $\left|Fm\right|$ is the modulus of the structure factor of the m^{th} Bragg peak, $\phi_{i,m}$ is the contribution of the m^{th} Bragg peak to the intensity at point i, which is calculated by equation 2.2 below;

$$\phi_{i,m} = M_m Lpm\,\sigma(2\theta_i - 2\theta_m)A_{i,m}$$

Equation 2.2: Contribution of the m^{th} Bragg peak to the intensity at point i.

Where M_m is the reflection multiplicity, L_{pm} gives a description of the peak shape and the Lorentz-polarization correction, $A_{i,m}$ represents the peak symmetry and $(2\theta_i - 2\theta_m)$ is the profile function of the m^{th} Bragg peak.

This direct space approach implicitly considers the extraction of individual structure moduli directly from the diffraction pattern, % R_{wp}, is a whole profile optimization function with the pattern digitalised to intensities at each point in the diffraction pattern. This approach results in an expensive cost function due to the size of calculation required when compared to the extraction of $\left|F(s)\right|$ values directly from the diffraction pattern.

In order to increase the efficiency and speed of the DE calculation, many aspects of the calculation remain constant and unaltered throughout the whole search, unit cell parameters and the peak profile parameters, which are a result of a combination of

indexing and pattern decomposition, remain constant. $\phi_{i,m}$ and $y_i(bg)$ also remain fixed.

The calculation of the cost function can also be reduced using other assumptions. The absorption of X-rays by the sample can be neglected as organic samples have a low absorption co-efficient and powder samples are nominally thin. X-ray extinction is not calculated as the sample is thin and therefore the crystallite length falls within the extinction length (Pendellösung period). The final calculation that can be omitted is the March-Dollase correction which tackles the problem of preferred orientation (section 1.6). This correction is mostly commonly applied at the refinement stage, but in severe cases can be introduced as a variable parameter in the % R_{wp} calculation to help guide the structure solution process.[7]

Direct space calculations rely on chemical knowledge in order to construct the % R_{wp} hypersurface. In this work the molecular model is constructed using standard bond lengths and geometries[8], using Chem3D pro (pro version 3.5.2)[9]. Trial crystal structures are then converted and described by a list of elements (Γ): e.g. the position (x,y,z) and orientation (θ,Φ,Ψ) of a molecular model in the unit cell and the conformation of the molecule defined by variable torsion angles ($\tau_1 \ldots \tau_n$).

The implementation of the DE is incorporated into the POSSUM[10] program package, along with routines for other direct space structure solution methods, such as grid search simulated annealing and Monte Carlo. POSSUM[10] is a cross-platform suite written in Perl.

As discussed in the introduction, DE maintains a population of trial structures using Equation 1.4, as offspring or trial structures are produced by a combination of vectors (mutation and recombination) as the hypersurface is searched. Initially, the trial

structures within the population are randomly distributed across the hypersurface, each described by a set of elements (Γ). Like many direct space methods, DE uses a greedy criterion to make the decision as to whether to accept the offspring trial structure over that of its parent in the previous generation; this is done by direct comparison of % R_{wp}. If the % R_{wp} of the trial structure is fitter than its parent, then it replaces its parent as a member of the population, otherwise the offspring is discarded and the parent trial structure remains in the population for the next generation. This 'greedy' decision process is relatively efficient and fast, but can be prone to be trapped in local minima upon the hypersurface (figure 2.1).

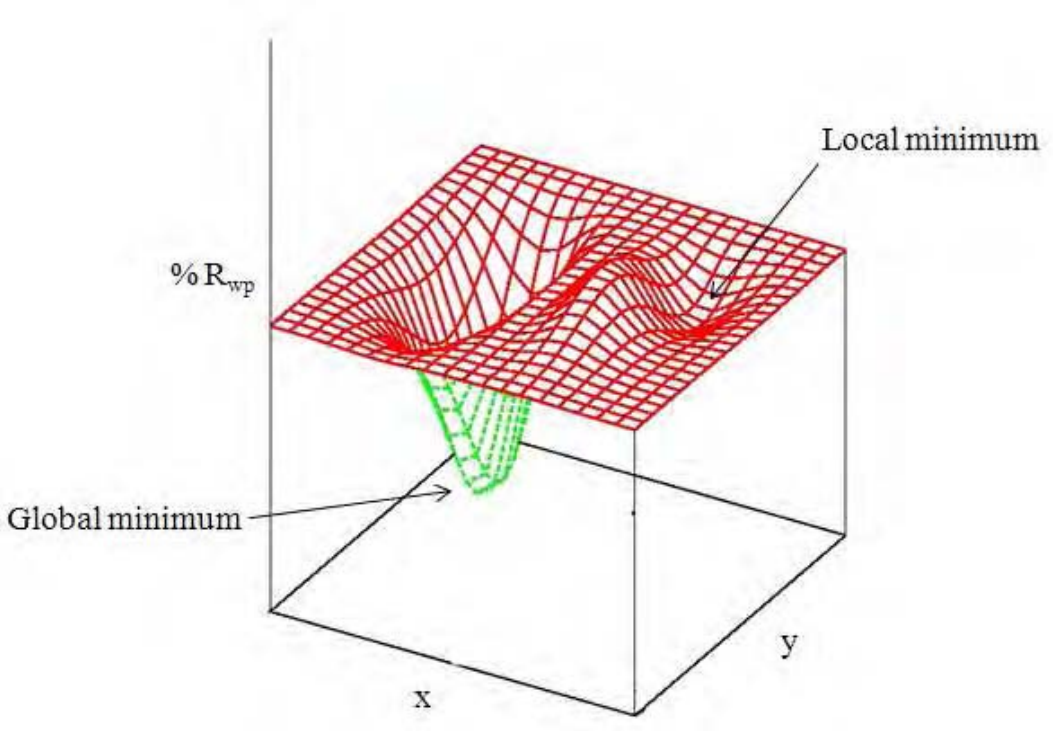

Figure 2.1 : An example of local minimum and the global minimum on an energy hypersurface

This problem can be overcome by using a diverse initial population and then searching the hypersurface using a combination of vectors (recombination and mutation). Due to random distribution of the initial generation of trial structures at the start of the DE calculation, these initial vectors will be large and distinct offspring will be produced (often far from the parents). As the generations progress, the population will become less diverse, resulting in the shortening of search vectors as the calculation reaches convergence (where mean and best % R_{wp} are equivalent). The production of offspring structures as presented in equation 1.4 is illustrated in figure 2.2 and the overall DE process in figure 2.3

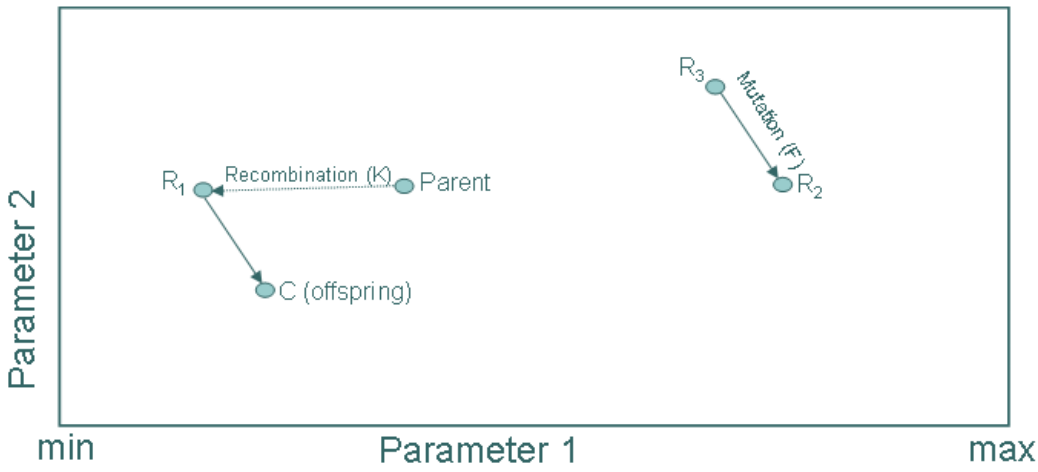

Figure 2.2: Production of an offspring trial structure using a combination of variables of the parent (P) and randomly selected individuals (R1, R2 and R3)

The recombination vector (K) represents the difference between genetic material from the parent to one random member (R_1) and the mutation vector (F) represents the difference in parameters possessed by two random members of the population (R_2 and R_3). The mutation component is to establish significant differences between the child and its original parent to discourage premature convergence

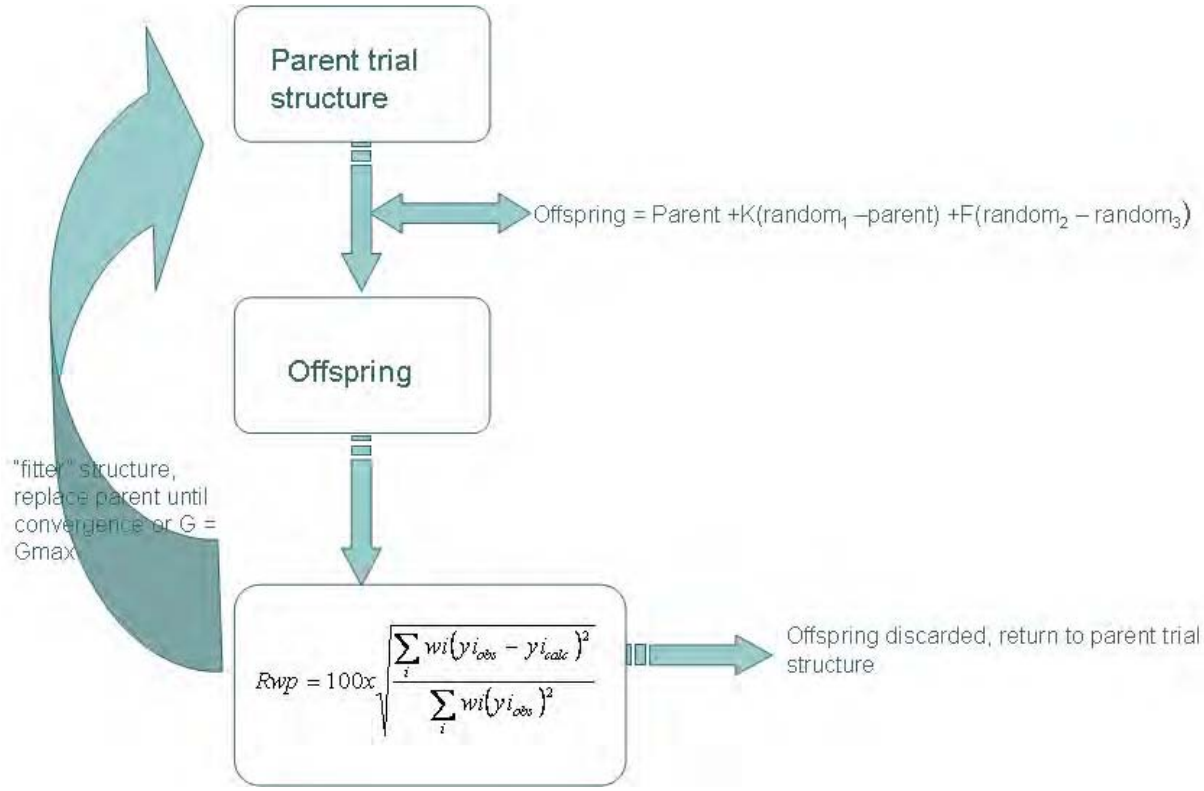

Figure 2.3 Flow diagram of the DE calculation process

The relative size of the vectors i.e. the values of K and F can be altered using POSSUM[10]. The selection of vector size is an important decision as vector size can have a direct influence on the success of the direct space search and its efficiency; vectors which are too large can miss narrow minima, whereas vectors which are too small can lead to premature convergence as the direct space calculation becomes trapped in a local minima. Figure 2.4 shows an DE progress plot, in which convergence (when R_{wp} of mean equals the best and all the population is in the same place on the hypersurface) is reached at generation 1438.

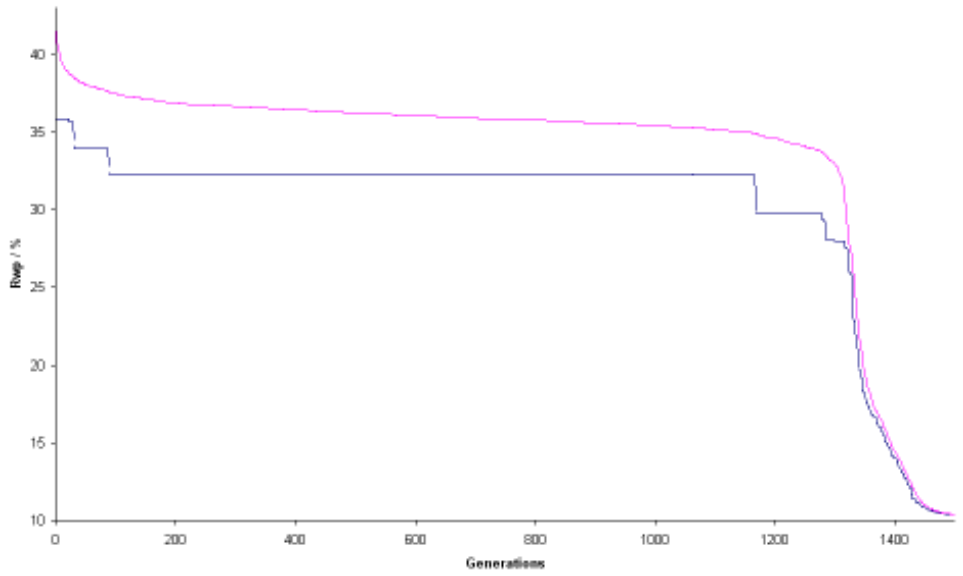

Figure 2.4: Evolutionary progress plot for the successful solution of oxamic acid:nicotinamide showing the best R_{wp} (blue) and the mean R_{wp} (pink) for each generation.

The DE calculation also invokes boundary conditions; this keeps the search within a defined space and is a useful way of introducing prior crystallographic knowledge to direct the search (e.g. unit cell size and molecular rotational parameters). If the sum of the two vectors were to place a trial structure outside the pre-defined boundary conditions, then a mid-point function approach is invoked, where the offspring is half way between the parameter value of the parent and the boundary value that has been exceeded.

DE searches can also be influenced by previous calculations by "seeding" the search. Seeding is incorporated by including the genetic information values for each parameter of up to 5 different solutions that look promising from previous calculations. This reduces the search space as the seeded DE will use 'good' parameter values as a starting point.

References:

1. S. R. Hall, F. H. Allen and I. D. Brown, *Acta Crystallographica Section A*, 1991, 47, 655-685.

2. C. F. Macrae, P. R. Edgington, P. McCabe, E. Pidcock, G. P. Shields, R. Taylor, M. Towler and J. van De Streek, *Journal of Applied Crystallography*, 2006, **39**, 453-457.

3. A. C. Larson and R. B. Von Dreele, *GSAS. General Structure Analysis System, Report No. LAUR 86-748, Los Alamos National Laboratory, Los Alamos, New Mexico, USA*, 1994.

4. R. W. Cheary and A. A. Collis, Deposited in the CCP14 Powder Diffraction Laboratory, Engineering and Physical Science Research Council, Daresbury Laboratory, Warrington, England, Editon edn., 1996.

5. R. A. Shirley, CRYSFIRE Powder Indexing System, University of Surrey, England., 2000.

6. Developed at laboratorie des Materiaux et du Genie Physique Ecole Nationale Superieure de Physique de Grenoble (INPG). Domaine Universitaire BP 46, 38402, Saint Martin d'Heres, France, Editon edn.

7. S. Y. Chong, C. C. Seaton, B. M. Kariuki and M. Tremayne, *Acta Crystallographica Section B-Structural Science*, 2006, 62, 864-874.

8. F. H. Allen, O. Kennard, D. G. Watson, L. Brammer, A. G. Orpen and R. Taylor, *Journal of the Chemical Society-Perkin Transactions 2*, 1987, S1-S19.

9. *CS Chem 3D pro(tm) Molecular modelling and analysis. Copyright 1986-1996*.

10. C. C. Seaton and M. Tremayne, *Possum Programs for Direct-Space Strucutre Solution from Powder Diffraction Data*, 2002, School of Chemistry, University of Birmingham, UK.

3. Experimental

3.1 Instrumentation

The following instruments were used for X-ray powder diffraction data collection:

3.1.1 Bruker AXS D5000 high-resolution powder diffractometer

The sample was ground using a pestle and mortar and mounted onto a flat disc with transparent tape, creating a circular area within the centre of the disc of approximately 10mm in diameter. The instrument was set in transmission mode with a position-sensitive detector covering 8˚ in 2θ using a Cu radiation source CuKα_1 1.54056 Å (Ge monochromated). Data was collected using several different ranges and scan times. The shorter runs were collected over a 2θ range from 10˚ ≤ 2θ ≤ 45˚ over 40 minutes and measured in steps of 0.020240˚ in 2θ, with an overnight scan from 10˚ ≤ 2θ ≤ 85 ˚and measured in steps of 0.020375˚ in 2θ.

3.1.2 Bruker AXS D5005 high-resolution X-ray powder diffractometer

This instrument was set in reflection mode with a position-sensitive detector covering 8˚ in 2θ using a Cu radiation source, CuKα 1.5418 Å. The low temperature stage used on this diffractometer was an Oxford Instruments CCC1101T. Data sets were collected over the range of 10˚ ≤ 2θ ≤ 45˚, measured in steps of 0.014102˚ over a total collection time of three hours. Each sample was run at the following range of temperatures 10, 50, 100, 150, 200, 250 and 295 K. The sample was ground using a pestle and mortar and using tape was attached on the reverse side of the sample holder.

This modification was made in order to reduce zero point and transparency effects in the data (section 3.1.4)

3.1.3 Sample effects using the Bruker AXS D5005 high-resolution X-ray powder diffractometer

The organic samples investigated here are affected by transparency. Transparency is caused by the penetration of the X-ray beam into the sample, effectively lowering the level of the diffraction surface with penetration depth being a function of Bragg angle. This affects the observed peak positions in the resulting diffraction pattern. As a consequence, there is a reduction in the quality of the data produced as a zero point error is effectively invoked. The effect of transparency is enhanced in organic samples are they display low absorbance of X-rays. Equation 3.1 shows the correction for transparency shift error, where *μeff is* the effective linear absorption coefficient and R the goniometer radius.

$$p = \frac{1}{2\mu effR} \qquad \text{[Equation 3.1]}$$

The problem of zero point error is enhanced further if the crystalline sample contracts anisotropically as the temperature is lowered and therefore the powder level does not remain in the calculated position. This problem of sample displacement leads to a shift in peak positions in the diffracted pattern, incorporating errors into the process of unit cell parameters calculation.

To counter these effects of transparency and thermal contraction, the sample holder was inverted and the sample mounted onto the brass stage as a thin layer within tape, as shown in figure 3.1. However, bespoke instrumental arrangement itself also leads to a zero point error, but with the distinct advantage of being constant throughout the temperature range in which the crystalline sample was investigated. The brass peaks

that appear in the diffraction pattern from the sample holder can easily be taken into account when analysing the data[1].

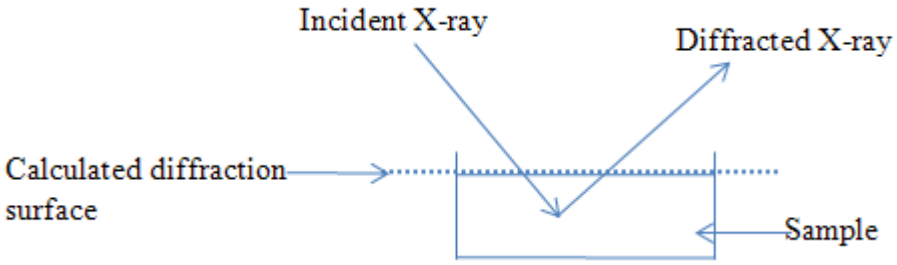

a) Traditional approach

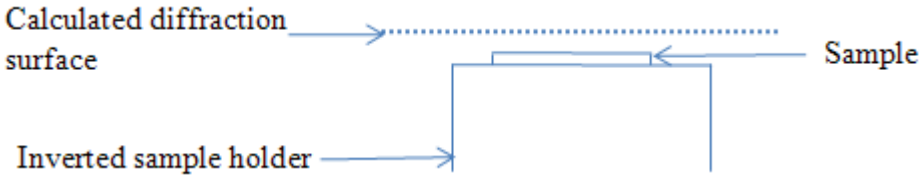

b) Modified setup

Figure 3.1: Diagram showing the techniques used to mount the sample onto the sample holder for collection of low-temperature data on D5005.

Preferred orientation is another sample effect that can lead to artificially intense or weak Bragg peaks in the diffraction pattern. In a 'perfect' powder sample with no preferred orientation the crystallites need to be randomly distributed throughout the sample, allowing all orientations to occur to satisfy the diffraction condition.

It is a combination of the instrumental geometry and the morphology of the crystals that determines the amount preferred orientation observed; the more anisotropic morphologies such as needle and plate like crystals suffer most from preferred orientation. In reflection mode (as in D5005), the crystallites often align themselves parallel to the sample bed, with very few crystallites aligning themselves perpendicular to the sample holder. Preferred orientation may be reduced, not completely, by careful sample preparation and placing of sample onto the stage, for example, mixing with amorphous silica, spray drying and grinding[2]. Experimental

setups, such as sample geometry can help to evenly distribute the orientations of crystallites, i.e. flatplates/capillaries.

3.1.4 Bruker AXS D5000 high-resolution powder diffractometer fitted with Oxford Cryostream and capillary stage

Due to the detrimental sample effects discussed in the previous section, additional low temperature data were collected on the Bruker AXS D5000 in a capillary setup. To record low temperature data, an Oxford crysostream 700 series was attached to the diffractometer. The cryostream has a temperature range of 80-500 K. The cryostream does not reach as low temperatures as achieved by the D5005 setup; due to the quality of the data produced, the crystream and capillary stage was the preferred option. Liquid nitrogen is drawn up, via a vacuum insulated transfer line, into the coldhead of the cryostream. Once inside the coldhead, the liquid nitrogen passes through a heater which boils the liquid nitrogen (77 K). The vapour flows to the heat exchanger, through the temperature controller, to arrive at the inlet of the pump at approximately 10 K below room temperature. The nitrogen gas is then dried to ensure there is no moisture in the gas flow which would cause icing on the walls of the capillary. The gas flows to the Cryostream head once more where it is re-cooled. The gas temperature is regulated by a heater and sensor before entering the nozzle and out over the sample.

As for other powder data collection, the sample was ground using a pestle and mortar. The sample was then transferred to the capillary and aligned on the vertical goniometer head. The capillary had a depth of 55 mm and a diameter of 0.5 mm. The instrument was set in transmission mode with a position-sensitive detector covering 8˚ in 2θ using a Cu radiation source CuKα_1 1.54056 Å (Ge monochromated). Data sets

were recorded for each sample at the following range of temperatures 295, 250, 200, 150 and 100 K.

3.1.5 Bruker APEXII CCD Single Crystal diffractometer

Single crystal data were collected off site by the EPSRC national crystallography service at the University of Southampton. A Bruker APEXII CCD diffractometer and a Bruker Kappa CCD diffractometer both at the windows of a Bruker FR591 rotating anode ($\lambda_{Mo\text{-}K\alpha}$ = 0.71073 Å) at 120 K, were used to collect data. The data collections were driven by COLLECT[3] and processed by DENZO.[4] Absorption corrections were applied using SADABS.[5] The structures were solved in SHELXS97[4] and were refined by a full-matrix least-squares procedure on F^2 in SHELXL-97.[4] All non-hydrogen atoms were refined with anisotropic displacement parameters. All hydrogen atoms were added at calculated positions and refined by use of a riding model with isotropic displacement parameters based on the equivalent isotropic displacement parameter (U_{eq}) of the parent atom. Figures were produced using ORTEP3 for Windows[6] while structural analysis was carried out in PLATON.[7]

3.1.6 Perkin Elmer Pyris 1 DSC (differential scanning calorimeter)

Thermal events were measured using a Perkin Elmer Pyris 1 DSC (Perkin Elmer Analytical Instruments, Norwalk, Connecticut, USA). DSC runs were performed in an atmosphere of flowing dry nitrogen gas of high purity (20 ml min^{-1}) using standard crimped aluminium pans. The instrument was calibrated within indium. Low temperature DSC traces were recorded using the method shown below;

- Hold 1.0 min at 20˚C
- Cool from 20 ˚C to -180˚C at a rate of 5˚C/min

- Hold for 1.0 min at -180˚C
- Heat from -180˚C to 20˚C at a rate of 5˚C/min
- Hold for 1.0 min at 20˚C

High temperature DSC traces were collected using the method shown below;

- Hold 1.0 min at 20˚C
- Heat from 20˚C to 240˚C at 5˚C/min
- Hold for 1 min at 240˚C
- Cool from 240˚C to 20˚C at 5˚C/min
- Hold for 1 min at 20˚C

3.1.7 Solid state NMR (nuclear magnetic resonance spectrometer)

Solid-state C^{13} NMR data were collected off site by the EPSRC solid-state NMR services at Durham University. The spectra were recorded using a Varian Unity Inova spectrometer and a 7.5mm (rotor o.d) MAS probe.

3.1.8 Solution NMR (nuclear magnetic resonance spectrometer)

Solution state ^{1}H NMR spectra were recorded at 300.18 MHz on a Bruker AC300 spectrometer with a 5mm diameter quad probe using residual solvent as a reference. Samples were dissolved in dimethyl sulfoxide (DMSO).

3.1.9 Solid state Infra-red

Spectra were obtained in the reflectance mode using an FT-NIR spectrometer (Thermo Fisher Scientific, Nicolet Anatris Near IR Analyzer) equipped withan InGaAs detector and a quartz lamp.

3.1.10 High pressure liquid chromatography (HPLC)

Analytical HPLC was performed using a Dionex summit HPLC system with chromeleon software. A Summit P580 quaternaty low pressure gradient pump with built-in vacuum degassor was used along with a Summit UVD 170s UV/VIS multi-channel detector with analytical flow cell. The analytical column was Luna 10u C18 (250mm x 4.6mm).

3.2 Synthetic technique for cocrystal/salt synthesis

3.2.1 Solvent mediated crystallisation

Starting materials were dissolved in the minimum amount of solvent and the solution was then hot filtered. The beaker was covered with Para-film then pierced. Solid material was then obtained following crystallisation from solution over a period of time depending on the system under investigation. The solid material was then filtered from the solution using a Büchner funnel vacuum filtration.

3.2.2 Incubator controlled solvent-mediated crystallisation

Starting materials were dissolved in the appropriate solvent and placed inside the Memmert incubator (IPP400). The temperature profile of the crystallisation was controlled using the Memmert MEMory card interface using the Celsius 2007 software[8]. The temperature profile used included (i) a temperature rise to 60 ˚C, (ii) a holding period of 3 hours, (iii) cooling to 20 ˚C over a period of a further 5 hours.

3.2.3 Liquid assisted grinding

Stoichiometric amounts of the starting materials were placed in a mortar along with 0.05 ml of solvent and ground together with a pestle for a period of time, ranging from 5 to 20 minutes.

3.2.4 Slurry sonication

Stoichiometric amounts of the starting materials were placed in a small glass vial. A small amount of solvent is then added to the vial which is then sonicated at room temperature for 10 minutes.

3.2.5 Dry Grinding

Stoichiometric amounts of the starting materials were placed in a mortar and ground with a pestle for a period of time, ranging from 5 to 20 minutes.

3.3 Preparation and characterisation of systems under investigation

3.3.1 Oxamic acid:isonicotinamide

3.3.2 Synthesis

All starting materials and solvents were purchased from Sigma Aldrich. Equimolar amounts of oxamic acid (0.17 g, 1.88 mmol) and isonicotinamide (0.23 g, 1.88 mmol), in warm methanol. The mixed solution was stirred, cooled to room temperature and on slow evaporation of the solvent, a white crystalline solid was formed after 1 day and filtered from the solution. The same product was obtained following (i) slow recrystallisation of equimolar amounts from ethanol, (ii) liquid

assisted grinding for 5 minutes using 1.2577 mmol of each starting material with 0.05 ml of methanol and (iii) sonic slurry in which 1.2577 mmol of each starting material was added to 5ml of solvent in a small vial and sonicated at room temperature for 10 minutes.

3.3.3 NMR analysis

The stoichiometry of the components in the new crystalline solid was confirmed as 1:1 from the solution ^{1}H nmr spectrum (figure 3.2).

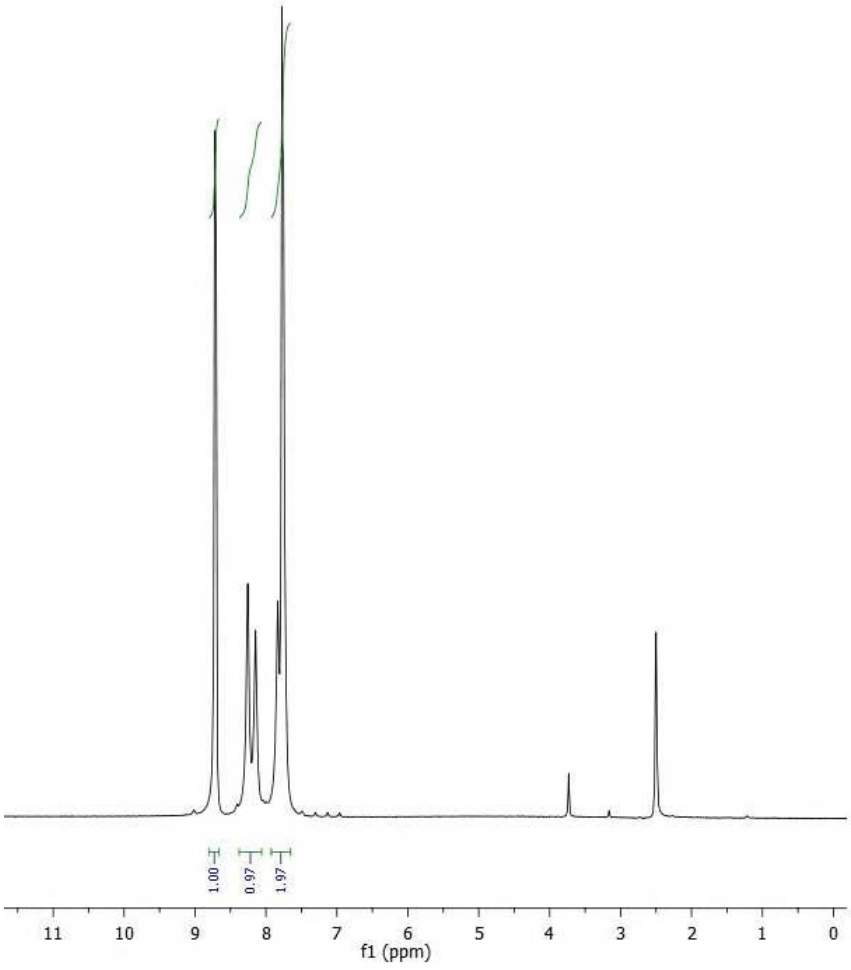

Figure 3.2: ^{1}H NMR of oxamic acid:isonicotinamide product (from 1:1 starting ratio) using DMSO as solvent. ^{1}H NMR 300MHz (DMSO-d_6): δ = 8.90 ppm (dd, 2H), 8.4 ppm (s, 1H), 8.21 ppm (s, 1H), 7.8 ppm (d, 4H).

As shown within the figure 3.2, the amide protons present on the isonicotinamide and oxamic acid exist in different chemical environments. This is due to the the C-N bond showing greater double bond character via resonance. This double bond character restricts free rotation around the double bond[9]. This is evident as two peaks are assigned to the amine protons, (8.4 ppm and 7.8 ppm). The same is true on the oxamic molecule, with two peaks assigned to the amine protons, (8.2 ppm and 7.8 ppm).

3.3.4 HPLC results

Please find the HPLC result in appendix A. The result confirmed the presence of both the oxamic acid and isonicotinamide in the new crystalline phase.

3.3.5 DSC analysis

The new 1:1 material was characterised by DSC (appendix B). This confirms that there is no phase transition from room temperature to the melt. Melting points of starting materials and the new adduct were measured using melting point apparatus, oxamic acid (210˚C), isonicotinamide (155-157˚C), oxamic:isonicotinamide (205-207˚C)

3.3.6 Preparation of sample for single crystal diffraction

A crystal of oxamic acid:isonicotinamide was successfully grown using 0.2300 g and 0.1677 g of isonicotinamide and oxamic acid respectively, following the incubator solvent-mediated crystallisation method (section 3.2.2).

3.3.7 Stoichiometric diversity

The stoichiometric diversity of this system was probed using 0.2302g (2.585mmol) and 0.6314g (5.17mmol) of oxamic acid and isonicotinamide respectively, following the recrystallisation method as described above in 3.11.1. Please see appendix C, for a comparison of oxamic acid:isonicotinamide in 1:1 and 1:2 stoichiometries. The powder patterns show that 1:2 stoichiometry matches the pure isonicotinamide powder pattern.

3.4 Oxamic acid:nicotinamide

3.4.1 Synthesis

All starting materials and solvents were purchased from Sigma Aldrich. Equimolar amounts of oxamic acid (0.2309 g, 2.58 mmol) and nicotinamide (0.3158 g, 2.58 mmol), were dissolved in warm methanol. The mixed solution was stirred, cooled to room temperature and on slow evaporation of the solvent, a white crystalline solid was formed after 5 days, and filtered from solution. The same product was obtained following (i) slow recrystallisation of equimolar amounts from ethanol, (ii) liquid assisted grinding for 5 minutes using 1.2577 mmol of each starting material with 0.05 ml of methanol and (iii) sonic slurry in which 1.2577 mmol of each starting material was added to 5ml of solvent in a small vial and sonicated at room temperature for 10 minutes.

3.4.2 NMR analysis

The stoichiometry of the components in the new crystalline solid was confirmed as 1:1 from the solution ^{1}H nmr spectrum (figure 3.3).

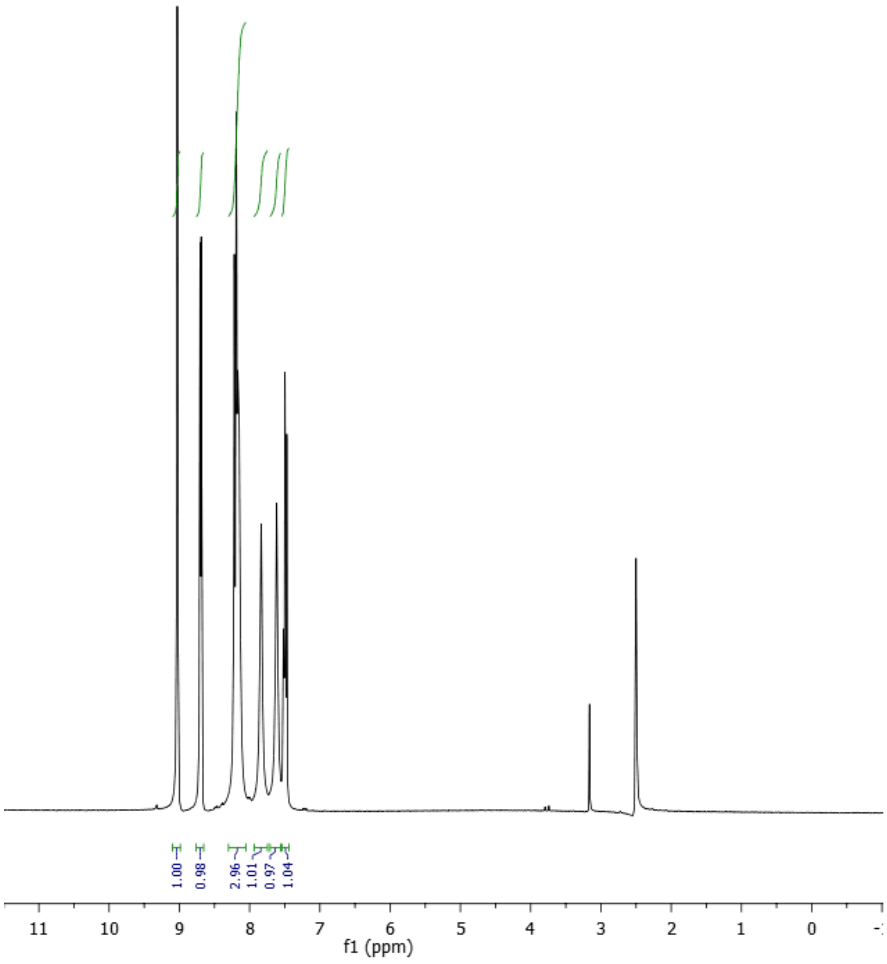

Figure 3.3: ^{1}H NMR of oxamic acid:nicotinamide multi-component crystal (from 1:1 starting ratio) using DMSO as solvent. ^{1}H NMR 300MHz (DMSO-d_6): δ = 9.10 ppm (dd, 1H), 8.7 ppm (d, 1H), 8.21 ppm (dt, 3H), 7.8 ppm (d, 1H) 7.7 (d, 1H), 7.5 (d, 1H).

As discussed in the case of oxamic acid:isonicotinamide the amide protons in both oxamic acid and nicotinamide are resolved producing two nmr singals.

3.4.3 HPLC result

Please find the HPLC result in appendix A. The result confirmed the presence of both the oxamic acid and nicotinamide the in the new crystalline phase.

3.4.4 DSC analysis

The new 1:1 material was thermally characterised by DSC (appendix D). This confirms that there is no phase transition from room temperature to the melt. The melting point of both starting materials and oxamic acid:nicotinamide were measured using melting point apparatus, oxamic acid (210˚C), nicotinamide (128˚C) and oxamic acid:nicotinamide (180-182˚C)

3.4.5 Preparation of sample for single crystal diffraction

A crystal of oxamic acid:nicotinamide was successfully grown using 0.23458 g and 0.3217 g of oxamic acid and nicotinamide respectively, following the incubator solvent-mediated crystallisation method (section 3.2.2).

3.5 Fumaric acid:nicotinamide

3.5.1 Synthesis

All starting materials and solvents were purchased from Sigma Aldrich. Equimolar amounts of fumaric acid (0.1829g, 1.498 mmol) and nicotinamide (0.1739g, 1.498 mmol), were dissolved in warm methanol. The mixed solution was stirred, cooled to room temperature and on slow evaporation of the solvent, a white crystalline solid weas formed after 8 days. The same product was obtained following (i) slow

recrystallisation of equimolar amounts from ethanol, (ii) liquid assisted grinding for 5 minutes using 1.2259 mmol of each starting material with 0.05 ml of methanol and (iii) sonic slurry in which 1.2259 mmol of each starting material was added to 5ml of solvent in a small vial and sonicated at room temperature for 10 minutes.

3.5.2 NMR analysis

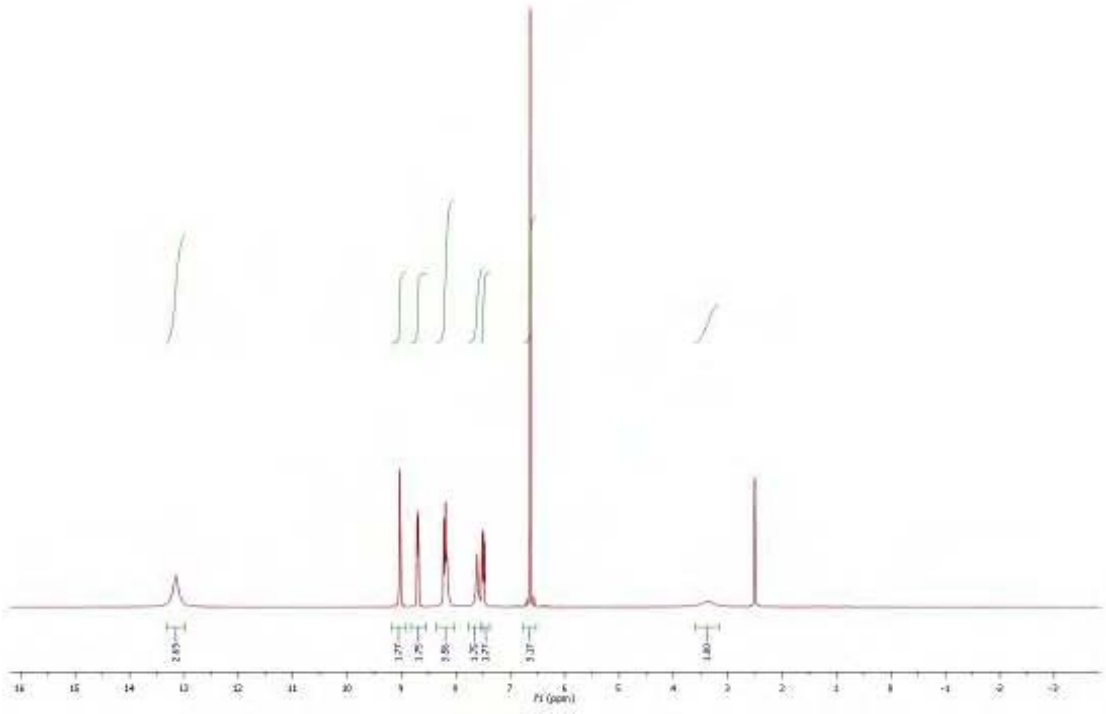

Figure 1.4: NMR of fumaric acid:nicotinamide product (from 1:1 starting ratio) using DMSO as solvent. ^{1}H NMR 300MHz (DMSO-d_6): δ = 13.2 ppm (s, 2H), 9.10 ppm (dd, 1H), 8.7 ppm (d, 1H), 8.21 ppm (dt, 1H), 8.19 ppm (s, 1H) 7.8 ppm (d, 1H) 7.6 (d, 1H), 6.6 (d, 2H).

The stiochoimetric ratio of fumaric acid and nicotinamide was confirmed by the integration of peaks from the ^{1}H NMR (figure 3.4).

3.5.3 Melting point analysis

The new phase was thermally characterised by measuring the melting point. This was found to be 171-172°C and compares to that of the starting materials, 287°C and 128°C for fumaric acid and nicotinamide respectively.

3.5.4 Preparation of sample for single crystal diffraction

A single crystal of fumaric acid:nicotinamide was successfully grown using 0.2421 g (2.0858 mmol) and 0.2547 g of fumaric acid and nicotinamide respectively, and following the incubator solvent-mediated crystallisation method (section 3.2.2).

3.5.5 Stoichiometric diversity

The stoichiometric diversity of the system was probed with 1(fumaric acid): 2(nicotinamide), using 0.2518068 g of fumaric acid and 0.531 g (4.34mmol) of nicotinamide, following the recrystallisation method (3.5.1). Please see appendix E for X-ray powder diffraction.

3.6 Maleic acid:nicotinamide

3.6.1 Synthesis (product A)

All starting materials and solvents were purchased from Sigma Aldrich. Equimolar amounts of maleic acid (0.2309g, 2.58 mmol) and nicotinamide (0.3158g, 2.58 mmol), were dissolved in warm ethanol. The mixed solution was stirred, cooled to room temperature and on slow evaporation of the solvent, a white crystalline solid was formed after 2 day. The same product was obtained following (i) slow recrystallisation of equimolar amounts from ethanol, (ii) liquid assisted grinding for 5

minutes using 0.931 mmol of each starting material with 0.05 ml of ethanol and (iii) sonic slurry in which 0.931 mmol of each starting material was added to 5ml of solvent in a small vial and sonicated at room temperature for 10 minutes.

3.6.2 NMR analysis (product A)

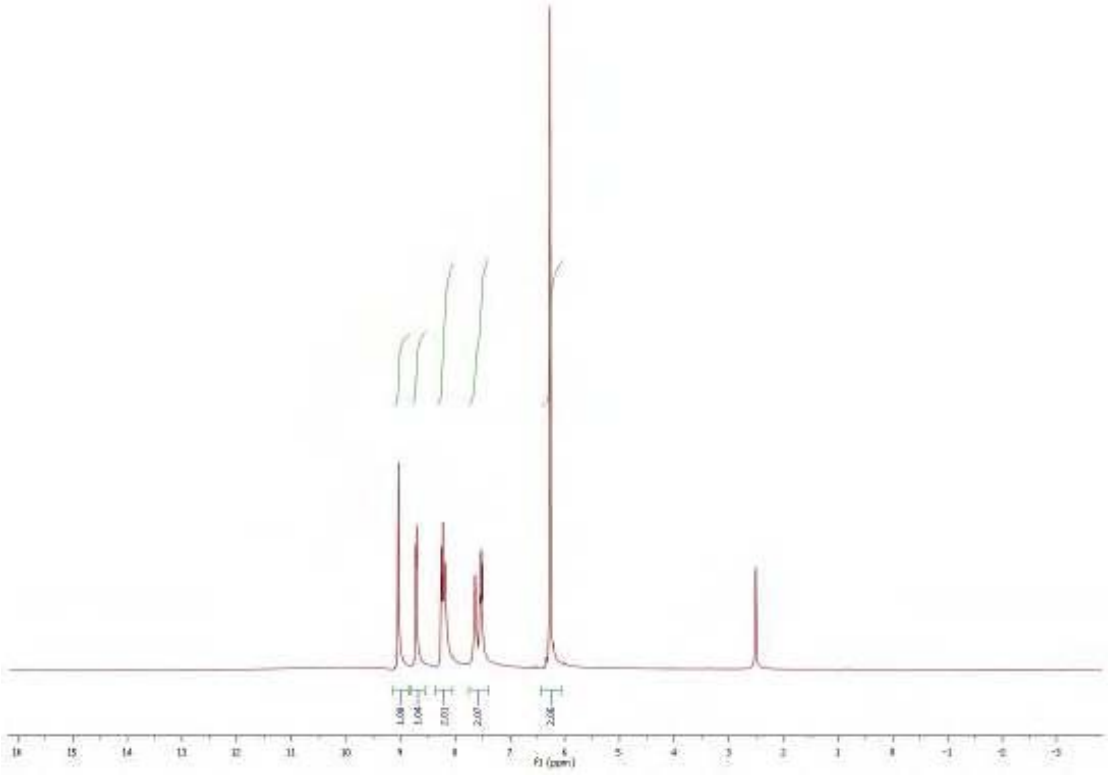

Figure 3.5: ^{1}H NMR of maleic acid and nicotinamide product A multi-component crystal (from 1:1 starting ratio) using DMSO as solvent. 1H NMR 300MHz (DMSO-d_6): δ = 9.10 ppm (dd, 1H), 8.7 ppm (dd, 1H), 8.21 ppm (dt, 2H), 7.8 ppm (d, 1H) 7.6 (d, 1H), 6.2 (d, 2H).

The stiochoimetric ratio (1:1) of maleic acid:nicotinamide product A was confirmed by the integration of peaks from the ^{1}H NMR. No hydroxyl signal was detected for maleic acid in the spectra, this due to the propensity of the hydroxyl proton to exchange with the water in the highly hygroscopic DMSO and the hydrogen bonding afforded by the close proximity of the hydroxyl groups in the maleic acid molecule.

3.6.3 DSC analysis (product A)

The new 1:1 material was thermally characterised by DSC (appendix F). This confirms that there is no phase transition from room temperature to the melt. The melting point of both starting materials and maleic acid:nicotinamide were measured using melting point apparatus, maleic acid (131˚C), nicotinamide (128˚C) and oxamic acid:nicotinamide (116-117˚C).

3.6.4 Preparation of sample for single crystal diffraction (product A)

A single crystal of maleic acid and nicotinamide product A was successfully grown using, 0.2213 g (1.907 mmol) and 0.2329 g of maleic acid and nicotinamide respectively, following the incubator solvent-mediated crystallisation method (section 3.2.2).

3.6.5 Synthesis (product B)

All starting materials and solvents were purchased from Sigma Aldrich. Equimolar amounts of fumaric acid (0.2309g, 2.58 mmol) and nicotinamide (0.3158g, 2.58 mmol), were dissolved in warm methanol. The mixed solution was stirred, cooled to room temperature and on slow evaporation of the solvent, a white crystalline solid was formed after 5 day (maleic acid and nicotinamide, product A). The crystallites were left in solution for a further 7 days and yellow crystallites had formed (maleic acid, product B). The same product (product B) was unattainable from (i) slow recrystallisation of equimolar amounts from ethanol, (ii) liquid assisted grinding for 5 minutes using 0.915 mmol of each starting material with 0.05 ml of methanol and (iii)

sonic slurry in which 0.915 mmol of each starting material was added to 5 ml of solvent in a small vial and sonicated at room temperature for 10 minutes.

3.6.6 NMR analysis (product B)

The stiochoimetric ratio (1:1) of maleic acid:nicotinamide product B was confirmed by the integration of peaks from the ^{1}H NMR. Unlike the ^{1}H NMR of product A, a hydroxyl signal is present at 13.2 ppm. The presence of the hydroxyl signal suggests the isomerisation[10] of maleic acid to the *trans* isomer, fumaric acid.

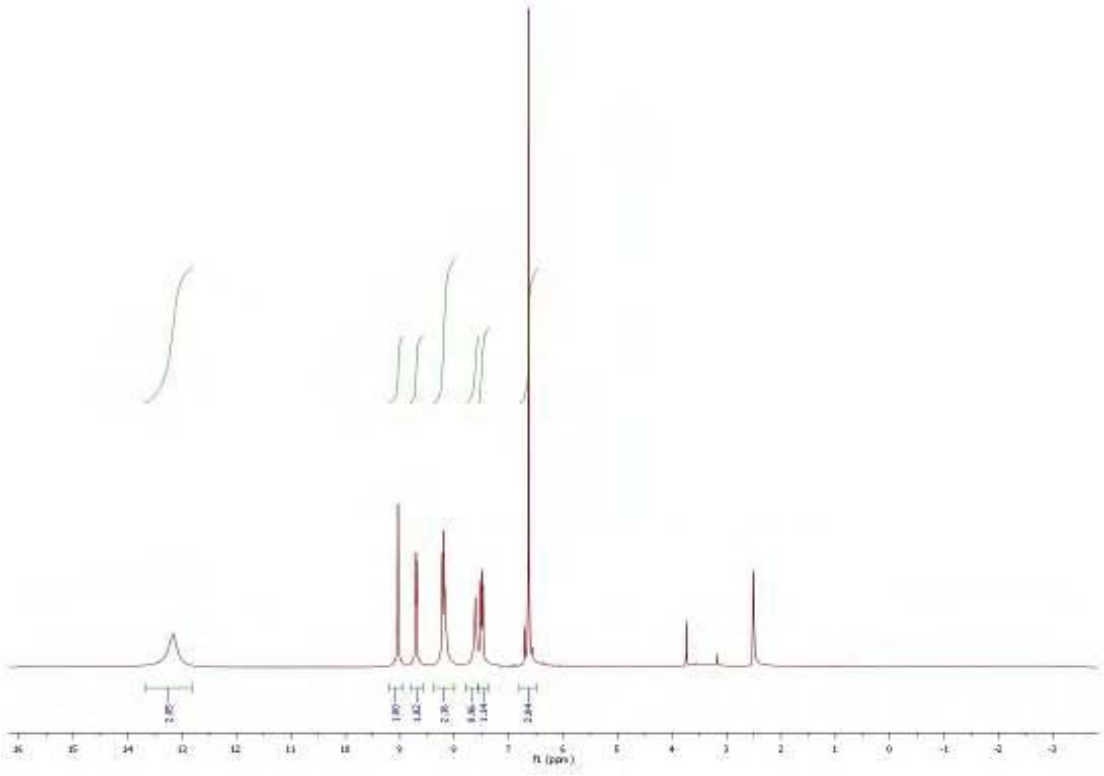

Figure 3.6: ^{1}H NMR of maleic acid and nicotinamide product B (from 1:1 starting ratio) using DMSO as solvent. ^{1}H NMR 300MHz (DMSO-d_6): δ = 13.2 (s, 2H), 9.10 ppm (dd, 1H), 8.7 ppm (dd, 1H), 8.21 ppm (dt, 2H), 7.8 ppm (d, 1H) 7.6 (d, 1H), 6.2 (d, 2H).

3.6.7 DSC analysis (product B)

The new 1:1 material was thermally characterised by DSC (appendix G). This confirms that there is no phase transition from room temperature to the melt. The

melting point of both starting materials and maleic acid:nicotinamide product B were measured using melting point apparatus, maleic acid (131˚C), nicotinamide (128˚C) and oxamic acid:nicotinamide (171-172˚C).

3.6.8 Preparation of sample (product B) for single crystal diffraction

A crystal of maleic acid:nicotinamide product B was successfully grown using 0.2050 g (1.766 mmol) and 0.2156 g of maleic acid and nicotinamide respectively, following the incubator solvent-mediated crystallisation method (section 3.2.2).

3.7 Maleic acid:isonicotinamide

3.7.1 Synthesis

All starting materials and solvents were purchased from Sigma Aldrich. Equimolar amounts of the two starting materials maleic acid (0.2867g, 2.47 mmol) and isonicotinamide (0.3021g, 2.47 mmol), were dissolved in warm methanol. The mixed solution was stirred, cooled to room temperature and on slow evaporation of the solvent, a white crystalline solid was formed after 2 days. The same product was obtained following (i) slow recrystallisation of equimolar amounts from ethanol, (ii) liquid assisted grinding for 5 minutes using 1.3150 mmol of each starting material with 0.05 ml of methanol and (iii) sonic slurry in which 1.054 mmol of each starting material was added to 5ml of solvent in a small vial and sonicated at room temperature for 10 minutes.

3.7.2 NMR analysis

The stiochoimetric ratio (1:1) of maleic acid:isonicotinamide was confirmed by the integration of peaks from the ^{1}H NMR. As described in section in 3.6.2, no signal is seen for the hydroxyl protons in maleic acid.

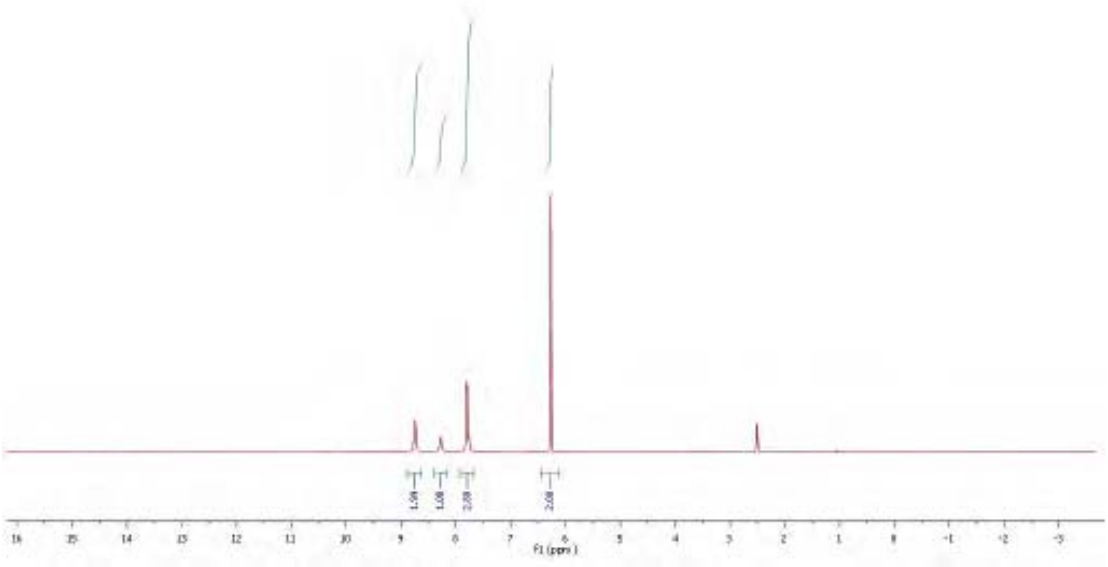

Figure 3.7: ^{1}H NMR of oxamic acid and isonicotinamide multi-component crystal (from 1:1 starting ratio) using DMSO as solvent. ^{1}H NMR 300MHz (DMSO-d_6): δ = 8.90 ppm (dd, 2H), 8.4 ppm (s, 1H), 8.21 ppm (s, 1H), 6.2 ppm (d, 2H).

3.7.3 Preparation of sample for single crystal diffraction

A crystal of maleic acid:isonicotinamide was successfully grown using, 0.2147 g (1.8502 mmol) and 0.2259g of maleic acid and nicotinamide respectively, and following the incubator method (section 3.2.2).

3.8 Succinic acid:nicotinamide

3.8.1 Synthesis

All starting materials and solvents were purchased from Sigma Aldrich. Equimolar amounts of the two starting materials succinic acid (0.2300g, 1.94 mmol) and nicotinamide (0.2378g, 1.94 mmol), were dissolved in warm methanol. The mixed solution was stirred, cooled to room temperature and on slow evaporation of the solvent, a white crystalline solid was formed after 3 days. Powder X-ray diffraction patterns of starting materials and new multi-component phase are shown in appendix H.

3.9 Adipic acid:nicotinamide

3.9.1 Synthesis

All starting materials and solvents were purchased from Sigma Aldrich. Equimolar amounts of the two starting materials adipic acid (0.180g, 1.23 mmol) and nicotinamide (0.1504g, 1.23 mmol), were dissolved in warm methanol. The mixed solution was stirred, cooled to room temperature and on slow evaporation of the solvent; a white crystalline solid was formed after 5 days. Powder X-ray diffraction patterns of starting materials and new multi-component phase are shown in appendix I.

3.10 Oxamic acid

3.10.1 Solvent mediated recrystallisation

Oxamic acid was purchased as a white powder (≥ 96 % pure) from Sigma Aldrich. The possibility of polymorphic behaviour of oxamic acid was investigated by

conducting a solvent screen, which included solvent mediated crystallisation (section 3.2.1) of oxamic acid from a plethora of solvents.

3.10.2 Neutron powder diffraction

Neutron powder diffraction data were collected using the BT-1 32 detector neutron powder diffractometer at the NIST Center for Neutron Research reactor, NBSR. A Cu(311) monochromator with a 90° take-off angle, $\lambda = 1.5402(1)$ Å, and in-pile collimation of 15 minutes of arc were used. Data were collected over the range of 3-168° 2θ with a step size of 0.05°.

The sample was loaded in a vanadium can sample container of length 50 mm and diameter 9.2 mm. Data were collected under ambient conditions.

Reference:

1. L. Vella-Zarb, *University of Birmingham*, 2009, PhD thesis.
2. K. D. M. Harris, M. Tremayne and B. M. Kariuki, *Angewandte Chemie-International Edition*, 2001, **40**, 1626-1651.
3. R. W. W. Hooft, COLLECT Data Collection Software, Nonius B.V, Delft., 1998.
4. G. M. Sheldrick, Acta Cryst, A64, Editon edn., 2008, pp. 112-122.
5. G. M. Sheldrick, Bruker AXS Inc., Madison, Wisconsin, USA, SADABS v2007/2., 2007.
6. L. J. Farrugia, J. Appl. Crystallogr, Editon edn., 1997, vol. 30, p. 565.
7. A. L. Spek, Acta Cryst., A46., 1990, vol. 34.
8. Memmert GmbH + Co. Kg, A. R. S. 38 and D.-S. Germany, *Celsius 2007, Verson 9.1*, 2007.
9. W. P. Purcell and J. A. Singer, *Journal of Physical Chemistry*, 1967, **7**1, 4316-4319.

10. S. Chatterjee, V.R. Pedireddi and C.N.R. Rao, *Tetrahedron letters,* 1998, 39, 2843-2846.

4.0 Cocrystallisation of oxamic acid:isonicotinamide and oxamic acid:nicotinamide

Within this chapter, the co-crystallisation or adduct formation of oxamic acid with both nicotinamide and isonicotinamide will be attempted. All of these materials are considered as GRAS (generally recognized as safe) and are FDA (Food and Drug Administration) approved. Oxamic acid itself has useful medicinal properties, in that it can affect the role of glycolysis in the growth of tumour cells[1]. To date, the crystal structure of oxamic acid is still unpublished, however it has been reported[2] that oxamic acid could potentially be an impurity in various APIs, hence the full structural characterisation of the molecule is important (chapter 6.0).

Isonicotinamide (pyridine-4-carboxamide) has been shown to act as a robust building block within a multi-component crystal[3-6] and is a strong candidate as a potential component in a multi-component crystal with a suitable API. Isonicotinamide is low cost, widely available, has a low melting point (155-157 °C) and a molecular weight under 300 amu. All these factors are considered in a pharmaceutical screening process and allow for the screen to be a cheaper and more efficient process[7]. Nicotinamide (3-pyridinecarboxamide) is also a well established co-crystal former[8-12]and is also a vitamin (B3). The molecular diagrams of all three individual components are given in figure 4.1.

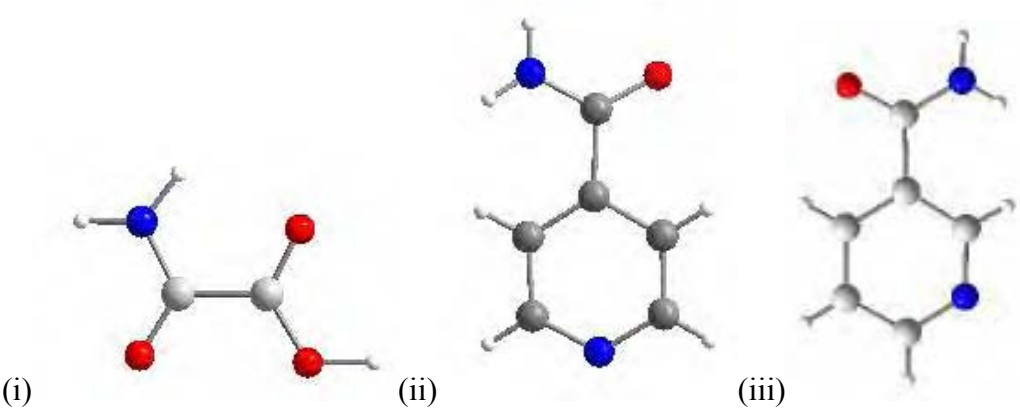

Figure 4.1: Molecular diagrams of (i) oxamic acid, (ii) isonicotinamide and (iii) nicotinamide

As discussed in the introduction, both isonicotinamide and nicotinamide have demonstrated their affinity for cocrystal formation with carboxylic acids. In addition the generation of a well defined hierarchy of supramolecular synthons makes their behaviour in this chapter potentially predictable (figure 1.12). Oxamic acid itself is also a useful architectural unit when designing hydrogen bonding synthons. The molecule contains both strong hydrogen bond acceptors (in the form of the carbonyl oxygen atoms) and donors (in the form of a hydroxyl oxygen and amide nitrogen). In other multi component materials contained in the CSD, oxamic acid is present in salt form, (oxamate). The tendency of an acid to give up a proton to form an acid-base complex is measured by the negative logarithm of the acid dissociation constant, pKa. Typically[13], a difference of 2 to 3 pKa units often results in the formation of a salt. However the application of an aqueous based measurement such as pKa to a solid state situation must be considered when using the differences in pKa as a predictive tool in solid salt or neutral cocrystal formation. Potential dimeric synthons formed by the oxamate anion are shown in figure 4.2.

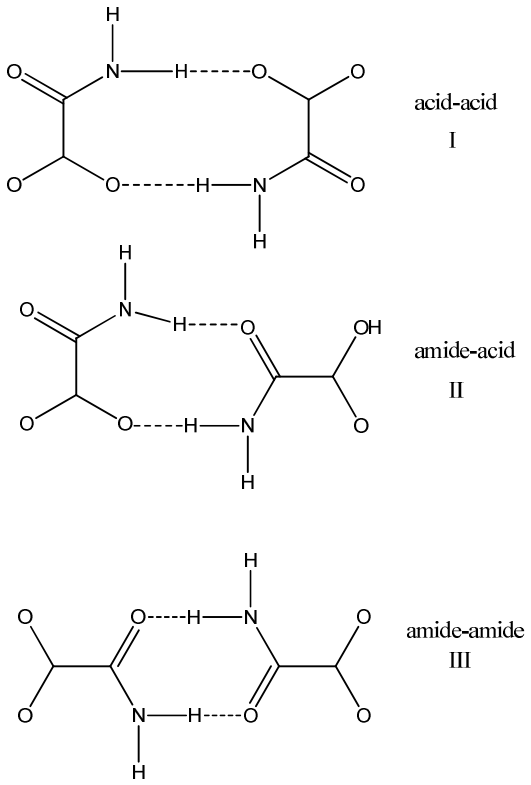

Figure 4.2: Potential dimeric sythons for the oxamate unit.

The other remaining hydrogen bond sites are available for providing a cross-link between neighbouring 1-D motifs creating a 2-D scaffolding. These architectures have been presented previously[14] and introduced as acid-acid(I), amide-acid (II) and amide-amide (III) synthons. Oxamic acid also lends itself well as a possible candidate to undergo polymorphic transitions and as a useful stepping-stone in the design of hydrogen-bonded supramolecular architectures.

4.1 Characterisation of oxamic acid and isonicotinamide

Pxrd was used to confirm that the product of crystallisation (1:1, methanol) was a new crystalline phase, and did not contain any of the two starting materials (figure 4.3). The stoichiometric ratio of the two starting materials was confirmed by ^{1}H NMR

(section 3.3.3) and the presence of both materials in the new crystalline system was confirmed by HPLC (section 3.3.4).

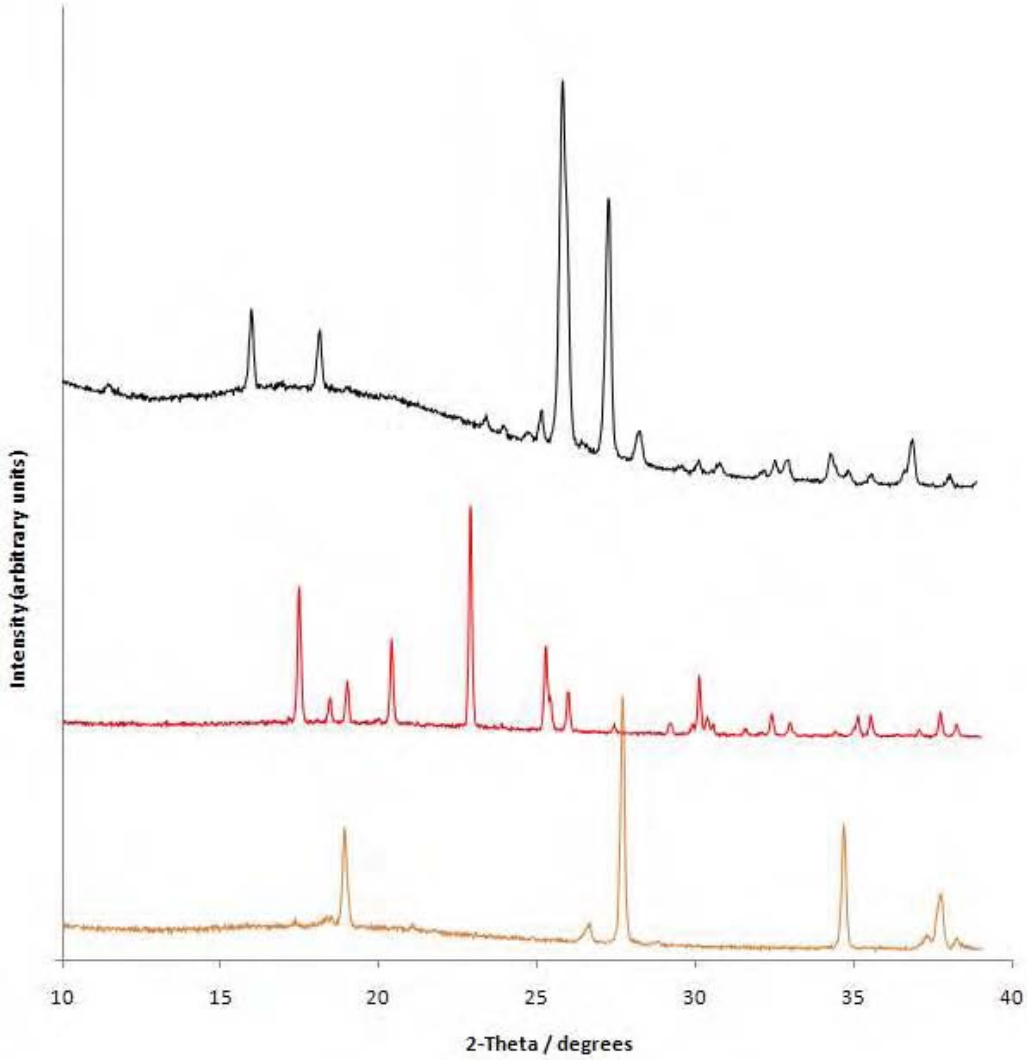

Figure 4.3: Powder X-ray diffraction patterns of the starting materials, oxamic acid (orange) and isonicotinamide (red) and the oxamic acid:isonicotinamide multi-component material(black)

Infra-red spectroscopy was performed on the new crystalline phase and compared to that recorded from a mixture of starting materials. The spectra of the two are significantly different, alluding to the synthesis of a new multi-component crystal with different hydrogen-bonding characteristics to that of the component mixture, (figure 4.4). The presence of two broad peaks at 2444 cm^{-1} and 1884 cm^{-1} is

characteristic of an acid----N heterocylic hydrogen bond, and is viewed as evidence for multi-component crystal formation. The absence of such bands would be interpreted as a lack of multi-component formation[15]. In terms of classifying the multi-component crystal as a salt or cocrystalline material from this data, it has been illustrated in the literature[16] that if an acidic proton is transferred to a heterocyclic nitrogen, very broad peaks would appear around 2500 ± 100 cm^{-1}, and for individual N^{+}-H bonds, peaks would appear at 3250 ± 50 cm^{-1}. As illustrated in figure 4.4, peaks are present at 2444 cm^{-1} and 3222 cm^{-1} allude to a proton transfer and consequently the new material is a salt.

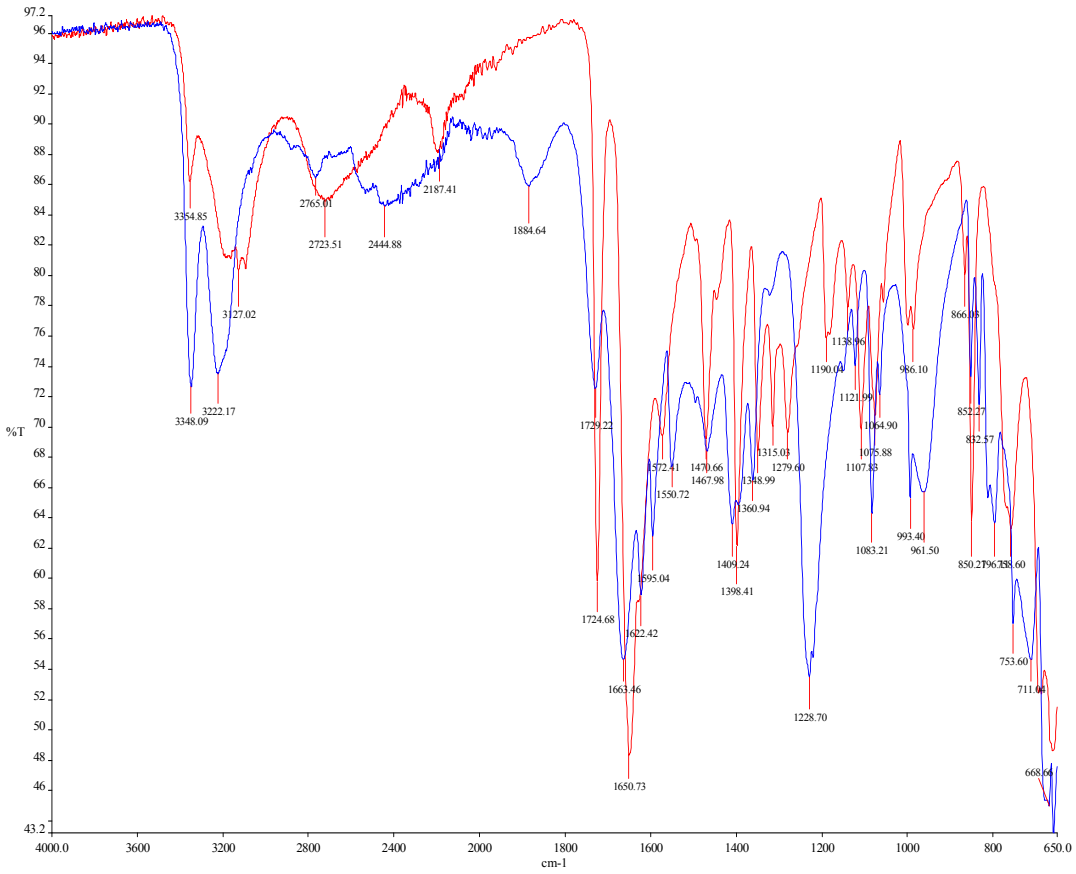

Figure 4.4: Solid state IR spectra of the oxamic acid and isonicotinamide mix (red) and the new multi-component crystal (blue).

In parallel with traditional solvent-mediated recrystallisation, pxrd (figure 4.5) was used to confirm that the same bulk crystalline phase was produced by both LAG (section 3.2.2) and sonic slurry (section 3.2.2) methods.

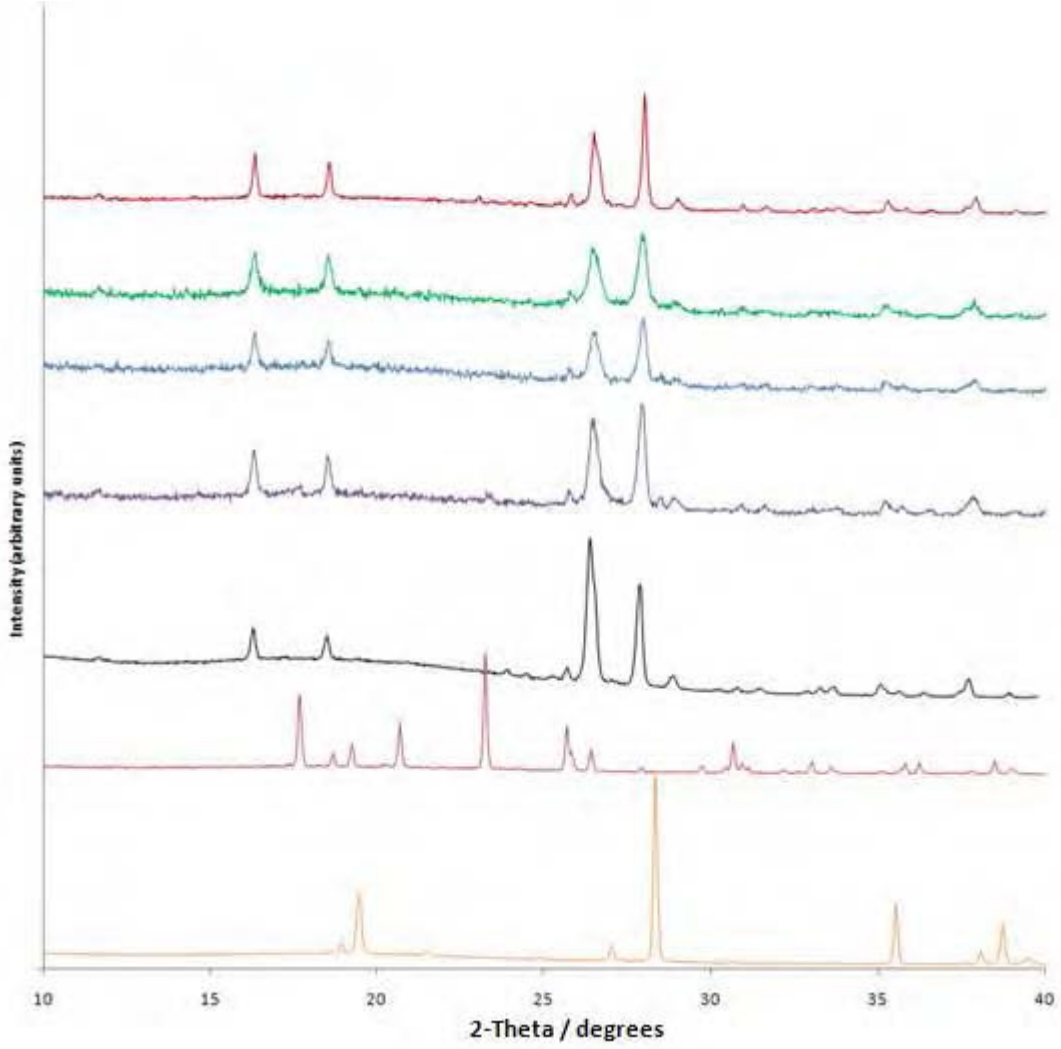

Figure 4.5: Powder X-ray diffraction data, listed from bottom to top, of the starting materials oxamic acid (orange) and isonicotinamide (red). Oxamic acid:isonicotinamide crystallised from solution mediated crystallisation (black), oxamic acid:isonicotinamide ground for 5 minutes(purple), oxamic acid:isonicotinamide ground for 15 minutes (blue), oxamic acid: isonicotinamide ground for 20 minutes (green) and oxamic acid:isonicotinamide from sonic slurry(dark red).

As discussed previously (section 1.11.4), the mechanochemical production of multi-component crystals can be advantageous over traditional approaches. However, a

distinct disadvantage is illustrated in figure 4.5, in the production of poor quality crystallites when compared to those produced by solvent-mediated evaporation. The synthesis by grinding is rapid; after only a period of 5 minutes, the synthesis of the multi-component crystal is achieved, albeit with some nicotinamide starting material being evident. The diffraction pattern shows signs significant peak broadening due to the increase in particle size. After more grinding the quality of the crystallites decreases significantly (figure 4.5). The crystallite quality produced by sonic solution, (figure 4.5), is better than that produced by the mechanochemical synthesis. However, in terms of solvent reduction, the sonic slurry method is not as environmentally sound as mechanochemical grinding.

4.2 Structure solution and refinement from laboratory pxrd data

The X-ray powder diffraction data set used for structural analysis was collected over a period of 8 hours and over the range $10^{\circ} \leq 2\theta \leq 85^{\circ}$. The data were indexed on the basis of the first 20 observable reflections using the indexing program CRYSFIRE[17] (appendix J) and the $P2_1/n$ space group assigned by consideration of systematic absences. The profile parameters were refined using the whole-profile-fitting LeBail[18] method in the GSAS[19] program to improve the fit of the lattice, zero-point and profile parameters. Structure solution was carried out using the DE; the technique (section 1.14) as implemented in the program POSSUM[20].

From density considerations it was concluded that the asymmetric unit contained one isonicotinamide and one oxamic acid molecule. Hence the structural model used in the DE calculation comprised both molecules, constructed using standard bond lengths[21] and angles, but excluding the hydroxyl and amine hydrogen atoms (figure

4.6). Each molecule is defined by 7 DE elements: 3 parameters (θ,Φ,Ψ) to define the orientation of each molecule within the unit cell (bounds 0 - 360˚), 3 parameters (*x,y,z*) to define the position of each molecule in the unit cell (bounds 0-1) and one unconstrained torsion angle (0-360˚) to define the conformation of each molecule. The molecules were moved independently in the structure solution resulting in a 14 parameter problem.

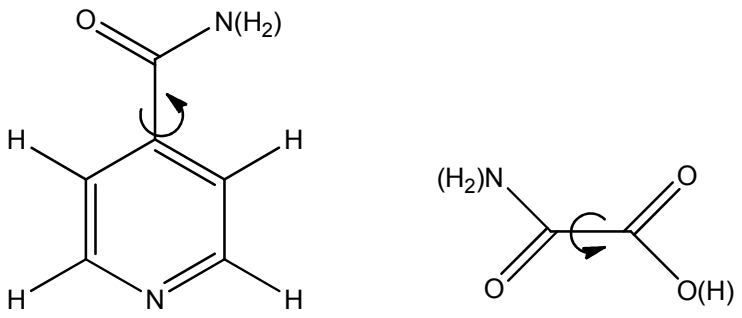

Figure 4.6: Molecular structures used in the DE structure solution, torsion angles are indicated by arrows, excluded hydrogen atoms are shown in brackets.

The parameters used in the successful DE calculation were, K = 0.99, F = 0.5, N_p = 140 and G_{max} = 2000. Convergence was achieved after 1638 generations with the best solution with R_{wp} = 20.53 %. Figure 4.7 illustrates the evolutionary progress of the DE calculation clearly showing a steep decline in R_{wp} after a prolonged plateau.

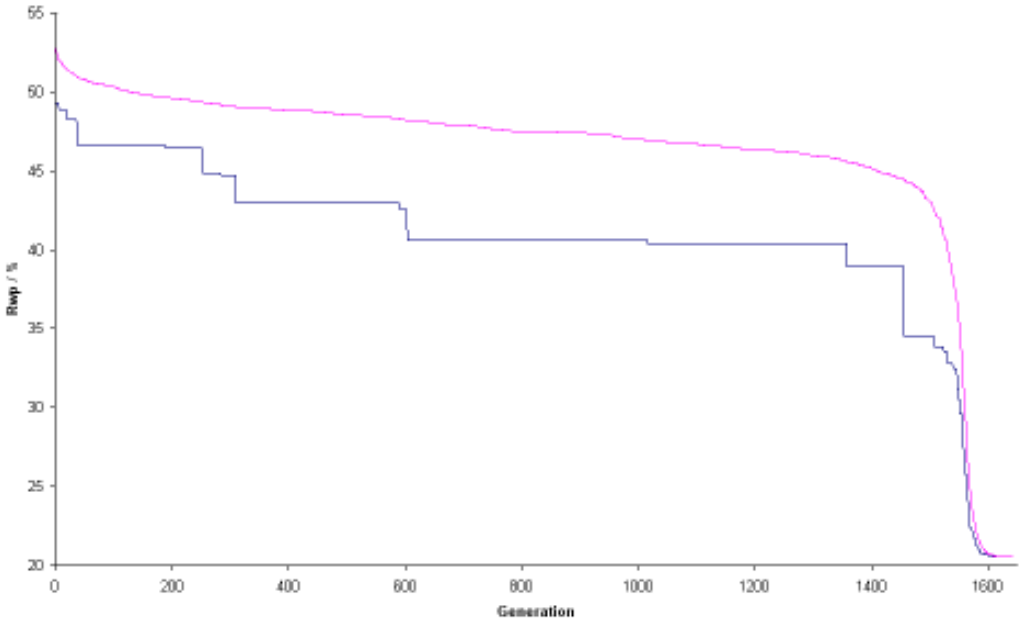

Figure 4.7: Differential evolution progress plot for the successful structure solution of oxamic acid:isonicotinamide showing the R_{wp} of the best individual in blue and the mean % R_{wp} of the population in pink.

4.3 Rietveld refinement

The DE solution was used as a starting point for refinement using the GSAS program package[22]. The positions of all atoms were refined subject to soft constraints (weighting factor of 0.001 for bond distances and 0.005 for geminal non-bonded distances) on standard geometry. Hydrogen atoms that were not included in the DE calculation and were placed in calculated positions according to the expected hydrogen bonding network. Isotropic atomic displacement parameters were refined. For the non-H atoms, isotropic atomic displacement parameters were refined constrained according to atom type or environment. Refinement of a preferred orientation parameter in the [010] direction was required, with the fraction of 1.02(1). Figure 4.8 shows the final Rietveld profile for oxamic acid:isonicotinamide. Structure solution parameters from both pxrd and sxrd are shown in Table 4.1.

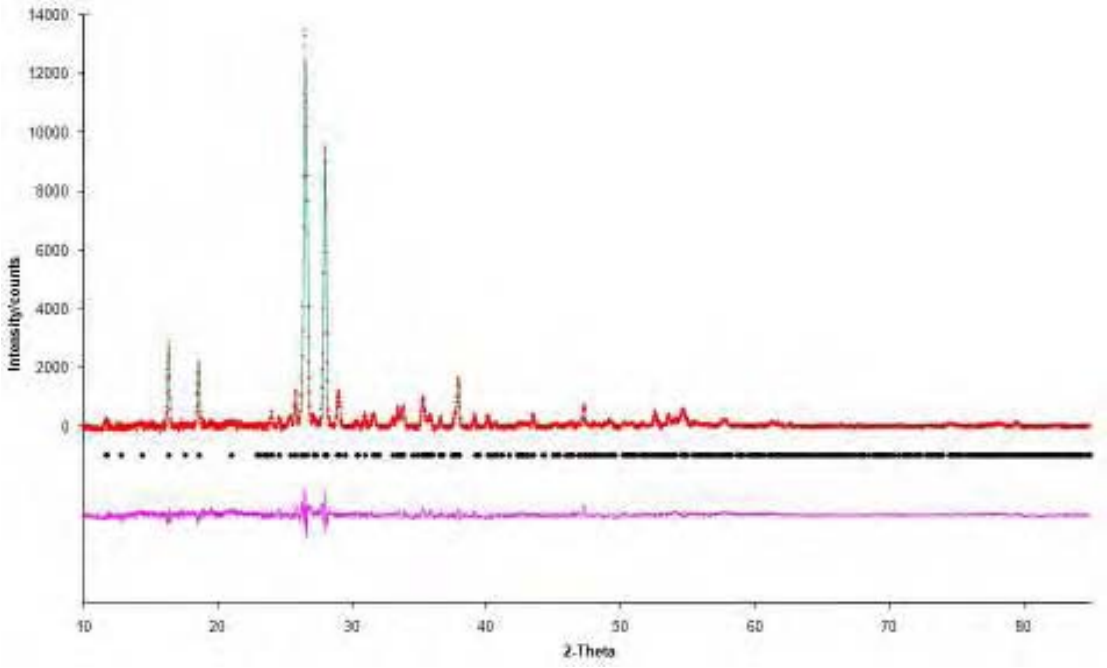

Figure 4.8: The final Rietveld profile for oxamic acid:isonicotinamide. The experimental diffraction pattern is shown by red circles, the calculated diffraction pattern is shown by a solid green line, and the difference plot as a solid pink line. Reflection positions are marked by black dots.

Table 4.1: Initial lattice parameters, DE structure solution parameters, refined lattice parameters from Rietveld refinement and single crystal determination and Rietveld agreement factors.

Compound	Oxamic acid and isonicotinamide	
Crystal data		
Chemical formula	$C_6H_6N_2O$+ $H_2NC(=O)C(=O)OH$	
M_r	211.17	
Indexing		
Space group	$P2_1/c$	
Initial a / Å	3.7319(1)	
Initial b / Å	7.7319(2)	
Initial c / Å	30.3089(1)	
Initial β / °	90.080(2)	
Initial V / Å ^{3}	876.838(3)	
Structure solution		
LeBail R_{wp} / %	3.07	
LeBail R_p / %	2.31	
LeBail χ^2	1.876	
DE elements		
K	0.99	
F	0.5	
N_p	140	
Average R_{wp} / %	50.25	
Best R_{wp} / %	20.53	
Refinement		
R_{wp} / %	3.35	
R_p / %	2.51	
R^2_F / %	0.2462	
χ^2	2.598	
Preferred orientation fraction [and direction]	1.02471 [010]	
No of parameters	70	
No. of restraints	51	***Single Crystal values***
Final a / Å	3.7311(1)	3.7386(18)
Final b / Å	7.7435(8)	7.771(3)
Final c / Å	30.284(3)	30.372(13)
Final β / °	90.21(1)	90.15(2)
Final V / Å ^{3}	874.91(13)	882.4(6)
Temperature K	295	296

4.4 Oxamic acid:Isonicotinamide structure

Even though the refinement of the crystal structure from pxrd data was deemed successful, a single crystal structure solution was also undertaken to afford a higher degree of confidence in the structure especially concerning the conformation of the amide group in the isonicotinamide and the groups in the oxamic acid molecule which contain similar scattering factors. The crystal structure description is based upon the single crystal data collected on a Bruker Smart 6000 diffractometer equipped with a CCD detector and a copper tube source. The structures were solved by direct methods and refined using Shelx97[23]. Hydrogen atoms were found by Fourier methods and constrained using a riding model. Anisotropic displacement parameters were used for non-H atoms; H-atoms were given isotropic displacement parameters equal to 1.2 times the equivalent isotropic displacement parameter of the atom to which they are attached. An incubator was used to grow a single crystal of suitable quality and size, as described in section 3.2.2.. The geometry of the oxamate anion displays similar characteristics to other published structures[14, 24] in that its almost planar, with an interplanar angle O1-C1-C2-O2 of 4.78(5) º, and that the variation in the C-O bond lengths shows localisation of the carboxylate carbonyl group indicating a *trans* geometry; the C2-O2 and C2-O3 bond lengths are 1.263(4) (C-O) and 1.230(4) Å (C=O) respectively (appendix K). The presence of an intramolecular hydrogen bond within the oxamate ion, donated from N1 via H1B to O3, also contributes to the planarity of the anion as noted in other structures of this type[14]. The conformation of the amide group in the isonicotinamide molecule shows considerable deviation from planarity, C4-C5-C8-O8 angle of 154.6(4) °, arising from the formation of strong hydrogen bonds by the amide group both within and between supramolecular layers

(Table 4.2). This distortion is not uncommon as the amide group is involved in formation of intermolecular interactions both within and above or below the plane of the dimer motif[4, 25] The single crystal structure also allows for the categorisation of the multi-component crystal, as the hydroxyl proton is transferred from the oxamic acid molecule to the heterocyclic nitrogen, forming a salt. Details of the oxamic acid:isonicotinamide single crystal structure can be found in appendix K. The molecular structure of oxamic acid:isonicotinamide and the atomic numbering system is shown in figure 4.9.

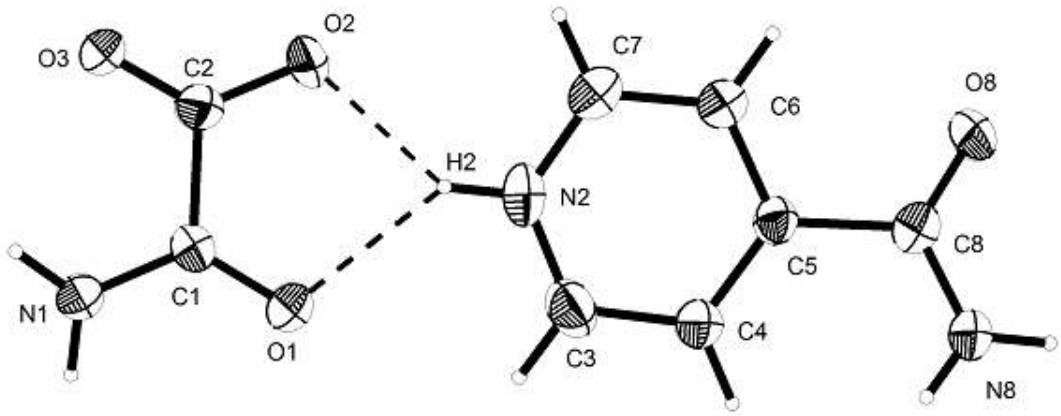

Figure 4.9: The molecular structure of oxamic acid:isonicotinamide. Showing the atom numbering scheme and the hard intermolecular hydrogen bonds within the asymmetric unit (dashed lines). Displacement ellipsoids are drawn at the 50% probability level and H atoms are shown as small spheres of arbitrary radii.

The supramolecular structure of oxamic acid:isonicotinamide is determined through six intermolecular hydrogen bonds; four strong N-H….O==C hydrogen bonds and two N(heterocyclic)-H+…O- (Table 4.2). All strong hydrogen-bond donors and acceptors are used in the hydrogen bond network. The isonicotinamide and oxamate ions are linked by a bifurcated N(heterocyclic)-H+…O- hydrogen bond in which the

protonated heterocyclic N2 of the isonicotinamide acts as a hydrogen bond donor, via H2, to both the amide oxygen O1 and the deprotonated carboxyl O3 on the oxamate anion. Each isonicotinamide molecule is then connected to another at (3-x,-1-y,-z) to form an $R_2^2(8)$ dimer through complementary N-H….O hydrogen bonds in which N8 acts as a donor via H8A to O8. The remaining four strong hydrogen bonds link together the oxamate anions forming an infinite zig-zag chain of dimers defined by $R_2^2(9)$ rings and propagated by the 2_1 screw-axis at (0.25, y, 0.25). The amide N1 acts as a donor through H1A to O3 at (0.5-x, -0.5+y, 0.5-z) while O3 accepts from (0.5-x, 0.5+y, 0.5-z), as shown in figure 4.10 and figure 4.11.

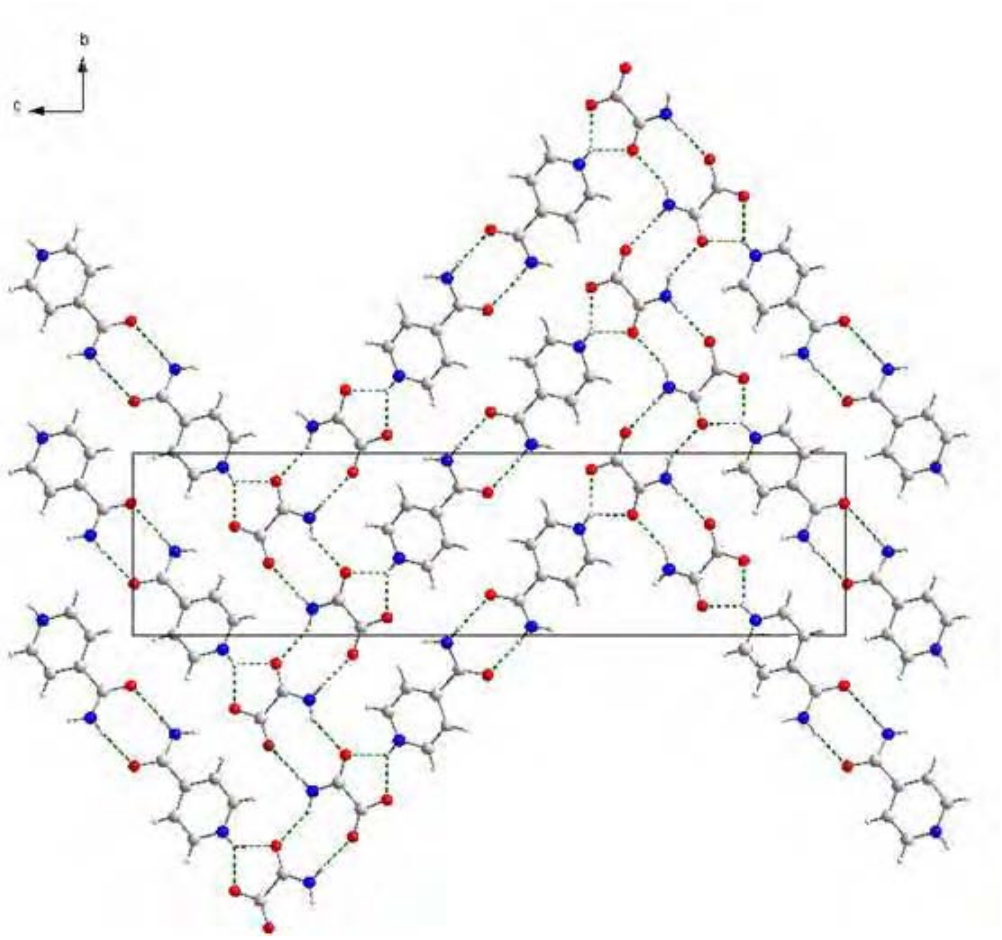

Figure 4.10: A view along the *a* axis showing an infinitely hydrogen bonded sheet in the (105) plane. Hydrogen bonds are shown by a dotted green line. (Unit cell shown)

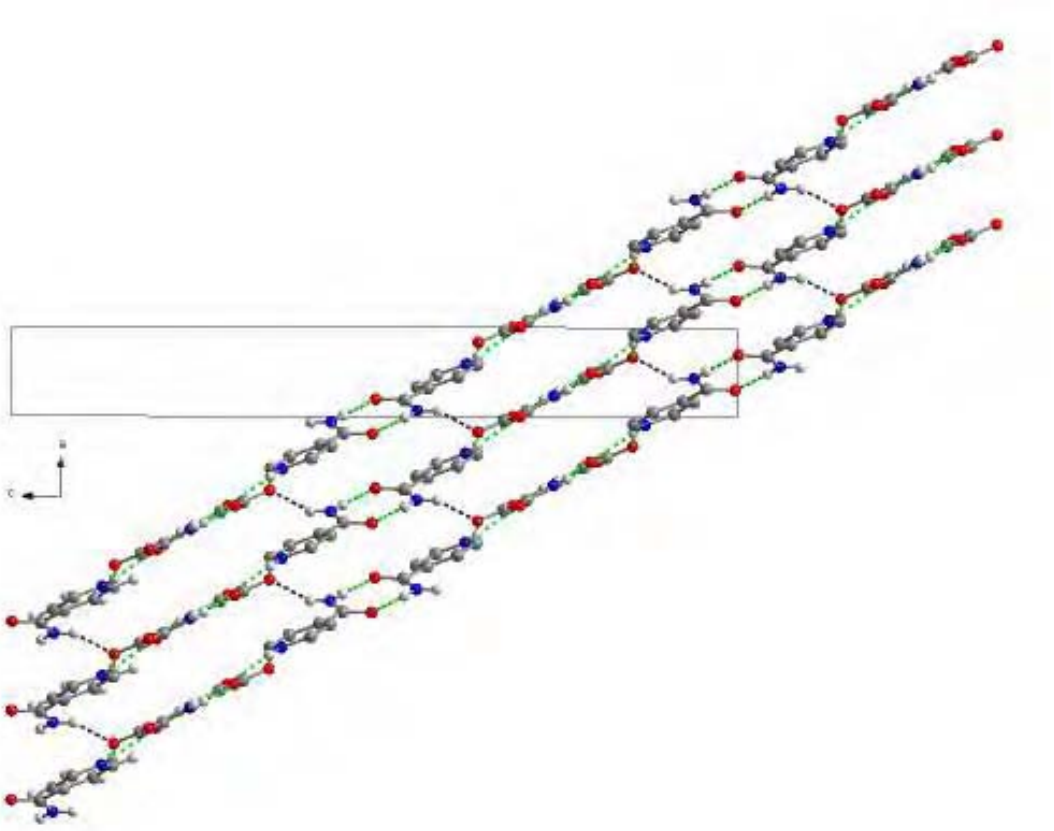

Figure 4.11: A view of the hydrogen-bonded crystal structure of oxamic acid:isonicotinamide shown in projection down the *a*-axis. All six intermolecular hydrogen bonds are indicated as dashed lines; five interactions within a sheet (green) and one between sheets (black). The intramolecular hydrogen bond within the oxamate ion is not shown and H atoms not involved in hydrogen bonding have been omitted for clarity. (Unit cell shown).

As postulated by Etter[26, 27], the hydrogen bond networks present in the oxamic acid: isonicotinamide structure are typical of acid-amide systems albeit in this case following protonation. The best donor (carboxyl) forms a hydrogen bond to the best acceptor (pyridine N) and the second best donor and acceptor combination are propagated via amide linkages in both the oxamic acid and isonicotinamide molecules. As previously synthon energy calculations show[28], the acid-pyridine hydrogen bond is favoured over the acid-amide.

Table 4.2: Hydrogen bond geometry in oxamic acid:isonicotinamide, (Å and °).

Donor—H---Acceptor	D—H	H---A	D....A	<(DHA)
N1-H1A....O3^{i}	0.86	2.01	2.872	177
N1-H1B....O1^{ii}	0.86	2.22	2.972	146
N1-H1B....O3	0.86	2.40	2.734	104
N2-H2...O1	0.86	2.16	2.826	133
N2-H2...O2	0.86	1.99	2.730	143
N8-H8A...O8^{iii}	0.86	2.09	2.948	176
N8-H8B...O2^{iv}	0.86	2.14	2.904	147

Symmetry codes: (i) 0.5 –x, -0.5 +y, 0.5 –z; (ii) 0.5-x, 0.5 +y, 0.5 –z; (iii) 3 –x, -1 –y, -z; (iv) 1 +x, -1 + y, z

4.5 Comparison of the Single crystal vs. Powder structure

To aid method development for the solution of multi-component crystal structures from pxrd, structures solved from pxrd data can be compared to those solved using single crystal methods. In cases such as this structure, with groups of similar scattering behaviour, this allows us to assess areas of potential problems, such as the orientation flip of similar functional groups, which can be indistinguishable for poor quality pxrd data and can result in false structure solutions. Figure 4.11 illustrates the crystal packing in both the powder and single crystal solutions.

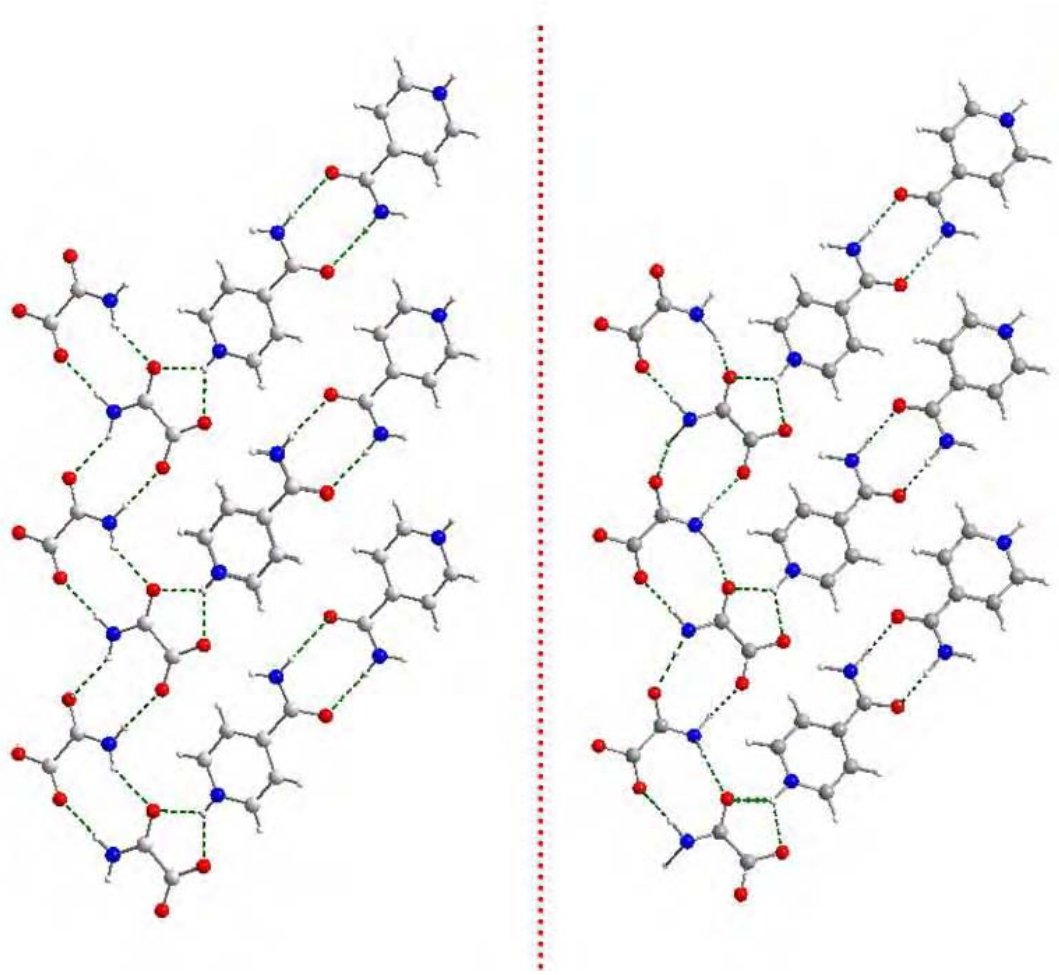

Figure 4.12: A section of the hydrogen bonded sheet of oxamic acid:isonicotinamide. From single crystal data (left) and from pxrd data (right).

As clearly shown in figure 4.12, the orientation of the functional groups in both the oxamate and isonicotinamide moieties are identical in both the single crystal (left) and the powder (right). This observation illustrates the power of the direct space approach in the solution of multi-component crystals. In this case, the structure is correct and functional groups of similar electron density have been placed in the correct orientation regardless of the intrinsic problems which are associated with pxrd data. A proton was placed on the pyridine N, on the basis of IR data (section 4.1).

However, one major advantage associated with single crystal experiment is the ability to confirm the classification of the multi-component crystal structure as either a co-crystal or a salt. The determination of the hydrogen atom (either as the neutral acid or protonated amide) is only achievable with the data quality and quantity available in a single crystal experiment, in comparison to that of a powder diffraction experiement. In this strucutre the proton transfer was confirmed by the single crystal experiment. Below in figures 4.13 and 4.14, direct comparisons between the single crystal atomic positions, the best DE solution and the final refined atomic positions are shown.

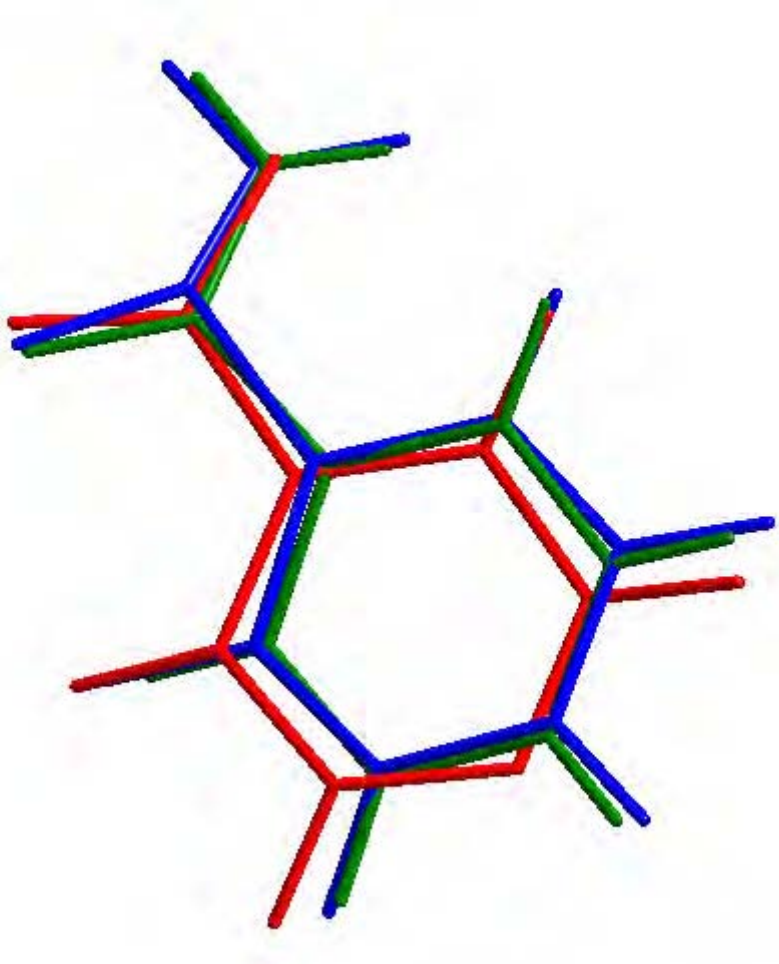

Figure 4.13: Isonicotinamide molecule from oxamic acid: isonicotinamide. The green molecule represent single crystal positions, red molecule represent DE solution 20.53 and the blue molecule represents final refined positions.

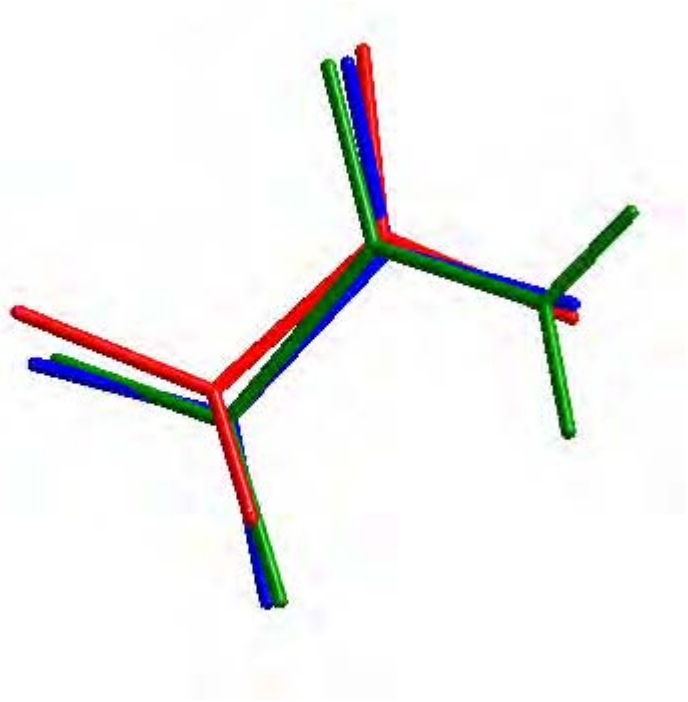

Figure 4.14: Oxamic acid molecule from oxamic acid:isonicotinamide. The green molecule represents single crystal positions, red molecule represent atoms from DE solution 20.53 and the blue molecule represents the final refined atom positions.

The subsequent analysis confirmed that the crystal packing obtained by powder methods was correct. The minimum, maximum and mean distances between pairs of corresponding atoms in the single and refined powder structures was calculated at 0.098, 0.3644 and 0.201 Å respectively.

4.6 The efficiency of the DE algorithm

As shown in figure 4.7, the evolutionary progress plot of the successful DE calculation on the oxamic acid:isonicotinamide structure highlights areas in the calculation where the DE plateau indicated little to no progress in terms of optimising the R_{wp}. The plateau is followed by a steep decline, indicative of the deterministic nature of the DE algorithm, but also suggesting a shallow and deep global minimum. The large plateau region allows for further enhancement of the algorithm efficiency in

tackling such parameterised problems as oxamic acid:isonicotinamide. In table 4.3, the results from a number of DE runs (and epochs) are shown. The DE structure solution of oxamic acid:isonicotinamide is the first 14 parameter problem with two independent molecules in the asymmetric unit, to which the DE has been applied. By variation of the DE control parameters in a number of calculations it should become clear which combination of parameters are suitable for this type of optimisation problem. Values of *F* and Np were chosen for variation between limits chosen from previous DE studies[29] and *K* was fixed throughout at 0.99. For each combination of parameters, five epochs were calculated.

Table 4.3 illustrates that as expected, the large population sizes coupled with a mutation factor of 0.5 fail to locate the narrow global minimum within the number of generations allowed. Many results did not converge and reached G_{max} (maximum number of generations allowed in one epoch before the calculation is halted and proceeding epoch initiates), extension to larger values of G_{max} would give more indication of the convergence of the DE calculation with these higher population values.

Table 4.3: The results from a number of DE calculations with variation in *F* (mutation rate) and NP (population size). For each epoch the final R_{wp} (in %) is given and figures within brackets indicate at which generation convergence was achieved. Runs giving the correct structure solution are indicated by green; the gold cell indicates the lowest R_{wp} achieved and the starting point for the successful structure refinement. Runs that have not converged by the maximum allowed number of generations are shaded grey.

Run	F	NP	epoch 1	epoch 2	epoch 3	epoch 4	epoch 5
1	0.3	130	31.59(276)	33.55(270)	32.68(342)	34.55(311)	30.53(337)
2	0.4	130	31.96(644)	30.27(842)	28.19(613)	33.88(806)	31.91(612)
3	0.5	130	23.67(1457)	22.85(950)	27.41(1197)	32.03(1415)	27.39(1253)
5	0.5	140	28.44(1500)	22.31(1500)	27.42(1459)	41.22(1500)	29.61(1075)
6	0.5	140	28.77(1238)	30.28(1329)	20.53(1642)	23.76(1705)	29.48(1483)
7	0.5	140	29.58(1467)	24.29(1689)	28.47(1073)	27.65(1187)	26.06(1800)
8	0.5	156	28.28(1500)	34.02(1419)	28.15(1260)	23.53(1260)	40.99(1500)
9	0.5	156	33.24(1239)	33.54(1500)	27.77(1420)	39.72(1500)	39.81(1500)
10	0.5	160	41.29(1500)	32.99(1500)	37.01(1500)	39.16(1500)	40.23(1500)
11	0.5	195	36.97(1500)	41.07(1500)	38.91(1500)	39.79(1500)	42.22(1500)
12	0.5	195	40.08(1500)	39.93(1500)	40.22(1500)	40.35(1500)	39.05(1500)
13	0.5	195	41.69(1500)	20.75(1383)	40.29(1500)	37.36(1500)	41.74(1500)
14	0.5	221	42.22(1800)	37.99(1800)	39.19(1800)	41.56(1800)	42.94(1800)
15	0.5	221	40.47(1800)	35.78(1800)	39.89(1800)	40.51(1800)	37.9(1800)
16	0.5	221	39.38(1800)	38.68(1800)	37.69(1800)	26.64(1800)	36.59(1800)
17	0.5	286	41.79(1500)	43.1(1500)	40.4(1500)	42.79(1500)	42.35(1500)

Smaller population sizes with a mutation factor $F = 0.5$ produced more successful runs, with a combination of $F = 0.5$ and NP = 140 leading to the successful global minimum. Figure 4.15, illustrates the effect of F (mutation parameter) on the progress of the DE calculation.

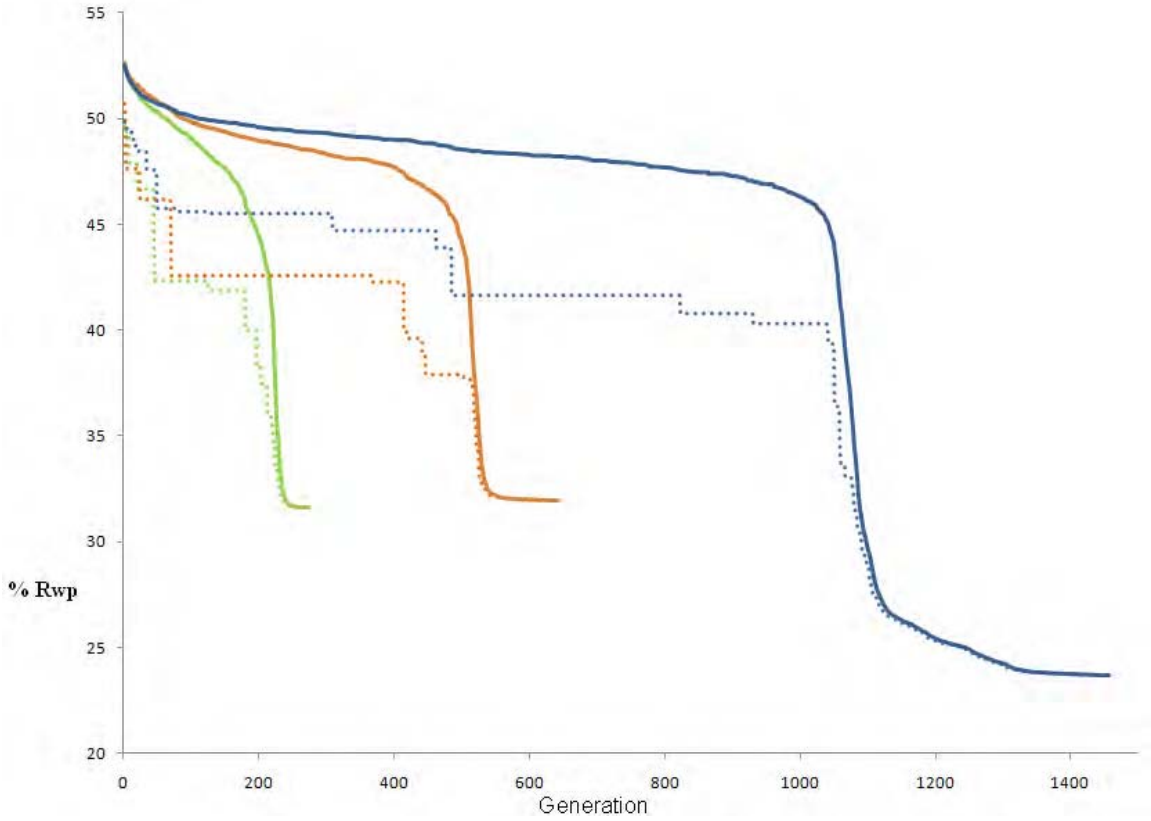

Figure 4.15: Variation of mutation rate *F* with constant population size. *F* = 0.3, 0.4 and 0.5 are shown by green, orange and blue lines respectively. Dotted lines represent the best R_{wp} of the population with the corresponding solid line representing the mean R_{wp} of the population.

The calculation with *F* = 0.5 (shown in blue), shows the greatest progression in terms of R_{wp}, as the larger mutation factor avoids the premature convergence demonstrated by *F* = 0.3 and 0.4.

As the structure solution from the DE has an R_{wp} higher than might be expected (DE solution Rwp = 20.53%; LeBail fit Rwp = 3.07 %) a 'mini DE' (MDE) calculation was performed (Table 4.4). In a mini DE the calculation is seeded with 5 previous solutions, from the main DE calculation. This aims to encourage the population towards promising solutions and excluding large areas of the R_{wp} hypersurface that have been covered by the DE calculation[29].

Table 4.4: MDE results for each epoch from five runs. For each epoch the final R_{wp} (in %) is given and figures within brackets indicate at which generation convergence was achieved. Runs giving the correct structure solution are indicated by green; the gold cell indicates the lowest R_{wp} achieved and the starting point for the successful structure refinement.

Run	F	NP	epoch 1	epoch 2	epoch 3	epoch 4	epoch 5
1	0.3	140	19.28(182)	19.98(272)	19.91(252)	19.78(1500)	19.96(1500)
2	0.4	140	19.14(307)	19.14(203)	19.14(213)	19.15(187)	19.94(203)
3	0.5	140	20.75(1480)	20.75(1055)	20.75(856)	20.75(999)	20.75(1304)
4	0.5	140	19.14(1179)	19.14(946)	19.14(980)	19.14(1420)	19.14(999)
5	0.5	180	19.14(307)	19.14(203)	19.14(213)	19.14(187)	19.14(203)

As illustrated in table 4.4, the mini DE, locates a structure solution (numerous times) on R_{wp} lower than that of the original DE calculation. On comparison of the structure itself it was deemed that this optimisation had not located a structure solution that was significantly different from the initial minimum (R_{wp} = 20.53 %) and hence refinement of this lower R_{wp} structure was not performed.

4.7 Thermal behaviour of oxamic acid:isonicotinamide

The thermal behaviour of oxamic acid:isonicotinamide was probed by collecting a series of data sets over the temperature range 100-295 K, using the Bruker AXS D5000 high-resolution X-ray powder diffractometer fitted with Oxford Cryostream and capillary stage (section 3.1.4). The process of extracting information regarding the thermal behaviour of the crystal lattice was based on a non-model biased LeBail fitting procedure[18]. Lattice parameters derived from the single crystal structure were used as a starting point for the LeBail fit based on the data collected at 295 K. After a stable refinement was achieved, the resulting lattice parameters were used as the

starting point for the LeBail fit of the data set collected at 250 K. The process was continued in this way for the data sets collected at 200, 150 and 100 K. There was no evidence of a phase change over the temperature range investigated.

Figure 4.16 illustrates the migration of diffraction peaks to a higher 2-theta with an increase in temperature.

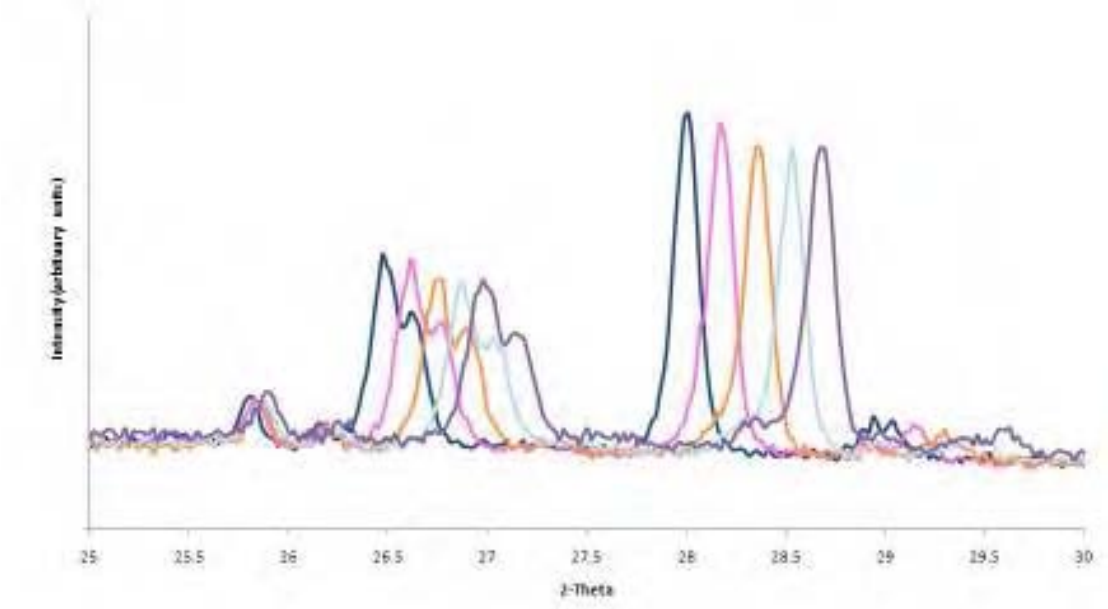

Figure 4.16: Two diffraction peaks of oxamate:isonicotinamide over the temperature range investigated, 295 K(blue), 250 K (pink), 200 K (orange), 150 K (sky blue) and 100 K(purple)

The lattice parameters from these LeBail fits are given in Table 4.5 and plotted in figure 4.17. It is clear from these that, the general trend is that of expansion, with the exception of β which decreases as the temperature rises. The ΔL/L0 values quoted in table 4.5, indicate the percentage change in the lattice parameter and are calculated by the difference between lattice parameter at given temperature and the lattice parameter at temperature 0 (in this study 100K), divided by the lattice parameter at temperature 0. Figure 4.16 illustrates clearly that the expansion is non-linear, with the parameters achieved at 250 K being larger than those at 295 K.

Table 4.5: Lattice parameters from the LeBail fitting of oxamate:isonicotinamide. ΔL/L0 values are given in square brackets.

Temperature (K)	a (Å)	b (Å)	c (Å)	β°	Volume (Å^3)	% R_{wp}	χ^2
100	3.6585(6) *[0.00]*	7.669(2) *[0.00]*	30.167(8) *[0.00]*	92.238(11) *[0.00]*	846.1(4) *[0.00]*	4.04	3.012
150	3.6776(6) *[0.0052]*	7.675(2) *[0.0008]*	30.214(8) *[0.0013]*	91.989(11) *[-0.0026]*	852.4(4) *[0.0075]*	6.00	3.050
200	3.6978(5) *[0.0107]*	7.692(1) *[0.0030]*	30.168(8) *[0.0038]*	91.762(10) *[-0.0050]*	857.7(4) *[0.0136]*	5.84	2.813
250	3.7392(7) *[0.0219]*	7.737(1) *[0.0089]*	30.289(9) *[0.0038]*	90.721(15) *[-0.0165]*	876.2(5) *[0.0355]*	7.77	4.078
295	3.7322(3) *[0.0201]*	7.743(1) *[0.0096]*	30.294(4) *[0.0039]*	90.168(8) *[-0.0223]*	875.4(3) *[0.0347]*	4.59	1.427

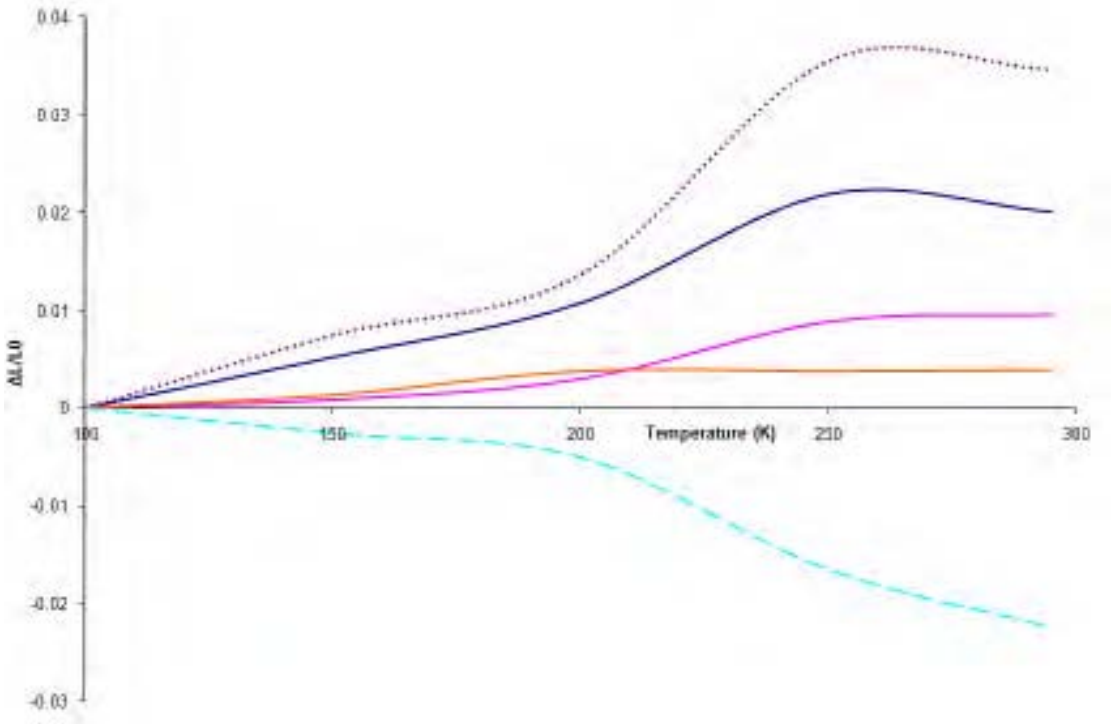

Figure 4.17: The fractional variation of lattice parameters obtained from the LeBail refinement, plotted against temperature; Unit cell volume (purple spots), a (blue line), b (pink line), c (orange line) and β (sky blue dashed line).

This is somewhat unexpected, so an alternative fitting procedure was employed to investigate whether this was a true structural effect or a refinement anomaly. It has been suggested elsewhere[30] that the process of pattern decomposition to obtain accurate and reliable lattice parameters from multi-temperature data sets may be potentially problematic. Low symmetry unit cells contain a high density of

reflections, unlike in a Rietveld refinement, which is model baised, there is no indication of the relative intensities of different reflections; this can lead to mis-identification of the reflections which pose little or no intensity. This can, in turn, result in errors being introduced into the cell refinement. In a model biased Rietveld refinement the problem of misidentification does not arise and hence Rietveld refinement[31] was performed for each data set with the aim of extracting more reliable lattice parameter information, the resulting lattice parameters are shown in Table 4.6 and in figure 4.18.

As is clear from figure 4.18, the thermal expansion of the lattice parameters is linear with respect to temperature, except for β in which the decrease is linear. This is a clear example, supporting previous literature[30, 32], that caution must be applied to thermal expansion data retrieved from using pattern decomposition methods such as LeBail fitting.

Table 4.6: Lattice parameters from the Rietveld refinement of oxamate acid:isonicotinamide. ΔL/L0 values are given in square brackets.

Temperature (K)	a (Å)	b (Å)	c (Å)	β°	Volume (Å^3)	% R_{wp}	χ^2
100	3.6526(6) *[0.00]*	7.7150(19) *[0.00]*	30.173(9) *[0.00]*	90.658(14) *[0.00]*	850.2(4) *[0.00]*	6.82	4.37
150	3.6687(8) *[0.0044]*	7.721(2) *[0.0009]*	30.197(11) *[0.0008]*	90.452(15) *[-0.0028]*	855.4(6) *[0.0061]*	4.89	6.274
200	3.6894(7) *[0.0101]*	7.728(3) *[0.0018]*	30.233(10) *[0.0020]*	90.263(13) *[-0.0044]*	862.0(6) *[0.0139]*	4.87	4.880
250	3.7109(5) *[0.0160]*	7.734(2) *[0.0025]*	30.265(8) *[0.0030]*	90.040(12) *[-0.0068]*	868.6(5) *[0.02160]*	5.59	3.315
295	3.7316(5) *[0.02162]*	7.7443(19) *[0.0038]*	30.287(8) *[0.0038]*	89.80(1) *[-0.0095]*	875.3(4) *[-0.02941]*	4.37	2.816

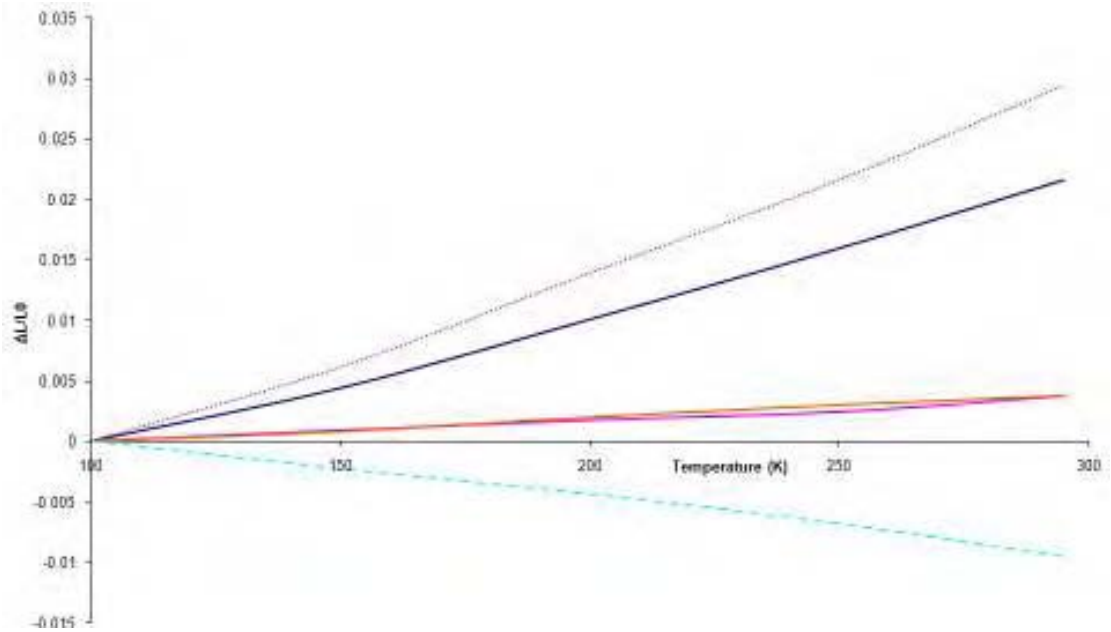

Figure 4.18: The fractional variation of lattice parameters obtained from Rietveld refinement, plotted against temperature; Unit cell volume (purple spots), a (blue line), b (pink line), c (orange line) and β (sky blue dashed line).

Thermal expansion at constant pressure (equation 4.1) can be described by a linear thermal expansion along its primary crystallographic axes. L_0, is the shortest length recorded, dL and dT are the change in length and temperature respectively over the temperature range.

$$\alpha = \frac{1}{L_0}\left(\frac{\partial L}{\partial T}\right)_p \qquad \text{[Equation 4.1]}$$

The linear thermal expansion of the lattice parameters along their principal crystallographic axes are listed in table 4.7.

Table 4.7: Linear thermal expansion co-efficients of the lattice parameters of oxamate:isonicotinamide.

Lattice parameter	Linear thermal expansion co-efficient (K^{-1})
a	1.1100×10^{-4}
b	1.9473×10^{-5}
c	1.92392×10^{-5}
β	-4.88169×10^{-5}
Volume	1.5081×10^{-4}

It is clear from these coefficients that there is a greater degree of expansion on *a* than the other crystallographic axes. As discussed previously and shown in figure 4.9, in the crystal structure of this material, infinitely hydrogen bonded sheets of oxamate:isonicotinamide run in the (105) plane. The *a* direction may be thermally labile in comparison to the *b* and *c* direction due to the relatively small amount of hydrogen-bonding in the a-direction; indeed there is only one type of inter-planar hydrogen bond (N(8) —H(8B) …O(2)) that possesses any significant *a* directionality. Expansion (and contraction) in the *a* direction will also be significantly less sterically hindered than the other crystallographic directions.

4.8 Characterisation of oxamic acid:nicotinamide

This section describes the characterisation of a related multi-component crystal, oxamic acid: nicotinamide. Comparison of the oxamic acid adducts of the related nicotinamide and isonicotinamide molecules aids in the understanding of both adduct formation and structural behaviour. The stoichiometric ratio of the two starting materials was confirmed by ^{1}H NMR (section 3.4.2) and the presence of both materials in the new crystalline system was confirmed by HPLC (section 3.4.3).

Pxrd was used to confirm that the product of crystallisation from a 1:1 starting stoichiometry using solvent-mediated synthesis was a new crystalline phase not containing the two starting materials (figure 4.19).

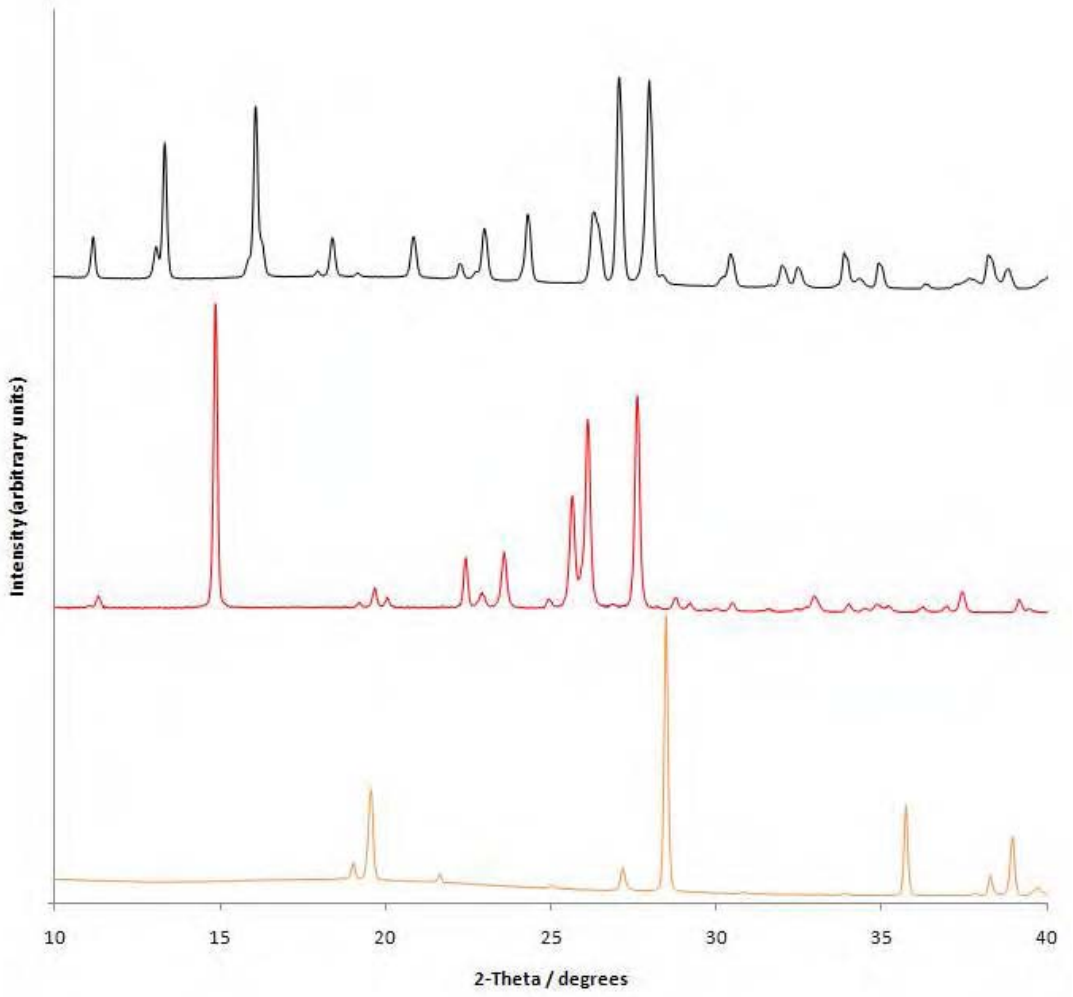

Figure 4.19: Powder X-ray diffraction patterns of the starting materials, oxamic acid (orange), nicotinamide (red) and oxamic acid:nicotinamide multi-component material (black).

Solid state infra-red spectroscopy was performed on the new crystalline phase and compared to that recorded from a mixture of starting materials. The spectra of the two are significantly different, alluding to the synthesis of a new crystalline material, with different hydrogen-bonding characteristics to that of the component mixture, (figure 4.20). The presence of two broad peaks at 2425 cm^{-1} and 1883 cm^{-1} is characteristic

of an acid----N heterocyclic hydrogen bond, and is viewed as evidence for multi-component crystal formation, whereas the absence of such bands would be interpreted as a lack of multi-component formation[15]. In terms of classification as a salt or a neutral cocrystalline material, it is illustrated in the literature[16] that if an acidic proton is transferred to a heterocyclic nitrogen, very broad peaks are present around 2500 ± 100 cm^{-1} and for individual N^{+}-H bonds, peaks are present at 3250 ± 50 cm^{-1}. As illustrated in figure 4.21, peaks are present at both 2425 cm^{-1} and 3230 cm^{-1}, implying that a proton transfer has taken place and that consequently the new material is a salt.

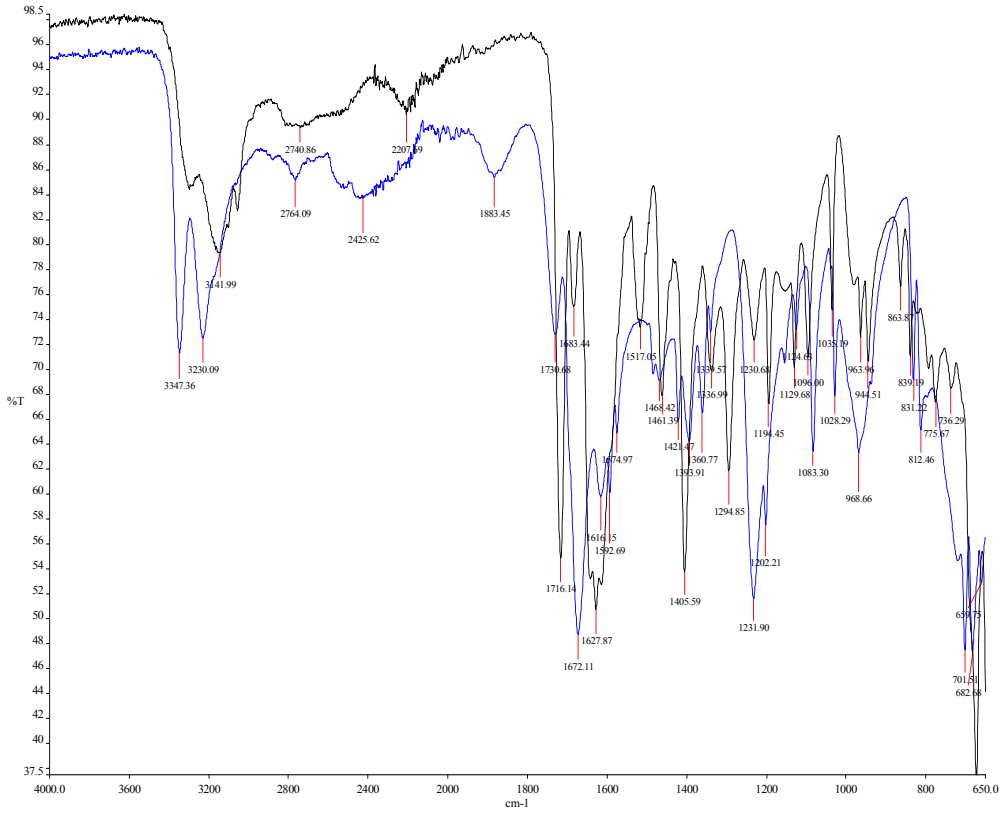

Figure 4.20: Solid state IR spectra of oxamic acid:nicotinamide mix (black) and the new multi-component crystal (blue).

In parallel with traditional solvent-mediated recrystallisation, pxrd (figure 4.21) was used to confirm that the same bulk crystalline phase was produced by both LAG

(section 3.4.1) and sonic slurry (section 3.4.1) methods. As discussed in section 1.18, LAG and slurry sonication provide an environmentally conscious route to the synthesis of these materials and potentially circumvent the problem of adverse solubilities of the starting components.

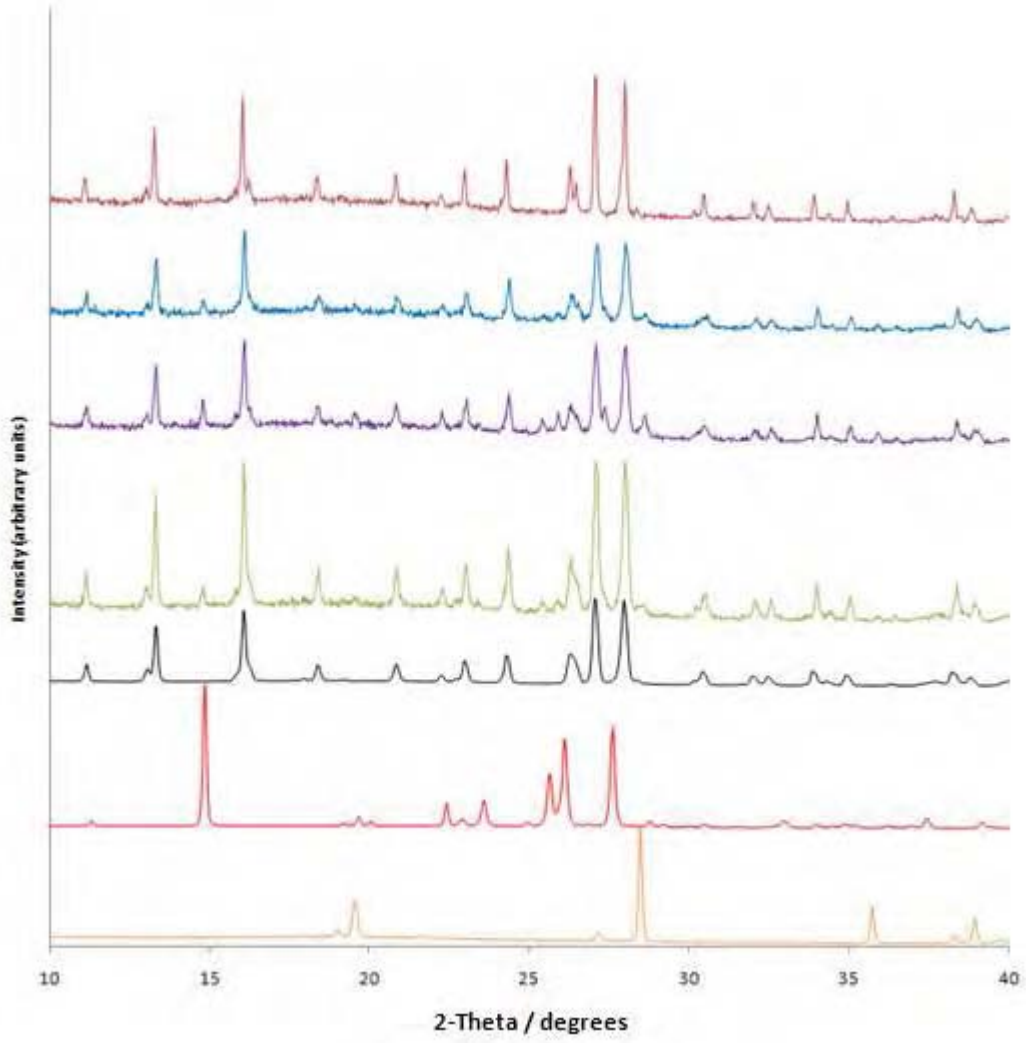

Figure 4.21: Powder X-ray diffraction data, listed from bottom to top, of the starting materials oxamic acid (orange) and nicotinamide (red). Oxamic acid:nicotinamide crystallised from solution mediated crystallisation (black), oxamic acid:nicotinamide ground for 5 minutes (green), for 15 minutes (purple), for 20 minutes (blue) and oxamic acid:nicotinamide from sonic slurry (dark red).

It is clear from figure 4.20, that the same new crystalline phase as produced by cold solution recrystallisation in methanol and ethanol was synthetically accessible via

both LAG (3.4.1) and sonic slurring (3.4.1). As with the isonicotinamide adduct (section 4.1), the sample produced by LAG contains some starting material; the extra peak at 14.8˚ matches that of the starting material nicotinamide. The diffraction pattern for LAG sample also shows signs of peak broadening and lattice strain. These sample effects reduce the resolution of unique reflections in the diffraction pattern and thus lead to an increase in complexity when solving multi-component crystals from pxrd data. As evident from figure 4.21, the crystallinity of the system does not depreciate linearly with time.

4.9 Structure solution and refinement from laboratory pxrd data

The X-ray powder diffraction data set used for structural analysis was collected over a period of 8 hours and over the range of $10^\circ \leq 2\theta \leq 85^\circ$. The data were indexed on the basis of the first 20 observable reflections using the indexing program CRYSFIRE[33] (appendix N) and the $P2_1/c$ space group was assigned by consideration of systematic absences. The profile parameters were refined using the whole-profile-fitting LeBail[18] method in the GSAS[19] program to improve the fit of the lattice, zero point and profile parameters. Structure solution was carried out using the DE technique (section 1.14); this was implemented using the program POSSUM[20].

From density considerations it was concluded that the asymmetric unit contained one oxamic acid and one nicotinamide molecule, hence the structural model used in the DE calculation comprised both complete molecules, constructed using standard bond lengths[21] and angles, but excluding hydroxyl and amine hydrogen atoms (figure 4.22). Each molecule is defined by 7 DE elements: 3 parameters (θ,Φ,Ψ) to define the orientation of each molecule within in the unit cell (bounds 0 - 360˚), 3 parameters

(*x,y,z*) to define the position of each molecule in the unit cell (bounds 0-1) and one unconstrained torsion angle (0-360˚) to define the conformation of each molecule. The molecules were moved independently in the structure solution resulting in a 14 parameter problem.

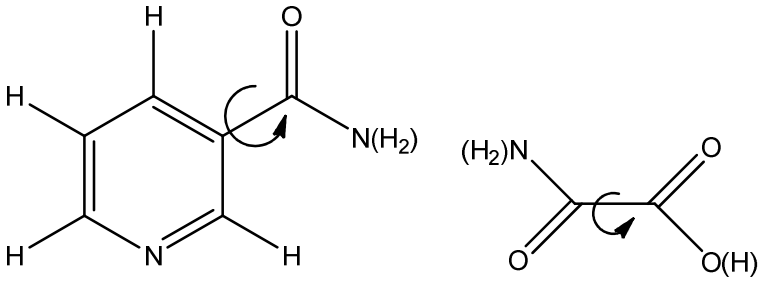

Figure 4.22: Molecular structures used in the DE structure solution, torsion angles are indicated by arrows. Hydrogen atoms excluded from the calculation are shown in brackets.

The parameters used in the successful DE calculation were, K = 0.99, F = 0.5, N_p = 140 and G_{max} = 1500. The progress plot for the successful DE solution of oxamic acid:nicotinamide (figure 4.23) shows the evolutionary progress of the DE calculation in terms of R_{wp} with generation. The progress plot highlights a large plateau as the mean R_{wp} remains relatively constant up to 1300 generations, followed by a steep decline in R_{wp} down to a minimum of 10.38%. This progress plot shape suggests both a deep and narrow minimum in the hypersurface of the direct space search. This is similar to the shape found in the oxamic acid:isonicotinamide solution and may be a feature indicative of the optimisation route of this type of parameterisation problem.

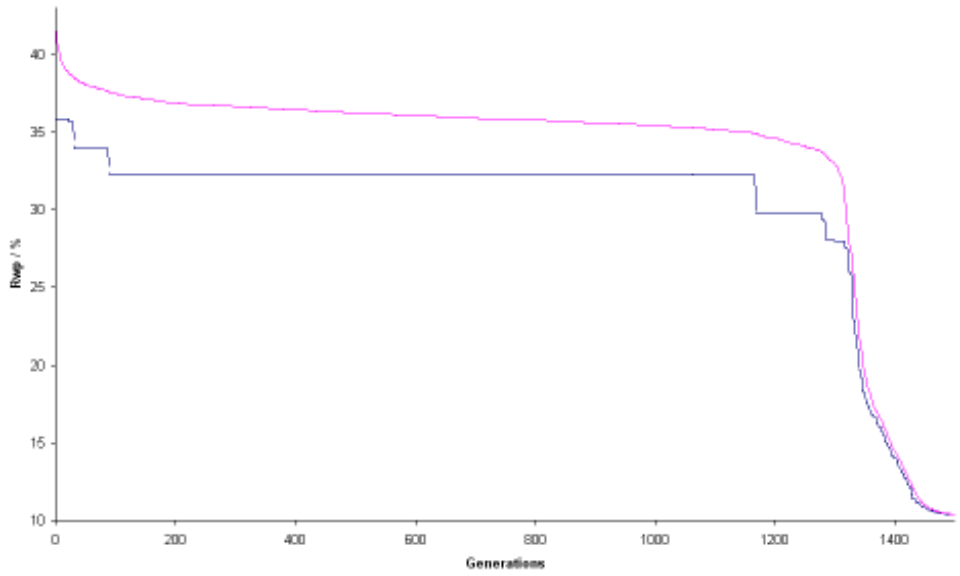

Figure 4.23: Evolutionary progress plot for the successful solution of oxamic acid:nicotinamide showing the best R_{wp} (blue) and the mean R_{wp} (pink) for each generation.

4.10 Rietveld refinement

The best structure from the DE solution was used as a starting point for refinement using the GSAS program package[19]. The positions of all atoms were refined subject to soft constraints (weighting factor of 0.001 for bond distances and 0.005 for geminal non-bonded distances) in standard geometry. Hydrogen atoms that were not included the DE calculation were placed in calculated positions according to the expected hydrogen bonding network. For the non-H atoms, isotropic atomic displacement parameters were refined constrained according to atom type or environment. Refinement of a preferred orientation parameter in the [011] direction was required, resulting in a fraction of 0.71(3). The final Rietveld profile for oxamic acid:nicotinamide is illustrated in figure 4.24. Parameters from indexing, DE structure solution, Rietveld refinement and single crystal determination are shown in Table 4.8.

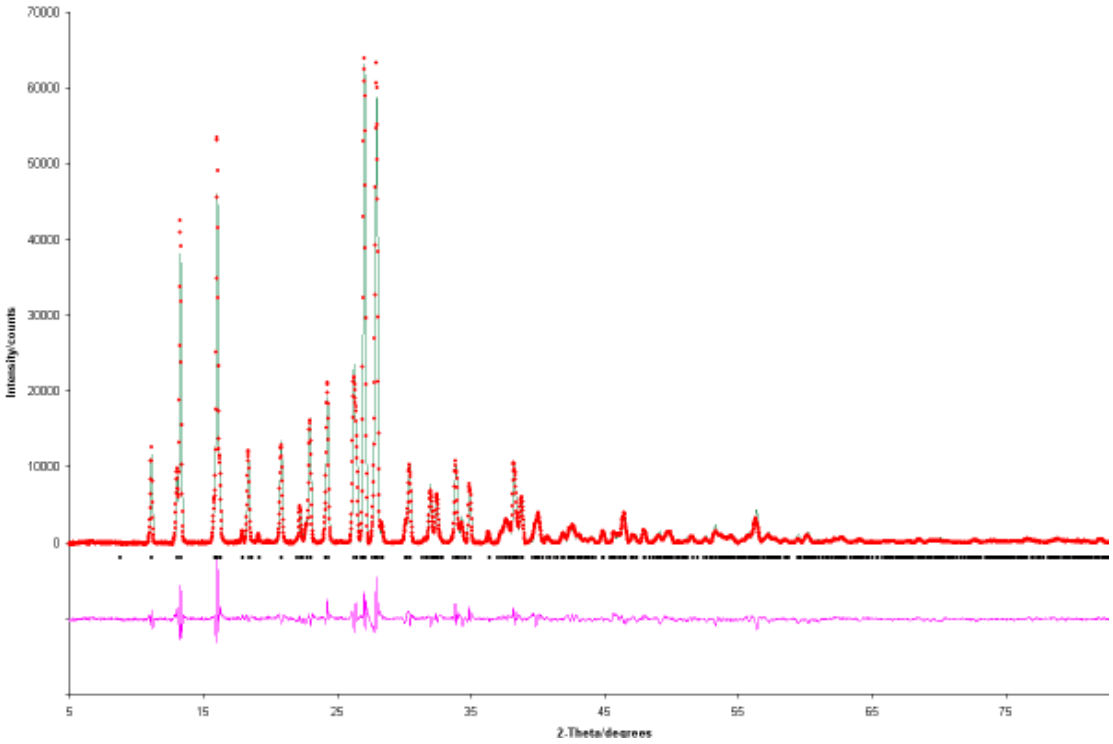

Figure 4.24: The final Rietveld profile for oxamic acid:nicotinamide. The experimental diffraction pattern is shown by red circles, the calculated diffraction pattern by a solid green line and the difference plot as a solid pink line. Reflection positions are marked by black dots.

Table 4.8: Initial lattice parameters, DE structure solution parameters, refined lattice parameters from Rietveld refinement and single crystal determination and Rietveld agreement factors.

Compound	Oxamic acid:nicotinamide		
Crystal data			
Chemical formula	$C_6H_6N_2O$ + H2NC(=O)C(=O)OH		
Mr	211.17		
Dx / mg m-3	1.534		
Indexing			
Space group	$P2_1/c$		
Initial a / Å	6.9878(1)		
Initial b / Å	9.8868(2)		
Initial c / Å	13.7035(1)		
Initial β / °	104.038(1)		
Initial V / Å3	918.468(2)		
Structure solution			
LeBail R_{wp} / %	4.94		
LeBail R_p / %	3.25		
LeBail $\chi 2$	10.73		
DE elements			
K	0.99		
F	0.5		
Np	140		
Average R_{wp} / %	32.45		
Best R_{wp} / %	10.38		
Refinement			
R_{wp} / %	5.18		
R_p / %	3.81		
R^2F / %	13.43		
$\chi 2$	14.40		
Preferred orientation fraction [and direction]	0.71603 [011]		
No of parameters	73		
No. of restraints	43	Single Crystal values	
Final a / Å	6.9794(1)	a / Å	6.9742(14)
Final b / Å	9.8731(3)	b / Å	9.8751(16)
Final c / Å	13.6899(4)	c / Å	13.676(2)
Final β / °	103.95(0)	β / °	103.86(1)
Final V / $Å^3$	914.86(4)	V / $Å^3$	914.5(3)

4.11 Oxamic acid:nicotinamide structure

The following crystal structure description is based upon the single crystal data collected on a Bruker Smart 6000 diffractometer equipped with a CCD detector and a copper tube source. The structures were solved by direct methods and refined using Shelx97[23]. Hydrogen atoms were found by Fourier methods and constrained using a riding model. Anisotropic displacement parameters were used for non-H atoms; H-atoms were given isotropic displacement parameters equal to 1.2 times the equivalent isotropic displacement parameter of the atom to which they are attached. An incubator was used to grow a single crystal of suitable quality and size to warrant a single crystal diffraction experiment, as described in section 3.4.5. As confirmed by the single crystal structure solution the multi-component system can be classified as a salt (figure 4.25) that crystallises in the $P2_1/c$ space group. The supramolecular structure of oxamic acid:nicotinamide is determined through eight intermolecular hydrogen bonds; four strong N-H…O hydrogen bonds, two N (heterocyclic)-H+…O- hydrogen bonds and two weak C-H…O (Table 4.9). Details of the oxamic acid:nicotinamide single crystal structure can be found in appendix L.

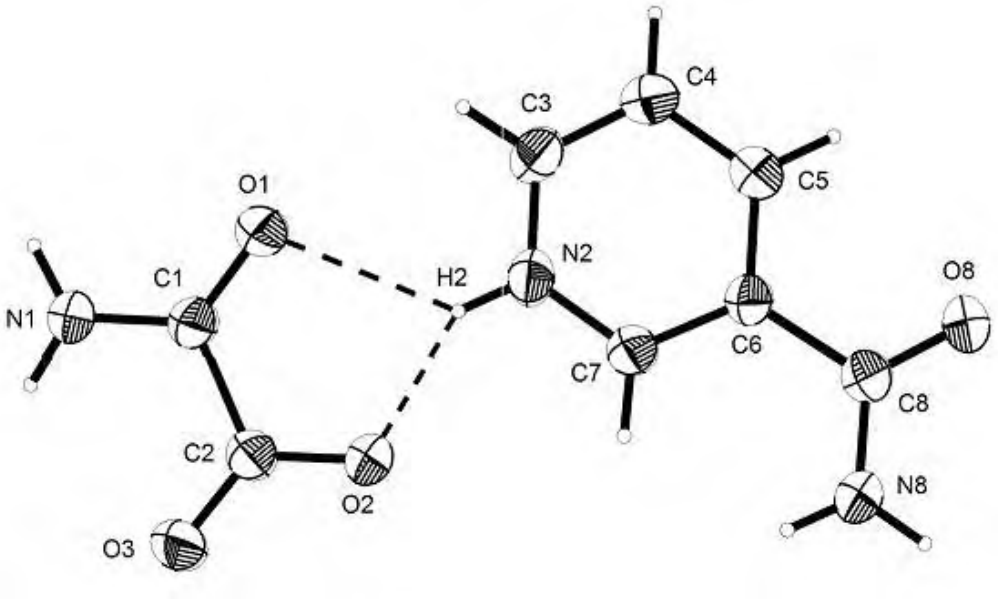

Figure 4.25: ORTEP diagram of the two asymmetric molecules in the multi-component crystal

The oxamate anion in this structure adopts the expected planar conformation (O1-C1-C2-O2 of -6.6(4)º) which can again be partly attributed to an intramolecular hydrogen bond formed by donation of H1B by N1 to O3 (Table 4.9). The distinction between the C-O bonds in the carboxylate group is not as clear as in oxamic acid:isonicotinamide but also infers a *trans* configuration with C2-O2 and C2-O3 bond distances of 1.256(3) (C-O) and 1.240(3) Å (C=O) respectively

All strong hydrogen bond donors and acceptors are used in the hydrogen bond network. The nicotinamide and oxamate ions are linked by a bifurcated N(heterocyclic)-H+…O- hydrogen bond in which the protonated heterocyclic N2 of the nicotinamide acts as a hydrogen bond donor, via H2, to both the amide oxygen O1 and the deprotonated carboxyl O2 on the oxamate anion. Each nicotinamide molecule is connected to another at (2-x,2-y,-z) to form an $R_2^2(8)$ dimer through complementary N-H…O hydrogen bonds in which N8 acts as a donor via H8A to O8 (figure 4.26).

These hydrogen bonds combine to form a tetrameric unit which acts as a link between alternative cationic or anionic sheets, as shown in figure 4.25.

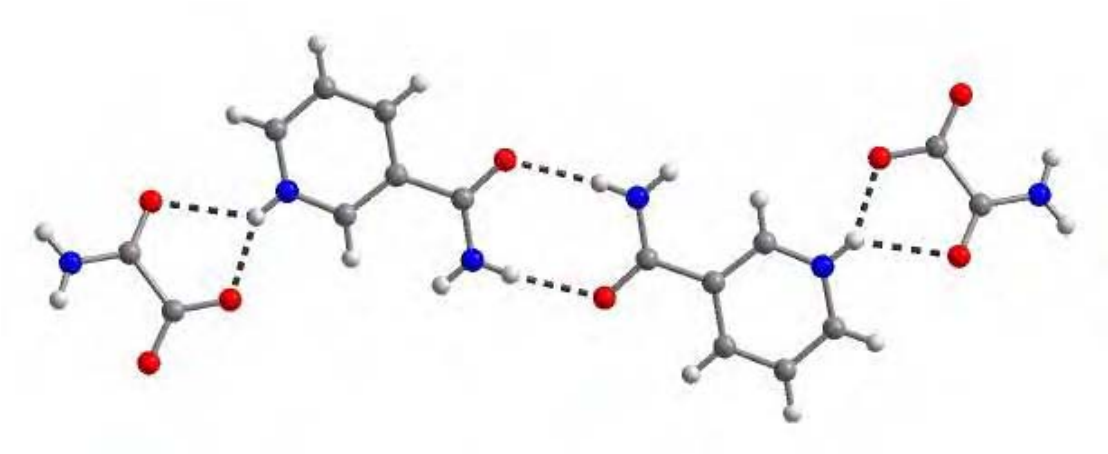

Figure 4.26: The tetrameric unit formed in the crystal structure oxamic acid:nicotinamide. Hydrogen bonds are indicated as dashed lines.

A further strong hydrogen bond is donated from the nicotinamide molecule via N8 acting as a donor through H8B to O3 (1-x,0.5+y,-0.5Z). Two weak hydrogen bonds are also donated from the cationic nicotinamide molecule, dimers of nicotinamide molecule are hydrogen bonded by C4 donating a hydrogen bond via H4 to O8 (2-x,-0.5+y, 0.5-z), this soft hydrogen bond forms a C(6) spiral along the 2_1 screw axis and in combination with the dimer $R^2_2(8)$ rings generate a nicotinamide only layer in the (011) plane. A second weak hydrogen bond donated from C7 via H7 to O3(1-x,0.5+y,-0.5Z).

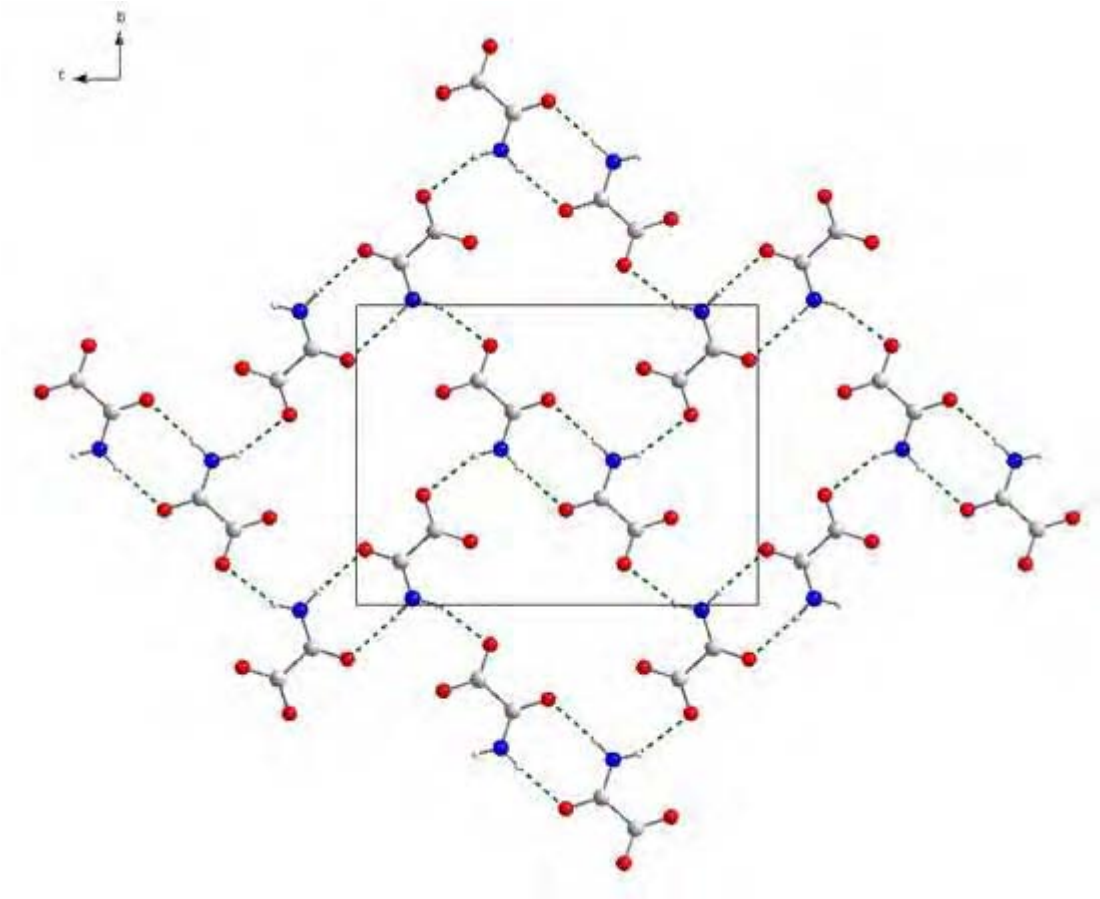

Figure 4.27: The plannar oxamate acid sheet as viewed along the *a* axis. Hydrogen bonds are shown by the dotted green line. (Unit cell shown)

The anionic layer of oxamate molecules also lies in the (011) plane. The two remaining strong hydrogen bonds link together the oxamate anions forming an infinite zigzag chain of dimers defined by $R_2^2(8)$ rings and propagated by a C(5) spiral running along the 2_1 screw-axis at (1/2,y,1/4). The amide N1 acts as a donor through H1A to O1 at (1-x,-y,-z), while O2 (1-x, 0.5+y, 0.5-z) accepts a hydrogen bond from N1 via H1B.

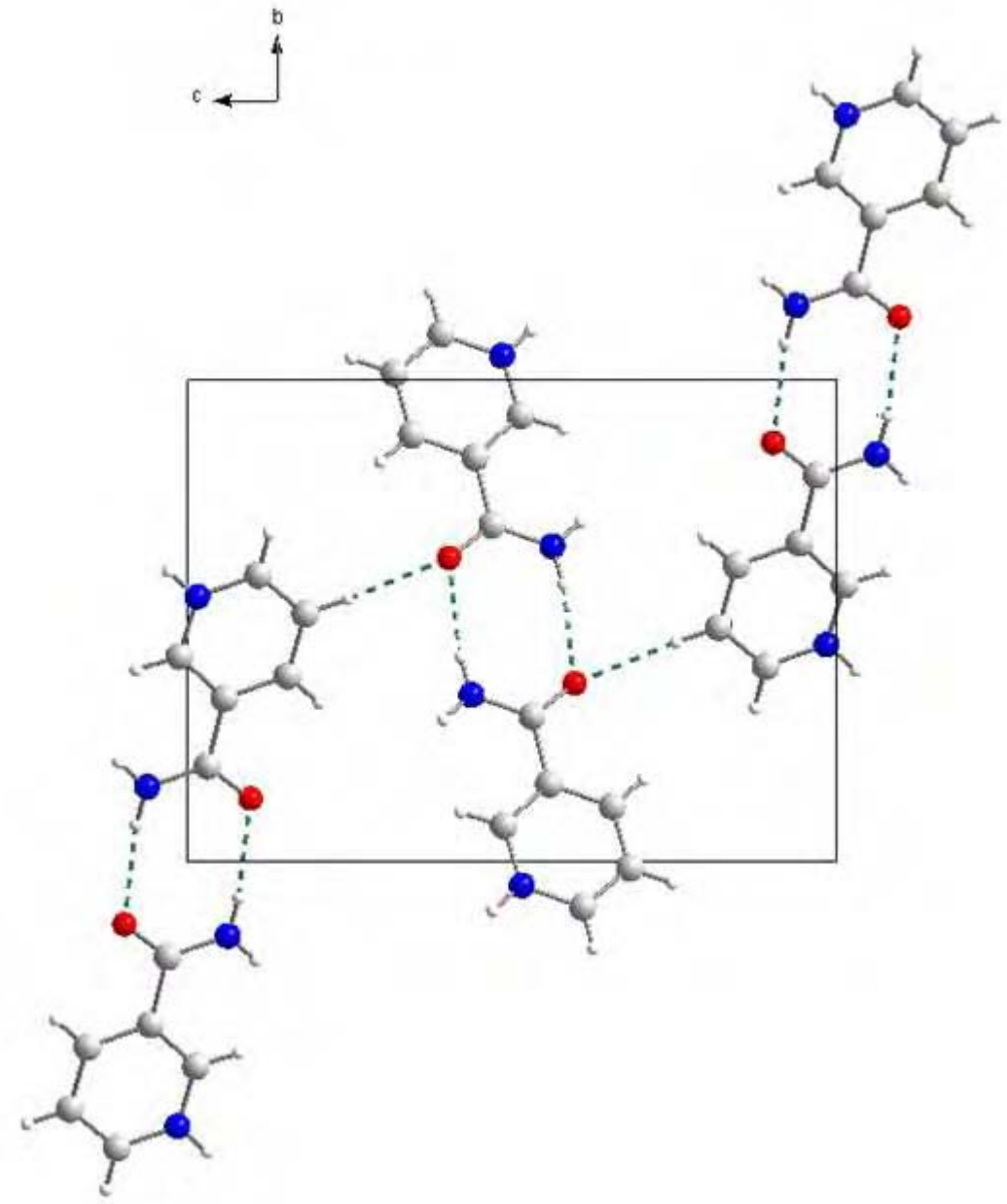

Figure 4.28: The nicotinamide sheet, viewed along the *a* axis. (Unit cell shown)

The anionic and cationic layers are linked by the bifurcated N(heterocyclic)-H+…O- interactions described earlier, by the last strong N-H…O hydrogen bond donated from the nicotinamide N8 acting as a donor through N8B to O3 at (1-*x*, 0.5+*y*, -0.5-*z*) and

reinforced by the second soft hydrogen bond so that O3 at (1-*x*, 0.5+*y*, -0.5-*z*) acts as a bifurcated acceptor also from C7 via H7. As shown by figure 4.27.

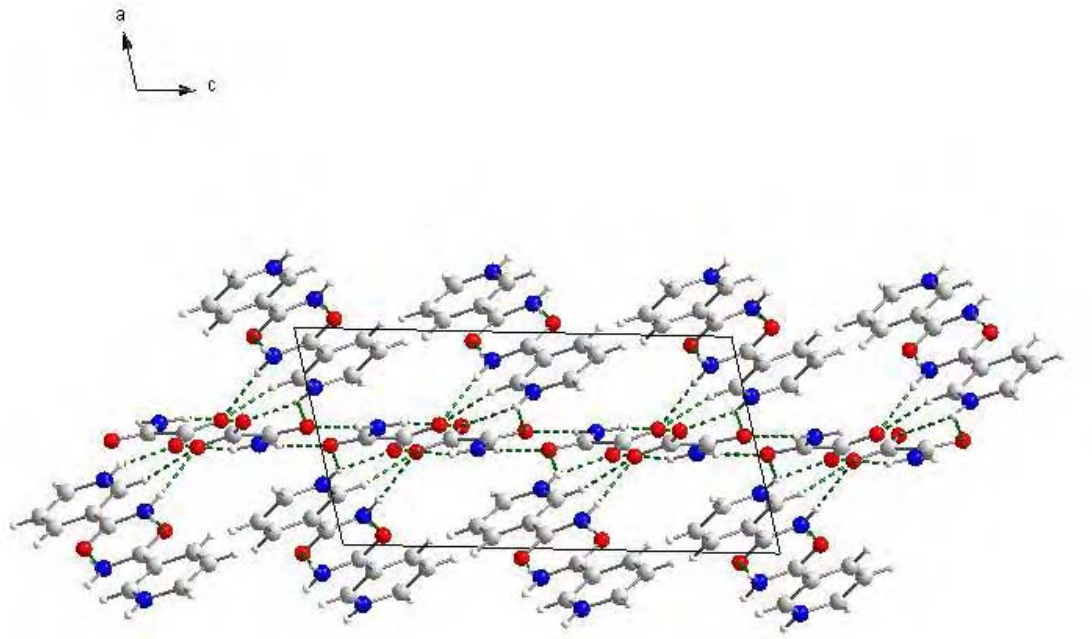

Figure 4.29: View along the *b* axis showing the layered structure of oxamic acid and nicotinamide co-crystal adduct. (Unit cell shown).

Table 4.9: Intermolecular parameters for the oxamic aicd:nicotinamide co-crystal adduct (Å)

Donor-----H… Acceptor	D-H	H---A	D…A	<(DHA)
N(1)—H(1A)…O(1)^{i}	0.86	2.13	2.9831	175
N(1)---H(1B)…O(2)^{ii}	0.86	2.24	3.0282	153
N(1)---H(1B)…O(3)	0.86	2.36	2.7037	104
N(8)---H(8A)…O(8)^{iii}	0.86	2.1	2.9456	169
N(8)—H(8B)…O(3)^{ii}	0.86	2.08	2.9227	167
N(2)---H(2)…O(1)	0.86	2.27	2.9224	132
N(2)---H(2)…O(2)	0.86	1.86	2.6164	146
C(7)---H(7)…O(3)^{ii}	0.93	2.21	3.1138	164
C(4)---H(4)….O(8)^{iv}	0.93	2.28	3.1795	162

Symmetry codes: (i) 1 - *x*, - *y*, - *z*; (ii) 1 - *x*, 0.5 + *y*, -0.5 - *z*; (iii) 2 - *x*, 2 - *y*, - *z*; (iv) 2 - *x*, -0.5 + *y*, 0.5 - *z*;

4.12 Single crystal vs. Powder structure

As discussed previously, a single crystal diffraction experiment provides a higher quality structure than from pxrd. However, the comparison of structures obtained from single crystal and powder methods highlights both the benefits and pitfalls of using pxrd data for structure solution and refinement. In the case of pxrd data, the loss of diffraction information, (through peak overlap) can make features in the molecule which contain similar electron density hard to distinguish due to the resolution available. This can potentially lead to false DE solutions, as the algorithm is looking to place a model as close as possible to areas of electron density in the unit cell. Although the structure solution of the isonicotinamide adduct was successful, this problem is highlighted when looking at the nicotinamide layer in the oxamate:nicotinamide structure, as shown in figures 4.30 and 4.31.

Figures 4.31 and 4.32 clearly show a flip in orientation for the amide functional group on the nicotinamide molecule when comparing the DE powder solution of R_{wp} 10.38 % to the single crystal structure. The DE solution (R_{wp} 10.38 %) upon refinement reached an R_{wp} of 5.59 %, however the soft bond restraints on the C-N and C-O bond lengths in the amide functional group alluded to a orientation problem. The amide group was flipped and further refined down to R_{wp} 5.19 %, using R_{wp} as a discrepancy to prove that the initial amide orientation in the DE solution R_{wp} 10.38 % was incorrect. However, the DE had located the global minimum as the equivalent crystal structure with the amide flipped gave an R_{wp} of 11.21 %. This anomaly between structure solution and refinement is maybe not surprising as the relaxation and flexibility introduced in refinement may alter the R_{wp} surface searched.

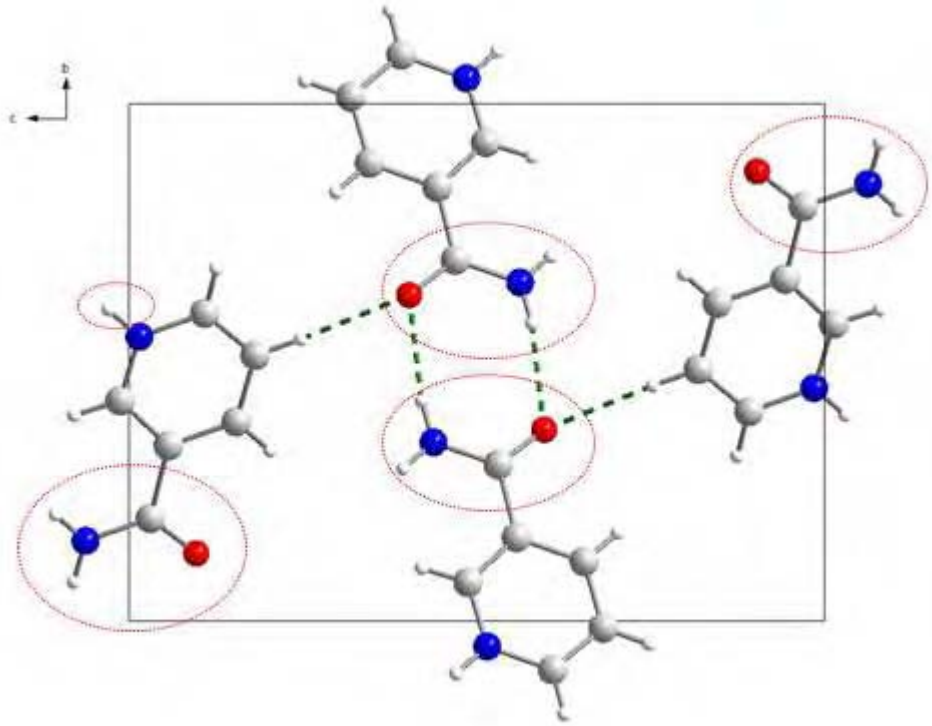

Figure 4.30: Nicotinamide layer from the single crystal structure of oxamate:nicotinamide.

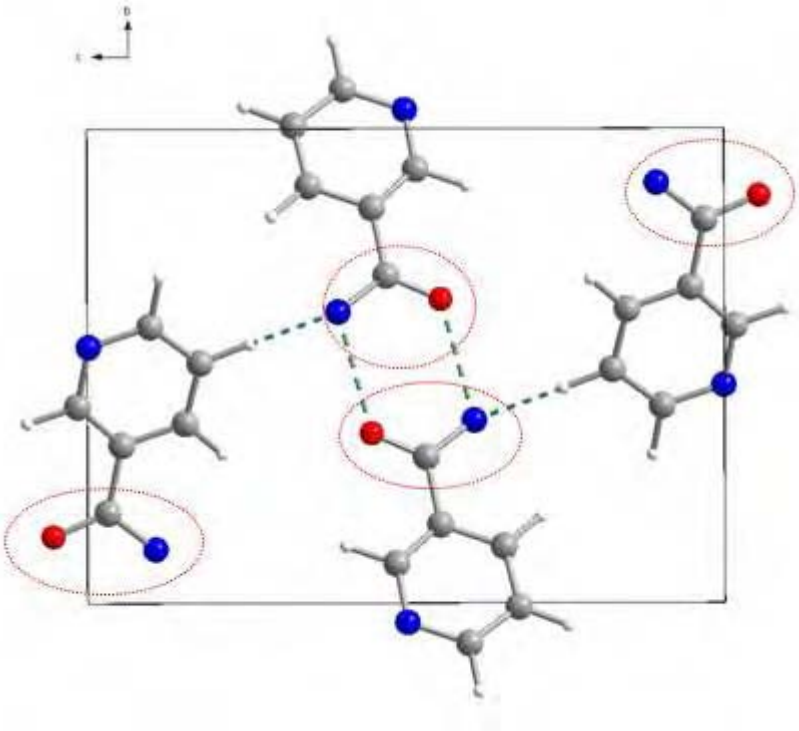

Figure 4.31: Nicotinamide layer from the DE solution (R_{wp} = 10.38%) of oxamate: nicotinamide.

Conversely, the oxamate layer in oxamate:nicotinamide shows that the functional group conformation is correct when comparing the powder to single crystal structure (figures 4.32 and 4.33).

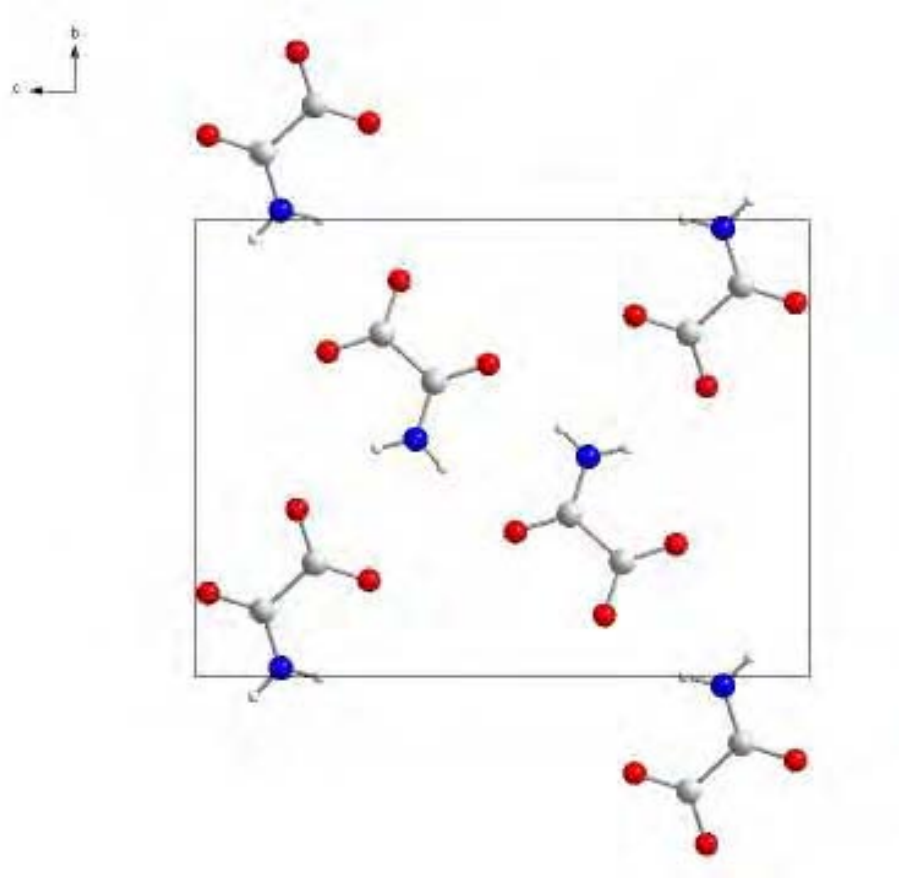

Figure 4.32: Oxamate layer from the single crystal structure of oxamate:nicotinamide

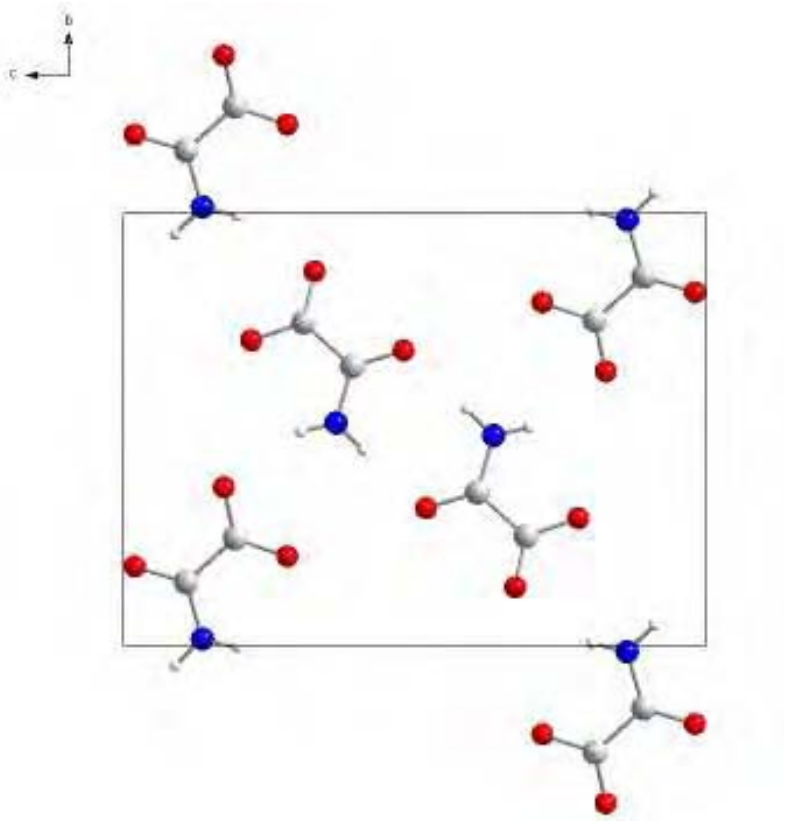

Figure 4.33: Oxamate layer from the DE solution (R_{wp} = 10.38 %) of oxamate acid:nicotinamide.

The importance of the amide orientation is confirmed by a search of 'like-nicotinamide' systems on the CSD. The search illustrated that both *syn* and *anti* nicotinamide (shown in figure 4.34) occur regularly in the organic solid state, with eleven out nineteen nicotinamide molecules adopting the *cis* orientation.

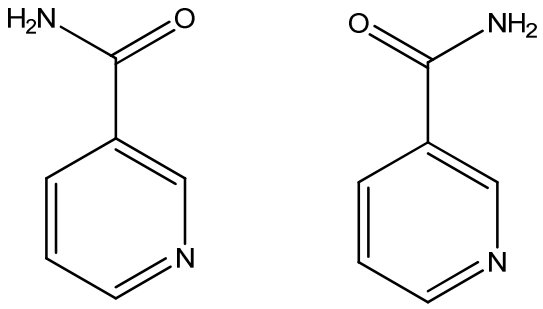

Figure 4.34: The *syn* (left) and *anti* nicotinamide molecule configuration(right)

Pxrd data alone does not possess sufficient resolution to accurately locate the position of hydrogen atoms. Complementary techniques to pxrd such as solid state IR are able to determine whether proton transfer has taken place (section 4.8). Differences in pKa values (greater than two) can be used as a predictive tool for the formation of a salt, but this has its shortfalls as pKa are used for the description of the labile nature of the acidic protons in solution and not in solids.

The figures below, 4.35 and 4.36, illustrate how close the pxrd structure is to that of the single crystal structure.

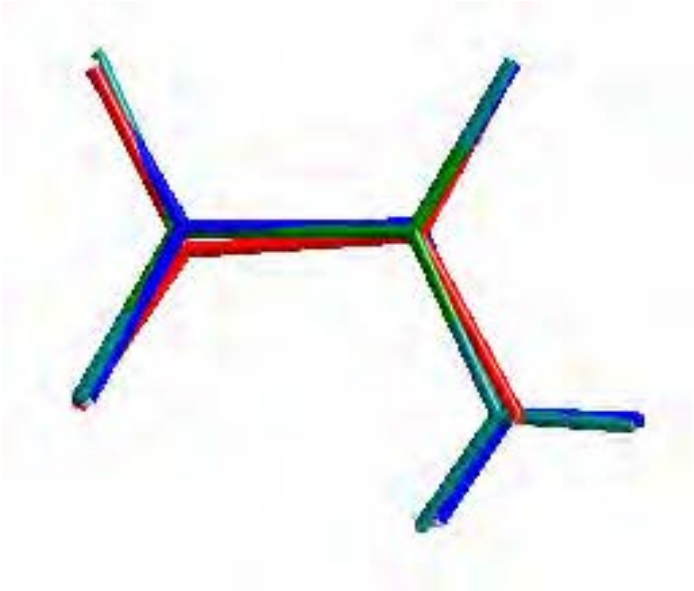

Figure 4.35: Oxamate ion molecule from oxamate: nicotinamide. The green molecule represents single crystal positions, the red molecule represents atoms from the DE solution (10.38) and the blue molecule represents the final refined atomic positions.

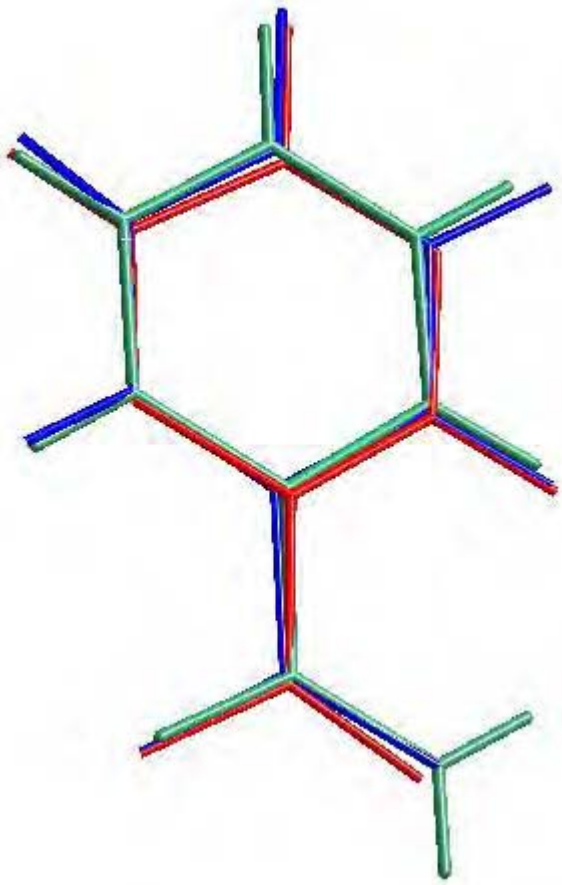

Figure 4.36: The nicotinamide molecule from oxamate acid: nicotinamide. The green molecule represents single crystal positions, the red molecule represents atom positions from the DE solution (10.38) and the blue molecule represents final refined positions.

Subsequent analysis confirmed that the crystal packing obtained by powder methods was correct, and that minimum, maximum and mean distances between pairs of corresponding atoms in the single and refined powder structures was calculated at 0.0394, 0.3336 and 0.113 Å respectively.

4.13 The efficiency of the DE algorithm

As discussed in section 4.9 and by further confirmed by the progress plot in figure 4.22, global optimisation of multi-component crystal systems often contain large plateau regions, subsequently followed by sharp decline in R_{wp} towards the global minimum. However, as illustrated by table 4.10, only one of the DE runs performed in this work resulted in a solution suitable for a starting point of a successful Rietveld refinement. All other runs were deemed unsuccessful. To fully investigate the efficiency of the DE algorithm, a diverse range of both *F* and N_P will need to be fully investigated.

Values of *F* were chosen for variation between limits chosen from previous DE studies[29] and *K* was fixed throughout at 0.99. For each combination of parameters, five epochs were calculated. Many results did not converge and reach G_{max}; extension to larger values of G_{max} would give more indication of the convergence of the DE calculation with these higher population values.

Table 4.10: The results from a number of DE calculations with variation in *F* (mutation rate). For each epoch the final R_{wp} (in %) is given and figures within brackets indicate at which generation convergence was achieved. Runs giving the correct structure solution are indicated by green; the gold cell indicates the lowest R_{wp} achieved and the starting point for the successful structure refinement. Runs that have not converged by the maximum allowed number of generations are shaded grey.

.

Run	F	NP	epoch 1	epoch 2	epoch 3	epoch 4	epoch 5
1	0.4	140	29.04(1500)	23.18(1425)	26.88(1500)	28.46(1500)	27.04(1003)
2	0.4	140	31.26(1500)	31.75(1500)	32.56(1499)	32.56(1500)	
3	0.4	140	26.23(1356)	26.63(1207)	28.99(1500)	25.27(1380)	24.45(1076)
4	0.4	140	29.92(1500)	25.06(1500)	31.11(1500)	30.31(1500)	22.26(1153)
5	0.4	140	22.12(1500)	21.91(1251)	22.26(1500)	21.73(1500)	21.88(1500)
6	0.4	140	34.44(1500)	35.56(1500)	27.6(1189)	26.26(1450)	25.97(1499)
7	0.5	140	35.24(1037)	33.7(1084)	35.36(1031)	35.34(1009)	35.51(1500)
8	0.5	140	32.19(1500)	10.38(1438)	33.19(1500)	31.73(1500)	31.49(1500)

4.14 Thermal Behaviour of oxamate:nicotinamide

Thermal expansion co-efficients can also give us an insight into the crystal structure of oxamate:nicotinamide, in particular the hydrogen bonding networks present within the crystal. Figure 4.37, illustrates the migration of diffraction peaks to a higher 2-theta value as the temperature decreases. The collection of variable temperature data sets also confirms that there is no phase transformation over the temperature range investigated (100-295 K).

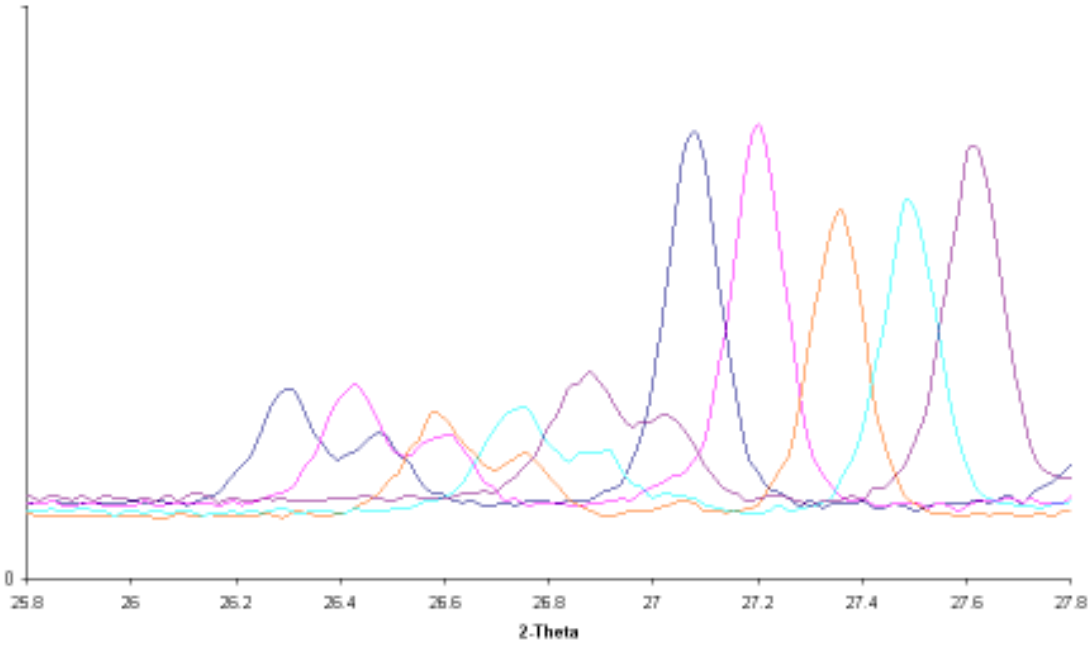

Figure 4.37: Two diffraction peaks of oxamic acid:nicotinamide over the temperature range investigated, 295 K(blue), 250 K (pink), 200 K(orange), 150 K(sky blue) and 100 K(purple).

The lattice parameters from these LeBail fits are given in Table 4.11 and plotted in figure 4.38. All bar the *b* direction, show the general trend of expansion. The ΔL/L0 values quoted in table 4.11, indicating the percentage change of the lattice parameter are calculated in the same manner as described in section 4.7.

Table 4.11 :Lattice parameters from the LeBail fitting of oxamate:nicotinamide. ΔL/L0 values are given in square brackets.

Temperature (K)	a (Å)	b (Å)	c (Å)	Beta (˚)	Volume (Å^3)	% R_{wp}	χ^2
100	6.8305(3) *[0.00]*	9.8826(6) *[0.00]*	13.6388(9) *[0.00]*	103.846(3) *[0.00]*	893.92(12) *[0.00]*	4.26	3.239
150	6.8650(4) *[0.0051]*	9.8810(6) *[-0.0002]*	13.6478(8) *[0.0007]*	103.921(4) *[0.0007]*	898.88(13) *[0.0056]*	4.45	2.936
200	6.9007(4) *[0.01027]*	9.8768(6) *[-0.0006]*	13.6578(12) *[0.0014]*	103.869(4) *[0.0002]*	903.73(15) *[0.0110]*	4.39	2.62
250	6.9435(3) *[0.0156]*	9.8723(6) *[-0.0010]*	13.6748(10) *[0.0026]*	103.921(4) *[0.0007]*	909.87(13) *[0.0179]*	4.37	3.143
295	6.9777(3) *[0.0213]*	9.8733(7) *[-0.0013]*	13.6842(12) *[0.0034]*	103.979(4) *[0.0015]*	914.82(16) *[0.0227]*	6.37	6.637

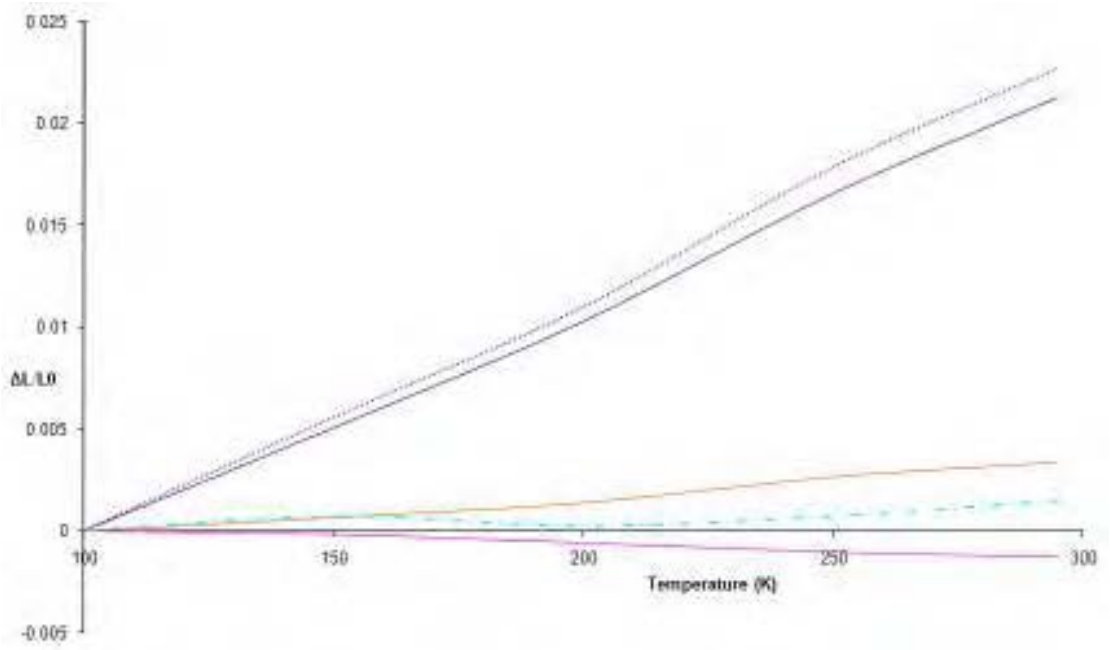

Figure 4.38: The fractional variation of lattice parameters obtained from LeBail refinement, plotted against temperature; Unit cell volume (purple spots), *a* (blue line), *b* (pink line), *c* (orange line) and *β* (sky blue dashed line).

The above quantitative data on the thermal expansion of oxamate:nicotinamide is based on lattice parameters derived from the LeBail[18] pattern decomposition technique. As discussed in the thermal expansion oxamate:isonicotinamide, Rietveld refinements[22] were performed for each data set, in order to derive more reliable results, with the values given in table 4.12 and shown in figure 4.39.

Table 4.12: Rietveld lattice parameters of oxamate:nicotinamide ΔL/L0 values are given in square brackets.

Temperature(K)	a (Å)	b (Å)	c (Å)	β (°)	Volume(Å^3)	% R_{wp}	χ^2
100	6.8268(8) *[0.00]*	9.8790(13) *[0.00]*	13.628(3) *[0.00]*	103.821(7) *[0.00]*	892.5(3) *[0.00]*	4.36	14.24
150	6.8410(7) *[0.0021]*	9.8789(12) *[-0.00001]*	13.634(3) *[0.0005]*	103.824(7) *[0.00003]*	894.8(3) *[0.0025]*	4.83	12.93
200	6.9003(6) *[0.0108]*	9.8756(10) *[-0.0004]*	13.657(2) *[0.0021]*	103.873(5) *[0.0005]*	903.5(3) *[0.0123]*	4.74	6.565
250	6.9432(5) *[0.0170]*	9.8755(9) *[-0.0004]*	13.673(2) *[0.0033]*	103.924(5) *[0.0010]*	909.9(2) *[0.0195]*	4.57	5.76
295	6.9778(8) *[0.0221]*	9.8739(14) *[-0.0005]*	13.6851(3) *[0.0042]*	103.977(7) *[0.0015]*	914.9(3) *[0.0251]*	4.72	12.84

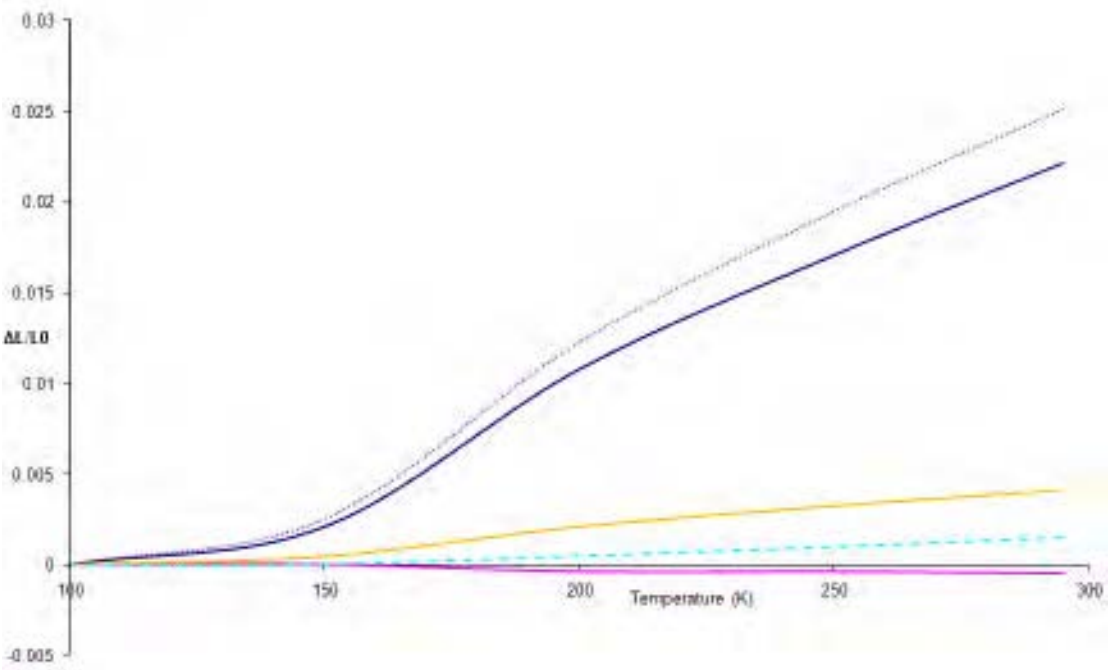

Figure 4.39: The fractional variation of lattice parameters obtained from Rietveld refinement, plotted against temperature; Unit cell volume (purple spots), *a* (blue line), *b* (pink line), *c* (orange line) and *β* (sky blue dashed line)

An alternative approach to the analysis of the thermal behaviour of this system is given in appendix M. Thermal expansion can be described by a linear thermal expansion, using equation 4.1. The results for each principal crystallography axes are shown in table 4.13.

Table 4.13: Linear thermal expansion co-efficients of the lattice parameters of oxamic acid:nicotinamide salt

Lattice parameter	Linear thermal expansion co-efficient (K^{-1})
a	1.08971×10^{-4}
b	-6.57774×10^{-6}
c	1.72475×10^{-6}
Unit cell volume	1.16296×10^{-4}

The most expansive crystallographic axis in terms of thermal expansion is the *a* axis, with a thermal expansion co-efficient of 1.0897×10^{-4} K^{-1}. The alternating layers of

oxamate and nicotinamide lie in the (011) plane, thus the fewest hydrogen bonds (i.e interplanar hydrogen bonds) align closest to this direction. The *c* axis also shows thermal expansion character, with a thermal expansion co-efficient of 1.72475×10^{-6} K^{-1}, but with a reduced tendency to expand in relation to the *a* axis. Within the structure there are strong directional hydrogen bonds that lie partially in the [110] direction, resulting in the relatively low thermal expansion co-efficient.

As illustrated in Figure 4.38 and by the thermal expansion co-efficient of -6.57774×10^{-6} K^{-1}, the *b* axis shows negative thermal expansion. Without the aid of the known crystalline structure as discussed earlier in this chapter (section 4.9), one would hypothesise that the *b* direction would contain strong and directional hydrogen bonds with the contraction potentially also aided by steric considerations. This hypothesis can clearly hold as the infinitely hydrogen bonded sheets lie in the (001) plane (figures 4.27, 4.28 and 4.29). Negative thermal expansion can then occur in the *b* direction in order to compensate for the thermal expansion occurring along the other crystallographic axes in order to limit unfavourable steric interactions.

4.15 Conclusion

Within this chapter, the crystal structures of the multi-component systems of oxamate:isonicotinamide and oxamate:nicotinamide have been solved by the both sxrd and pxrd. The structures have highlighted both the merits and pitfalls of solving structures via pxrd, with the amide flip the oxamate:nicotinamide illustrating the potentials problems associated with pxrd. Both structures have also been synthesised via reduced solvent methods. The use of complementary techniques has confirmed the proton transfer in both structures, allowing the systems to be classified as salts and not cocrystals.

References:

1. J. Papaconstantinou and S. P. Colowick, *Journal of Biological Chemistry*, 1961, **236**, 278-284.

2. L. Yang, L. Liu, B. Olsen and M. Nussbaum, *J. Pharm and Biomed. Analy*, 2000, **22**, 487-493.

3. C. B. Aakeroy, A. M. Beatty, B. A. Helfrich and M. Nieuwenhuyzen, *Crystal Growth & Design*, 2003, **3**, 159-165.

4. C. B. Aakeroy, A. M. Beatty and B. A. Helfrich, *Journal of the American Chemical Society*, 2002, **124**, 14425-14432.

5. I. D. H. Oswald, W. D. S. Motherwell and S. Parsons, *Acta Crystallographica Section E-Structure Reports Online*, 2005, **61**, O3161-O3163.

6. I. D. H. Oswald, W. D. S. Motherwell and S. Parsons, *Acta Crystallographica Section E-Structure Reports Online*, 2004, **60**, O2380-O2383.

7. S. N. Black, E. A. Collier, R. J. Davey and R. J. Roberts, *Journal of Pharmaceutical Sciences*, 2007, **96**, 1053-1068.

8. N. Chieng, M. Hubert, D. Saville, T. Rades and J. Aaltonen, *Crystal Growth & Design*, 2009, **9**, 2377-2386.

9. D. J. Berry, C. C. Seaton, W. Clegg, R. W. Harrington, S. J. Coles, P. N. Horton, M. B. Hursthouse, R. Storey, W. Jones, T. Friscic and N. Blagden, *Crystal Growth & Design*, 2008, **8**, 1697-1712.

10. S. Nicoli, S. Bilzi, P. Santi, M. R. Caira, J. Li and R. Bettini, *Journal of Pharmaceutical Sciences*, 2008, **97**, 4830-4839.

11. J. F. Remenar, M. L. Peterson, P. W. Stephens, Z. Zhang, Y. Zimenkov and M. B. Hickey, *Molecular Pharmaceutics*, 2007, **4**, 386-400.

12. N. Chieng, M. Hubert, D. Saville, T. Rades and J. Aaltonen, *Crystal Growth & Design*, 2009, **9**, 2377-2386.

13. D. A. Haynes, W. Jones and W. D. S. Motherwell, *Crystengcomm*, 2006, **8**, 830-840.

14. C. B. Aakeroy, D. P. Hughes and M. Nieuwenhuyzen, *Journal of the American Chemical Society*, 1996, **118**, 10134-10140.

15. C. B. Aakeroy, J. Desper and M. E. Fasulo, *Crystengcomm*, 2006, **8**, 586-588.

16. R. F. Evans and W. Kynaston, *Journal of the Chemical Society*, 1963, 3151.

17. R. Shirley, *The Crysfire 2002 System for Automatic Powder Indexing: User's Manual, 41 Guildford Park Avenue, Guildford, Surry, GU2 7NL, England, 2002.*, 2002.

18. A. Lebail, H. Duroy and J. L. Fourquet, *Materials Research Bulletin*, 1988, **23**, 447-452.

19. A. C. Larson and R. B. Von Dreele, *GSAS. General Structure Analysis System, Report No. LAUR 86-748, Los Alamos National Laboratory, Los Alamos, New Mexico, USA*, 1994.

20. C. C. Seaton and M. Tremayne, *Possum Programs for Direct-Space Strucutre Solution from Powder Diffraction Data*, 2002, School of Chemistry, University of Birmingham, UK.

21. F. H. Allen, O. Kennard, D. G. Watson, L. Brammer, A. G. Orpen and R. Taylor, *Journal of the Chemical Society-Perkin Transactions 2*, 1987, S1-S19.

22. H. M. Rietveld, *Journal of Applied Crystallography*, 1969, **2**, 65-71.

23. G. M. Sheldrick, Acta Cryst, A64, Editon edn., 2008, pp. 112-122.

24. M. M. Belmonte and D. J. Price, *Acta Crystallographica Section C-Crystal Structure Communications*, 2010, **66**, O147-O150.

25. C. B. Aakeroy and A. M. Beatty, *Australian Journal of Chemistry*, 2001, **54**, 409-421.

26. M. C. Etter, *Accounts of Chemical Research*, 1990, **23**, 120-126.

27. M. C. Etter, *Journal of Physical Chemistry*, 1991, **95**, 4601-4610.

28. P. Vishweshwar, A. Nangia and V. M. Lynch, *Crystal Growth & Design*, 2003, **3**, 783-790.

29. C. C. Seaton and M. Tremayne, *Chemical Communications*, 2002, 880-881.

30. V. K. Peterson, *Powder Diffraction*, 2005, **20**, 14-17.

31. H. M. Rietveld, *Journal of Applied Crystallography*, 1969, **2**, 65-&.

32. P. S. Whitfield, Y. Le Page, P. H. J. Mercier and J. Y. Kim, *Journal of Applied Crystallography*, 2007, **40**, 1019-1026.

33. R. A. Shirley, CRYSFIRE Powder Indexing System, University of Surrey, England., 2000.

5. Cocrystallisation of fumaric acid:nicotinamide, maleic acid: nicotinamide and maleic acid:isonicotinamide

As discussed in section 4.0, co-crystallisation provides the chemist with an alternative approach in delivering APIs, in which the physical properties can be enhanced whilst retaining the chemical properties of the individual components. This chapter describes the extension of the attempted cocrystallisation of nicotinamide with unsaturated dicarboxylic isomers fumaric acid and maleic acid and isonicotinamide with maleic acid; the molecular structures of all starting components are shown in figure 5.1. Fumaric acid, maleic acid, nicotinamide and isonicotinamide have pKa values of 3.5, 1.5, 3.6 and 3.4 respectively. As discussed previously, a ΔpKa greater than 3 often results in salt.

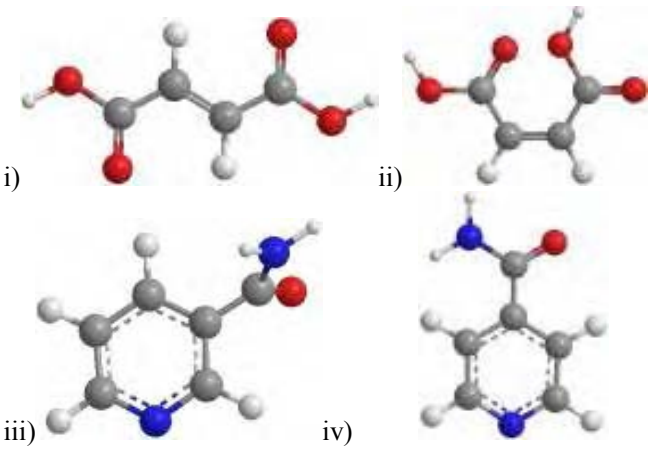

Figure 5.1: Molecular diagrams of fumaric acid (i), (ii) maleic acid , (iii) nicotinamide and iv) isonicotinamide

Fumaric acid (trans-butenedioic acid), contains two carboxylic acid moieties, which would potentially lend themselves to form hydrogen bonded motifs in the solid state. Fumaric acid

also has a number of prospective medicinal uses, particularly for the treatment of multiple sclerosis, a condition where the immune system attacks the central nervous system, leading to demyelination[1]. Another common use for fumaric acid is an acidity regulator when added to food and is also known as E297.

Fumaric acid has been previously reported in a 1:2 ratio in a cocrystal with isonicotinamide[2]. Following the structure determination and characterisation of fumaric acid:nicotinamide (1:1) described in this chapter the structure of this co-crystal was published[3] and the diversity of stoichiometry probed, producing crystals containing both 1:2 and 1:1 ratios. In both cases, the crystal structures[2, 3] were solved using single crystal methods. In this chapter we will describe the solution of the crystal structure of fumaric acid:nicotinamide 1:1 using pxrd data and single crystal methods, independent of the previously solved crystal structures.

5.1 Characterisation of fumaric acid:nicotinamide

Pxrd was used to confirm that the product of crystallisation was a new crystalline phase with no significant presence of the starting materials (figure 5.2). The stoichiometric ratio of the starting components in the new material was confirmed as 1:1 by ^{1}H NMR (section 3.5.2).

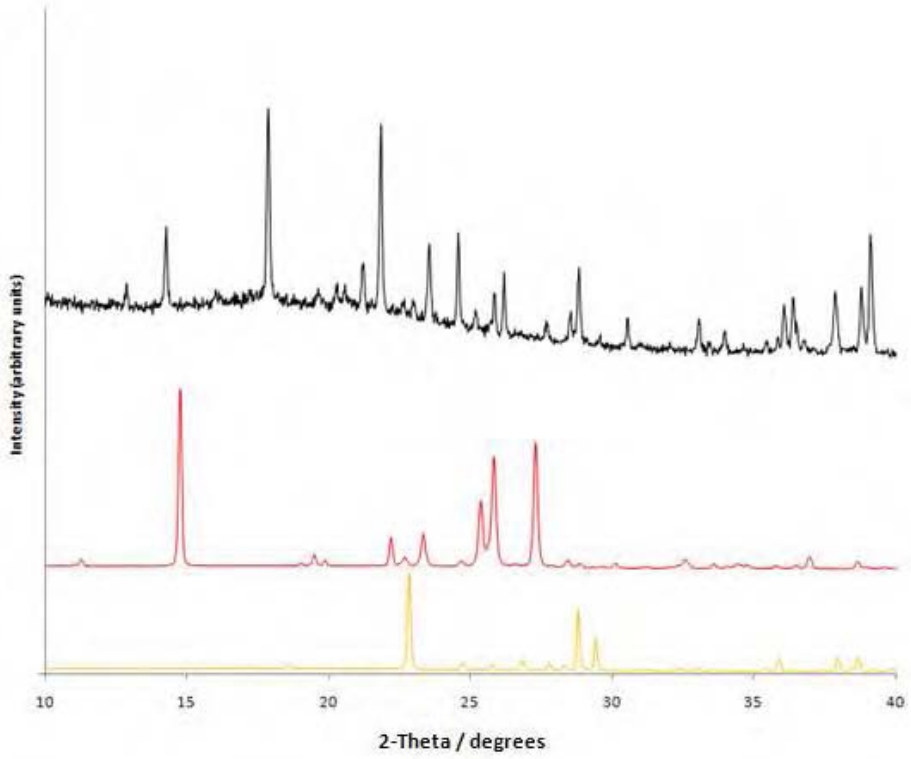

Figure 5.2: Powder X-ray diffraction patterns of the starting materials, fumaric acid (orange), nicotinamide (red) and the fumaric acid:nicotinamide multi-component material (black).

Further characterisation of the new multi-component crystalline phase was undertaken by solid state infra-red spectroscopy which confirmed the presence of a new phase (when compared to the spectrum of a mix of the two starting materials), alluding to the synthesis of a new multi-component crystal with different hydrogen-bonding characteristics to that of the component mixture, (figure 5.3). The presence of two broad peaks at 2340 cm^{-1} and 1859cm^{-1} is characteristic of an acid----N heterocyclic hydrogen bond, and is viewed as evidence for multi-component formation[4]. As illustrated in the literature[5], if an acidic proton is transferred to a heterocyclic nitrogen, individual N^{+}-H, peaks would appear at 3250 ± 50 cm^{-1}, (as observed in the spectra of both oxamic acid:isonicotinamide and oxamic

acid:nicotinamide).This is not evident in the IR spectra for fumaric acid:nicotinamide, suggesting that the material under investigation is a cocrystal.

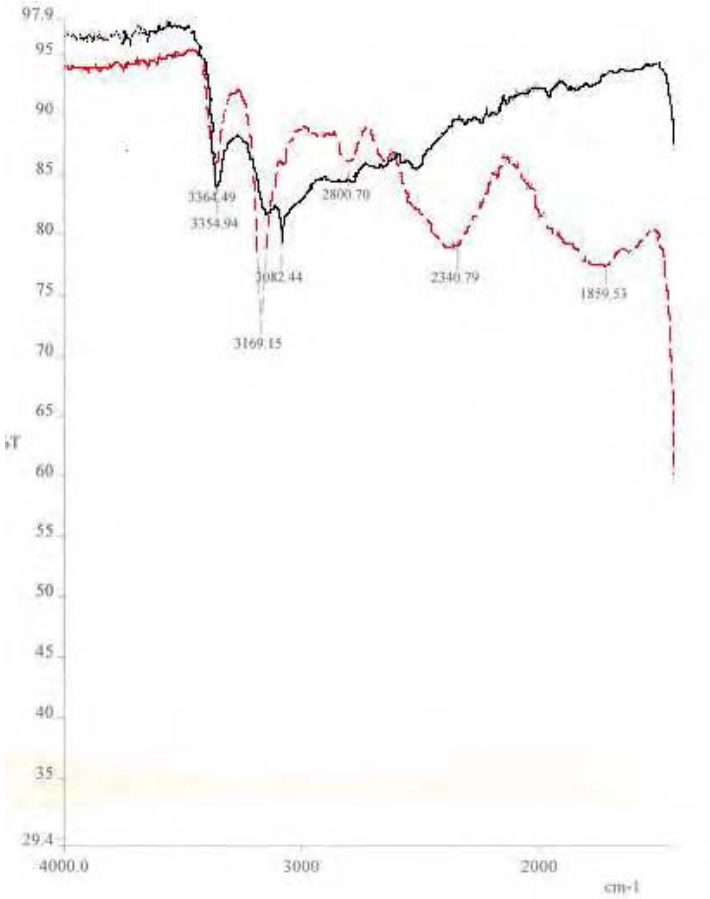

Figure 5.3: Solid state IR spectra of the fumaric acid and nicotinamide mix (red dashed line) and fumaric acid:nicotinamide multi-component crystal (solid black line)

In parallel with traditional solvent-mediated recrystallisation, pxrd was used to confirm that the same bulk crystalline phase (figure 5.4) was produced by both LAG (section 3.2.3) and sonic slurry (section 3.2.4) methods.

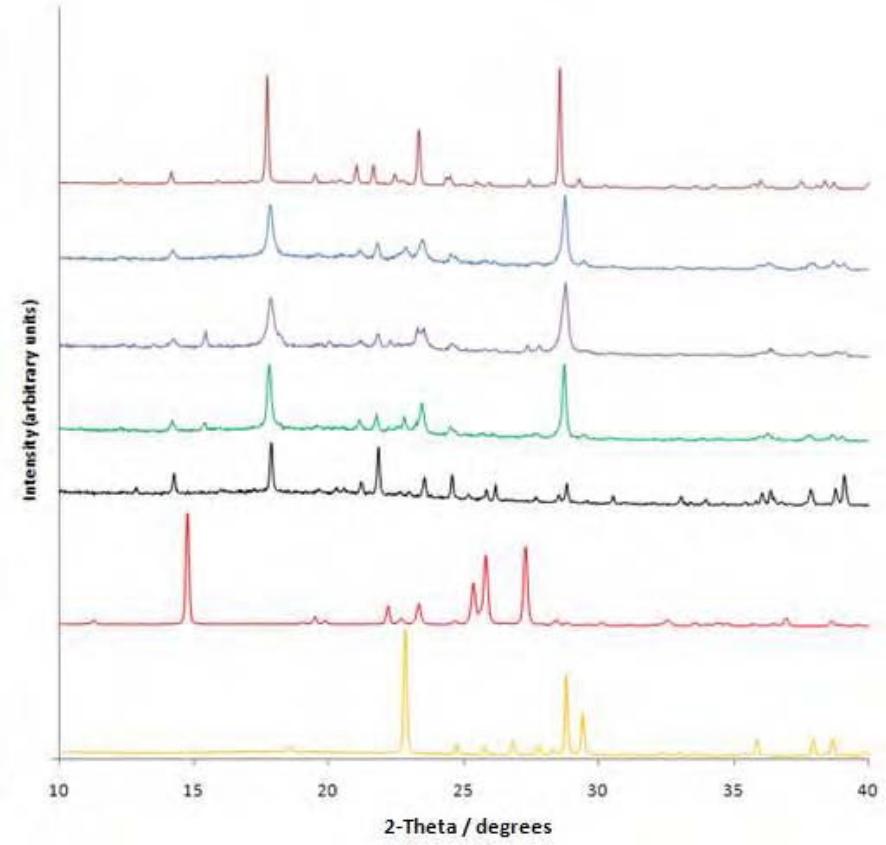

Figure 5.4: Powder X-ray diffraction data of the starting materials fumaric acid (orange) and nicotinamide (red). The fumaric acid:nicotinamide multi-component from solvent mediated recrystallisation (black), fumaric acid:nicotinamide from 10 minutes of LAG (green), from 15 minutes of LAG (purple), from 20 minutes of LAG (blue) and fumaric acid:nicotinamide from sonic slurry (dark red).

The merits and pitfalls of liquid drop grinding and other solvent reduced synthesis of multi-component crystals are discussed in greater detail in section 1.18. Variation in intensity can arise from the practical considerations involved in sample preparation and the crystal morphology of the samples leading to preferred orientation of the crystallites (section 1.11.4). Research into the stoichiometric diversity of the starting moieties in multi-component crystals via mechanochemical and other solvent reduced synthesis methods opens up the possibility in

future work to solve crystal structures from pxrd of mixed phase diffraction patterns. Mechanochemical crystal synthesis in particular, could lead to a mixture of starting materials and new multi-component crystalline phases, where attempts could be made to solve each phase separately by direct space methods. This method development in mechanochemical synthesis would allow the probing of potential crystalline phases unreachable in terms of structure solution via single crystal methods.

5.2 Structure solution and refinement from laboratory pxrd data

The X-ray powder diffraction data set used for structural analysis was collected over a period of 8 hours, and a range of $10^\circ \leq 2\theta \leq 60^\circ$. The data were indexed on the basis of the first 20 observable reflections using the indexing program CRYSFIRE[6] (appendix O) and the $P2_1/a$ space group assigned by consideration of systematic absences. The profile parameters were refined using the whole-profile-fitting LeBail[7] method in the GSAS[8] program to improve the fit of the lattice, zero point and profile parameters. Structure solution was carried out using the DE technique (section 1.14) as implemented in the program POSSUM[9].

From density considerations it was concluded that the asymmetric unit contained one fumaric acid and one nicotinamide molecule, hence the structural model used in the DE calculation comprised both molecules, constructed using standard bond lengths[10] and angles, but excluding the hydroxyl and amine hydrogen atoms. The nicotinamide molecule is defined by 7 DE elements and the fumaric acid molecule by 8 DE elements: for each molecule 3 parameters (θ,Φ,Ψ) were used to define the orientation within the unit cell (bounds 0 - 360˚), and 3 parameters (*x,y,z*) were used to define the position of the molecule in the unit cell (bounds 0-1). Nicotinamide contains one unconstrained torsion angle whereas fumaric acid contains 2 bounds (0-360˚) to define the conformation of each molecule, as shown in figure

5.5. The molecules were moved independently in the structure solution resulting in a 15 parameter problem.

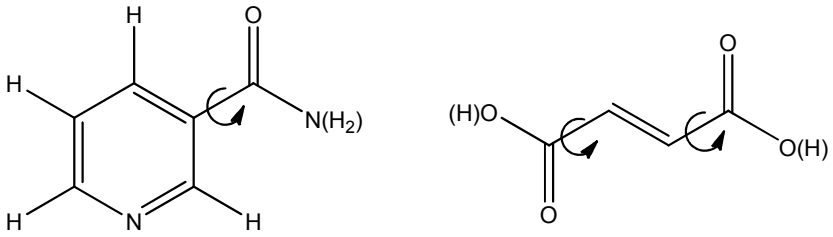

Figure 5.5: Molecular structures used in the DE structure solution, torsion angles are indicated by arrows. Hydrogen atoms excluded from the calculation are shown in brackets.

The parameters used in the successful DE calculation were, $K = 0.99$, $F = 0.4$, $N_p = 330$ and $G_{max} = 2000$. The evolutionary progress plot for the successful DE solution of fumaric acid:nicotinamide (figure 5.6) shows the progression of the DE calculation in terms of R_{wp} with generation. As shown in previous examples of DE progress plots (figures 4.6 and 5.6), the plots take a characteristic profile as an initial decline in R_{wp} is followed by a prolonged plateau region. After the plateau, the plot declines steeply as it heads rapidly to the minimum of the hypersurface, again suggesting a deep and narrow well in the R_{wp} hypersurface.

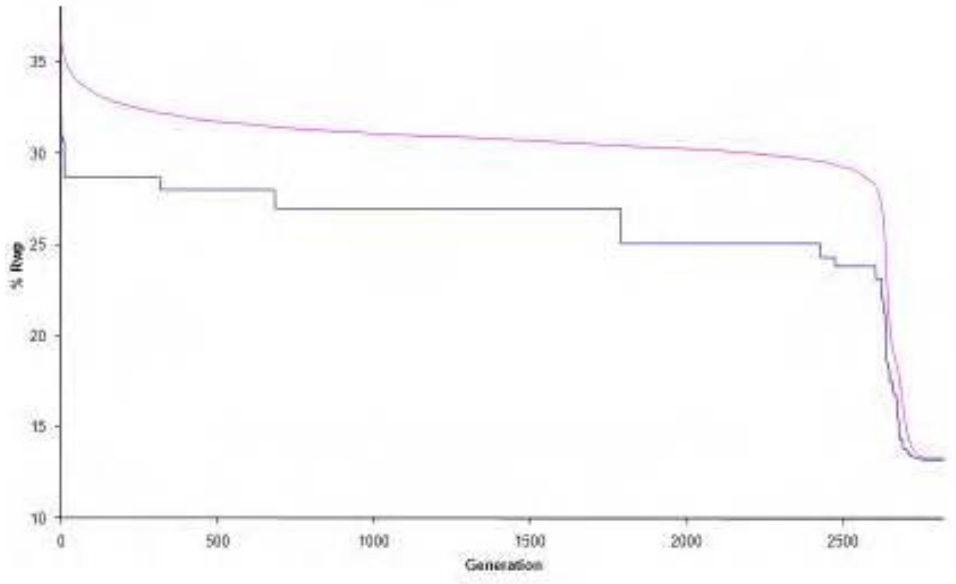

Figure 5.6: Evolutionary progress plot for the successful solution of fumaric acid:nicotinamide showing the best R_{wp} (blue) and the mean R_{wp} (pink) for each generation.

5.3 Rietveld refinement

The best structure from the DE solution was used as a starting point for refinement using the GSAS program package[8]. The positions of all atoms were refined subject to soft restraints (weighting factor of 0.001 for bond distances and 0.005 for geminal non-bonded distances) on standard geometry. Hydrogen atoms that were not included the DE calculation were placed in calculated positions according to the expected hydrogen bonding network. For the non-H atoms, isotropic atomic displacement parameters were refined constrained according to atom type or environment. Refinement of a preferred orientation parameter in the [100] direction was required, resulting in a fraction of 0.82750. The final Rietveld plot can be found in figure 5.7. Table 5.1 contains structure parameters from both single and powder X-ray diffraction determinations.

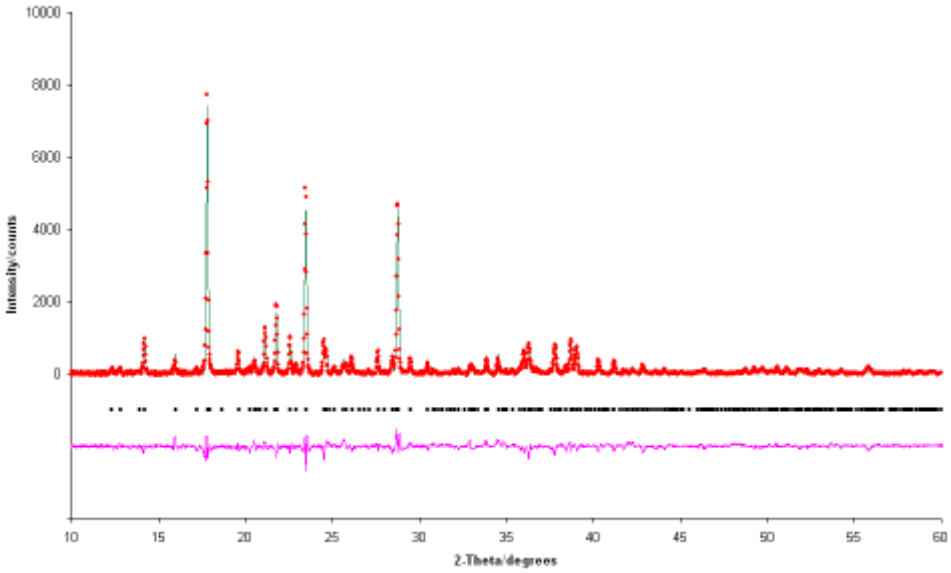

Figure 5.7: The final Rietveld plot for fumaric acid:nicotinamide. The experimental diffraction data is shown by red circles, the calculated diffraction pattern by solid green line and reflection positions are marked by black dots. The difference between the experimental and calculated diffraction pattern is shown by the pink line.

Table 5.1: Initial lattice parameters, DE structure solution parameters, refined lattice parameters from Rietveld refinement and single crystal determination and Rietveld agreement factors.

Compound	*Fumaric acid:nicotinamide*		
Crystal data			
Chemical formula	$C_4H_4O_4 + C_6N_2H_6O$		
M_r	238.2		
Indexing			
Space group	$P2_1/a$		
Initial a / Å	14.3889(3)		
Initial b / Å	13.8156(2)		
Initial c / Å	5.5583(2)		
Initial β / °	93.517(1)		
Initial V / Å^3	1102.980(2)		
Structure solution			
LeBail R_{wp} / %	6.36		
LeBail R_p / %	4.85		
LeBail χ^2	1.633		
DE elements			
K	0.99		
F	0.4		
N_p	330		
Average R_{wp} / %	13.23		
Best R_{wp} / %	13.23		
Refinement			
R_{wp} / %	9.40		
R_p / %	7.00		
R^2_F / %	0.2762		
χ^2	3.657		
Preferred orientation fraction	0.82750 [100]		
No of parameters	76	***Single Crystal***	
No. of restraints	52		
Final a / Å	14.3763(13)	a / Å	5.5376(4)
Final b / Å	13.8049(19)	b / Å	13.785(1)
Final c / Å	5.5560(3)	c / Å	14.2006(11)
Final β / °	93.53(0)	β / °	92.54(1)
Final V / Å^3	1100.(3)	V / Å^3	1082.9 (3)
		Space group	$P2_1/c$
		Temperature (K)	200

5.4 Fumaric acid:nicotinamide structure

The following crystal structure description is based upon the single crystal data collected on Bruker SMART 6000 diffractometer ($\lambda_{Cu\text{-}K\alpha}$ = 1.54178 Å) at 200 K. Further details on the single crystal structure solution can be found in appendix P. The structure was solved by direct methods and refined using Shelx[11]. Hydrogen atoms were found by Fourier methods and constrained using a riding model. Anisotropic displacement parameters were used for non-H atoms; H-atoms were given isotropic displacement parameters equal to 1.2 times the equivalent isotropic displacement parameter of the atom to which they are attached. An incubator was used to grow a single crystal of suitable quality and size to warrant a single crystal diffraction experiment, as described in section 3.2.2. As confirmed by the single crystal structure solution, this adduct can be classified as a neutral cocrystal that crystallises in the $P2_1/c$ space group. The final ORTEP diagram from the single crystal solution is shown in figure 5.8

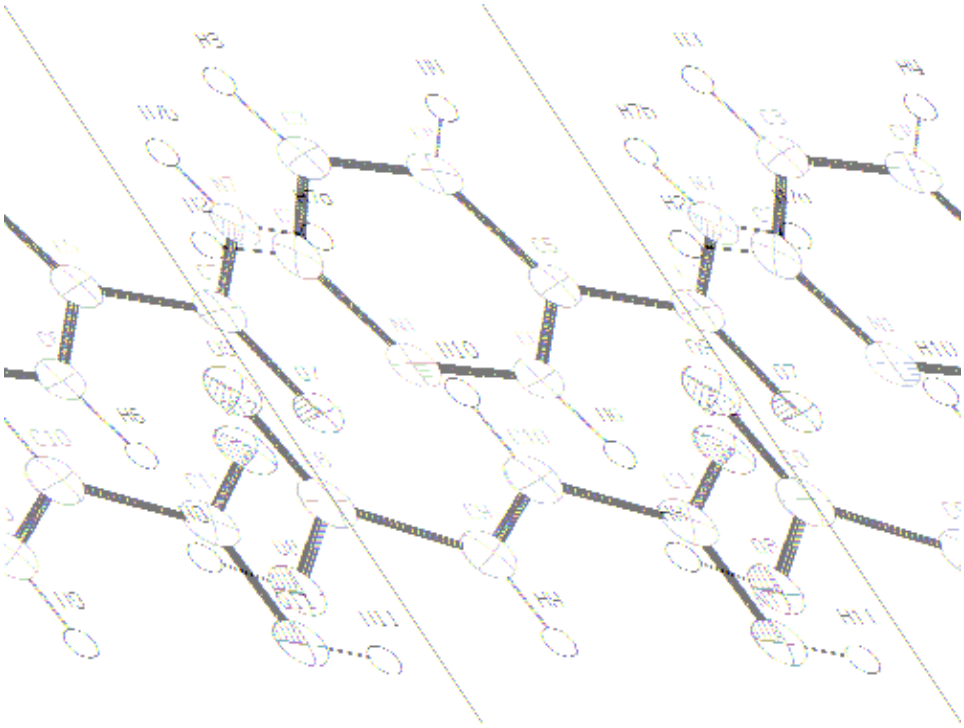

Figure 5.8: The molecular structure of fumaric acid:nicotinamide (1:1) showing the atom numbering scheme. Displacement ellipsoids are drawn at the 50 % probability level and H atoms are shown as small spheres of arbitrary radii.

The supramolecular structure of fumaric acid:nicotinamide is determined through five intermolecular hydrogen bonds; two strong N-H….O==C hydrogen bonds, one O-H….O==C hydrogen bond, one O-H....N(heterocyclic) hydrogen bond and one C-H...O=C interaction, all details shown in table 5.2. All strong hydrogen-bond donors and acceptors are used in the hydrogen bond network. The conformation of the amide group in the nicotinamide group is approximately planar, with a torsion angle of C4-C5-C7-O7 of 174.75(14)°. This planarity is due to the formation of strong hydrogen bonds by the amide group only within in flat supramolecular layers.

The fumaric acid and nicotinamide molecules are linked via the amide nitrogen N7, which acts as a double hydrogen bond donor, donating a hydrogen bond via H7A to O9 (1-x,y,z), and a second hydrogen bond to O12 (1-x,1-y,-z). The fumaric acid molecule donates two hydrogen bonds via its hydroxyl oxygens; from O8 via H8 to O7 (this hydrogen bond in combination with the N7-H7A…O9 hydrogen bond forms an acid-amide $R_2^2(8)$ dimer) and a second strong hydrogen bond is donated from O11 via H11 to the pyridine N1. A weak C-H....O hydrogen bond is formed from C4 via H4 to the carbonyl oxygen O12, this hydrogen bond propagates in the [010] direction (as illustrated in figure 5.9).

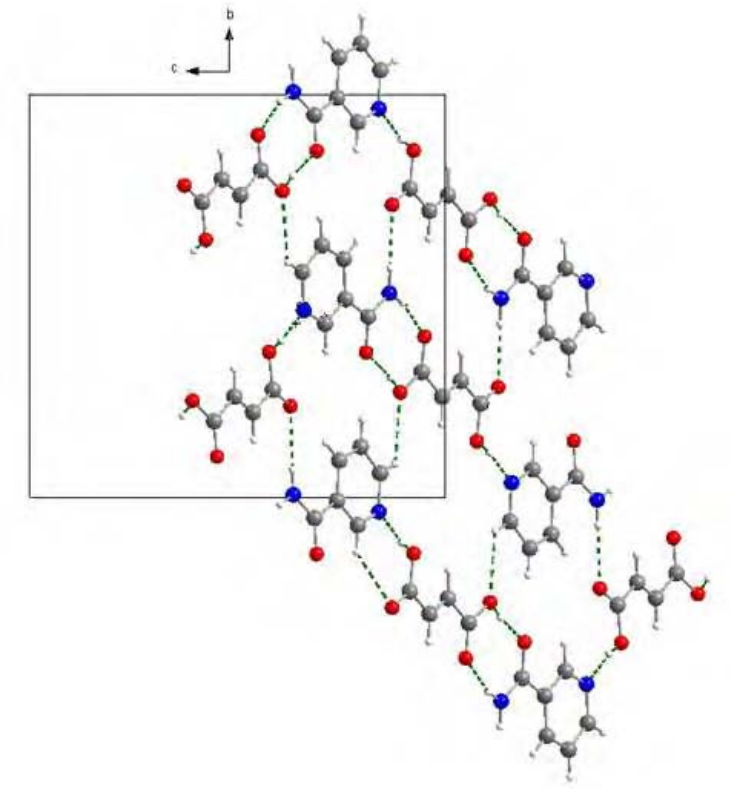

Figure 5.9: Fumaric acid:nicotinamide looking down the *a* axis. Carbon, nitrogen, oxygen and hydrogen atoms are shown in black, blue, red and white respectively. (Unit cell shown)

The structure consists of infinitely hydrogen bonded sheets, in the (104) plane, containing both fumaric acid and nicotinamide molecules, see figure 5.10. The planar sheets are not connected by hydrogen bonds, with a distance of 3.081 Å between the layers.

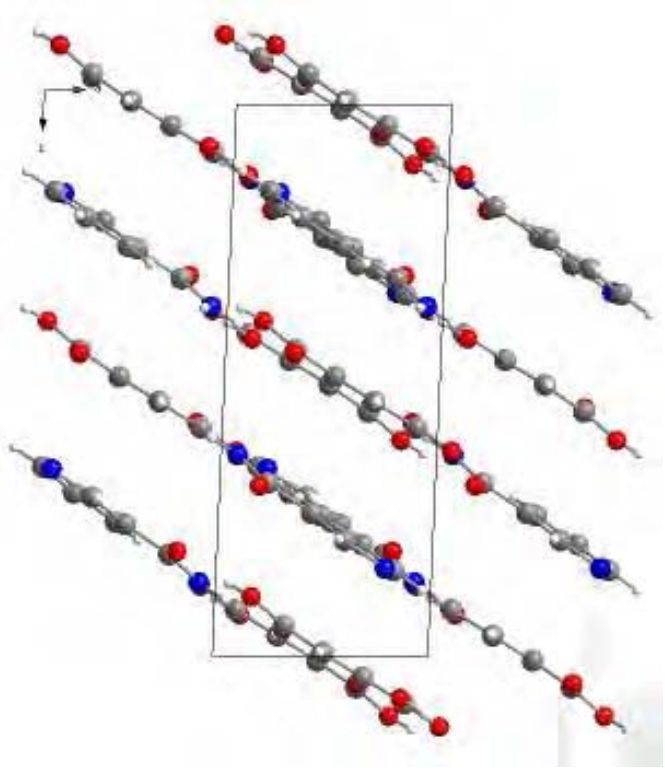

Figure 5.10: A view along the *b* axis, showing the hydrogen bonded sheets in the (101) plane. Carbon, nitrogen, oxygen and hydrogen atoms are shown in black, blue, red and white respectively.

Table 5.2: Hydrogen bonds geometry in fumaric acid:nicotinamide (Å and °).

Donor—H---Acceptor	d(D—H)	d(H-A)	d(D-A)	<(DHA)
N(7) —H(7A)….O(9)#1	0.880(1)	2.0200(1)	2.8814(17)	166.1
N(7) —H(7B)…O(12)#2	0.880(1)	2.1800(1)	3.0315(17)	163.2
O(8) —H(8)……O(7)#3	0.840(1)	1.7900(1)	2.6193(15)	170.8
O(11) —H(11)….N(1)#4	0.840(2)	1.7900(1)	2.5885(17)	170.0
C(5) —H(5)…..O2	0.950(1)	2.7500(2)	3.4141(17)	1.31.9

Symmetry transformations used to generate equivalent atoms: ***#1(*** x-1, y, z) ***#2*** (2-x, y+1, -z) ***#3*** (x+1, y,z) ***#4*** (x-1, y+1/2, z-1/2)

5.5 Comparison of the Single crystal vs. Powder structure

To aid the method development for the solution of this type of multi-component crystal structures from pxrd, structures solved from pxrd are also compared to those solved using single crystal methods. In cases such as this structure, with groups of similar scattering behaviour, this allows us to assess areas of potential problems, such as the orientation flip of similar functional groups, which can be indistinguishable from poor quality pxrd data and can lead to false structure solutions.

Below in figures 5.11 and 5.12, direct comparison between the single crystal atomic positions and the final refined atomic positions of the nicotinamide molecule in fumaric acid:nicotinamide.

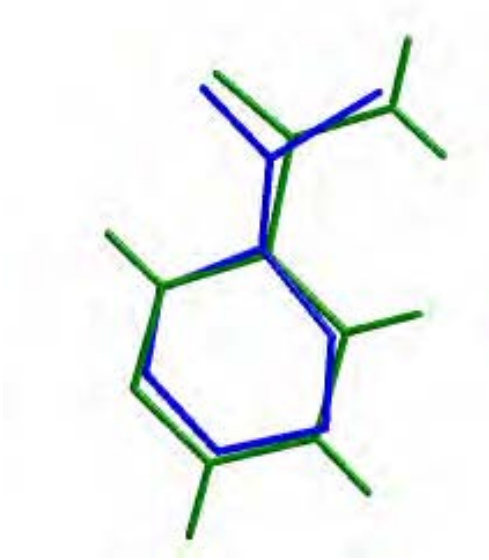

Figure 5.11: Nicotinamide molecule from fumaric acid:nicotinamide. The green molecule represents single crystal positions and the blue molecule represents final refined powder positions (non-hydrogen atoms only)

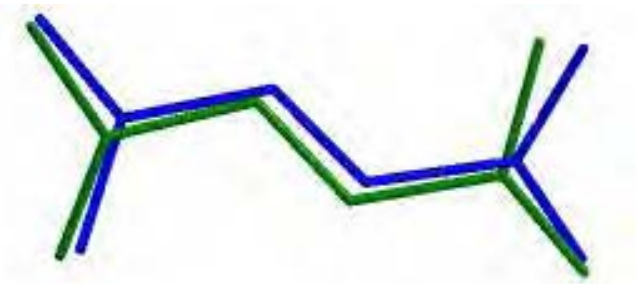

Figure 5.12: Fumaric acid molecule from fumaric acid:nicotinamide. The green molecule represents single crystal positions and the blue molecule represents final refined powder positions (non-hydrogen atoms only)

The subsequent analysis confirmed that the crystal packing obtained by powder methods was correct; minimum, maximum and mean distances between pairs of corresponding atoms in the single and refined powder structures was calculated at 0.0621, 0.5556 and 0.2888 Å respectively.

5.6 Efficiency of the DE algorithm

Table 5.3, illustrates that a large population coupled with a mutation rate (*F*) equal to 0.3 produced the most successful epoch with a % R_{wp} of 13.23, this was the starting point for a successful Rietveld refinement. As illustrated in figure 5.6, a plateau in R_{wp} is followed by a steep decline, indicative of the deterministic nature of the DE algorithm, but also, suggesting a shallow and deep global minimum.

Values of *F* and N_p were chosen for variation between limits chosen from previous DE studies[12] and *K* was fixed throughout at 0.99. For each combination of parameters, five epochs were calculated. As shown in figure 5.6, the progression of the DE calculation has a prolonged stagnation period followed by a sharp decline towards the global minimum, coupled with a trend in this case of smaller mutation vector resulting in lower R_{wp}.

Table 5.3 illustrates that as expected, the large population sizes coupled with a mutation factor of 0.5 fail to locate the narrow global minimum within the number of generations allowed. Many results did not converge and reached G_{max} (maximum number of generations allowed in one epoch before the calculation is halted and proceeding epoch initiates), extension to larger values of G_{max} would give more indication of the convergence of the DE calculation with these higher population values. In this case, larger population size, $N_p = 375$ but small F (0.3).

Table 5.3: The results from a number of DE calculations with variation in *F* (mutation rate) and NP (population size). For each epoch the final R_{wp} (in %) is given and figures within brackets indicate at which generation convergence was achieved. The gold cell indicates the lowest R_{wp} achieved and the starting point for the successful structure refinement. Runs that have not converged by the maximum allowed number of generations are shaded grey.

Run	F	NP	epoch 1	epoch 2	epoch 3	epoch 4	epoch 5
1	0.3	140	20.89(304)	18.18(284)	23.5(286)	20.59(255)	22.11(243)
2	0.3	140	21.37(334)	18.01(237)	20.44(212)	20.87(208)	24.57(272)
3	0.4	140	21.94(899)	21.53(580)	16.36(655)	18.87(789)	20.82(613)
4	0.4	140	16.21(736)	17.77(478)	20.52(553)	14.88(451)	16.75(447)
5	0.5	150	23.53(954)	17.31(1268)	22.51(1374)	16.6(1498)	27.24(871)
6	0.6	180	27.34(1500)	25.82(1500)	25.23(1500)	27.92(1500)	27.05(1500)
7	0.3	225	20.26(297)	22.77(347)	19.72(354)	22.19(467)	20.64(401)
8	0.3	300	19.59(614)	21.5(480)	14.39(550)	14.41(380)	16.95(560)
9	0.3	300	22.18(489)	19.48(632)	18.21(627)	17.89(512)	15.86(529)
10	0.8	300	26.01(3000)	26.34(3000)	27.47(3000)	21.55(3000)	26.66(3000)
11	0.4	330	17.12(1172)	16.65(1396)	12.95(1658)	20.28(1340)	16.11(1259)
12	0.4	330	17.34(1632)	17.81(1356)	18.94(1584)	15.29(1451)	15.35(1345)
13	0.6	330	26.69(3000)	24.83(3000)	13.99(2895)	24.33(3000)	25.03(3000)
14	0.2	375	16.5(186)	21.99(247)	15.74(230)	17.92(220)	17.21(191)
15	0.3	375	15.57(725)	15.04(587)	15.96(589)	18.55(557)	15.04(709)
16	0.3	375	20.2(2948)	13.23(2822)	17.71(3000)	22.84(3000)	26.21(3000)
17	0.3	375	19.64(619)	16.32(555)	14.1(592)	16.65(812)	18.27(509)
18	0.4	375	13.34(1798)	13.88(1518)	15.05(1992)	14.76(1930)	19.73(1749)
19	0.4	375	15.12(2061)	15.4(1532)	20.17(1768)	17.38(1953)	13.7(1926)
20	0.5	375	25.98(2000)	26.41(2000)			
21	0.5	375	24.95(3000)	22.58(3000)	19.06(3000)	24.77(3000)	26.72(3000)
22	0.6	375	25.79(3000)	27.35(3000)	25.33(3000)	25.73(3000)	27.01(3000)

5.7 Thermal behaviour of fumaric acid:nicotinamide

The thermal behaviour of fumaric acid:nicotinamide was investigated using a Bruker AXS D5000 high-resolution X-ray powder diffractometer fitted with an Oxford cryostream and capillary stage (3.1.4) over the temperature range 100-295K. The variable temperature data also confirms that there was no phase transformations over the temperature range investigated (100-295 K). As described in section 4.7, lattice parameters from the single crystal study were used as a starting point for the LeBail fit based on the data collected at 295 K. Figure 5.13, illustrates the movement in scattering angle of diffraction peaks as the temperature is varied; as the temperature increases, the lattice parameters increase and the peak shifts to a lower 2θ value.

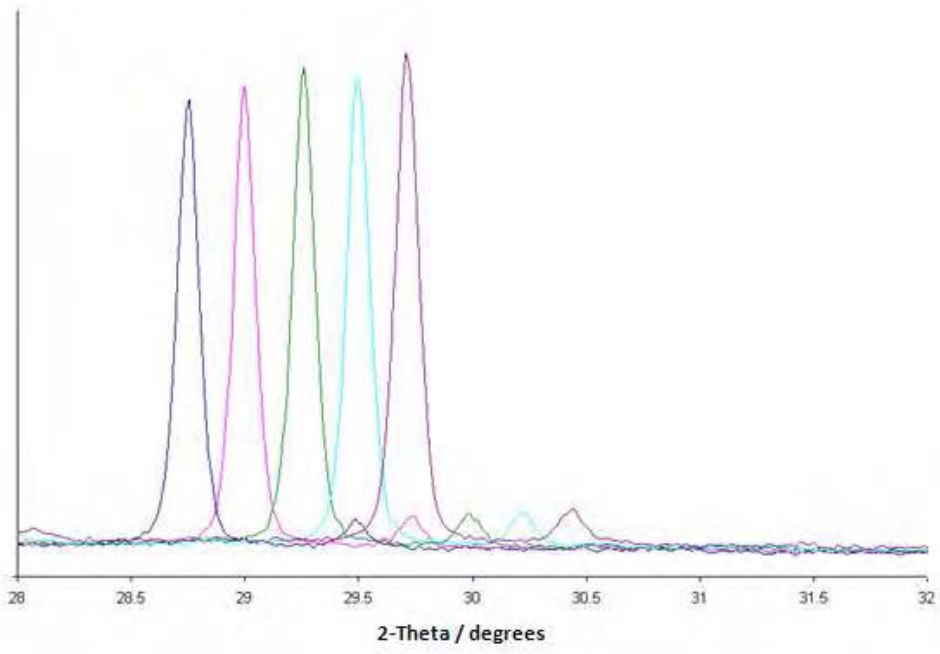

Figure 5.13: X-Ray powder diffraction peak of fumaric acid:nicotinamide over the temperature range investigated, 295 K (blue), 250 K (pink), 200 K (green), 150 K (sky blue) and 100 K (purple).

The lattice parameters from these LeBail fits are given in Table 5.4 and plotted in figure 5.14. It is clear from these that, the general trend in all lattice parameters is that of expansion. The ΔL/L0 values quoted in table 5.4 indicate the fractional change in the lattice parameter, (as in section 4.7).

Table 5.4: Lattice parameters from the LeBail fitting of fumaric acid:nicotinamide. ΔL/L0 values are given in square brackets.

Temperature (K)	a (Å)	b (Å)	c (Å)	β˚	Volume (Å^3)	% R_{wp}	χ^2
100	14.027(5) *[0.00]*	13.740(9) *[0.00]*	5.507(3) *[0.00]*	91.90(4) *[0.00]*	1060.0(1) *[0.00]*	6.218	8.106
150	14.103(4) *[0.0054]*	13.758(6) [0.0013]	5.526(2) *[0.0034]*	92.172(2) *[0.0030]*	1071.45(9) *[0.0100]*	9.63	7.199
200	14.190(2) *[0.0116]*	13.771(3) *[0.0023]*	5.5334(12) *[0.0048]*	92.663(1) *[0.0083]*	1080.1(5) *[0.0180]*	6.3	3.292
250	14.282(3) *[0.0182]*	13.793(3) *[0.0039]*	5.545(2) *[0.0073]*	93.14(2) *[0.0134]*	1090.8(7) *[0.0283]*	5.82	2.664
295	14.378(2) *[0.0250]*	13.802(3) *[0.0045]*	5.5641(12) *[0.0103]*	93.50(1) *[0.0175]*	1102.1(5) *[0.0389]*	6.16	2.676

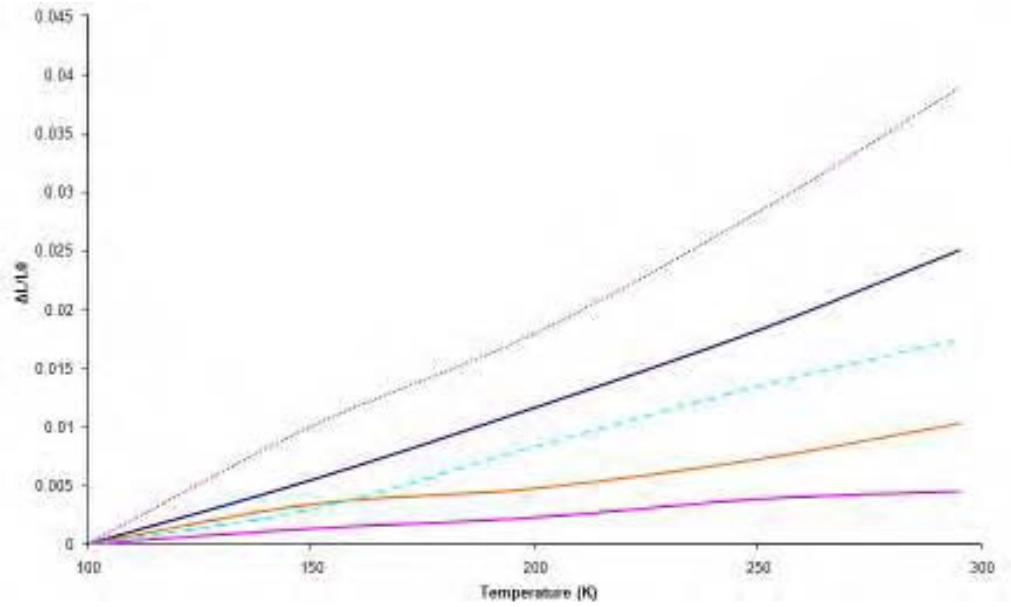

Figure 5.14: The fractional variation of lattice parameters obtained from LeBail refinement, plotted against temperature; Unit cell volume (purple spots), a (blue line), b (pink line), c (orange line) and β (sky blue dashed line).

As previously mentioned (section 4.7), lattice parameters obtained from structureless pattern decomposition methods such as the LeBail method can be potentially problematic; consequently a series of Rietveld refinements were also performed on each data set (Table 5.5 and figure 5.15). Lattice parameters acquired via Rietveld refinement should, however, also be viewed with caution as the refinement is now model biased, and unlike a LeBail fit, the position and intensity of the reflection is no longer independent of atom type and position.

Table 5.5: Rietveld lattice parameters of fumaric acid:nicotinamide

Temperature (K)	a (Å)	b (Å)	c (Å)	β°	Volume (Å^3)	% R_{wp}	χ^2
100	14.036(6) *[0.00]*	13.752(7) *[0.00]*	5.512(4) *[0.00]*	91.87(5) *[0.00]*	1063.3(1) *[0.00]*	8.82	8.384
150	14.112(4) *[0.0054]*	13.767(7) *[0.0011]*	5.522(2) *[0.0019]*	92.25(2) *[0.0041]*	1072.0(9) *[0.0082]*	12.74	14.38
200	14.184(4) *[0.0106]*	13.771(5) *[0.0014]*	5.529(3) *[0.0031]*	92.72(4) *[0.0093]*	1078.7(9) *[0.0145]*	7.55	7.297
250	14.281(4) *[0.0175]*	13.793(5) *[0.0030]*	5.546(2) *[0.0062]*	93.14(3) *[0.0139]*	1090.7(1) *[0.0258]*	7.01	4.998
295	14.380(3) *[0.0245]*	13.809(4) *[0.0042]*	5.565(2) *[0.0097]*	93.52(3) *[0.0180]*	1103.0(8) *[0.0374]*	6.54	3.133

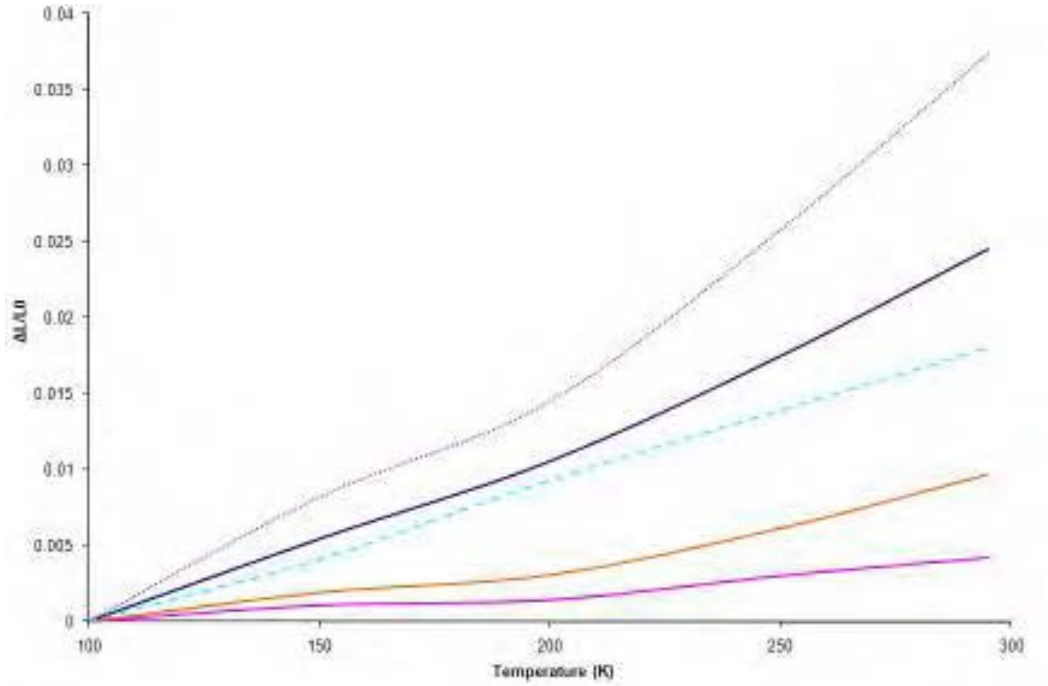

Figure 5.15: The fractional variation of lattice parameters obtained from Rietveld refinement, plotted against temperature. Unit cell volume (purple dashes), *a* (blue), *b* (pink), *c* (orange) and β (sky blue dashes).

Table 5.6 contains the linear thermal expansion co-efficients along the principal crystallographic axis of the monoclinic system, (this is calculated using equation 4.1 in section 4.7.

Table 5.6: Linear thermal expansion co-efficients of the lattice parameters of fumaric acid:nicotinamide.

Lattice parameter	Linear thermal expansion co-efficient (K^{-1})
a	1.2583×10^{-4}
b	2.1372×10^{-5}
c	4.9772×10^{-5}
Beta	9.2216×10^{-5}
Unit cell volume	1.9171×10^{-4}

As evident from figure 5.15, all the parameters increase with temperature. As presented in section 5.4, the structure contains hydrogen bonded sheets that run in the (101) plane. This direction corresponds to the smallest amount of thermal expansion. The N7 via H7B to O12 (2+x, 0.5-y, 0.5+Z) runs parallel to the *b* axis. The infinitely hydrogen bonded sheet dissects both the *a* and *c* axes, the [011] direction is the most thermally liable of the crystallographic axes suggesting thermal expansion in this direction is less sterically hindered than the [110].

5.8 Cocrystallisation of maleic acid:nicotinamide

Maleic acid (*cis*-butenedioic acid), as shown in figure 5.1 (ii), is one of two isomeric unsaturated carboxylic acids, the other being fumaric acid (figure 5.1), studied as cocrystal formers in this project. The isomerisation of maleic acid to fumaric acid occurs in the melting point range 130-140 °C but below 230 °C, at which fumaric acid is dehydrated to make maleic anhydride[13]. Isomerisation can also occur with the aid of a photochemical reaction[14]. The maleic acid ion (maleate) has medicinal properties; VASOTEC (Enalapril Maleate) is a maleate salt of analapril, the ethyl ester of enaloprlat, a long-acting angiotension converting enzyme inhibitor which lowers blood pressure.[15] Maleic acid was reported as monomorphic for nearly 124 years after the initial X-ray data were collected in 1881[16] and followed by additional determinations of the crystal structure[17, 18]. A second crystalline structure was discovered[19] after a co-crystal of caffeine and maleic acid (2:1) was dissolved in chloroform, inducing a polymorphic transition in maleic acid generating form II. The ability of maleic acid to form more than one crystalline form implies that it would make a good co-crystallising agent[20]. The structural flexibility possessed by the maleic acid molecule advocates that the molecule is not locked into an energetically single conformation.

In the remainder of this chapter, attempts to perform the co-crystallisation of maleic acid with nicotinamide (section 5.8) via a number of solid state synthetic routes will be discussed.

5.9 Characterisation of maleic acid:nicotinamide

Suitable crystals for single crystal diffraction were grown by solvent mediated recrystallisation (section 3.6.1) and full structural characterisation was carried out by single crystal diffraction.

Pxrd was used to confirm that crystallisation produced two new crystalline phases, (figure 5.16). These two phases will be labelled as product A and product B. The products are sensitive to the solvent selected for crystallisation. Product A was crystallised from a 1:1 starting ratio of maleic acid and nicotinamide in ethanol, and product B was recrystallised from a 1:1 ratio of starting materials but in methanol, (see section 3.6.1 and 3.6.5). The stoichiometric ratio of the two starting materials in both products A and B was confirmed by ^{1}H NMR (section 3.6.2 and 3.6.6).

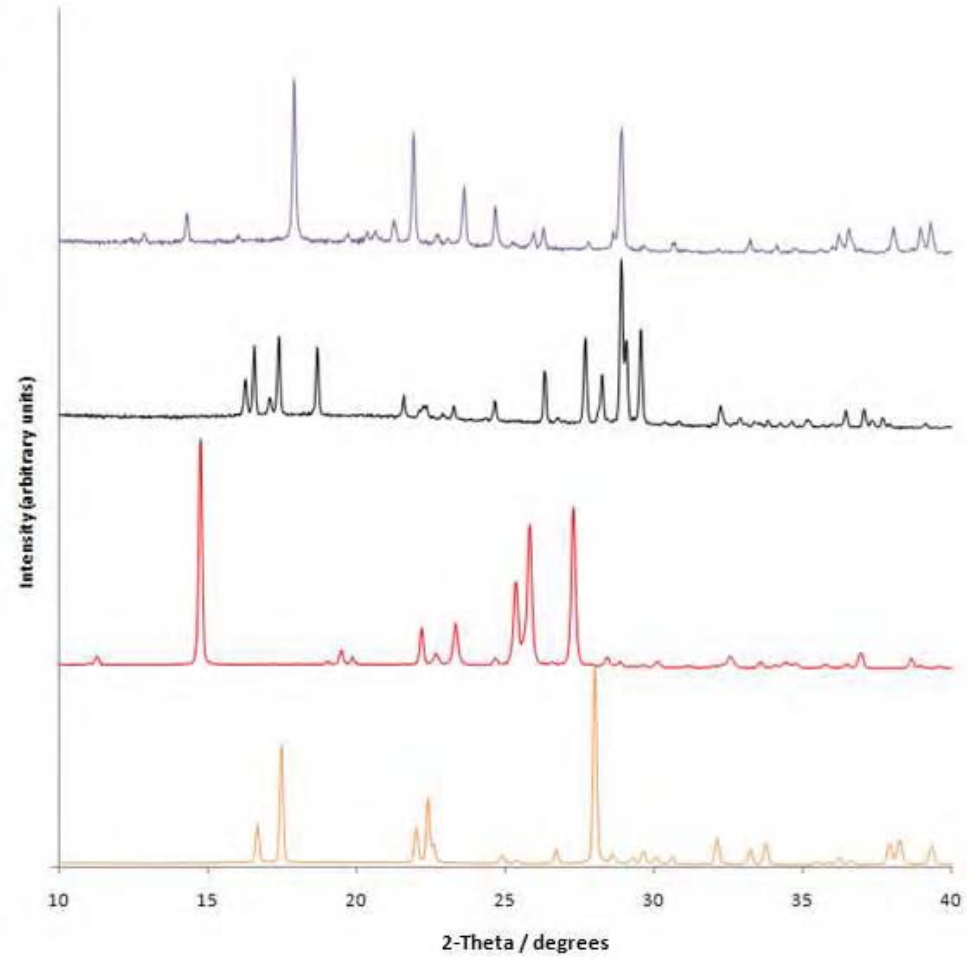

Figure 5.16: Powder X-ray diffraction patterns of the starting materials, maleic acid (orange) and nicotinamide (red), the maleic acid:nicotinamide multi-component material product A (black) and product B (purple)

Product B was subjected to prolonged thermal exposure by heating to 100 ˚C for one week to ensure that product B was not a solvate of product A**.** This exposure to elevated temperature turned the crystallites from yellow to red but did not change the crystalline phase.

Further characterisation of the new multi-component crystalline phase A was undertaken by solid state infra-red spectroscopy which confirmed the presence of a new phase when compared to the spectrum of a mix of the two starting materials, alluding to the synthesis of a

new multi-component crystal with different hydrogen-bonding characteristics to that of the component mixture, (figure 5.17). The presence of two broad peaks at 2501 cm^{-1} and 1896 cm^{-1}, is characteristic of an acid----N heterocyclic hydrogen bond, and is viewed as evidence for multi-component formation[4].

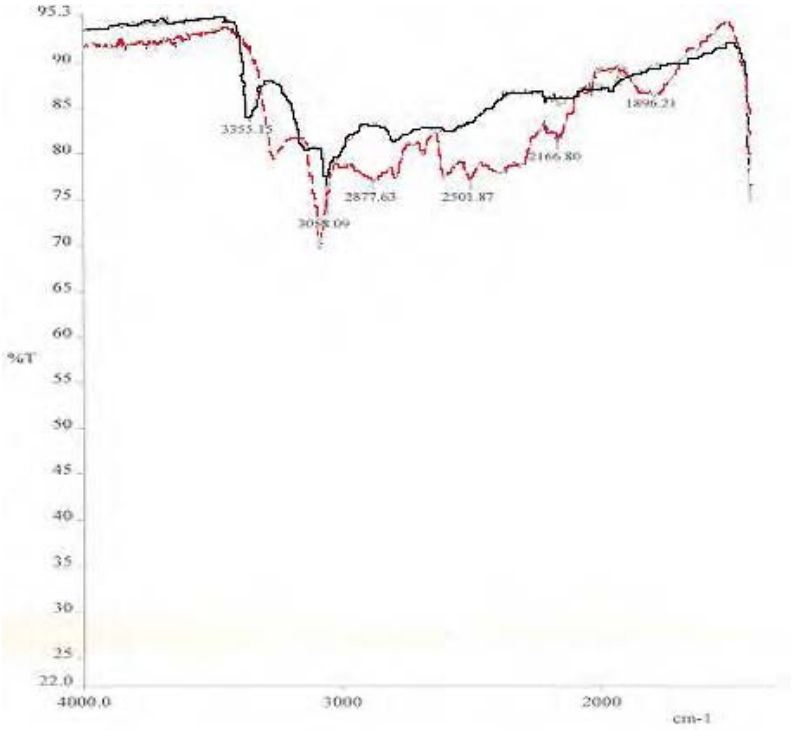

Figure 5.17: Solid state IR spectra of maleic acid and nicotinamide mix (black line) and the new multi-component crystal product A (red line).

The diffraction pattern of maleic acid:nicotinamide product B was compared to that of fumaric acid:nicotinamide, (as illustrated in figure 5.17). This comparison and the subsequent single crystal structure determination indicated the occurrence of an unexpected isomerisation reaction; the transformation of the maleic acid molecule from a *cis* to a *trans* conformation during the cocrystallisation process. As mentioned previously, the isomerisation of maleic

acid to fumaric acid is normally induced by either by thermal or via photochemical routes. The isomerisation of maleic acid to fumaric acid through co-crystallisation has been reported in the literature only once[21], where it is suggested that a highly polar solvent such as DMF, is the driving force behind the mechanism of the isomerisation. In this work, the isomerisation only occurs in methanol and not ethanol, even though both solvents share many physical properties including both being polar protic solvents. A proposed mechanism for the isomerisation is postulated below in figure 5.18.

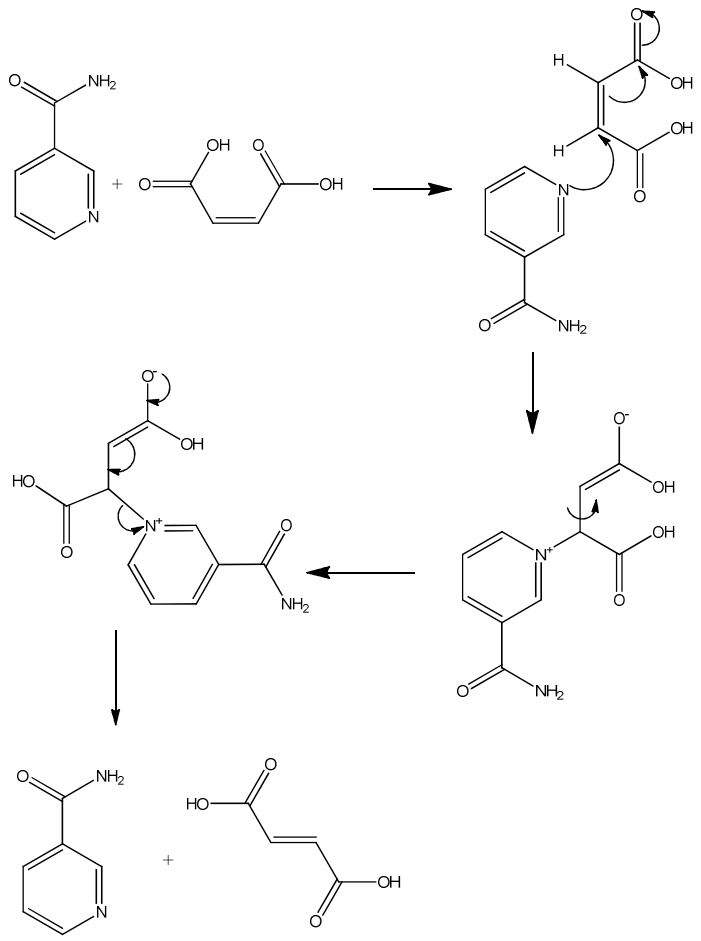

Figure 5.18: Proposed mechanism for the isomerisation of maleic acid when cocrystallised with nicotinamide

When cocrystallised from methanol, as explained in section 3.6.5, product A crystallises first (maleic acid: nicotinamide); product A then re-dissolves in the solvent and recrystallises as product B (fumaric acid:nicotinamide). Both products A and B were isolated when crystallising in methanol, the diffraction patterns of these isolated products are shown in figure 5.19.

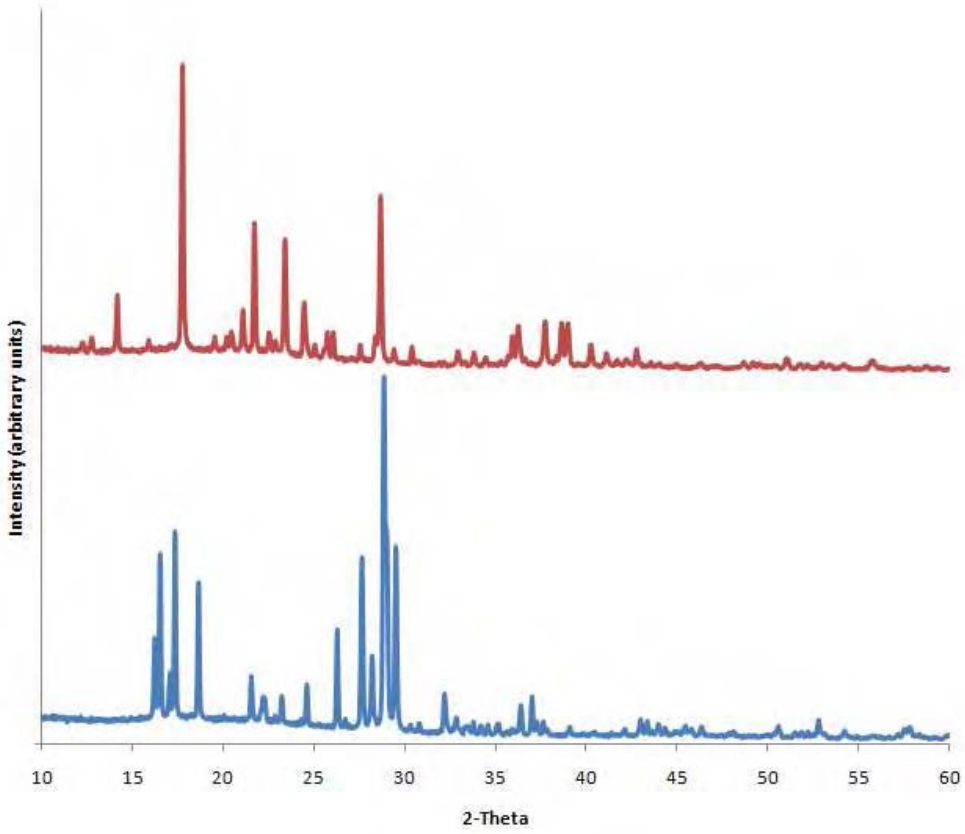

Figure 5.19: The powder X-ray diffraction patterns of product A (blue) and product B (red)

The result of this isomerisation is a conversion from a salt to a cocrystalline product. The pxrd patterns of fumaric acid:nicotinamide and maleic acid:nicotinamide product B are shown in figure 5.20.

Ostwald's rule[22, 23] states that a thermodynamically unstable phase may appear first, with more stable forms recrystallising subsequently. Unfortunately, this rule cannot be applied to a system such as considered here as it contains two chemically distinct species.

Deleted:

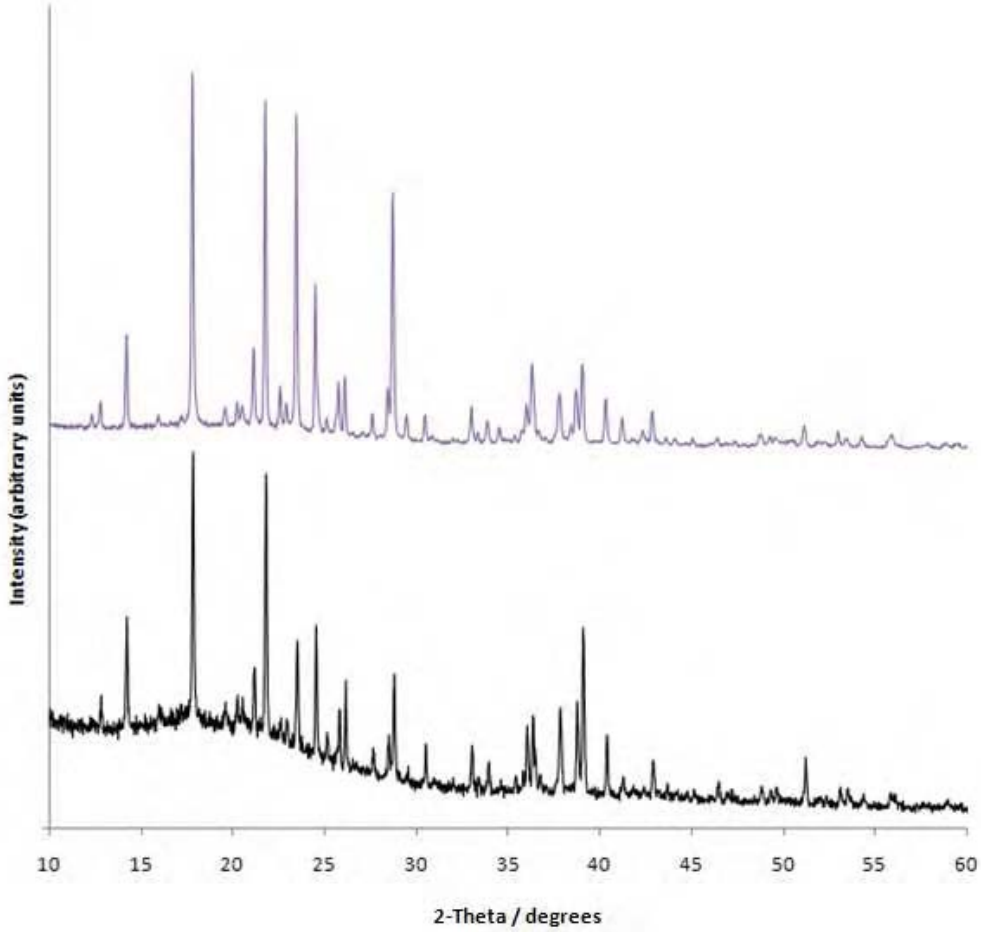

Figure 5.20: The powder X-ray diffraction patterns of fumaric acid:nicotinamide (black) and maleic acid:nicotinamide product B (purple).

A mechanochemical screen was conducted alongside a sonic slurry approach with only product A being accessible via the reduced solvent co-crystal synthetic routes, (see figure 5.21). The diffraction patterns indicate again that the mechanochemical approach creates crystallites which are lower in quality as the diffraction peaks are broader and of less relative intensity to that of sonic approaches to co-crystal production.

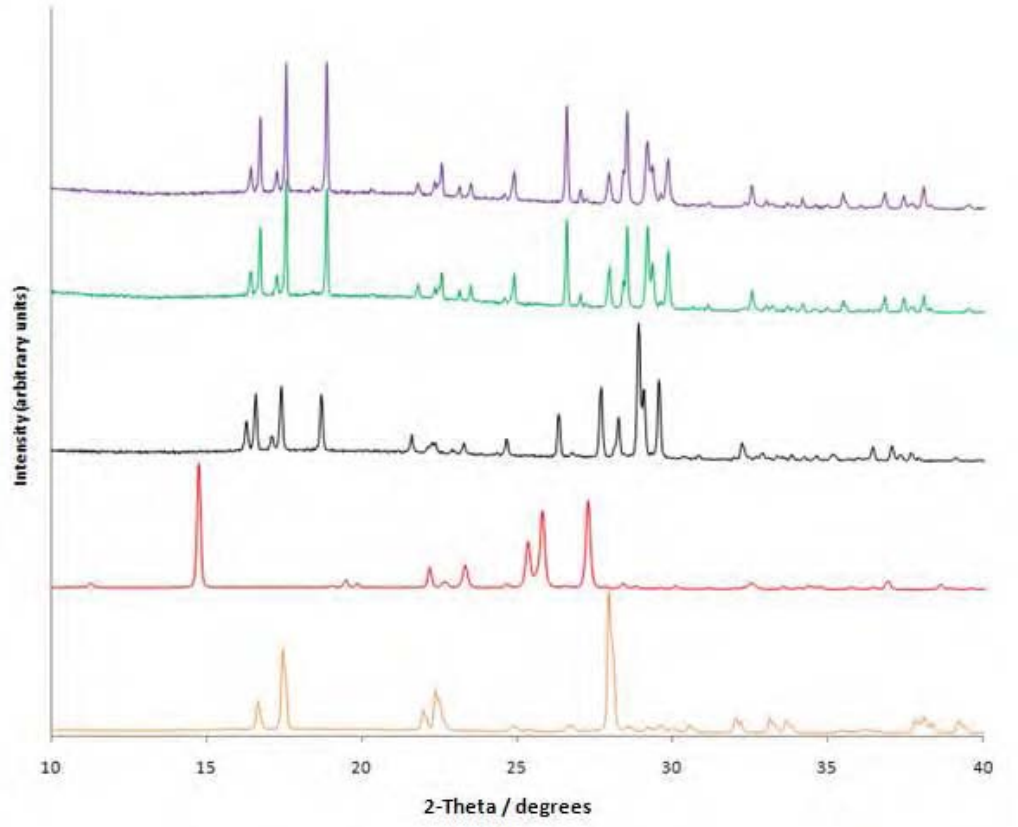

Figure 5.21: Powder X-ray diffraction patterns of the starting materials, maleic acid (orange), nicotinamide (red). The maleic acid:nicotinamide multi-component material product A from solvent mediated crystallisation (balck), sonic slurry (green) and mechanochemical grinding (purple).

5.10 Structure solution of maleic acid:nicotinamide (product A)

The X-ray powder diffraction data set used for structural analysis was collected over a period of 8 hours and the range of $10^{\circ} \leq 2\theta \leq 60^{\circ}$. The data were indexed on the basis of the first 20 observable reflections using the indexing program CRYSFIRE[6] (appendix Q) and the Pbca space group assigned by consideration of systematic absences. The profile parameters were refined using the whole-profile-fitting LeBail[7] method in the GSAS[8] program to improve the fit of the lattice, zero point and profile parameters. Structure solution was carried out using the DE technique (section 1.7.5) as implemented is the program POSSUM[9].

From density considerations it was concluded that the asymmetric unit contained one maleic acid and one nicotinamide molecule, hence the structural model used in the DE calculation comprised both molecules, constructed using standard bond lengths[10] and angles, but excluding the hydroxyl and amine hydrogen atoms. The nicotinamide molecule is defined by 7 DE elements and the maleic acid molecule by 8 DE elements: for each molecule 3 parameters (θ,Φ,Ψ) were used to define the orientation within the unit cell (bounds 0 - 360˚), 3 parameters (*x,y,z*) were used to define the position of the molecule (bounds 0-1). Nicotinamide contains one unconstrained torsion angles (0-360˚) and maleic acid contains 2 unconstrained torsion angle (0-360˚) to define the conformation of each molecule, (figure 5.22). The molecules were moved independently in the structure solution resulting in a 15 parameter problem.

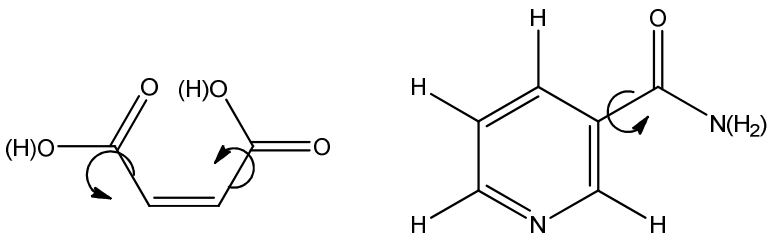

Figure 5.22: Molecular structures used in the DE structure solution, torsion angles are indicated by arrows. Excluded hydrogen atoms are shown in brackets.

Initial DE solutions were unsuccessful in locating the global minimum (a successful structure solution), with the best DE solution having R_{wp} of 29.94 %, (Lebail R_{wp}= 6.60 %). In isolation to the powder DE calculation, a single crystal diffraction data set was obtained and the structure solution obtained from this. The resulting single crystal structure was refined against the powder data, showing a discrepancy in peak intensities between the calculated and experimental diffraction patterns, implying a severe case of preferred orientation in the powder data. The preferred orientation fraction was refined using the March-Dollase correction, in the direction giving a significant 001 ratio of 1.64575. A correction for preferred orientation is not refined during the DE calculation, so that the overall efficiency of the calculation is maintained. Subsequent DE calculations with this parameter used to describe the preferred orientation, gave a better solution, with a best R_{wp} of 16.43 % (figures 5.23 and 5.24).

Figure 5.23: Maleic acid molecule from maleic acid:nicotinamide. The red molecule represents single crystal positions and the blue molecule from the DE solution 16.43. (non-hydrogen atoms only)

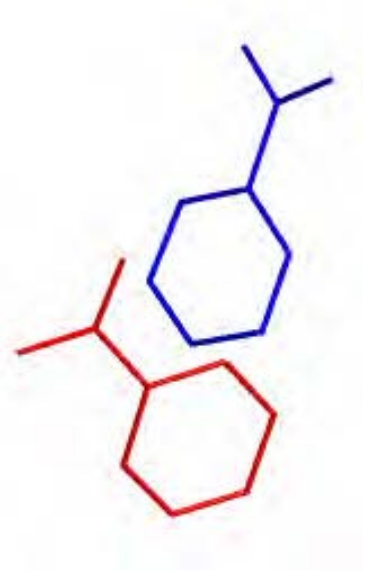

Figure 5.24: Nicotinamide molecule from maleic acid:nicotinamide. The red molecule represents single crystal positions and the blue molecule from the DE solution 16.43. (non-hydrogen atoms only)

The subsequent analysis confirmed that the crystal packing obtained by powder methods was incorrect; minimum, maximum and mean distances between pairs of corresponding atoms in the single and refined powder structures was calculated at 2.7208, 6.2564 and 3.932 Å respectively. The initial lattice parameters, DE structure solution parameters and single crystal determination details are shown in table 5.7

Table 5.7: Initial lattice parameters, DE structure solution parameters and single crystal determination.

Compound	*maleic acid:nicotinamide product A*
Crystal data	
Chemical formula	$C_4H_4O_4$ + $C_6N_2H_6O$
M_r	238.2
Indexing	
Space group	Pbca
Initial a / Å	6.4374(1)
Initial b / Å	10.8654(1)
Initial c / Å	29.1677(2)
Initial V / Å ^{3}	2040.138(2)
Structure solution	
LeBail R_{wp} / %	6.60
LeBail R_p / %	5.24
LeBail χ^2	1.431
DE elements	
K	0.99
F	0.4
N_p	330
Average R_{wp} / %	16.43
Best R_{wp} / %	16.43
Preferred orientation fraction [and direction]	1.64575 [001]
No of parameters	15
No. of restraints	62
Single Crystal values	
a / Å	6.3710(2)
b / Å	10.8535(3)
c / Å	29.1693(8)
β / °	92.54(1)
V / Å ^{3}	2016.99
Space group	Pbca

5.11 Efficiency of the DE algorithm

The DE calculation for maleic acid:nicotinamide was unsuccessful, as discussed in section 5.10. Values of *F* and N_p were chosen for variation between limits chosen from previous DE studies[12] and *K* was fixed throughout at 0.99. For each combination of parameters, five epochs were calculated. Table 5.8, illustrates the impact of preferred orientation upon the algorithms progress.

Table 5.8: The results from a number of DE calculations with variation in F (mutation rate) and NP (population size). For each epoch the final R_{wp} (in %) is given and figures within brackets indicate at which generation convergence was achieved. Runs that have not converged by the maximum allowed number of generations are shaded grey. Runs 6-9 the preferred orientation was set to 1.64575 in the [001] direction.

Run	F	NP	epoch 1	epoch 2	epoch 3	epoch 4	epoch 5
1	0.5	300	38.96(2000)	38.66(2000)	/	/	/
2	0.5	150	30.78(3000)	39.37(3000)	/	/	/
3	0.5	210	39.71(4000)	37.78(2662)	30.37(3832)	30.81(3573)	29.94(2199)
4	0.4	210	32.39(1758)	31.00(2200)	33.68(1741)	31.6(2484)	31.4(2989)
5	0.5	300	31.06(3690)	32.1(2726)	38.38(4000)	/	/
6	0.4	300	25.8(2689)	25.29(3016)	/	/	/
7	0.3	280	23.49(551)	20.93(221)	19.52(153)	17.3(114)	17.15(142)
8	0.4	280	20.1(1846)	16.43(1650)	16.44(1680)	16.44(1753)	16.45(1855)
9	0.5	280	19.25(3577)	19.28(2554)	19.50(3600)	19.25(3590)	19.25(1842)

5.12 Maleate acid:nicotinamide (product A) structure

The following crystal structure description is based on the single crystal data collected on Bruker SMART 6000 diffractometer ($\lambda_{Cu\text{-}K\alpha}$ = 1.54178 Å) at 200 K. Further details on the single crystal structure solution can be found in appendix R. An incubator was used to grow a single crystal of suitable quality and size to warrant a single crystal diffraction experiment, as (see section 3.6.4). The crystalline structure is a disordered material, with 50% occupancy of the disordered hydrogen across both the H8 site and H11 site. The single crystal structure also

confirms the migration of a proton from one carboxyl site on the maleic acid moiety onto the heterocyclic nitrogen of the nicotinamide moiety giving a salt. The ORTEP diagram showing the atom labelling and hydrogen atom positions is shown in figure 5.25.

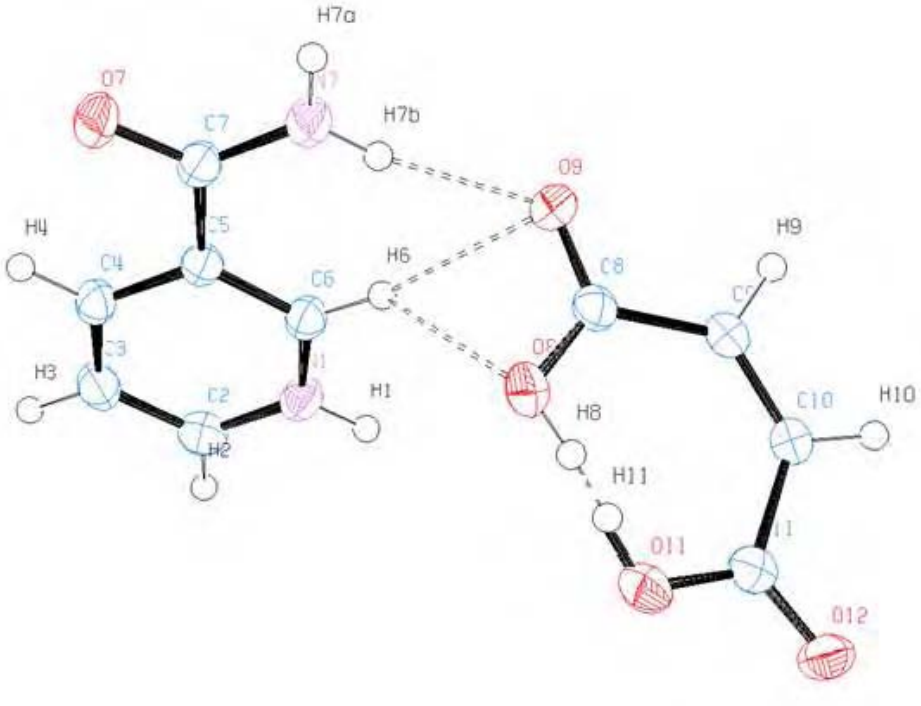

Figure 5.25: The molecular structure of maleate:nicotinamide, showing the atom numbering and the hard and soft intermolecular hydrogen bonds within the asymmetric unit (dashed lines). Displacement ellipsoids are drawn at the 50 % probability level and H atoms are shown as small spheres of arbitrary radii.

The supramolecular structure of maleate:nicotinamide is determined through three intermolecular hydrogen bonds and one intramolecular hydrogen bonds; three strong N-H….O hydrogen bonds (two N-H....O and one N^{+}-H....O^{-}), and one disordered O-H….O hydrogen bonds, all details are shown in table 5.9. All strong hydrogen-bond donors and acceptors are used in the hydrogen bond network. The conformation of the amide group in

the nicotinamide group is approximately planar, with a torsion angle of C4-C5-C7-N7 of 175.9(3)°. A complementary hydrogen bond is donated by N7 via H7A to the acceptor O7 (1-x,-y,-z) resulting in an $R_2^2(8)$ nicotinamide dimer. N7 donates a second hydrogen bond via H7B to the maleic acid O9. N1 also donates a hydrogen bond via H1 to O12 (1+x,y,z), as shown in figure 5.26.

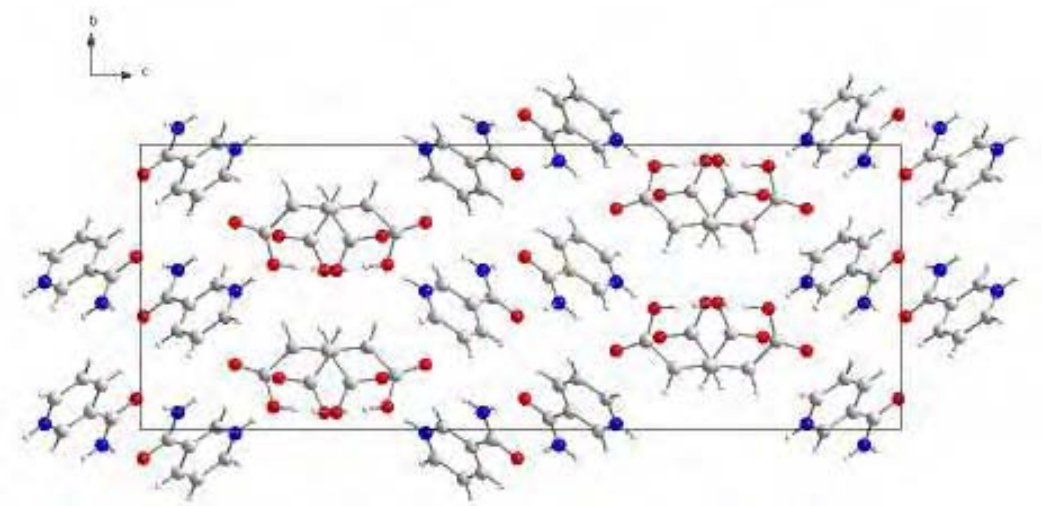

Figure 5.26: Packing of maleate ions and nicotinamide molecules, viewed along the *a* axis. (Unit cell shown)

The combination of these hydrogen bonds forms an infinitely hydrogen bonded sheet running in the [001], within the sheet dimers of nicotinamide molecules are linked via maleic acid molecules, as shown in figure 5.27.

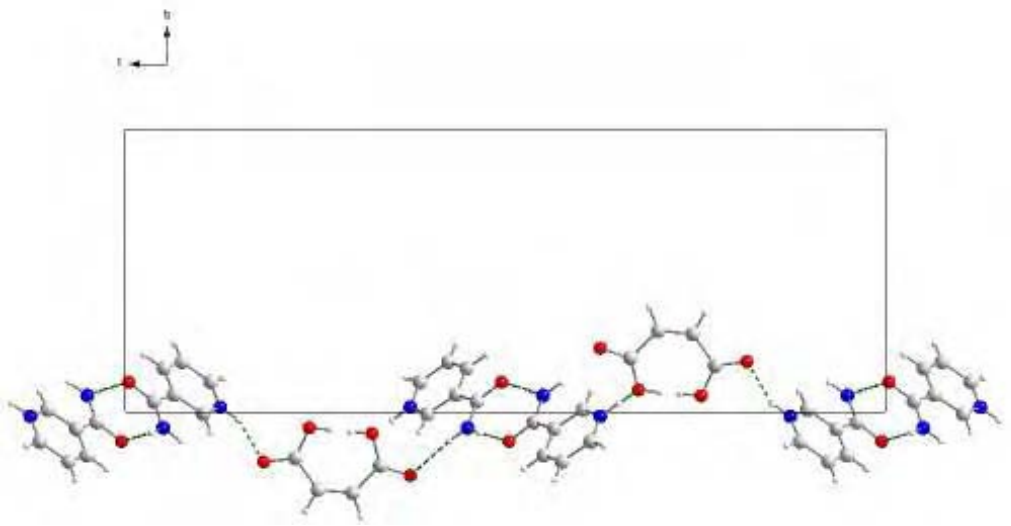

Figure 5.27: A Hydrogen bonding network running in maleate:nicotinamide.

Table 5.9: Hydrogen bonds geometry in maleic acid:nicotinamide (Å and °).

Donor-----H… Acceptor	d(D-H)	d(H….A)	d(D…A)	<(DHA)
N(1)—H(1)…O(12)#1	0.8800(1)	1.9300(1)	2.6953(16)	144.9
N(7)—H(7A)…O(7)#2	0.8800(1)	2.1200(1)	2.9976(17)	176.8
N(7)—H(7B)…O(9)	0.8800(1)	2.0100(1)	2.8692(16)	165.7
O(8)—H(8)…O(11)*	0.8400(2)	1.6000(1)	2.4288(15)	167.6
O(11)-H(11)….O(8)*	0.8400(1)	1.6000(2)	2.4288(15)	170.4

Symmetry transformations used to generate equivalent atoms: (#1) *x*+1/2,*y*,-*z*+1/2 (#2) -*x*,-*y*,-*z*. * denotes hydrogen bonds on disordered hydrogen positions.

5.13 Thermal behaviour of maleate:nicotinamide (product A)

The thermal behaviour of maleate:nicotinamide was probed by collecting a series of powder diffraction data sets collected over the range 100-295 K, using the Bruker AXS D5000 high-resolution X-ray powder diffractometer fitted with Oxford Cryostream and capillary stage (section 3.1.4). Lattice parameters derived from the single crystal experiment were used as a

starting point for a LeBail fit, starting with the data collected at 295 K. As a stable refinement was achieved, the resultant lattice parameters were used as a starting point for the subsequent fitting of the next data set at 250 K. The process was repeated until the fitting of the final data set at 100 K. There was no evidence of a phase change over the temperature range investigated. Figure 5.28 illustrates the shift of the diffraction peaks to a lower 2-theta with increasing temperature.

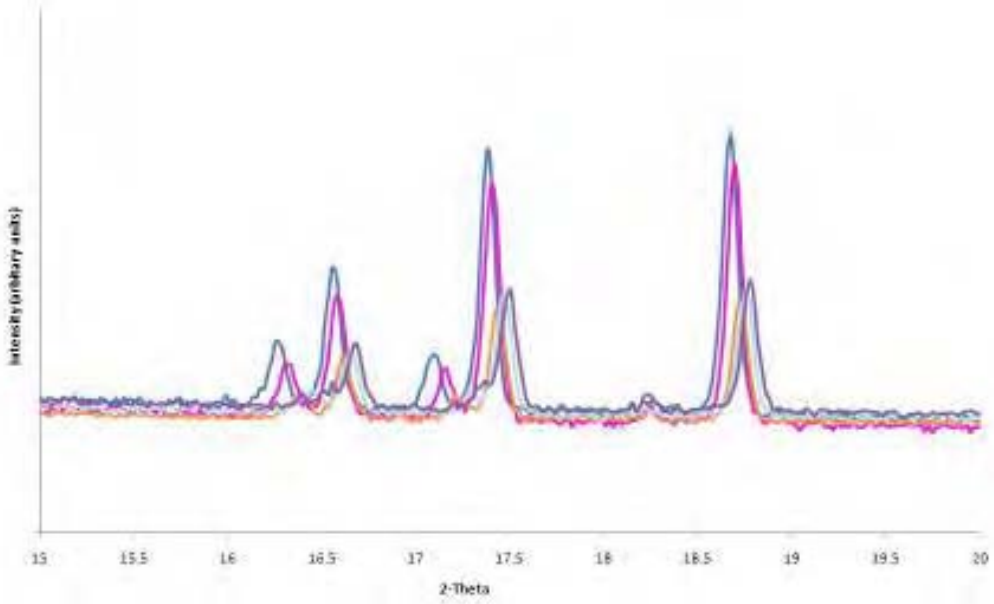

Figure 5.28 X-ray powder diffraction peaks of maleate:nicotinamide over the temperature range investigated, 295 K (blue), 250 K (pink), 200 K (green), 150 K (sky blue) and 100 K (purple).

The lattice parameters from these LeBail fits are given in Table 5.8, and plotted in figure 5.29. It is clear from these that, the general trend is that of expansion. The ΔL/L0 values quoted in Table 5.10, indicate the fractional change in the lattice parameter (section 4.7).

Table 5.10: Lattice parameters from the LeBail fitting of maleate:nicotinamide product A. ΔL/L0 are given in square brackets

Temperature (K)	a (Å)	b (Å)	c (Å)	Volume (Å^3)	R_{wp}	χ2
100	6.308(1) *[0.00]*	10.678(3) *[0.00]*	28.927(6) *[0.00]*	1948.5(1) *[0.00]*	10.75	8.956
150	6.354(1) *[0.0073]*	10.739(3) *[0.0057]*	28.983(5) *[0.0019]*	1977.7(1) *[0.0150]*	10.53	7.910
200	6.398(1) *[0.0142]*	10.817(2) *[0.0130]*	29.066(5) *[0.0048]*	2011.4(9) *[0.0323]*	11.34	6.99
250	6.4076(2) *[0.0158]*	10.859(1) *[0.0169]*	29.154(2) *[0.0078]*	2028.5(4) *[0.0411]*	4.21	2.486
295	6.4412(6) *[0.0211]*	10.873(2) *[0.0183]*	29.157(3) *[0.0080]*	2042.1(6) *[0.0481*]	4.76	3.839

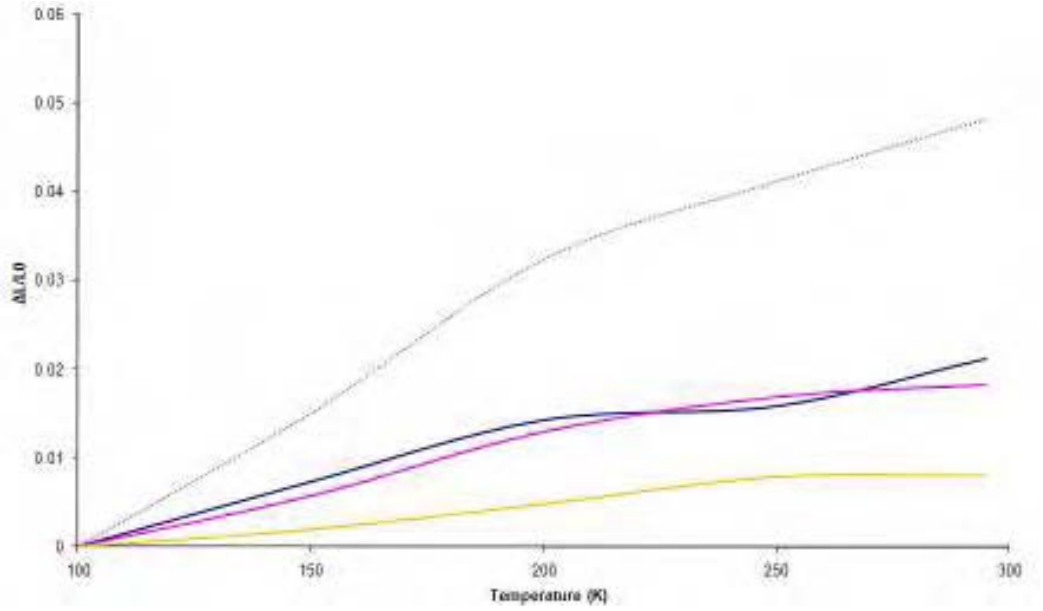

Figure 5.29: The fractional variation of lattice parameters obtained from the LeBail refinement against temperature, Unit cell volume (purple spots), *a* (blue line), *b (*pink line)*, c* (orange line).

In order to address the problems as previously discussed with the calculation of lattice parameters from LeBail pattern decomposition, Rietveld analysis was performed on each set, with subsequent lattice parameters acting as a starting point for the next data set (table 5.11 and figure 5.30).

Table 5.11: Lattice parameters from the Rietveld fitting of maleate:nicotinamide product A. ΔL/L0 are given in square brackets

Temperature (K)	a (Å)	b (Å)	c (Å)	Volume (Å^3)	R_{wp}	χ2
100	6.3127(8) *[0.00]*	10.796(2) *[0.00]*	29.148(4) *[0.00]*	1986.6(8) *[0.00]*	6.27	3.031
150	6.3385(8) *[0.0041]*	10.812(2) *[0.0015]*	29.143(4) *[-0.0002]*	1997.3(8) *[0.0054]*	6.47	3.2
200	6.3711(6) *[0.0093]*	10.8357(17) *[0.0036]*	29.147(3) *[-0.00003]*	2012.2(6) *[0.0129]*	6.24	2.444
250	6.4072(4) *[0.0150]*	10.858(1) *[0.0057]*	29.152(2) *[0.0001]*	2028.1(4) *[0.0209]*	4.26	2.907
295	6.442(1) *[0.0205]*	10.876(3) *[0.0074]*	29.160(5) *[0.0004]*	2043.2(1) *[0.0285]*	4.65	1.922

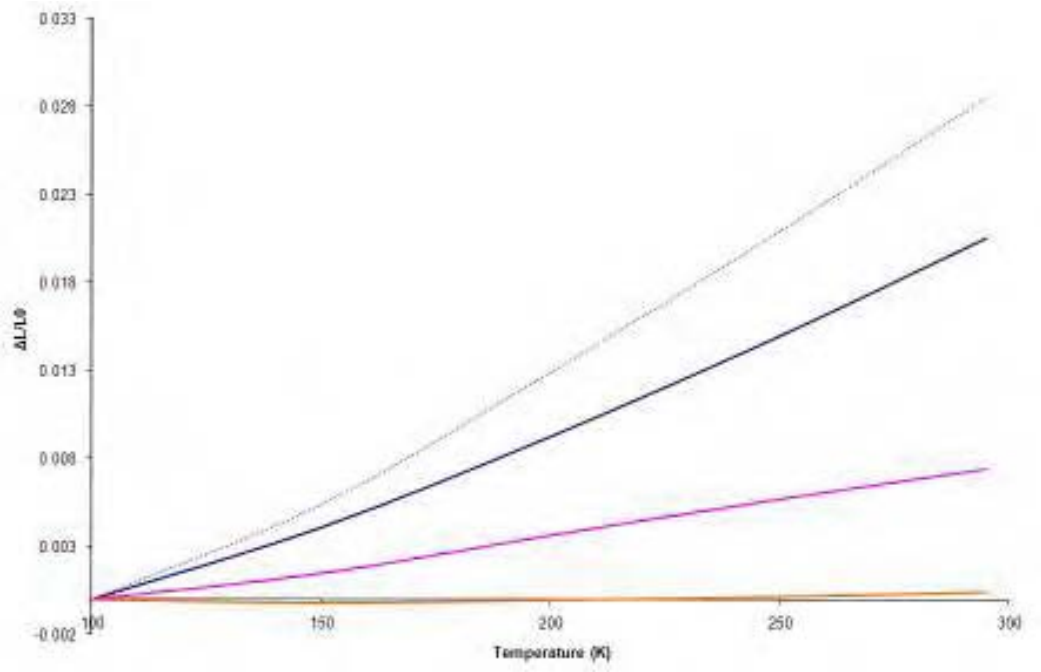

Figure 5.30: The fractional variation of lattice parameters obtained from the Rietveld refinement against temperature. Unit cell volume (purple spots), *a* (blue line), *b (*pink line)*, c* (orange line).

As evident from figure 5.30, the *c* direction corresponds to the direction of the lowest thermal expansion and correlates with the predominant hydrogen bonding network with alternating nicotinamide dimers connected via maleate moieties. The *b* direction is privy to lower energy

interactions, as π-π stacking of the nicotinamide molecules exist in the (101) plane. The *a* axis is the most thermally liable.

Thermal expansion can be described by a linear thermal expansion along its primary crystallographic axes, (using equation 4.1). Table 5.12, contains the linear thermal expansion coefficients for each lattice parameter in maleate:nicotinamide.

Table 5.12: Linear thermal expansion co-efficients of maleate:nicotinamide

	linear thermal expansion
a	1.05256×10^{-4}
b	3.80547×10^{-5}
c	2.07183×10^{-6}
volume	1.46224×10^{-4}

5.14 Cocrystallisation of maleic acid:isonicotinamide

Within this section, maleic acid (*cis*-butenedioic acid), is co-crystallised with isonicotinamide (pyridine-4-carboxamide), (figure 5.1). As well as investigating the potential comparison in cocrystallisation behaviour of nicotinamide and isonicotinamide, this study should also give valuable insight of the two crystal structures.

5.15 Characterisation of maleic acid:isonicotinamide

Pxrd was used to confirm that the product of crystallisation was a new crystalline phase, and did not contain any of the starting materials (figure 5.31).

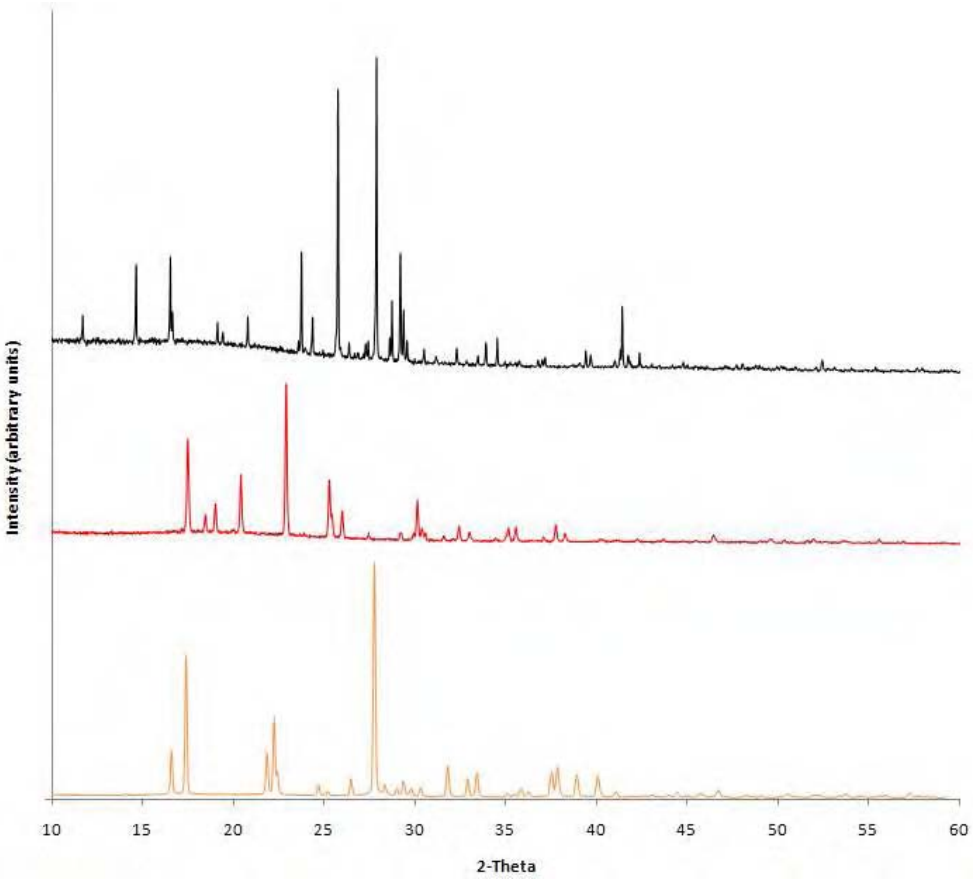

Figure 5.31: Powder X-ray diffraction patterns of the starting materials, maleic acid (orange) and isonicotinamide (red) and the maleic acid:isonicotinamide multi-component material (black).

In parallel with traditional solvent-mediated recrystallisation, pxrd was used to confirm that the same bulk crystalline phase was produced by both LAG (section 1.11.4) and sonic slurry (section 1.11.4) methods. The diffraction patterns indicate (as previously reported) that the mechanochemical approach creates crystallites which are lower in quality than that of sonic approaches to co-crystalline preparation (figure 5.32).

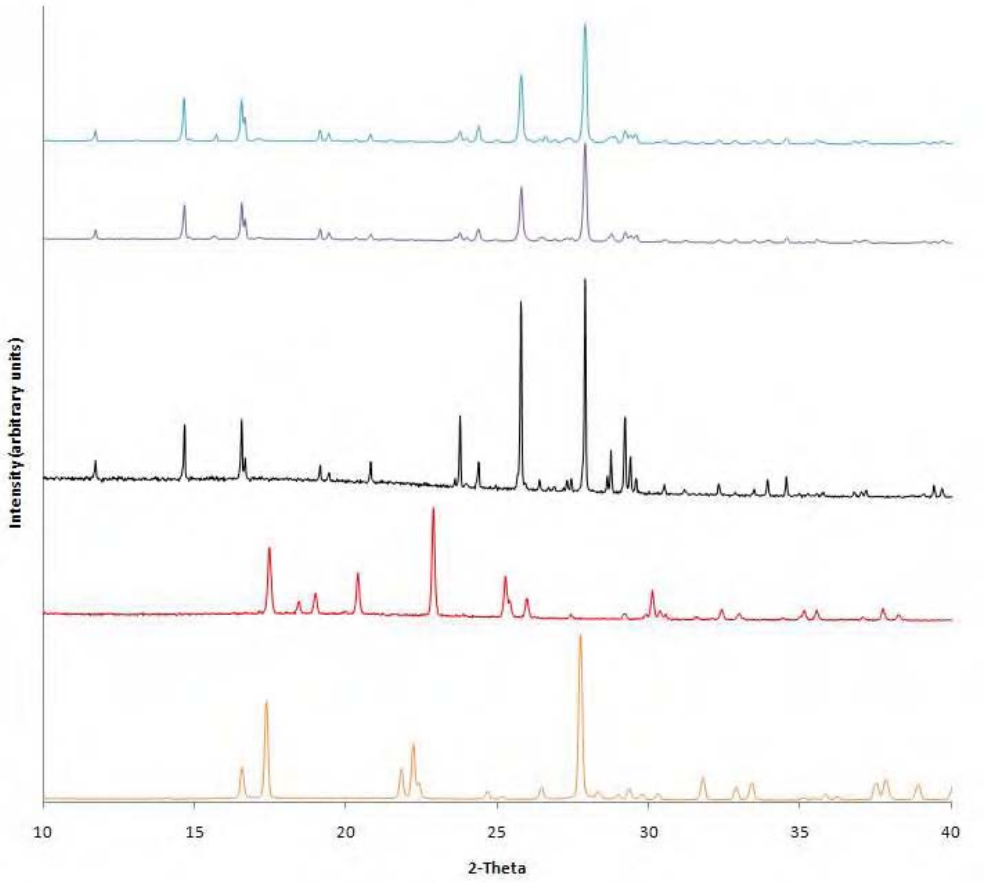

Figure 5.32: Powder X-ray diffraction patterns of the starting materials, maleic acid (orange) and isonicotinamide (red). The maleic acid:isonicotinamide solvent mediated multi-component material (black), sonic slurry (purple) and mechanochemically ground (orange).

5.16 Maleic acid:isonicotinamide structure

The following crystal structure description is based upon the single crystal data collected on a Bruker Smart 6000 diffractometer equipped with a CCD detector and a copper tube source (lattice parameter shown in table 5.13). The crystal selected for single crystal analysis was grown using an incubator (section 3.7.3), and recrystallised from ethanol to produced white

crystallites. This crystalline structure is also disordered, with 50% occupancy of a hydrogen atom across the H8 site and H11 site, in a similar way to that in maleate:nicotinamide. The single crystal structure also confirms the transfer of a proton from one carboxyl site on the maleic acid moiety to the heterocyclic nitrogen on the isonicotinamide moiety (figure 5.33) forming a salt. Further single crystal details can be found in appendix S.

Table 5.13: Single crystal parameters of maleate:isonicotinamide

Single Crystal values	
Space group	P-1
a / Å	3.7240(3)
b / Å	10.8616(10)
c / Å	13.1664(10)
α/ °	99.8200(3)
β / °	97.2700(1)
γ/ °	95.9900(1)
V / Å^3	2016.99

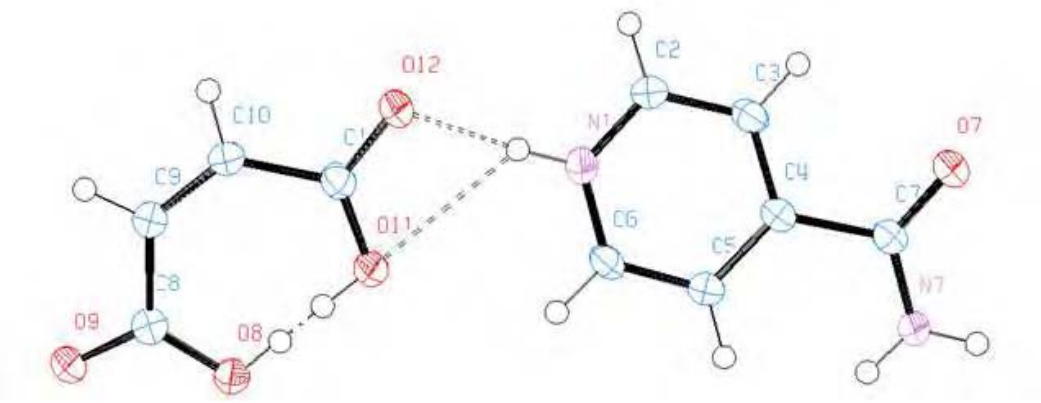

Figure 5.33: The molecular structure of maleate:isonicotinamide. Showing the atom numbering scheme and the hard intermolecular hydrogen bonds within the asymmetric unit (dashed lines). Displacement ellipsoids are drawn at the 50 % probability level and H atoms are shown as small spheres of arbitrary radii.

The supramolecular structure of maleate:isonicotinamide is determined through six intermolecular hydrogen bonds, two N(heterocyclic)$^{+}$H...O^{-} bonds, two N-H....O bonds and two O-H....O (Table 5.11). The conformation of the amide group in the isonicotinamide is approximately planar, with a torsion angle of C5-C4-C7-O7 of 164.277(20)°.

Table 5.14: Hydrogen bonds geometry in maleate:isonicotinamide (Å and °).

Donor—H---Acceptor	D—H	H---A	D----A	<(DHA)
N(1) —H(1)….O(12)	0.8800(1)	1.7400(2)	2.610(2)	170.1
N(1)---H(1).....O(11)	0.8800(1)	2.5200(1)	3.124(2)	126.6
N(7) —H(7A).....O(9)	0.8800(1)	2.0200(1)	2.890(2)	170.1
N(7) —H(7B)…O(9)	0.8800(2)	2.1000(2)	2.929(2)	157.1
O(8)—H(8)…O(11)*	0.8400(1)	1.6000(1)	2.4288(15)	167.6
O(11)-H(11)….O(8)*	0.8400(2)	1.6000(1)	2.4288(15)	170.4

. * denotes hydrogen bonds on disordered hydrogen positions.

All strong hydrogen-bond donors and acceptors are used in the hydrogen bond network. The maleate ion and the isonicotinamide ion are linked via a protonated hetrocyclic N1, donating a hydrogen bond via H1 to the carbonyl oxygen O12. The amide N7, acts as a bifurcated hydrogen bond donor, firstly to O9 via H7A and secondly to O9 via H7B (figure 5.34)

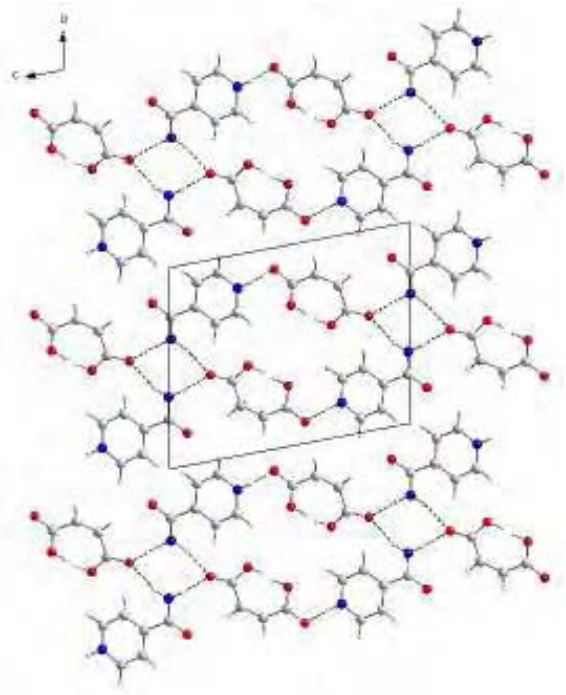

Figure 5.34: Maleate ions and isonicotinamide molecules ribbons running in the (011) plane. (Unit cell shown)

Hydrogen bonded sheets of maleate ions and isonicotinamide molecules are shown in figure 5.35.

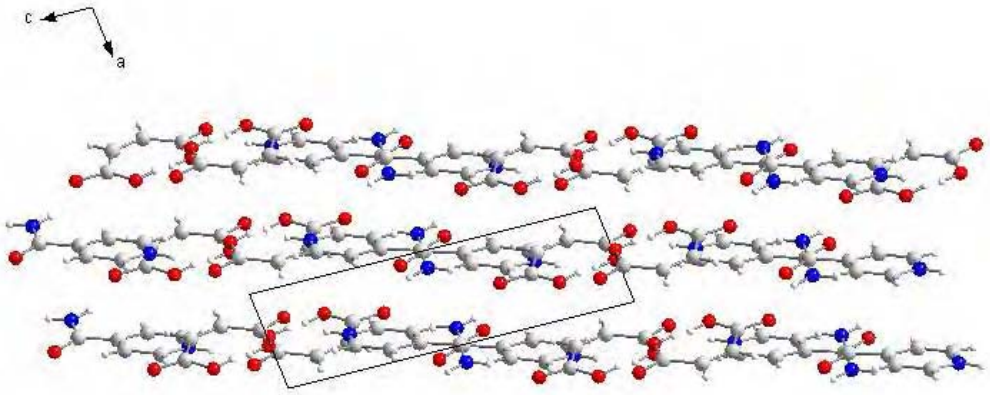

Figure 5.35: Sheets of meleate ions and isonicotinamide molecules. (Unit cell shown)

Unlike in the maleate:nicotinamide structure, the favourable amide dimer synthon is not formed. No pxrd solution was undertaken for the maleate:isonicotinamide.

5.17 Conclusions

All three structures discussed in this chapter had a Δpka between 0 and 3. As discussed in 1.11.1, in the range $0 < \Delta pKa < 3$ crystallisation can produce a salt, cocrystal or a disordered material, with the precise location of the proton highly dependent upon the packing and local steric environment. This is seen to be true, as in this chapter there are two salts (maleate:nicotinamide and maleate:isonicotinamide) and one cocrystal (fumaric acid:nicotinamide). The maleate:isonicotinamide was recrystallised from both methanol and ethanol, and unlike in the maleate:nicotinamide system the maleate ion did not undergo isomerisation when cocrystallised with isonicotinamide.

References

1. C. Gasperini, L. A. Cefaro, G. Borriello, G. Tosto, L. Prosperini and C. Pozzilli, *Expert Opinion on Emerging Drugs*, 2008, **13**, 465-477.

2. C. B. Aakeroy, A. M. Beatty and B. A. Helfrich, *J. Am. Chem. Soc.*, 2002, **124**, 14425-14432.

3. L. Orola and M. V. Veidis, *Crystengcomm*, 2009, **11**, 415-417.

4. C. B. Aakeroy, J. Desper and M. E. Fasulo, *Crystengcomm*, 2006, **8**, 586-588.

5. R. F. Evans and W. Kynaston, *Journal of the Chemical Society*, 1963, 3151-3153.

6. R. Shirley, *The Crysfire 2002 System for Automatic Powder Indexing: User's Manual, 41 Guildford Park Avenue, Guildford, Surry, GU2 7NL, England, 2002.*, 2002

7. A. Lebail, H. Duroy and J. L. Fourquet, *Materials Research Bulletin*, 1988, **23**, 447-452.

8. A. C. Larson and R. B. Von Dreele, *GSAS. General Structure Analysis System, Report No. LAUR 86-748, Los Alamos National Laboratory, Los Alamos, New Mexico, USA*, 1994.

9. C. C. Seaton and M. Tremayne, *Possum Programs for Direct-Space Strucutre Solution from Powder Diffraction Data*, 2002, School of Chemistry, University of Birmingham, UK.

10. F. H. Allen, O. Kennard, D. G. Watson, L. Brammer, A. G. Orpen and R. Taylor, *Journal of the Chemical Society-Perkin Transactions 2*, 1987, S1-S19.

11. G. M. Sheldrick, Acta Cryst, A64, 2008, pp. 112-122.

12. M. Tremayne, C. C. Seaton and C. Glidewell, *Acta Crystallographica Section B-Structural Science*, 2002, **58**, 823-834.

13. A. Ihde, *Journal of Chemistry*, 1959, **36**, 330.

14. A. J. Castro, S. R. Ellenberger and J. P. Sluka, *Journal of Chemical Education*, 1983, **60**, 521-521.

15. M. Lehr, *Drugs of the Future*, 2000, **25**, 857-858.

16. C. Bodewig, *Z. Kristallogr*, 1881, **5**, 559.

17. M. Shahat, *Acta Crystallographica* 1952, **5**, 763-768.

18. G. J. B. Williams and M. N. G. James, *Acta Crystallogr., Section B: Crystallogr. Cryst. Chem.*, 1974, **30**, 1249-1257.

19. G. M. Day, A. V. Trask, W. D. S. Motherwell and W. Jones, *Chem. Commun.*, 2006, 54-56.

20. C. B. Aakeroy, A. M. Beatty, B. A. Helfrich and M. Nieuwenhuyzen, *Crystal Growth Design*, 2003, **3**, 159-165.

21. S. Chatterjee, V. R. Pedireddi and C. N. R. Rao, *Tetrahedron Letters*, 1998, **39**, 2843-2846.

22. W. Ostwald, Physical Chemistry, Editon edn., 1897, p. 289-330.

23. T. Threlfall, *Organic Process Research & Development*, 2003, **7**, 1017-1027.

6. Polymorphism of oxamic acid

6.1. Oxamic acid

The title material under investigation in this chapter is oxamic acid (figure 6.1).

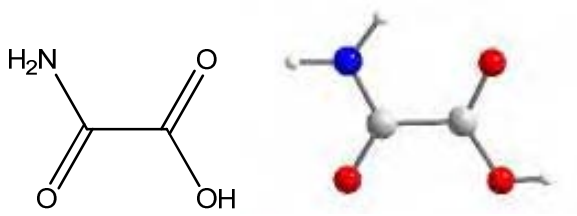

Figure 6.1: Molecular structure of oxamic acid

As previously discussed in section 4.1, oxamic acid is an important API, where it can affect the role of glycolysis in the growth of tumour cells[1]. Its acts on the tumour cell pathway of 'aerobic glycolysis' which is the conversion of glucose to lactic acid under conditions in which oxygen is readily available. For a tumour cell to survive and divide, energy must be derived from its own metabolic processes, as hypothesised by Warburg[2, 3]. Oxamic acid has a similar structure to pyruvic acid and acts as an inhibitor to the metabolic pathways of the tumour cells.

Oxamic acid contains both strong hydrogen bond acceptors, in form of the carbonyl oxygens, and donors, in the form of a hydroxyl oxygen and amide nitrogen, potentially lending itself as a useful building block in the design of hydrogen-bonded supramolecular architectures. The potential variation in intermolecular hydrogen-bonding network can lend itself to a wide range of packing motifs and therefore in theory, oxamic acid has the potential ability to exhibit polymorphic behaviour.

To date, the crystal structure of oxamic acid is still unreported. However it has been reported that oxamic acid is a potential impurity in various APIs[4] so its

physiochemical characterization is as important as an understanding of its polymorphic behaviour.

In terms of the determination and rationalisation of the crystal structure of the oxamic acid molecule from pxrd data, there are inherent difficulties associated with this molecule that make it a non-trivial task. The functional groups in the molecule contain similar electron density; and hence the direct space approach (section 2.2) may find it difficult to distinguish between possible packings or even *syn* and *anti* confirmations (figure 6.2) when limited by the data resolution obtained in a conventional pxrd experiment.

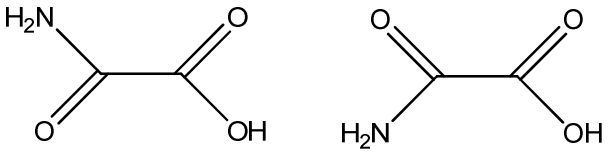

Figure 6.2: *Anti* and *syn* isomers of oxamic acid

Any DE solution will have to undergo further chemical and structural scrutiny before it is deemed to be successful.

6.2 Polymorph screen

Oxamic acid was purchased as a white powder (≥ 96 % purity) and the possibility of polymorphic behaviour investigated by conducting a solvent screen by traditional solvent mediated crystallisations (section 3.10.1) of oxamic acid from a number of solvents. The solvent screen identified two possible forms of oxamic acid, as shown by table 6.1.

Table 6.1: Solvent screen of oxamic acid

Solvent	Form I	Form II
Ethyl Acetate	✓	
Acetonitrile	✓	
Methanol		✓
Butanol		✓
Ethanol		✓
Propanol		✓
D_2O		✓
Ethanol-$_{d6}$		✓

Table 6.1 clearly demonstrates that Form I is obtained by recrystallisation from aprotic solvents, i.e. ethyl acetate and acetonitrile, whereas Form II is recrystallised from protic solvents and their deuterated analogs. This suggests that there may be a strong link between the solvent behaviour and the consequential interactions with the molecules in the solid state. The presence of acidic hydrogens and the potential for strong hydrogen bonding between the solute and solvent molecules during recrystallisation in the presence of a protic solvent will affect the overall structural outcome. Aprotic solvents are still polar in nature, but unlike protic solvents contain no acidic protons and the solvent does not display the same degree of hydrogen bonding with the solute. The formation of strong hydrogen bonding in a protic solvent, may affect the intermolecular energy profile of the system and explain the occurrence of a second possibly metastable form of oxamic acid (form II) which may be disordered or closely related to form I, as the energy for the nucleation of this crystalline form is lowered.

The powder diffraction pattern of form I matches that of the commercial sample, (figure 6.3), and differs (but not significantly) from that of form II (figure 6.3). At first glance both diffraction patterns are similar, and could conceivably arise from a purification process by recrystallisation (from form I to form II). The most distinct

difference between the two patterns is the first peak at 2θ = 19.2° which is present in form I but not in form II. There are further low intensity peaks which again are present in form I but not form II (i.e. 2θ = 21.69, 23.10, 25.20, 29.87, 30.95, 32.84, 34.00)

The generation of form II from a number of different solvents in the solvent screen (table 6.1) suggests that it is a new polymorphic form rather than a solvate.

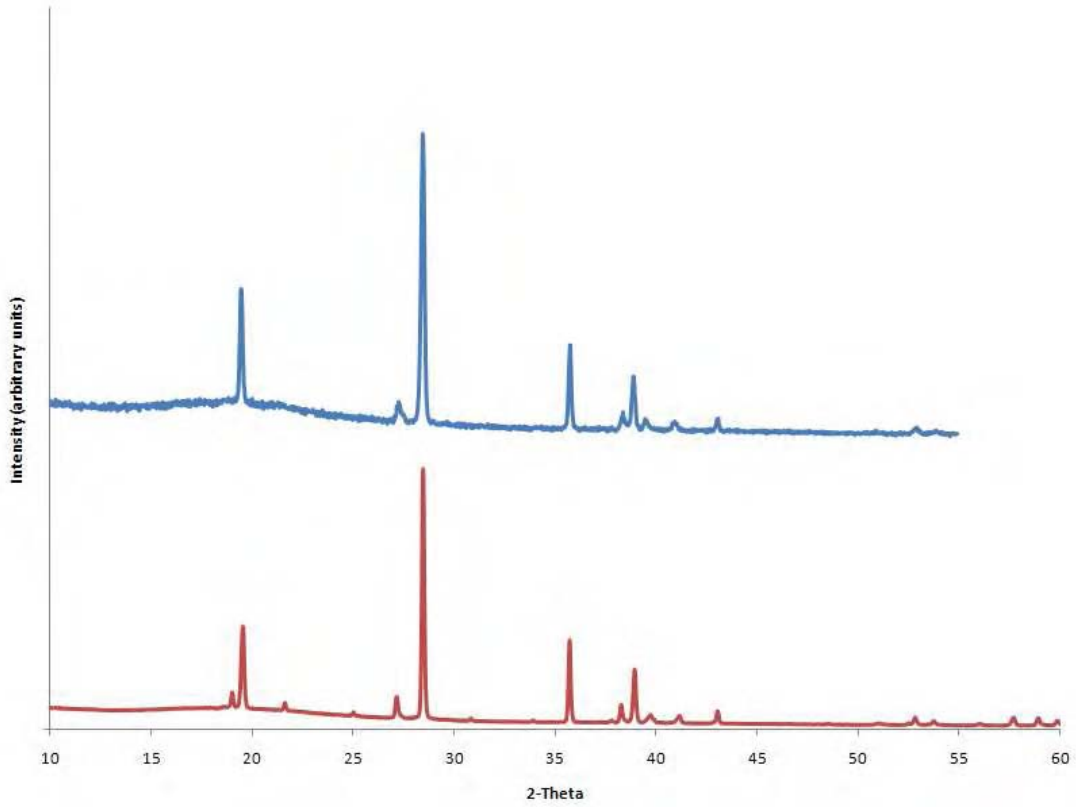

Figure 6.3: The powder diffraction pattern of oxamic acid Form I (red) and Form II (blue)

Consideration of the powder diffraction pattern alone shows that the structure of form II is similar to that of form I, just with some peaks missing. This suggests that form II is possibly of higher symmetry than form I, (hence fewer unique reflections in the diffraction pattern) raising the possibility that form II may have a metastable disordered structure.

6.3 Liquid assisted grinding

Liquid assisted grinding (or solvent drop grinding) was then investigated as a possible method of inducing a polymorphic transition between the two forms, as a complement to the traditional solvent based approach to polymorph screening. Figure 6.4, shows the result of oxamic acid grinding for 10 minutes, in both a protic and aprotic solvent.

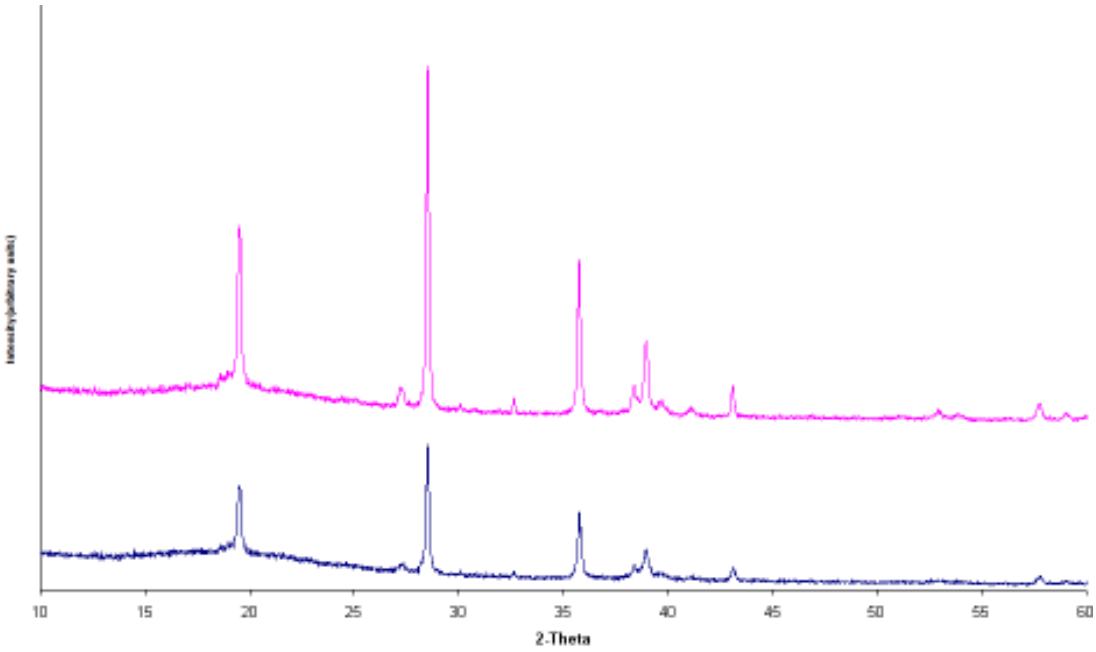

Figure 6.4: Diffraction pattern of oxamic acid ground for 10 minutes in ethyl acetate (pink) and methanol (blue)

From these patterns it is clear that both mechanochemically treated samples of oxamic acid, (from grinding with both protic and aprotic solvents), resemble the pattern of form II. However, the sample obtained from grinding in ethyl acetate does contain a peak 'shoulder' at ~19° which may be indicative of form I. In addition, the grinding process often results in a reduction in crystallinity and hence the other small peaks also indicative of form I may not be apparent. Hence it is difficult to be sure whether

or not the results of this experiment reproduce those from solvent-based recrystallisation.

6.4 DSC results

DSC was then used to investigate any phase transition between the two possible forms. Low temperature runs on both forms showed no significant thermal event, suggesting that there is no phase transition in the range 20.00 °C to –180 °C. However the high temperature trace of form II showed a small but significant thermal event at the onset temperature 179.2 °C, before sublimation at 208 °C. No thermal events were observed in the high temperature trace for form I.

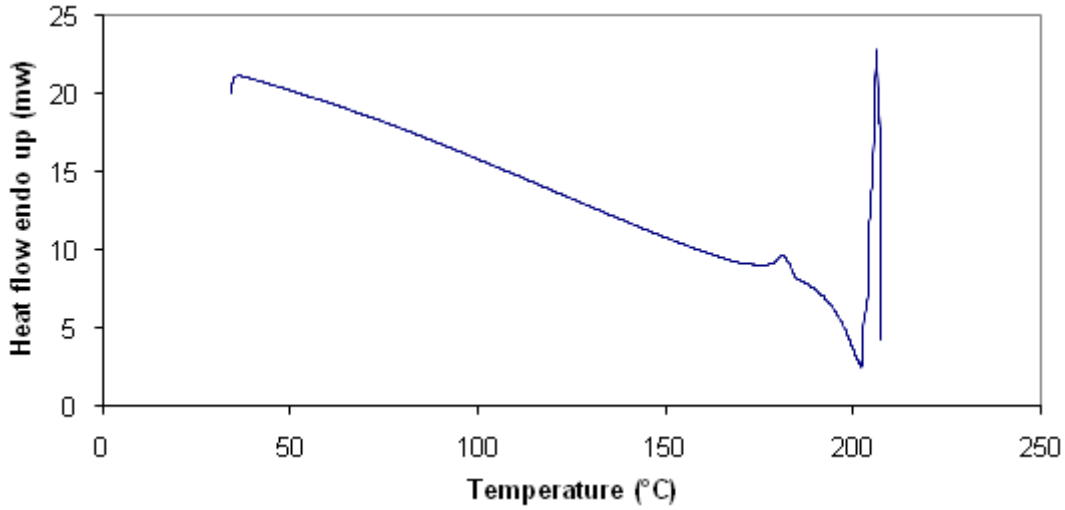

Figure 6.5: High temperature DSC trace of oxamic acid form II

The small endotherm in figure 6.5, represents a phase transition possibly from form II to form I. The small intensity of this peak suggests that the forms are similar in energy; this could be the case if the crystal packing in both structures is similar, as supported by the significant similarity of the diffraction patterns of both forms.

6.5 Solution ^{1}H NMR results

In order to facilitate further characterisation of both forms and confirm the purity of the commercial form, solution ^{1}H NMR spectra were recorded of both forms of oxamic acid (appendix T). Other than removal of an impurity, the ^{1}H NMR of the recrystallised form I is the same as that of the commercial form.

6.6 Solid-state NMR results

Solid-state ^{13}C MAS NMR spectroscopy was used to provide information about the possible contents of the asymmetric unit in both forms (see appendix U) for solid-state NMR spectra). Both spectra show only one centred signal at 163 ppm with a pair of (unlabelled) spinning sidebands indicating that the chemical shifts of the two carbons are unresolved. There is no clear difference between the spectra of the forms and no sign of additional lines that might indicate more than one molecule in the asymmetric unit. However, the relaxation properties of the samples are different, but this unfortunately does not distinguish between possible polymorphic forms, it gives an insight into the crystal size of the sample investigated[5].

^{15}N MAS NMR was also used to probe the samples but the long recycle delay in ^{15}N NMR impacts on the quality of the final spectra, (see appendix U). These results, indicate that both forms have only one molecule in the asymmetric unit but that solid-state ^{15}N NMR cannot distinguish between the two polymorphic forms.

The results from the solid-state NMR experiments are consistent with those from both PXRD and DSC in that it is clear that both forms are similar. All these results are consistent with the possibility that the two forms may be related by disorder. Disorder introduces a distinct difference in the contents of the asymmetric unit of a crystal structure. There are two types of disorder; dynamic disorder where each atom is vibrating with large amplitudes of vibration, and static disorder which consists of alternate positions for atoms or groups of atoms. X-ray diffraction gives us a 'time averaged' crystal structure and the absence/presence of disorder between the forms may give rise to an increase or decrease in crystal symmetry, giving rise to the presence or absence of a small number of diffraction peaks.

6.7 Structure prediction results

As discussed in section 1.9, crystal structure prediction remains a challenge even when used to study small molecular materials from first principles. In this section we endeavour to use powder diffraction analysis to compare experimental patterns and those simulated from predicted structures using the PolySNAP[6] program.

PolySNAP[6] is a 'pattern-matching' program designed to compare an extensive number of patterns by generation of an (n x n) correlation matrix (using Pearson and Spearman correlation coefficients) to match the full profile of each of the n diffraction patterns with every other pattern in the group. The predicted structures of oxamic acid and their powder diffraction patterns were generated by collaborators at University College London. The structures were calculated by producing a set of densely packed crystal structures generated in common crystal types using MOLPAK[7]. The intermolecular lattice energy is contributed from a distributed multipole analysis[8] of

the *ab intio* molecular charge density in the molecule under consideration. PolySNAP was then used to compare all the powder diffraction patterns produced.

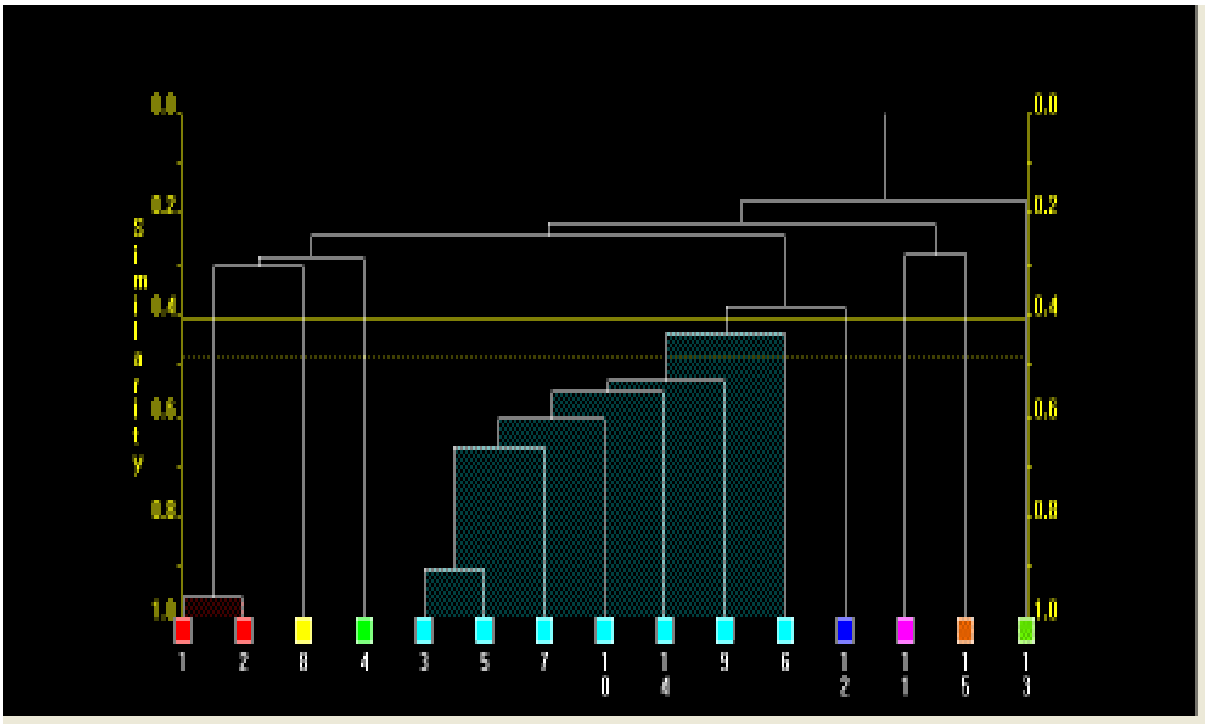

Figure 6.6: A dendogram produced by a PolySNAP, comparing simulated and experimental powder diffraction patterns for oxamic acid. Codes 1 and 2 represent forms I and II of oxamic acid, 3 (ciscis_ai50), 4 (ciscis_ak61), 5 (transcis_ai48), 6 (transcis_aj74), 7 (transcis_ak35), 8 (transcis_am52), 9 (transtrans_de50), 10 (transcis_fc58), 11 (transtrans_am58), 12 (transtrans_am62), 13 (transtrans_da59), 14 (transtrans_am56), 15 (transtrans_af42).

The numbers along the bottom of the dendrogram in figure 6.6, correspond to different experimental and simulated diffraction powder data sets; 1 and 2 represent the experimentally isolated forms I & II respectively, the other codes represent simulated patterns produced from the theoretical structures calculated by our collaborators at UCL. It is clear from the dendrogram, that the experimental and predicted patterns do not compare well, suggesting that the predicted crystal structures are not similar to those from the experimental screen in this study. For a visual comparison of these diffraction patterns and the energy landscape of the predicted

oxamic acid structures see appendix V. There are a number of different molecular conformations to be considered theoretically and hence further work is needed to enable better prediction and to facilitate unambiguous characterisation of the experimental forms from a theoretical basis.

6.8 Structure solution of oxamic acid form I from pxrd

The X-ray powder diffraction data set used for structural analysis was collected over a period of 1 hour, and range of $10^{\circ} \leq 2\theta \leq 50^{\circ}$. The data were indexed on the basis of the first 20 observable reflections using the indexing program CRYSFIRE[9] and the Cc space group assigned to each material by consideration of systematic absences. The profile parameters were refined by whole-profile-fitting LeBail[10] method in the program GSAS[11] to improve the fit of the lattice, zero point and profile parameters. Structure solution was carried out using DE; this was implemented using the program POSSUM[12].

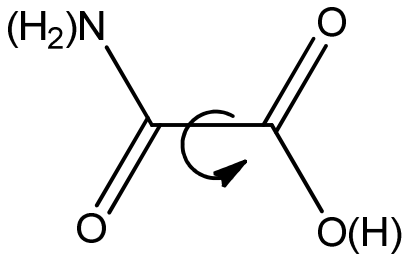

Figure 6.7: Molecular structure used in the DE structure, torsion angles are indicated by arrows. Hydrogen atoms excluded from the calculation are shown in brackets.

The structural model of oxamic acid used in the DE calculation comprised the molecule constructed using standard bond lengths[13] and angles, excluding hydroxyl and amide hydrogens. The molecular structure is defined by 7 elements: 3 parameters (θ,Φ,Ψ) to define the orientation of the molecule (bounds 0 - 360˚), 3 parameters

(x,y,z) to define the position of the molecule and one freely rotating torsion angle (0-360˚).

Out of the 25 epochs calculated, 24 adopted the *syn* confirmation. The solution that adopted the *anti* conformation the lowest R_{wp} = 6.02 %. The lowest *syn* conformation had an R_{wp} = 6.12 %. The following description of the successful DE calculation and resulting structure description is that of this *anti* conformation.

The optimum DE calculation had a population of 210 and the maximum number of generations was set to 2000. The calculation had a K = 0.99 and F = 0.3. The progress plot for the anti DE solution of oxamic acid (figure 6.8) shows the progression of the DE calculation in terms of % R_{wp} with generation.

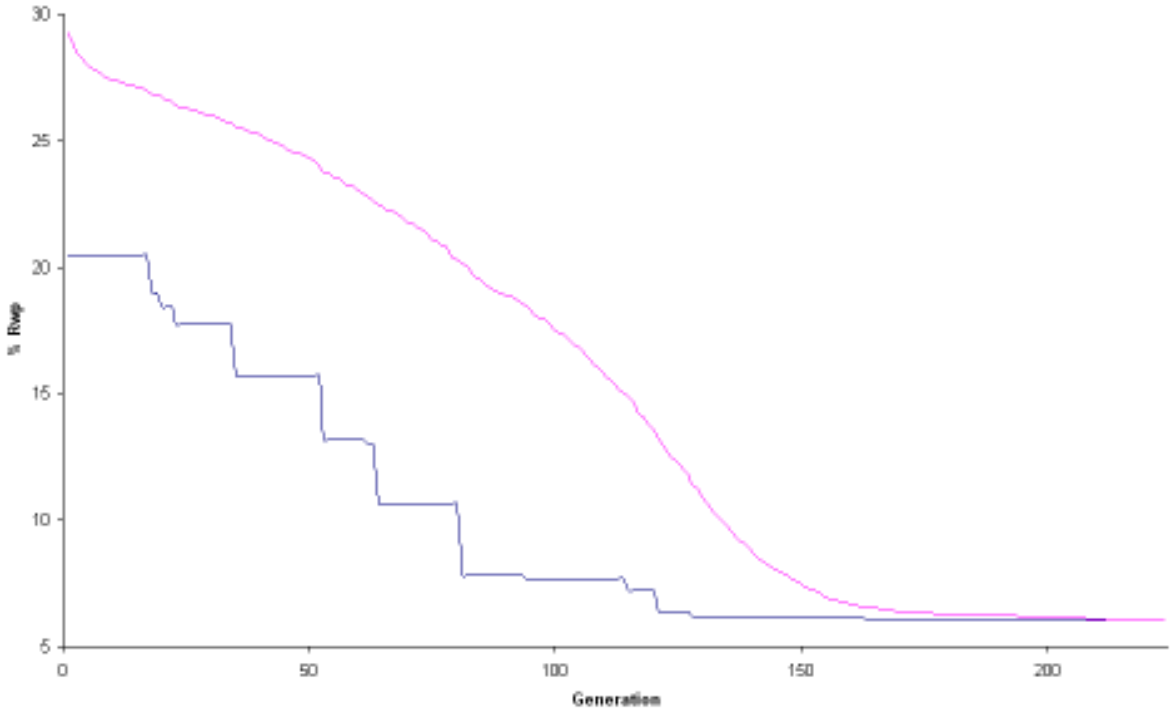

Figure 6.8: Differential evolution progress plot for the solution of oxamic acid showing the best % R_{wp} (blue) and the mean % R_{wp} (pink).

Figure 6.8 demonstrates the efficiency of the DE calculation for a 7 parameter problem, when compared to the 14 and 15 multi-component parameter problems

presented in previous chapters (4, 5, 6 and 7). The progress plots of the multi-component crystals display a large plateau region in where there is no decline in either best or mean % R_{wp}, whereas in this single molecule problem, there is a step decline to convergence at generation 224.

6.9 Rietveld refinement

The anti structure obtained from the DE structure solution was used as a starting point for Rietveld refinement using the GSAS program package[14]. The positions of all atoms were refined subject to soft restraints (weighing factor of 0.001 for bond distances and 0.005 for geminal non-bonded distances) on standard geometry. No preferred orientation correction was applied. Hydrogen atoms that were not included in the DE calculation were placed in calculated positions according to the expected hydrogen bonding network. For the non-Hatoms, isotropic atomic displacement parameters were refined constrained according to atom type or environment. The final Rietveld plot can be found in figure 6.9.

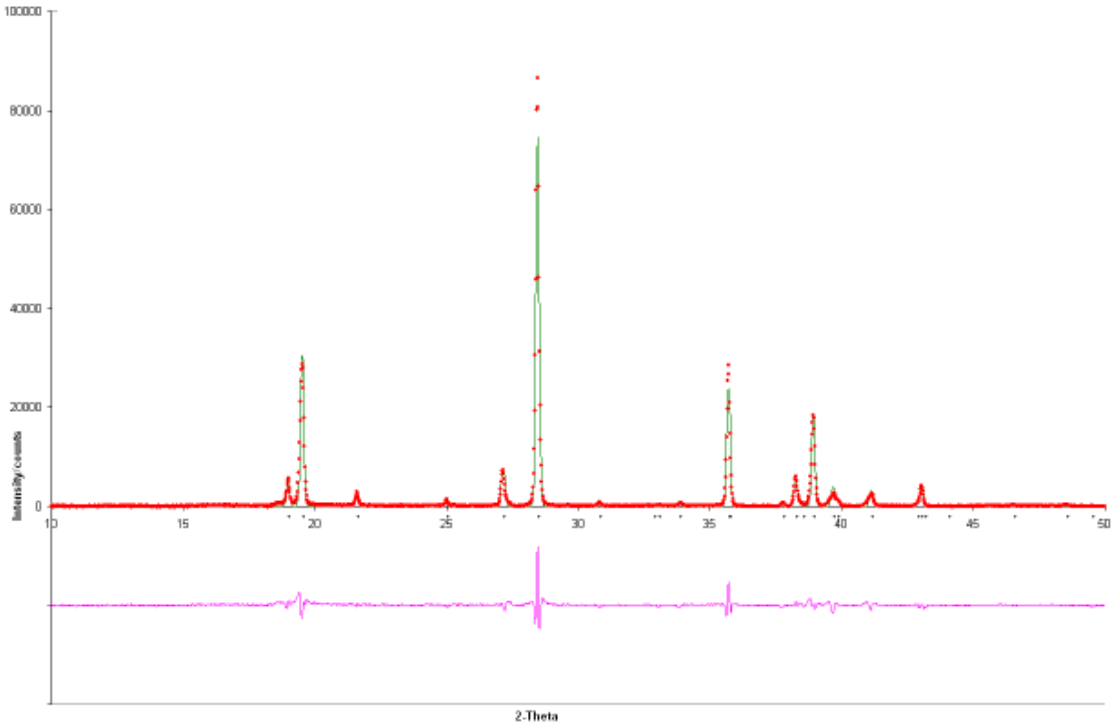

Figure 6.9: The final Rietveld profile for oxamic acid form I. Experimental diffraction data is shown by red circles, the calculated pattern is shown by a solid green line and the difference in pink. Reflection positions are marked as black dots.

Table 6.2 Initial lattice parameters, DE structure solution parameters, refined lattice parameters from Rietveld refinement and single crystal determination and Rietveld agreement factors

Compound	Oxamic acid	
Crystal data		
Chemical formula	$H_2NC(=O)C(=O)OH$	
M_r	89.05	
D_x / mg m^{-3}	1.250	
Indexing		
Space group	Cc	
Initial a / Å	9.471(1)	
Initial b / Å	5.590(2)	
Initial c / Å	6.824(1)	
Initial β / °	107.250(2)	
Initial V / $Å^3$	338.350(2)	
Structure solution		
LeBail R_{wp} / %	5.36	
LeBail R_p / %	3.54	
LeBail χ^2	14.64	
DE elements		
K	0.99	
F	0.3	
N_p	210	
Best R_{wp} / %	6.02	
Refinement		
R_{wp} / %	5.50	
R_p / %	3.60	
R^2_F / %	5.78	
χ^2	15.50	
		Single Crystal parameters
Final a / Å	9.4949(8)	9.530(5)
Final b / Å	5.4351(3)	5.424(3)
Final c / Å	6.8598(4)	6.866(4)
Final β / °	107.15(0)	107.18(4)
Final V / $Å^3$	338.27(3)	339.3(2)

6.10 Structure of Oxamic acid form I from powder diffraction data

Oxamic acid crystallises in the monoclinic space group Cc. The structure consists of infinitely hydrogen bonded sheets running in the [101] direction (figure 6.10). The sheets run along the axes at (½, y, ½). The oxamic acid molecule acquires the *anti* orientation in the powder solution of form I.

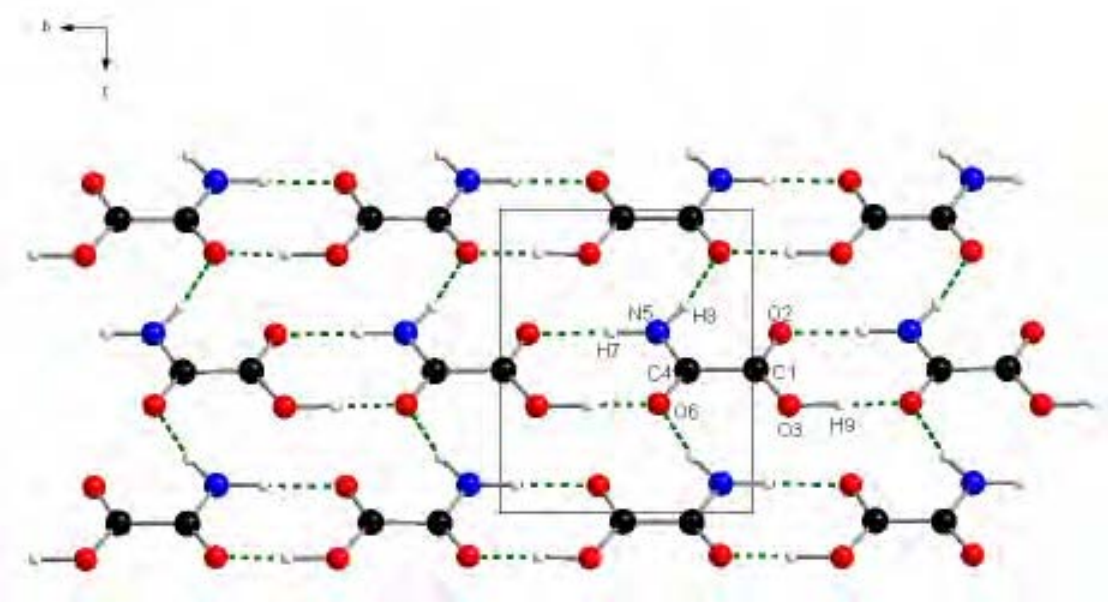

Figure 6.10: Projection down the *a* axis showing the infinitely hydrogen bonded sheet of oxamic acid form I. (Unit cell shown)

Within an individual hydrogen sheet, there are three types of hydrogen bond that exist, table 6.3. Chains of oxamic acid molecules run along the [010] direction, held together by $R_2^2(8)$ dimmer linkages. N5 donates a hydrogen bond via H7 to O2 (x, 1+y, Z) and O6 accepts a hydrogen bond to complete the $R_2^2(8)$ dimer. The chains of oxamic acid are bonded together via N5 (0.85560, 0.37460, 0.40480) donating a

hydrogen bond via H8 to O6 (-0.5x, -0.5y, -0.5z). The combination of the dimer hydrogen bonds and the inter-chain hydrogen bond results in a higher motif of $R_3^3 14$.

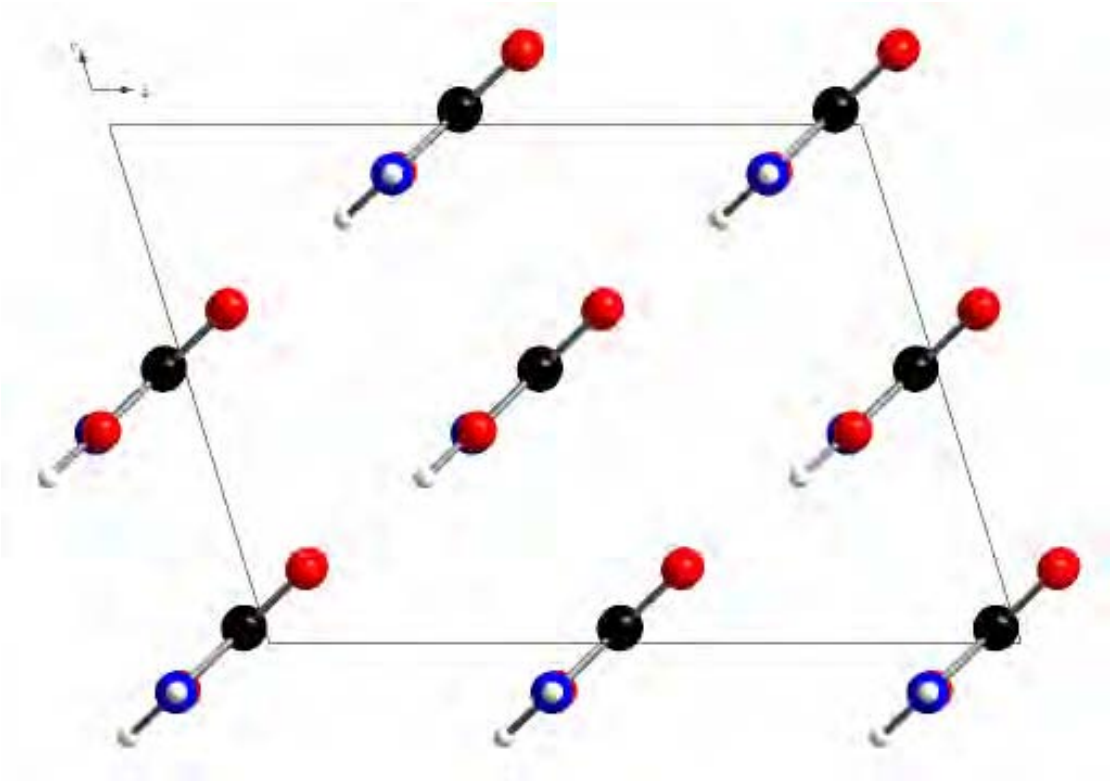

Figure 6.11: A view along the *b* axis of oxamic acid. Infinitely hydrogen sheets running along the b axis. (Unit cell shown).

Table 6.3: Hydrogen bond geometry in oxamic acid, Å and °.

Donor-----H… Acceptor	D-H	H….A	D…A	<(DHA)
N(5)---H(7)….O(2)	1.008	1.788	2.7967	178.3
O(3)---H(9)…O(6)	1.1	1.529	2.6284	180
N(5)---H(8)…O(6)	1.025	2.0438	3.0331	165

6.11 Single crystal vs. Powder structure of oxamic acid form I

Single crystal data were collected on a Bruker smart 6000 diffractometer equipped with a CCD detector and a copper tube source. The structure was solved and refined

using SHELXL. Please see appendix W for further details of the single crystal refinement of oxamic acid. The single crystal structure adopted the *syn* confirmation, a single crystal structure would normally warrant unequivocal structural confidence in the conformation in the molecule but due to the poor quality of the single crystal and the resultant poor quality refinement (see appendix W), reasonable doubt remains over this structure.

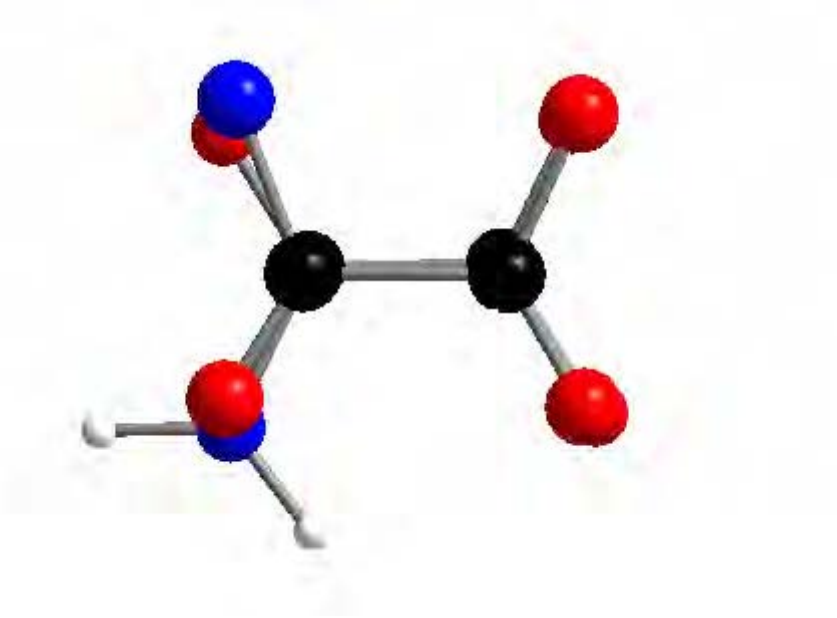

Figure 6.12: Overlay of single crystal structure and *syn* DE solution of oxamic acid

Figure 6.12 illustrates the inherent problems of solving a small molecular material like oxamic acid from laboratory powder X-ray data. Both single crystal and powder structures are in accord, in terms of packing, as the oxamic acid molecules form chains running in the *b* direction. Differences between the two crystal structures are highlighted by overlaying the asymmetric group of the single crystal over that of the powder structure. Both have adopted the *syn* conformation, but the difference lies in the position of the *syn* carbonyl oxygens, as in the single crystal the carbonyl carbons lie below the carbon backbone of the molecule where the converse is true in the

powder structure. This is also occurs when comparing the *anti* (R_{wp} = 6.02 %) DE solution to the single crystal structure. As alluded to before, functional groups containing similar electron density can be hard to differentiate between, due to the resolution possessed in a powder X-ray experiment.

Many positives can be taken from the powder structure solution of oxamic acid, as the packing of the molecules in the *b* direction is in agreement with the single crystal structure. In the powder DE solutions, 24 out of the 25 epoch's that were run were also in agreement with single crystal solution in adopting the *syn* conformation. Neither the powder, nor single crystal experiment, provided high enough resolution to place hydrogen atoms. Unfortunately, even with the combination of single crystal and powder X-ray diffraction, the final crystal structure of oxamic acid remains unclear and perplexing.

One approach in order to rationalise the orientation of the oxamic acid molecule is to look into the hydrogen bonding networks afforded by either *syn* or *anti* conformers. Within the *syn* conformer, the hydroxyl hydrogen atom possesses flexibility and can either take up an *anti* position (as shown by figure 6.13) or a *syn* (shown in figure 6.14). The position of the hydroxyl hydrogen has a profound effect upon the hydrogen bonding networks present in the final crystalline structure. As shown in figure 6.10, the anti conformer gives rise to chains of oxamic acid molecules running along the [010] direction, held together by $R_2^2(8)$ dimer linkages, whereas in the both forms of the *syn* conformers no dimer linkage is former, only a C(5) chain in the *syn(anti)* conformer and merely the inter-chain hydrogen bond C(4) running in the (101) plane. The *syn(syn)* conformer in particular would give rise to unfavourable steric interactions due to proximity of the hydrogen atoms. In terms of hydrogen bonding

networks, all 3 conformers are possible but the *anti*-oxamic acid is afforded more lattice stability by its hydrogen bonding network and is favourable over both syn conformers.

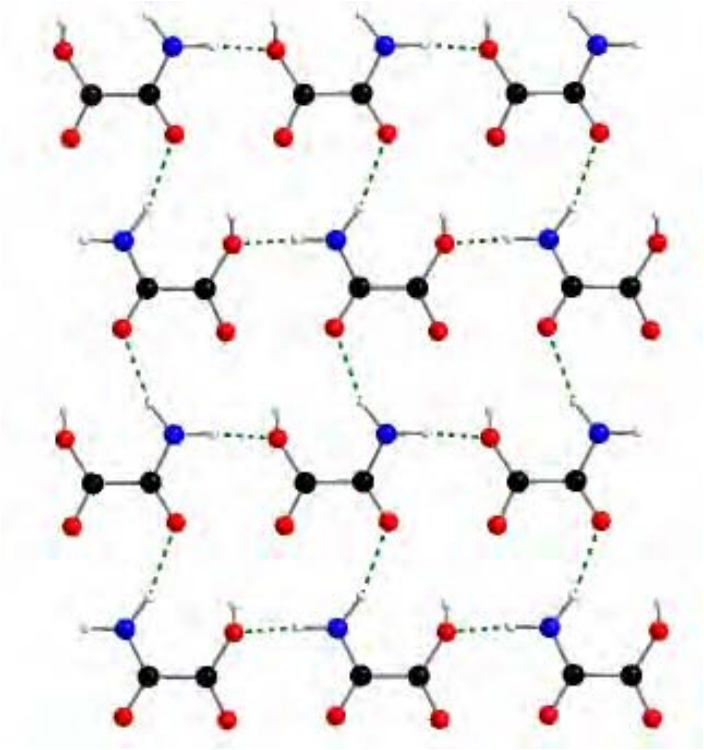

Figure 6.13: Hydrogen bonding network in *syn(anti)*-oxamic acid conformer.

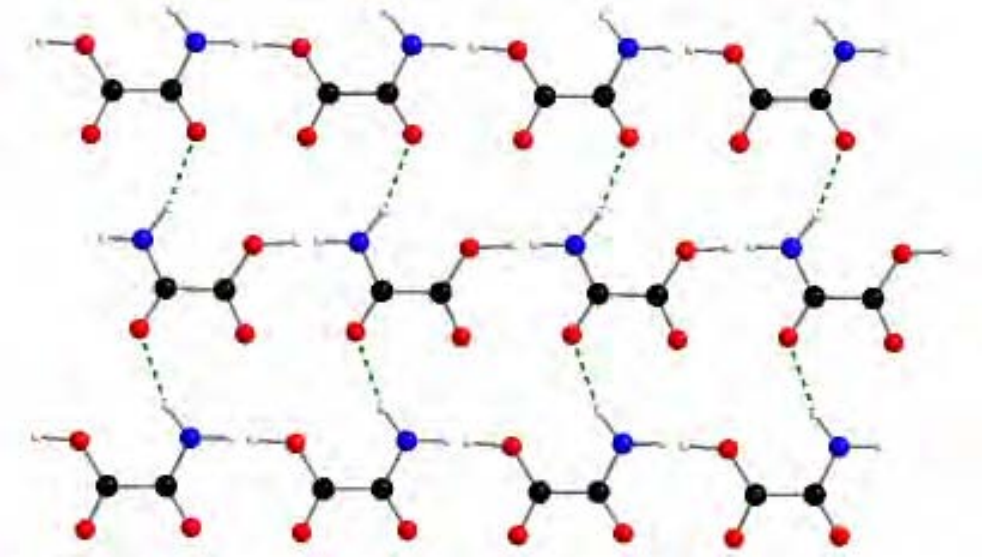

Figure 6.14: Hydrogen bonding network in *syn(syn)*-oxamic acid conformer

Higher resolution data collected at a synchrotron source or neutron diffraction data would allow for higher certainty in the placement of the functional groups in oxamic acid.

6.12 The attempted structure solution of oxamic acid from II pxrd

Pxrd data was collected on a Siemens D5000 over a period of 1 hour, and a range of $10^{\circ} \leq 2\theta \leq 50^{\circ}$. The data set was indexed on the basis of the first 20 observable reflections using the indexing program CRYSFIRE[9] and a space group of P1 was assigned on the basis of the lack of systematic absences. The profile parameters were refined by whole-profile-fitting LeBail[10] method in the program GSAS[11] to improve the fit of the lattice and profile parameters. Structure solution was carried out using differential evolution (section 1.7.5); this was implemented using the program POSSUM[12].

Table 6.4: Indexed lattice parameters of oxamic acid form II

Lattice parameter	
a	4.773(1) Å
b	5.324(2) Å
c	3.679(1) Å
α	108.359(1) °
β	106.074(3) °
γ	78.888(1) °
Unit cell volume	84.728(1)Å^3
Space group	P1
LeBail parameters	
LeBail R_{wp} / %	7.48
LeBail R_p / %	5.80
LeBail χ^2	1.421

The volume of the indexed unit cell indicates an error has occurred in the indexing process, as the unit cell volume was indexed to 84.728 Å^3. From the unit cell the

number of non-hydrogen atoms per unit cell can be estimated, and hence the number of molecules in the asymmetric unit. A general rule is that each non-hydrogen atom requires an average volume of 18 $Å^3$, which equates to this case to, 6 X 18 = 108 $Å^3$, which is larger than the indexed unit cell, 84.728 $Å^3$.

6.13 Neutron diffraction data

The nature of scattering from neutrons by atomic species, offers a higher degree of precision in comparison to that X-ray diffraction. The same level of precision is afforded for each atom in the structure due to the fact the neutrons are scattered by the atomic nucleus and not the electron cloud surrounding the atom, and hence the scattering power is not directly linked to the electron density. Scattering power does not significantly fall off with a higher diffraction angle as experienced with X-ray diffraction, due to the nature of the neutron and nucleus interaction. Neutrons interact with both hydrogen and deuterium, and therefore neutron diffraction acts as vital tool in molecular crystallography, as X-rays scarcely interact with hydrogen atoms. This interaction allows confidence in classifying oxamic acid in either the *syn* or *anti* conformation. Good quality neutron data will yield high precision atomic and vibrational parameters, including higher thermal effects.

Data was collected on both a hydrogenated sample of oxamic acid and a deuterated sample. Neutron scattering techniques particularly profit from the availability of deuterated samples, as the scattering noise is greatly reduced.

6.14 Hydrogenated neutron data

The profile parameters were refined by whole-profile-fitting LeBail[10] method in the program GSAS[11] to improve the fit of the lattice and profile parameters. Structure solution was carried out using differential evolution (section 1.7.5); this was implemented using the program POSSUM[12]. Three input model, models A, B and C, were employed in separate structure solution searches. Model A contains full structural rotation, model B is fixed in *anti* conformation and model C is fixed in the *syn* conformation. All the models, A-C, encompass all possible conformations for the oxamic acid molecule in the solid state (figure 6.15).

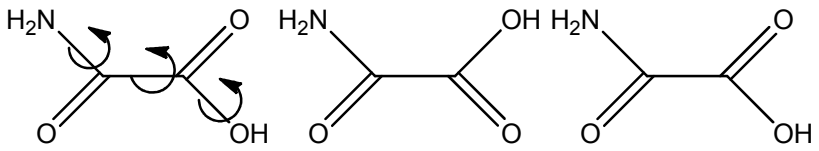

Figure 6.15: Model A, B and C, of oxamic acid

All solutions retrieved from the DE calculations packed oxamic acid molecules in the (101) plane, which is in agreement with both the powder and single crystal X-ray solutions.

6.14.1 Model A Results

In table 6.5, information on each run is presented along with generation of convergence and whether the solution adopted the *syn* or the *anti* conformation, as model A contained full structural rotation.

Table 6.5: The results from a number of DE calculations with variation in *F* (mutation rate) and NP (population size). For each epoch the final R_{wp} (in %) is given and figures within brackets indicate at which generation convergence was achieved. Each run has been classed as either *syn* or *anti.*

Run	F	Np	Epoch 1	Epoch 2	Epoch 3	Epoch 4	Epoch 5
1	0.3	180	4.63(374)-*syn*	4.46(307)-*syn*	4.73(892)-*syn*	4.52(317)-*syn*	4.46(280)-*syn*
2	0.4	180	4.68(2000)-*anti*	4.41(599)-*anti*	4.94(704)-*anti*	4.26(606)-*syn*	4.27(766)-*syn*
3	0.5	180	4.46(1180)-*syn*	4.26(980)-*syn*	4.29(1180)-*syn*	4.26(976)-*syn*	4.69(1062)-*syn*
4	0.3	270	4.53(414)-*syn*	4.26(385)-*syn*	4.49(334)-*anti*	4.71(389)-*anti*	4.46(2000)-*anti*

As illustrated in table 6.5, the neutron data serves up a mixture of both *syn* and *anti* solutions, with the *syn* conformation being more favoured, in terms of regularity, with 13 out of 20 solutions adopting a *syn* conformation, also the solution with the lowest % R_{wp} was in the syn conformation, with a $R_{wp} = 4.26\%$. The lowest *anti* $R_{wp} = 4.41$ %.

Even though the data is strongly suggesting that the oxamic acid molecule has adopted the syn conformation, as in agreement with the single and powder crystal structure solutions, there remains uncertainty over the final confirmation of oxamic acid, even with the introduction of neutron data.

6.14.2 Model B results

In table 6.6, information on each run is presented along with generation of convergence, as previously mentioned in section 6.14, model B is fixed in the *syn*

confirmation, in order to explore whether the conformation and rigidity of the input model can locate minima on the hypersurface lower than that found using model A.

Table 6.6: The results from a number of DE calculations with variation in *F* (mutation rate) and NP (population size). For each epoch the final R_{wp} (in %) is given and figures within brackets indicate at which generation convergence was achieved.

Run	F	Np	Epoch 1	Epoch 2	Epoch 3	Epoch 4	Epoch 5
1	0.5	60	4.51(160)	4.51(236)	4.51(2000)	4.51(2000)	4.51(243)
2	0.5	90	4.51(2000)	4.51(181)	4.51(2000)	4.51(88)	4.51(138)
3	0.4	90	4.51(151)	4.51(2000)	4.51(174)	4.51(113)	4.51(89)
4	0.3	90	4.51(84)	4.51(74)	4.6(261)	4.51(489)	4.59(49)
5	0.3	180	4.51(115)	4.51(71)	4.51(66)	4.51(2000)	4.51(282)
6	0.4	180	4.51(157)	4.51(104)	4.51(2000)	4.51(167)	4.51(315)
7	0.5	180	4.51(342)	4.51(210)	4.51(117)	4.51(2000)	4.51(482)

As illustrated by table 6.6, all epochs in every run find a minimum R_{wp} = 4.51 %. This is higher than the % R_{wp} achieved for model A.

6.14.3 Model C results

In table 6.7, information on each run is presented along with generation of convergence, as previously mentioned in section 8.91, model B is fixed in the *anti* confirmation. As shown in table 6.7, the bulk of epochs reach an Rwp = 4.8%, which is 0.29 higher than the R_{wp} achieved for the *syn* model.

Table 6.7: The results from a number of DE calculations with variation in *F* (mutation rate) and NP (population size). For each epoch the final R_{wp} (in %) is given and figures within brackets indicate at which generation convergence was achieved.

Run	F	Np	epoch 1	epoch 2	epoch 3	epoch 4	epoch 5
1	0.3	60	5.14(60)	4.81(53)	4.82(62)	4.95(73)	4.8(64)
2	0.3	120	4.8(95)	4.8(101)	4.8(142)	4.8(105)	4.8(90)
3	0.5	120	4.8(269)	4.8(171)	4.8(236)	4.8(121)	4.8(150)
4	0.4	120	4.8(233)	4.8(97)	4.8(96)	4.8(102)	4.8(2000)
5	0.3	180	4.8(136)	4.8(113)	4.8(523)	4.8(93)	4.8(81)
6	0.4	180	4.8(125)	4.8(2000)	4.8(125)	/	/
7	0.5	180	4.8(109)	4.8(1143)	4.8(249)	4.8(136)	4.8(334)

6.14.4 Neutron data conclusion

As mentioned in section 6.13, neutron diffraction data offers a higher degree of precision in comparison to that offered by X-ray diffraction. The three input models A, B and C has allowed all possible conformations of the oxamic acid molecule to be investigated equally. The DE, in combination with the neutron data points to the *syn* conformer being the most likely. This is confirmed by the propensity of the *syn* conformer when using input model A, combined with the lowest R_{wp} of 4.26.

6.15 Thermal behaviour of oxamic acid

As discussed in section 4.7, thermal expansion co-efficients give us an extraordinary insight into the molecular crystal structure of oxamic acid, in particular the hydrogen bonding networks present within the crystal. The variable temperature data was collected on a Siemens D5005, in the reflection transition mode, over a 2θ range of $10^{\circ} \leq 85^{\circ}$. The variable temperature data confirms that there was no phase transformations over the temperature range investigated (50-295 K). Figure 6.16 contains the variation of the lattice parameters over the temperature range investigated, as determined by the LeBail[10] method.

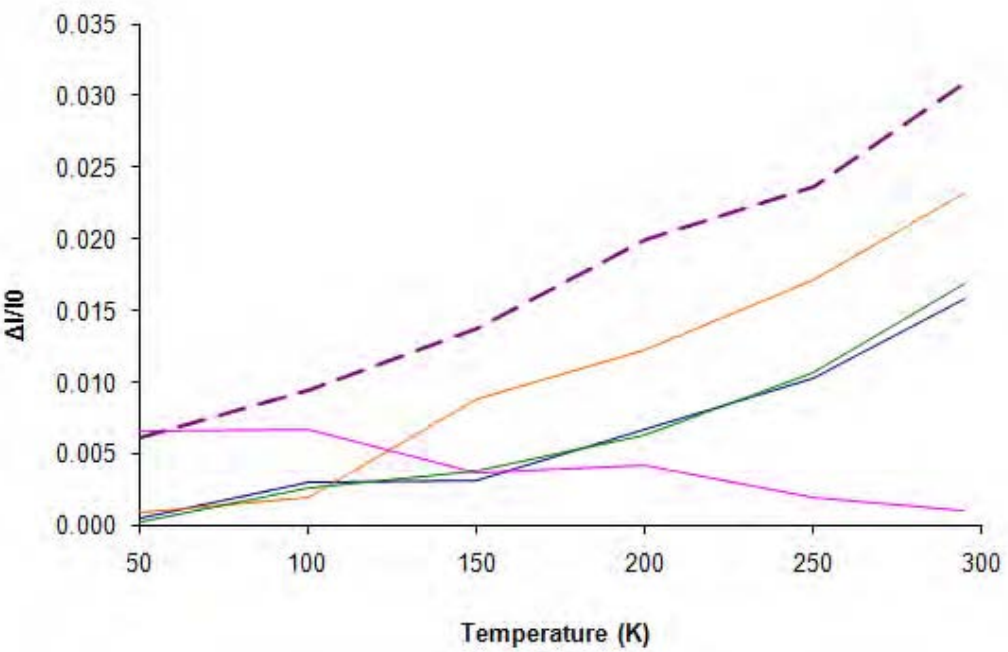

Figure 6.16: The fractional variation of lattice parameters obtained from LeBail refinement, plotted against temperature. Unit cell volume (purple dashes), *a* (blue), *b* (pink), *c* (orange) and *β* (green).

As evident from both figure 6.16 and table 6.8, the *c* axis is the most thermally liable, followed by *a* and finally the *b* axis which experiences negative thermal expansion. If we relate the thermal information back to the proposed crystal structure, as discussed in section 6.10, the negative expansion in the b direction is not unexpected as the chains of oxamic acid molecules run the (101) plane.

Table 6.8: Linear thermal expansion co-efficients of the lattice parameters of oxamic acid

Lattice parameter	Linear thermal expansion co-efficient (K^{-1})
a	6.23986×10^{-5}
b	-2.26067×10^{-5}
c	9.8254×10^{-5}
Unit cell volume	1.0075×10^{-4}

6.16 Conclusions

Within this chapter, the structure solution of oxamic acid has been pursued by a combination of pxrd, sxrd and powder neutron diffraction. The packing of the oxamic acid molecule, with infinitely hydrogen bonded hydrogen sheets running in the [010] direction has been confirmed by the different diffraction methods. The conformation of the oxamic acid molecule within the hydrogen bonded sheets has been harder to confirm, due to the similarities in electron density surrounding the functional groups. Both single crystal and neutron diffraction allude to the *syn* conformation, whereas the pxrd refinement points to an *anti* conformation. Due to the nature of the refinements in this chapter, further crystallographic work would need to be carried out to confirm the conformation of the molecule.

References

1. J. Papaconstantinou and S. P. Colowick, *Journal of Biological Chemistry*, 1961, **236**, 278-&.

2. O. Warburg, *Science*, 1956, **123**, 309-314.

3. O. Warburg, *Science*, 1956, **124**, 269-270.

4. L. Yang, L. Liu, B. A. Olsen and M. A. Nussbaum, *Journal of Pharmaceutical and Biomedical Analysis*, 2000, **22**, 487-493.

5. M. Adam-Berret, A. Riaublanc, C. Rondeau-Mouro and F. Mariette, *Crystal Growth & Design*, 2009, **9**, 4273-4280.

6. G. Barr, W. Dong and C. J. Gilmore, *Journal of Applied Crystallography*, 2004, **37**, 658-664.

7. J. R. Holden, Z. Y. Du and H. L. Ammon, *Journal of Computational Chemistry*, 1993, **14**, 422-437.

8. A. J. Stone and M. Alderton, *Molecular Physics*, 1985, **56**, 1047-1064.

9. R. Shirley, *The Crysfire 2002 System for Automatic Powder Indexing: User's Manual, 41 Guildford Park Avenue, Guildford, Surry, GU2 7NL, England, 2002.*, 2002

10. A. Lebail, H. Duroy and J. L. Fourquet, *Materials Research Bulletin*, 1988, **23**, 447-452.

11. A. C. Larson and R. B. Von Dreele, *GSAS. General Structure Analysis System, Report No. LAUR 86-748, Los Alamos National Laboratory, Los Alamos, New Mexico, USA*, 1994.

12. C. C. Seaton and M. Tremayne, *Possum Programs for Direct-Space Strucutre Solution from Powder Diffraction Data*, 2002, School of Chemistry, University of Birmingham, UK.

13. F. H. Allen, O. Kennard, D. G. Watson, L. Brammer, A. G. Orpen and R. Taylor, *Journal of the Chemical Society-Perkin Transactions 2*, 1987, S1-S19.

14. A. C. Larson and R. B. Von Dreele, " General Structure Analysis System (GSAS)", Los Alamos National Laboratory Report LAUR 86-748 (1994).

7.0 Conclusion

The research presented in this thesis is based on three main areas of small organic molecular crystallography; synthesis, crystal structure determination and the thermal behaviour of crystalline systems.

The DE has been successfully implemented for the structure solution of three unknown binary multi-component materials (oxamate:nicotinamide, oxamate:isonicotinamide and fumaric acid:nicotinamide). The use of this technique to solve binary molecular crystal structures directly from powder X-ray diffraction has become a robust option. The comparison of pxrd structures vs. single crystal structures has illustrated both the strengths and the potential pitfalls of solving binary materials from powder methods. The orientation of an amide group, as seen in the oxamate:nicotinamide structure, needs careful attention from the crystallographer, with bond restraints acting as a strong indicator to whether the correct orientation has been assigned. As seen in all of the successful structure solutions the profile of the DE calculation is one of a small initial decline in R_{wp} followed by a prolonged plateau and finally a steep decline in R_{wp} as the calculation approaches the global minimum. As this profile is typical of many deterministic problems, an area of future work could include the development of the DE algorithm. Work has already begun within the group to improve the DE efficiency, through the use of eugenics to cut down population size throughout the calculation. A systematic analysis of the DE control parameters would also aid in improving the efficiency of the DE when tackling multi-component materials.

The successful implementation of the DE is vitally important in the method development of solvent free or solvent reduced synthetic routes. Reduced solvent methods have obvious environmental and economic advantages but are not conducive to producing crystals of sufficient size and quality to warrant a single crystal experiment, therefore, the development

of structure solution from pxrd is significant. The reduced solvent synthetic methods were successful in producing the same phase as the traditional solvent mediated route. Reduced solvent synthetic methods circumvent the issue of both starting materials having similar solubilities in the chosen solvent and allow a wider range of materials to be used in the design of cocrystalline material. The next step in the continuation of the method development of the solvent reduced synthetic process is to move from using the pxrd data from a LAG crystallite, and placing into the DE. This will present inherent problems associated with solvent reduced synthetic methods, as often, peaks associated with starting materials will be present in the diffraction pattern. This mix of starting materials and the new multi-component material could be tackled by searching for separate phases in the DE. This will obviously impact upon the complexity of the problem and work would need to be employed to improve the efficiency of the algorithm. The simplicity of the DE algorithm offers scope for strategies to improve the convergence rate of the search.

Within the systems presented in this thesis there has been a display of robust preferential synthons, i.e. amide dimers. As discussed in chapter 5, from a cocrystal design aspect it was interesting to observe an absence of an amide dimer in the maleate:iconicotinamide structure, unlike in the maleate:nicotinamide structure. The cocrystallisation of maleic acid with nicotinamide produced an unexpected isomerisation to its conformer fumaric acid. As mentioned in section 5.9, the isomerisation of maleic acid to fumaric acid is normally induced by either thermal or via photochemical routes. The isomerisation is interesting in the terms of a salt isomerising to form a cocrystalline material.

The thermal analysis of structures has given extra insight to the crystal structures of the new binary materials. The expansion and contraction of lattice parameters from 100 to 295 K has allowed for both quantitative and qualitative structural analysis to be performed. To take this work further, the data collected could be used to aid future crystal structure prediction.

A combined use of powder X-ray, neutron and single crystal diffraction has been used to explain the crystal structure of oxamic acid. It is clear that the oxamic acid molecules line up in a regular fashion in the [010] direction, but due to conformational (*syn* or *anti*) flexibility, it becomes hard to place electron density within the unit cell. In the analysis performed thus far the *syn* conformation is the most predominate, as the majority of the powder structures adopted the *syn* conformation, as did the single crystal structure, along with the neutron data. Only one DE solution adopted the *anti* conformer, but that did relate to the lowest % R_{wp} structure. A *anti*-oxamic acid molecule would give rise to a more favourable hydrogen bond network over the *syn* conformer. The structure solution of oxamic acid portrays the problem of structural analysis of small molecular materials with functional groups of similar electron density, even with the aid of multiple diffraction techniques, only further analysis would prevent discussion on the final structure solution.

Appendix A: The HPLC analysis of oxamic acid:isonicotinamide and oxamic acid:nicotinamide

749 Isonicotinamide

Sample Name:	Isonicotinamide	Injection Volume:	20.0
Vial Number:	1	Channel:	UV_VIS_1
Sample Type:	unknown	Wavelength:	210
Control Program:		Bandwidth:	1
Quantif. Method:	default	Dilution Factor:	1.0000
Recording Time:	17/4/07 9:12	Sample Weight:	1.0000
Run Time (min):	24.63	Sample Amount:	1.0000

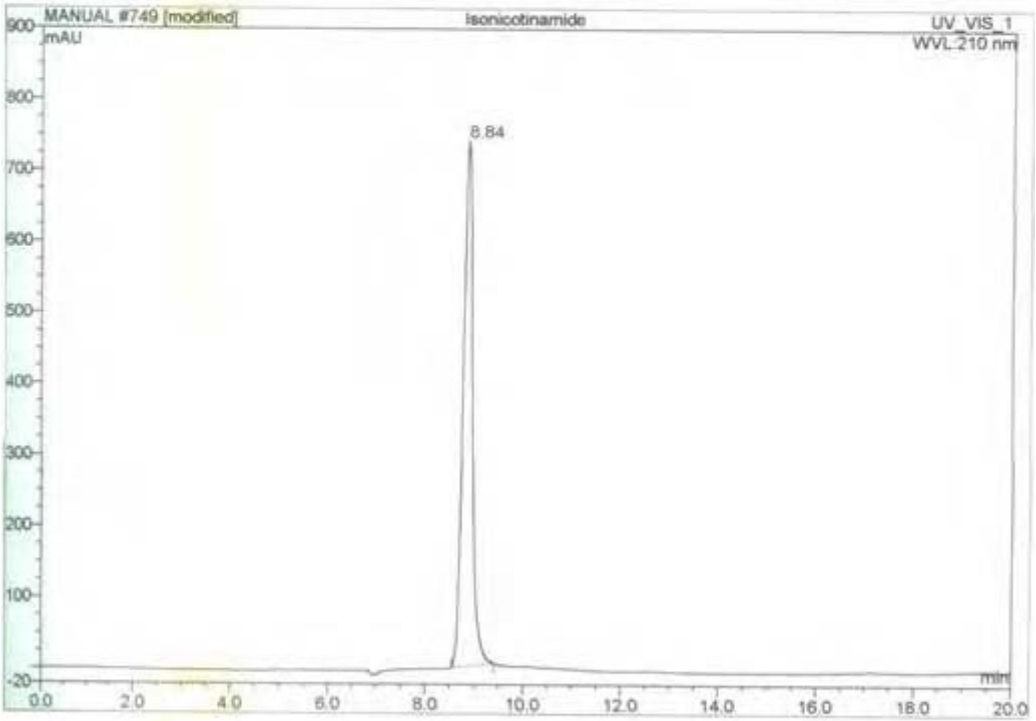

No.	Ret.Time min	Peak Name	Height mAU	Area mAU*min	Rel.Area %	Amount	Type
1	8.84	n.a.	736.981	165.779	99.40	n.a.	BMB*
2	23.59	n.a.	0.741	1.003	0.60	n.a.	BMB
Total:			737.723	166.783	100.00	0.000	

Figure A1: HPLC spectra of isonicotinamide

748 Oxamic acid (1% MeCN in Water+0.05% TFA)(0.5ml/min)

Sample Name:	**Oxamic acid (1% MeCN in Water+0.05% TF**	*Injection Volume:*	**20.0**
Vial Number:	**1**	*Channel:*	**UV_VIS_1**
Sample Type:	**unknown**	*Wavelength:*	**210**
Control Program:		*Bandwidth:*	**1**
Quantif. Method:	**default**	*Dilution Factor:*	**1.0000**
Recording Time:	**17/4/07 8:45**	*Sample Weight:*	**1.0000**
Run Time (min):	**23.40**	*Sample Amount:*	**1.0000**

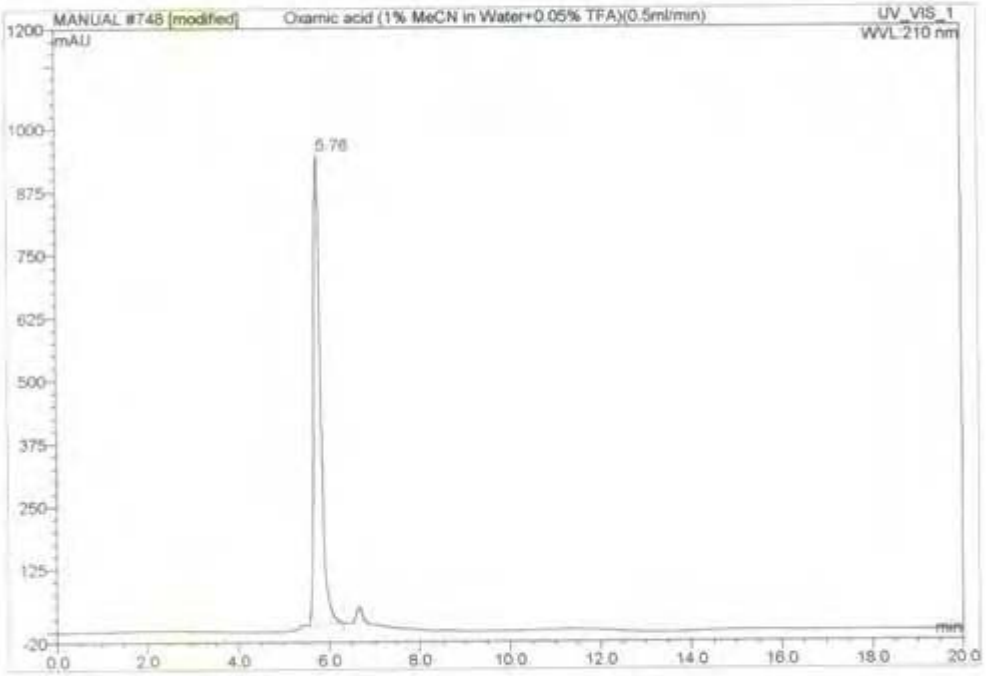

No.	Ret.Time min	Peak Name	Height mAU	Area mAU*min	Rel.Area %	Amount	Type
1	5.76	n.a.	933.770	160.916	100.00	n.a.	BMB*
Total:			933.770	160.916	100.00	0.000	

Figure A2: HPLC spectra of oxamic acid

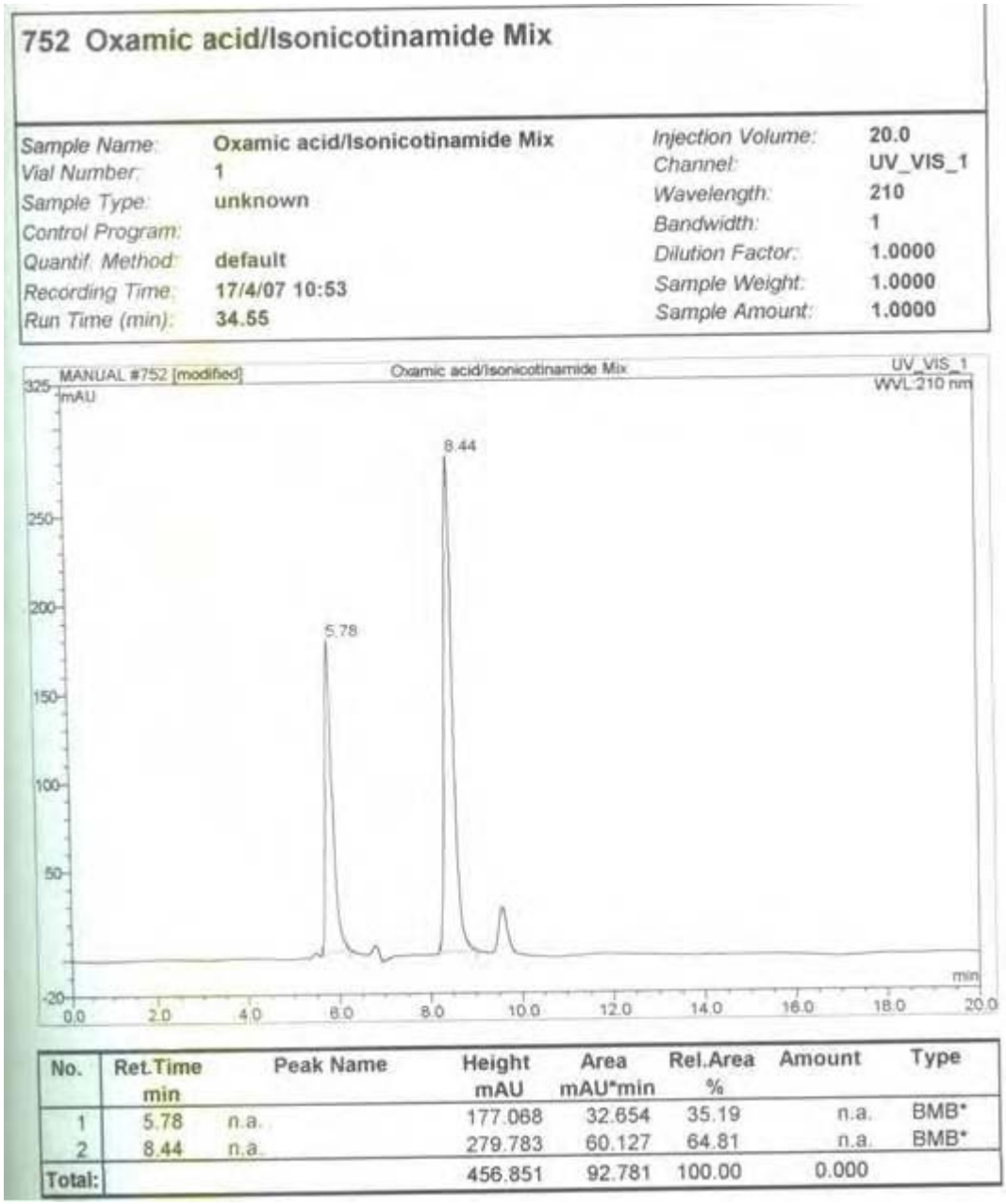

No.	Ret.Time min	Peak Name	Height mAU	Area mAU*min	Rel.Area %	Amount	Type
1	5.78	n.a.	177.068	32.654	35.19	n.a.	BMB*
2	8.44	n.a.	279.783	60.127	64.81	n.a.	BMB*
Total:			456.851	92.781	100.00	0.000	

Figure A3: The HPLC spectra of oxamic acid:isonicotinamide

750 Nicotinamide

Sample Name:	**Nicotinamide**	*Injection Volume:*	**20.0**
Vial Number:	**1**	*Channel:*	**UV_VIS_1**
Sample Type:	**unknown**	*Wavelength:*	**210**
Control Program:		*Bandwidth:*	**1**
Quantif. Method:	**default**	*Dilution Factor:*	**1.0000**
Recording Time:	**17/4/07 9:38**	*Sample Weight:*	**1.0000**
Run Time (min):	**27.02**	*Sample Amount:*	**1.0000**

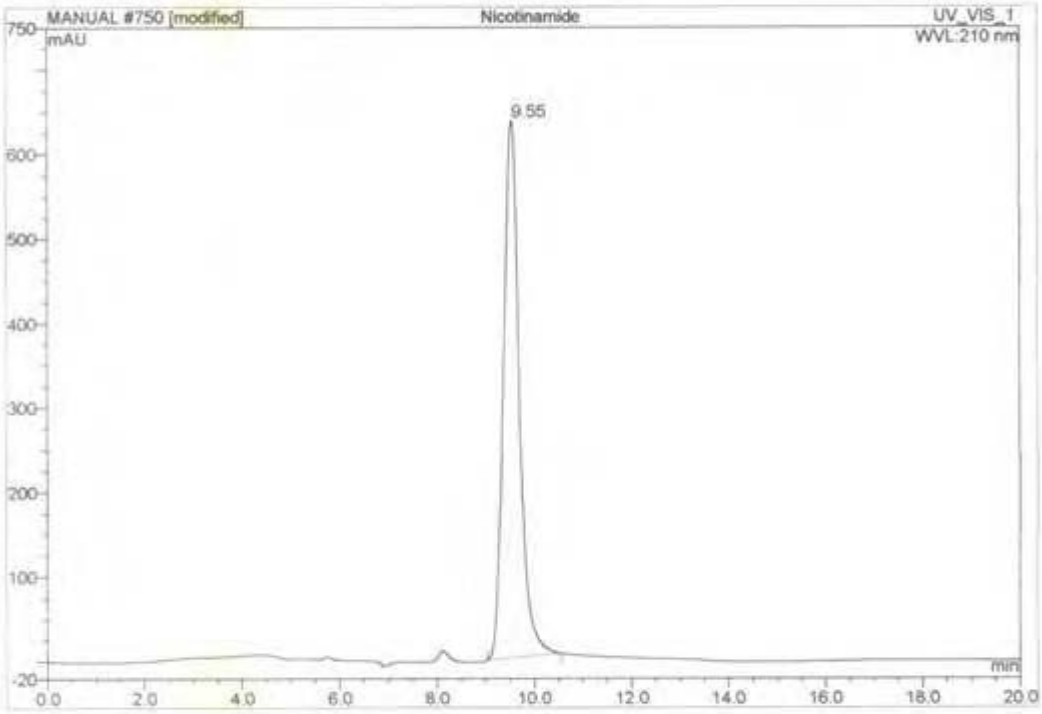

No.	Ret.Time min	Peak Name	Height mAU	Area mAU*min	Rel.Area %	Amount	Type
1	9.55	n.a.	635.072	240.624	100.00	n.a.	BMB*
Total:			635.072	240.624	100.00	0.000	

Figure A4: HPLC spectra of nicotinamide

751 Oxamic acid/Nicotinamide Mix

Sample Name:	**Oxamic acid/Nicotinamide Mix**	*Injection Volume:*	**20.0**
Vial Number:	**1**	*Channel:*	**UV_VIS_1**
Sample Type:	**unknown**	*Wavelength:*	**210**
Control Program:		*Bandwidth:*	**1**
Quantif. Method:	**default**	*Dilution Factor:*	**1.0000**
Recording Time:	**17/4/07 10:11**	*Sample Weight:*	**1.0000**
Run Time (min):	**39.09**	*Sample Amount:*	**1.0000**

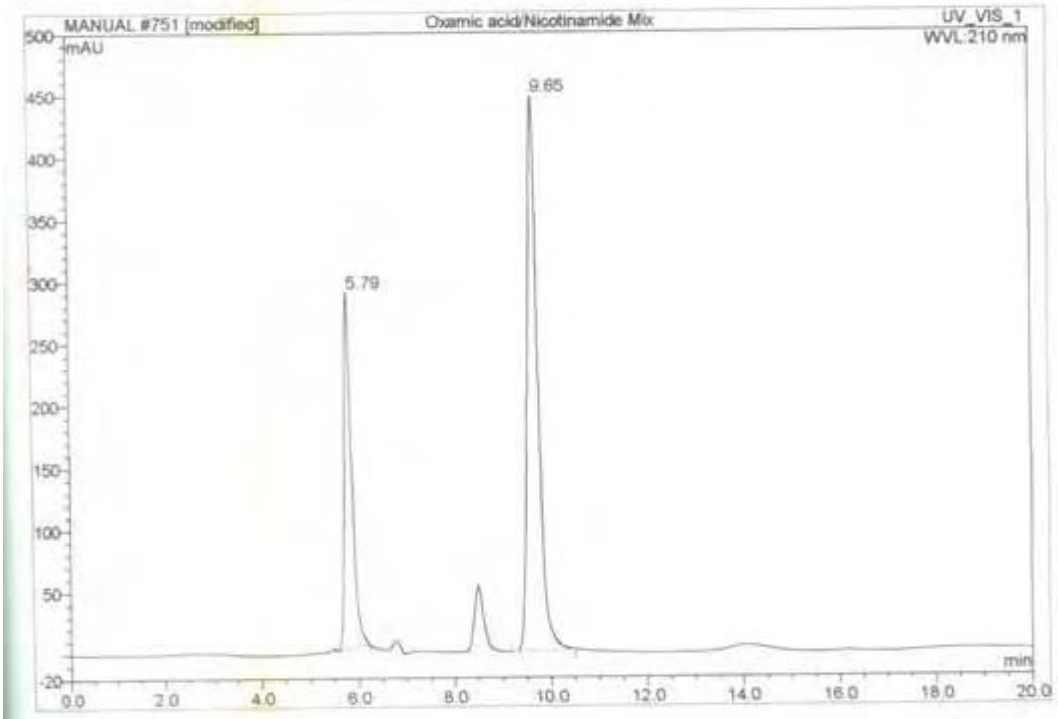

No.	Ret.Time min	Peak Name	Height mAU	Area mAU*min	Rel.Area %	Amount	Type
1	5.79	n.a.	287.180	51.738	31.25	n.a.	BMB*
2	9.65	n.a.	447.476	113.805	68.75	n.a.	BMB*
Total:			734.657	165.542	100.00	0.000	

Figure A5: HPLC spectra of oxamic acid:nicotinamide

Appendix B: The DSC trace of oxamic acid:isonicotinamide

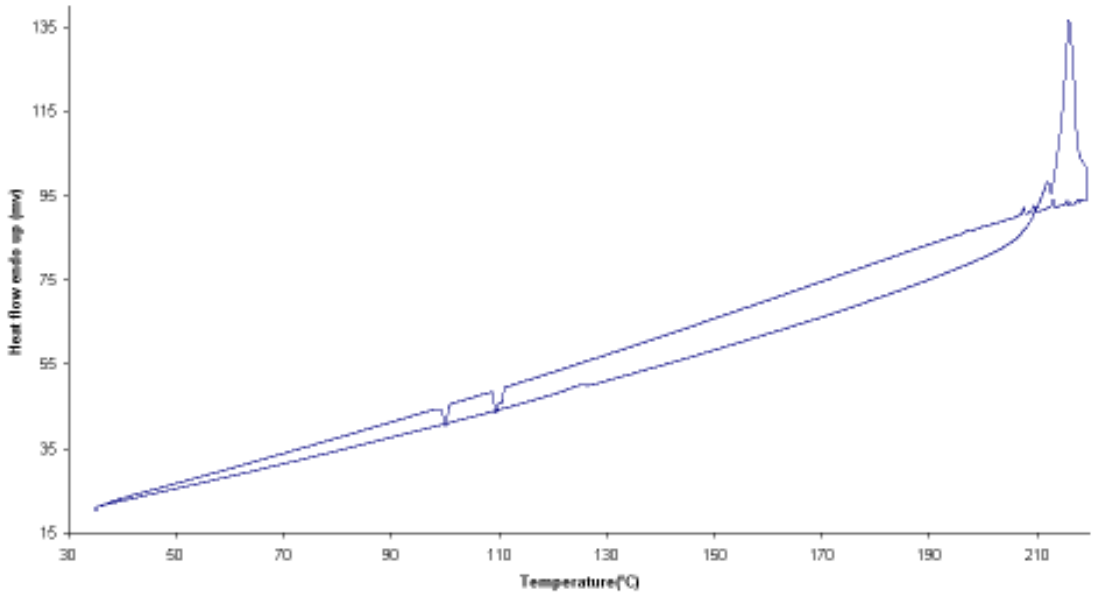

Figure B1: DSC trace of oxamic acid and isonicotinamide

Appendix C: Stoichiometric diversity of oxamic acid:isonicotinamide

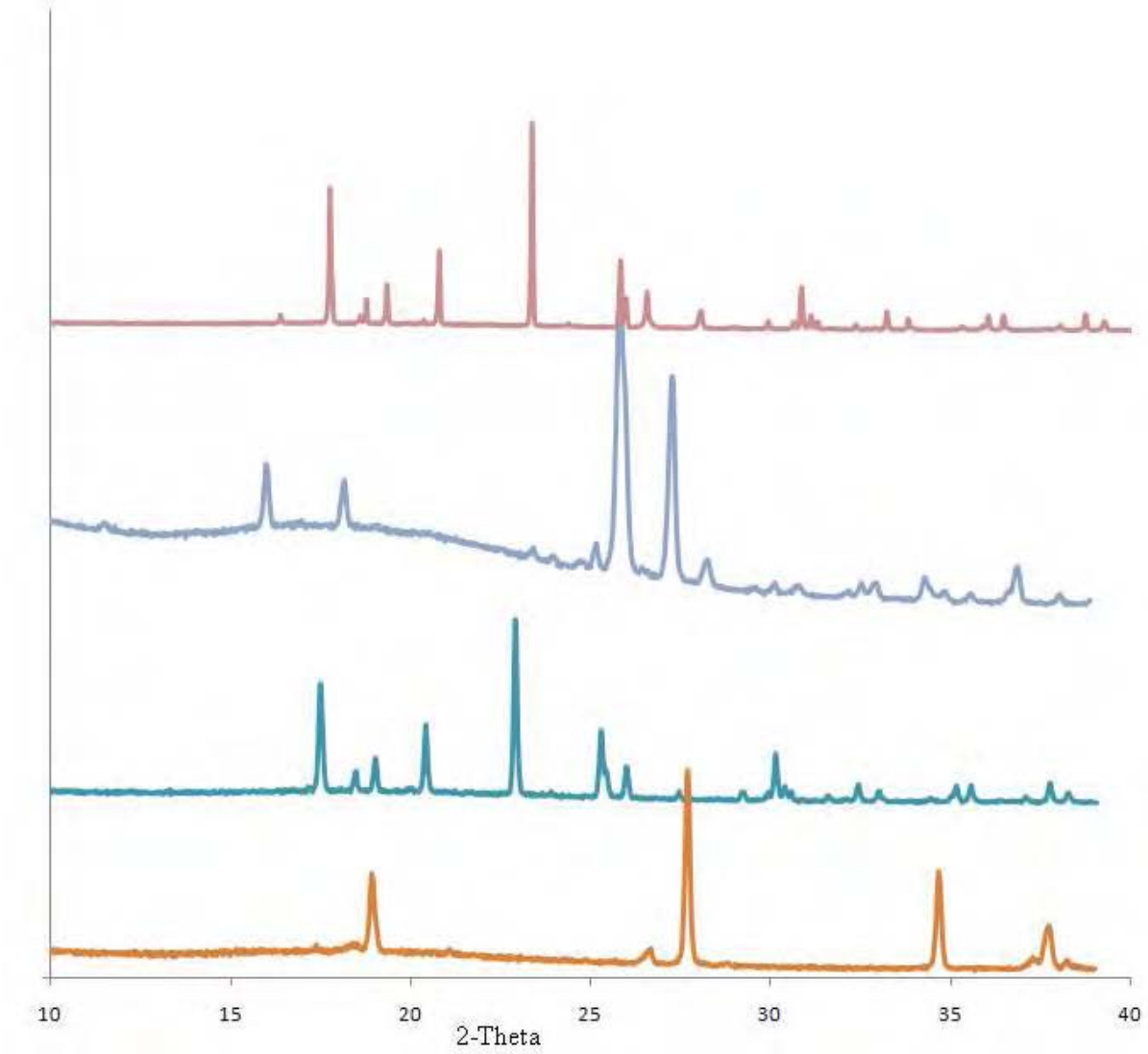

Figure C1 : The pxrd patterns of oxamic acid (orange), isonicotinamide (aqua), oxamic acid 1:1 isonicotinamide(blue), oxamic acid 1:2 isonicotinamide(red).

Appendix D: DSC trace of oxamic acid:nicotinamide

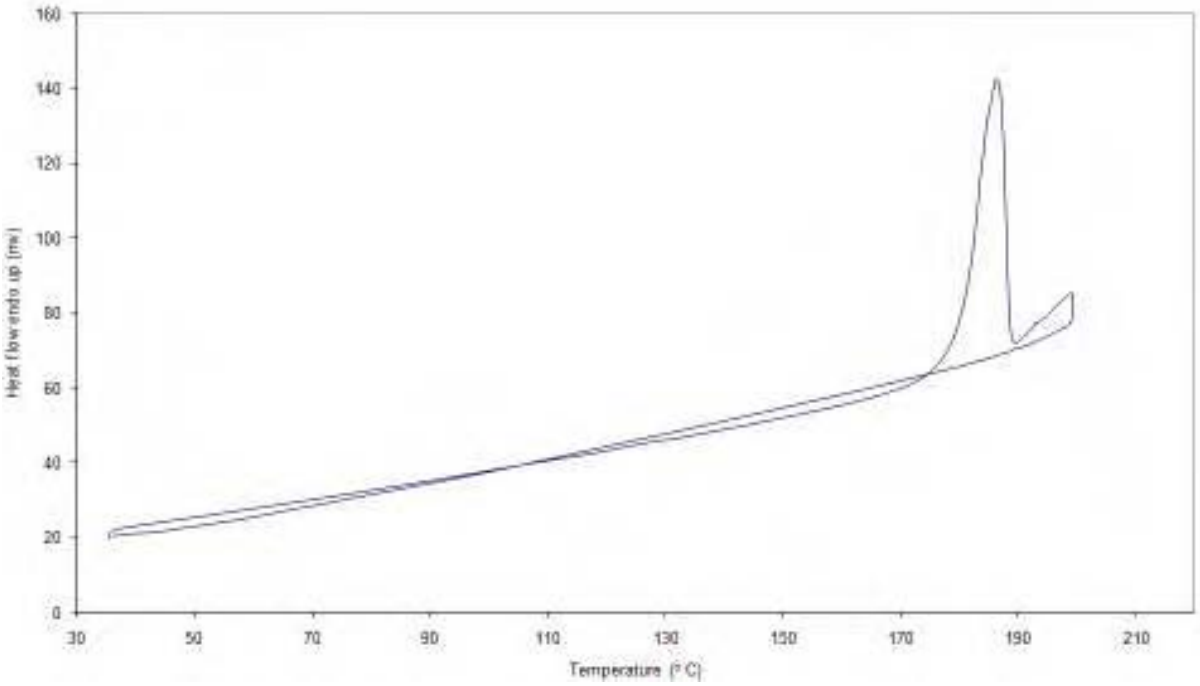

Figure D1: DSC trace of oxamic acid:nicotinamdie

Appendix E: Stoichiometric diversity of fumaric acid:nicotinamide

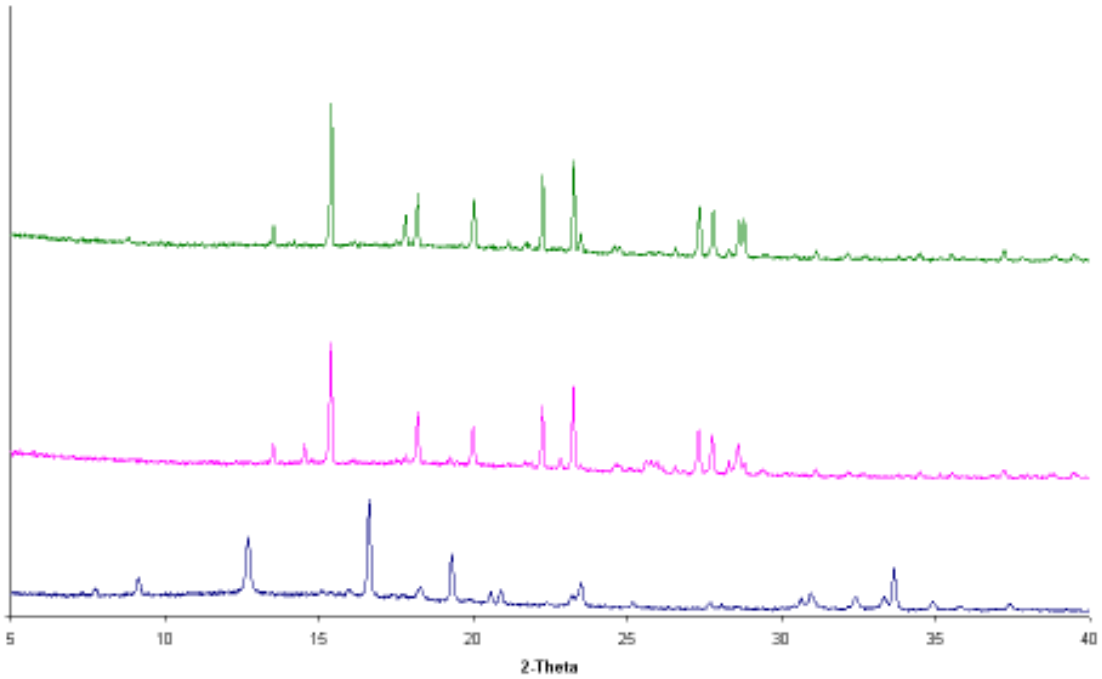

Figure E1: Diffraction patterns of fumaric acid and nicotinamide in 1:1 (from solution) in blue and 1:2 ratios (ground in pink and sonic slurry in green).

Appendix F: DSC trace of maleic acid:nicotinamide product A

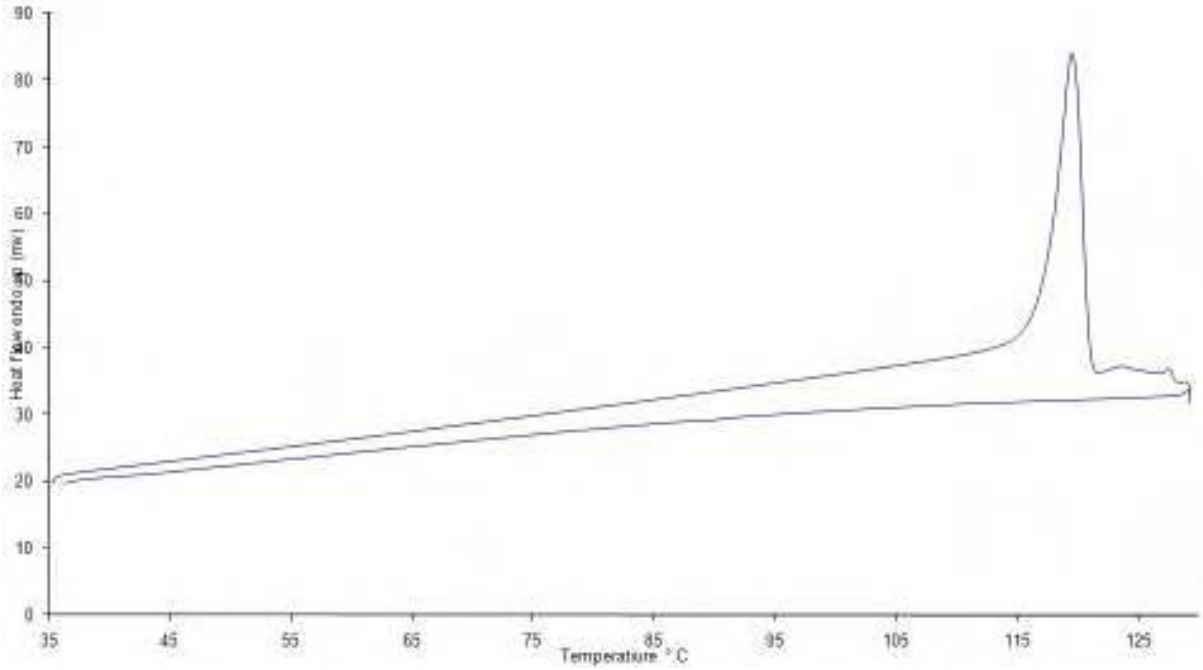

Figure F1: DSC trace of maleic acid:nicotinamide product A

Appendix G: DSC trace of maleic acid:nicotinamide product B

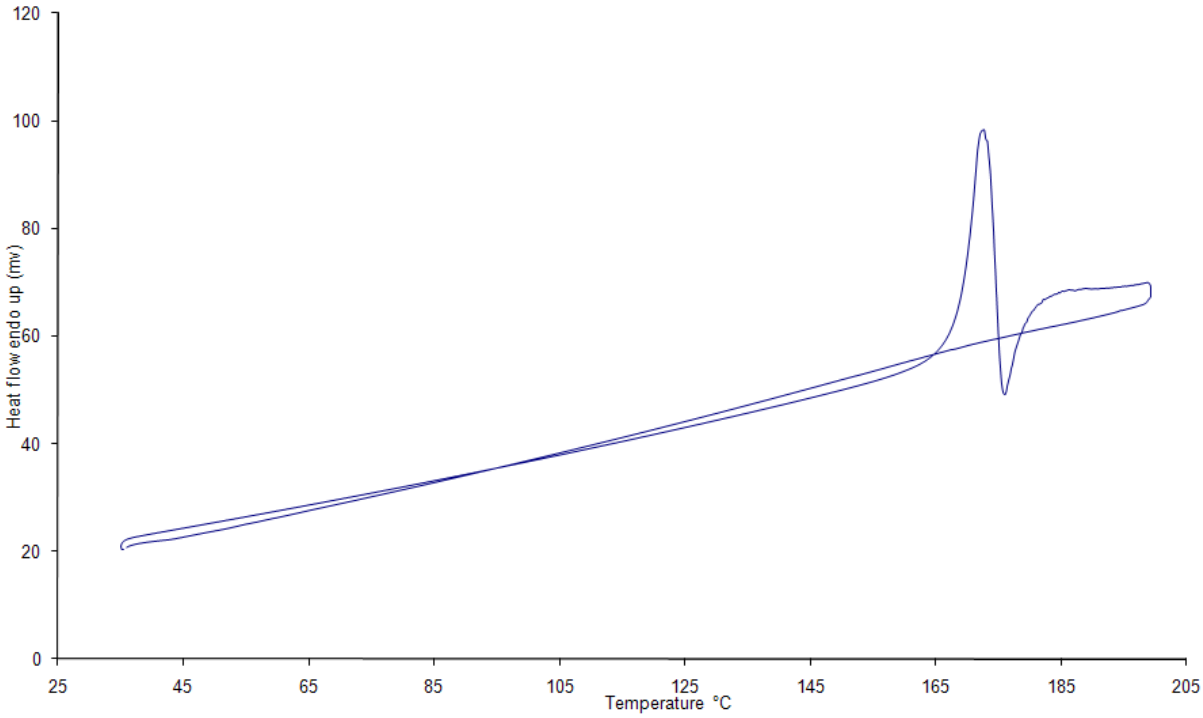

Figure G1: DSC trace of maleic acid:nicotinamide product B

Appendix H: Cocrystallisation of succinic acid:nicotinamide

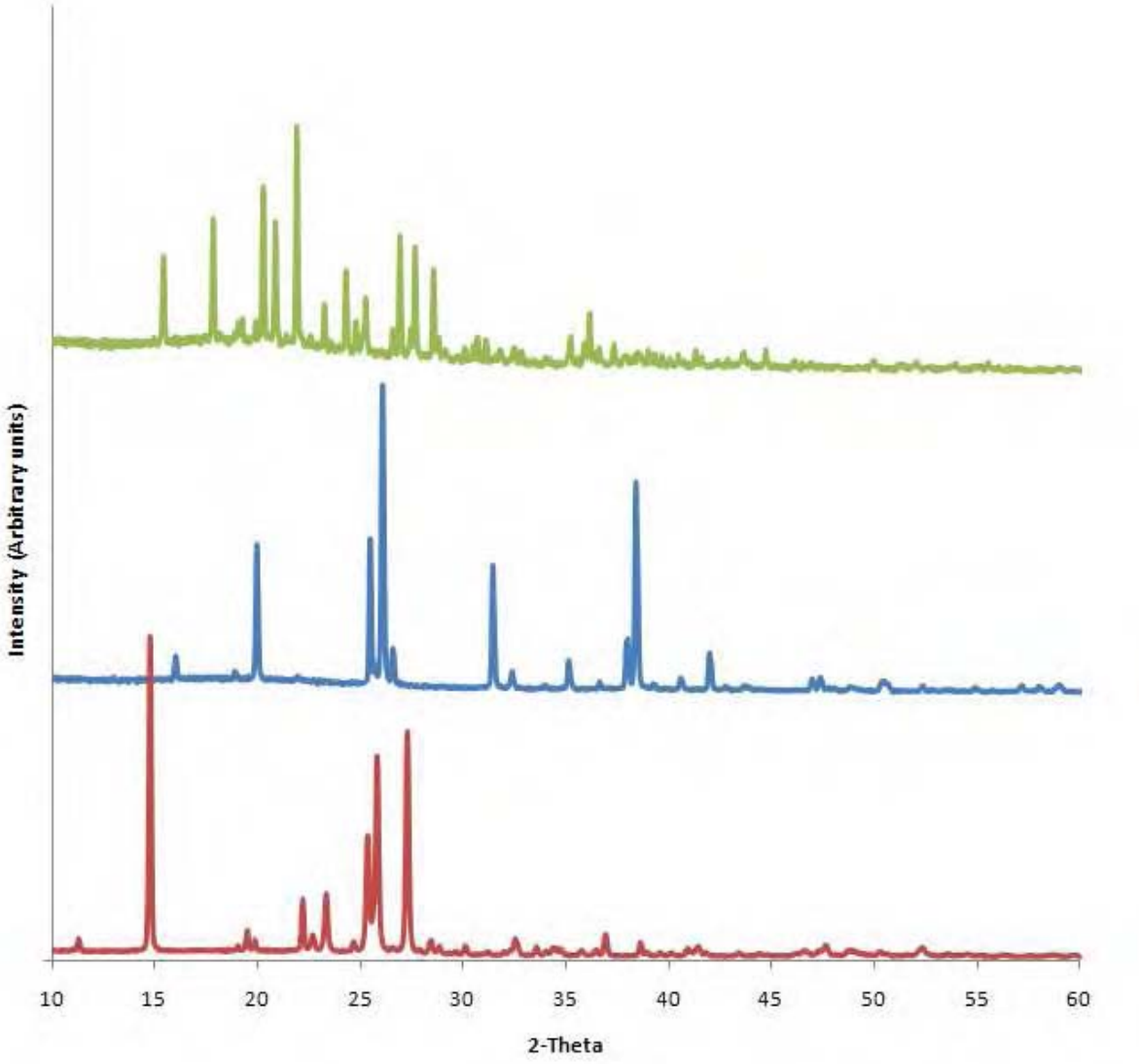

Figure H1: Powder X-ray diffraction patterns of the starting materials, nicotinamide(red), succinic acid (blue) and succinic acid:nicotinamide (green)

Appendix I: Cocrystallisation of adipic acid:nicotinamide

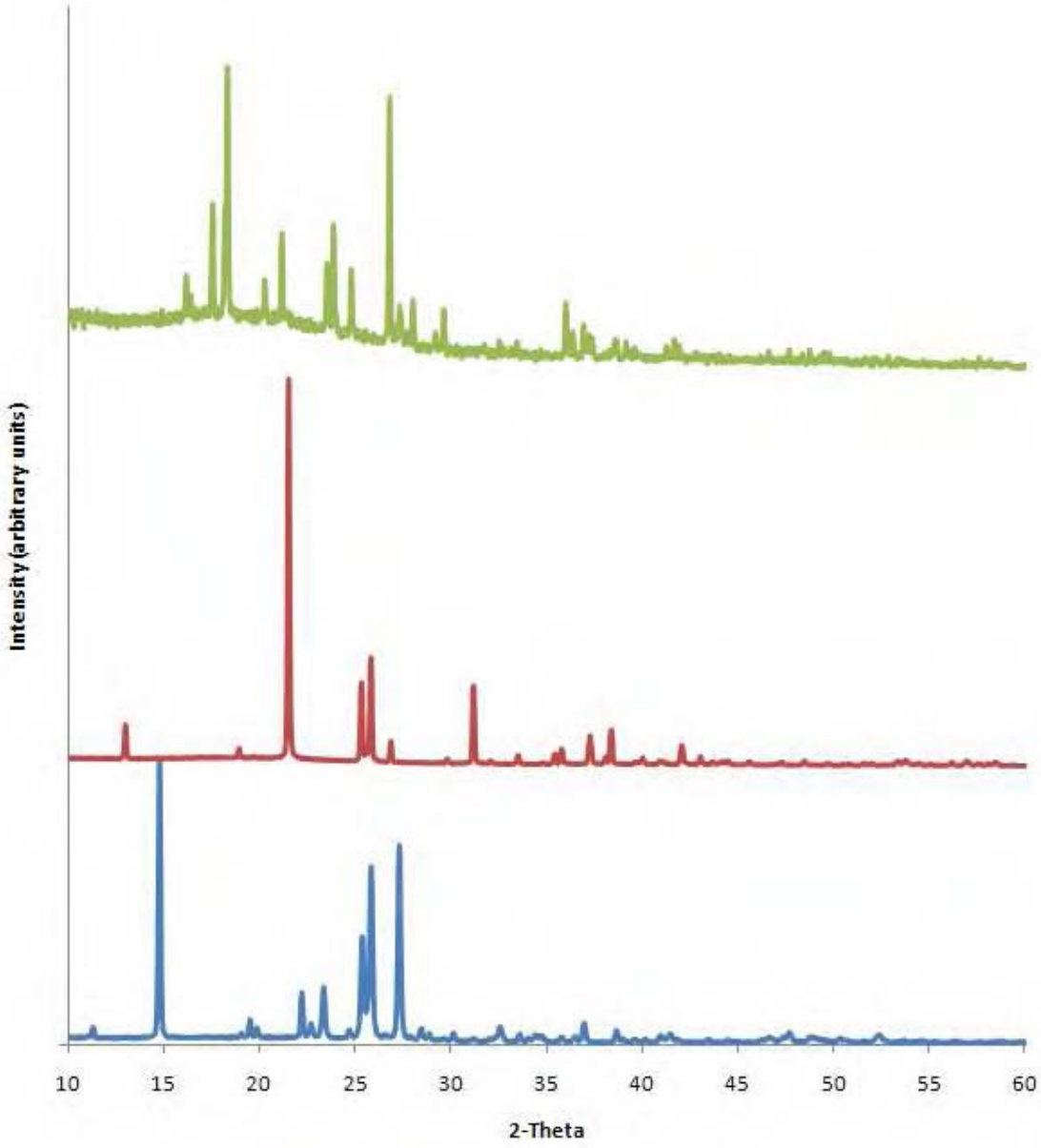

Figure I1: Powder X-ray diffraction pattern of starting materials, nicotinamide(blue), adipic acid(red) and adipic acid:nicotinamide (green)

Appendix J: Indexing oxamic acid:isonicotinamide

Merit	Volume	V/Vl	BL	IndexProg	Date	Time	Pedig	a	b	c	alpha	beta	gamma
18.8	876.002	1.00	P	DICVOL91/log	18May07	16:59:58	Mon_10	30.5282	7.7522	3.7285	90.000	96.898	90.000
18.8	876.002	1.00	P	DICVOL91/log	18May07	15:42:04	Mon_10	30.5282	7.7522	3.7285	90.000	96.898	90.000
18.8	876.002	1.00	P	DICVOL91/log	18May07	15:35:29	Mon_10	30.5282	7.7522	3.7285	90.000	96.898	90.000
18.6	876.175	1.00	P	DICVOL91/log	18May07	16:59:58	Mon_17	31.2233	7.7529	3.7292	90.000	103.932	90.000
18.6	876.175	1.00	P	DICVOL91/log	18May07	15:42:04	Mon_17	31.2233	7.7529	3.7292	90.000	103.932	90.000
18.6	876.175	1.00	P	DICVOL91/log	18May07	15:35:29	Mon_17	31.2233	7.7529	3.7292	90.000	103.932	90.000
17.3	875.887	1.00	P	DICVOL91/log	18May07	16:59:58	Mon_27	33.7474	7.7541	3.7280	90.000	116.124	90.000
17.3	875.887	1.00	P	DICVOL91/log	18May07	15:42:04	Mon_27	33.7474	7.7541	3.7280	90.000	116.124	90.000
17.3	875.887	1.00	P	DICVOL91/log	18May07	15:35:29	Mon_27	33.7474	7.7541	3.7280	90.000	116.124	90.000
16.7	876.838	1.00	P	DICVOL91/log	18May07	16:59:58	Mon__2	7.7521	30.1089	3.7319	90.000	90.080	90.000
16.7	876.838	1.00	P	DICVOL91/log	18May07	15:42:04	Mon__2	7.7521	30.1089	3.7319	90.000	90.080	90.000
16.7	876.838	1.00	P	DICVOL91/log	18May07	15:35:29	Mon__2	7.7521	30.1089	3.7319	90.000	90.080	90.000
16.3	876.379	1.00	P	DICVOL91/log	18May07	16:59:58	Mon__8	30.3027	7.7532	3.7302	90.000	90.188	90.000
16.3	876.379	1.00	P	DICVOL91/log	18May07	15:42:04	Mon__8	30.3027	7.7532	3.7302	90.000	90.188	90.000
16.3	876.379	1.00	P	DICVOL91/log	18May07	15:35:29	Mon__8	30.3027	7.7532	3.7302	90.000	90.188	90.000
16.2	876.434	1.00	P	DICVOL91/log	18May07	16:59:58	Mon__7	30.3081	7.7523	3.7303	90.000	90.191	90.000
16.2	876.434	1.00	P	DICVOL91/log	18May07	15:42:04	Mon__7	30.3081	7.7523	3.7303	90.000	90.191	90.000
16.2	876.434	1.00	P	DICVOL91/log	18May07	15:35:29	Mon__7	30.3081	7.7523	3.7303	90.000	90.191	90.000
15.8	876.656	1.00	P	DICVOL91/log	18May07	16:59:58	Mon_26	31.8222	7.7488	3.7314	90.000	116.306	90.000
15.8	876.656	1.00	P	DICVOL91/log	18May07	15:42:04	Mon_26	31.8222	7.7488	3.7314	90.000	116.306	90.000
15.8	876.656	1.00	P	DICVOL91/log	18May07	15:35:29	Mon_26	31.8222	7.7488	3.7314	90.000	116.306	90.000
15.4	876.745	1.00	P	DICVOL91/log	18May07	16:59:58	Mon_21	32.3271	7.7521	3.7318	90.000	110.365	90.000
15.4	876.745	1.00	P	DICVOL91/log	18May07	15:42:04	Mon_21	32.3271	7.7521	3.7318	90.000	110.365	90.000
15.4	876.745	1.00	P	DICVOL91/log	18May07	15:35:29	Mon_21	32.3271	7.7521	3.7318	90.000	110.365	90.000
14.8	876.722	1.00	P	DICVOL91/log	18May07	16:59:58	Mon_28	33.7783	7.7459	3.7303	90.000	116.068	90.000
14.8	876.722	1.00	P	DICVOL91/log	18May07	15:42:04	Mon_28	33.7783	7.7459	3.7303	90.000	116.068	90.000
14.8	876.722	1.00	P	DICVOL91/log	18May07	15:35:29	Mon_28	33.7783	7.7459	3.7303	90.000	116.068	90.000
14.8	876.719	1.00	P	DICVOL91/log	18May07	16:59:58	Mon_19	32.3132	7.7459	3.7303	90.000	110.116	90.000
14.8	876.719	1.00	P	DICVOL91/log	18May07	15:42:04	Mon_19	32.3132	7.7459	3.7303	90.000	110.116	90.000
14.8	876.719	1.00	P	DICVOL91/log	18May07	15:35:29	Mon_19	32.3132	7.7459	3.7303	90.000	110.116	90.000
11.2	875.516	1.00	P	DICVOL91/log	18May07	16:59:58	Mon_20	32.3175	7.7556	3.7273	90.000	110.419	90.000
11.2	875.516	1.00	P	DICVOL91/log	18May07	15:42:04	Mon_20	32.3175	7.7556	3.7273	90.000	110.419	90.000
11.2	875.516	1.00	P	DICVOL91/log	18May07	15:35:29	Mon_20	32.3175	7.7556	3.7273	90.000	110.419	90.000
12.7	876.803	1.00	P	DICVOL91/log	18May07	16:59:58	Ort__1	30.3491	7.7446	3.7304	90.000	90.000	90.000
12.7	876.803	1.00	P	DICVOL91/log	18May07	15:42:04	Ort__1	30.3491	7.7446	3.7304	90.000	90.000	90.000
12.7	876.803	1.00	P	DICVOL91/log	18May07	15:35:29	Ort__1	30.3491	7.7446	3.7304	90.000	90.000	90.000
11.6	876.994	1.00	P	DICVOL91/log	18May07	16:59:58	Mon__1	7.7455	30.3450	3.7313	90.000	90.023	90.000
11.6	876.994	1.00	P	DICVOL91/log	18May07	15:42:04	Mon__1	7.7455	30.3450	3.7313	90.000	90.023	90.000
11.6	876.994	1.00	P	DICVOL91/log	18May07	15:35:29	Mon__1	7.7455	30.3450	3.7313	90.000	90.023	90.000
11.4	876.287	1.00	P	DICVOL91/log	18May07	16:59:58	Mon__5	30.3140	3.7309	7.7480	90.000	90.043	90.000
11.4	876.287	1.00	P	DICVOL91/log	18May07	15:42:04	Mon__5	30.3140	3.7309	7.7480	90.000	90.043	90.000
11.4	876.287	1.00	P	DICVOL91/log	18May07	15:35:29	Mon__5	30.3140	3.7309	7.7480	90.000	90.043	90.000
10.2	877.082	1.00	P	DICVOL91/log	18May07	16:59:58	Mon__3	30.3125	3.7321	7.7525	90.000	89.979	90.000
10.2	877.082	1.00	P	DICVOL91/log	18May07	15:42:04	Mon__3	30.3125	3.7321	7.7525	90.000	89.979	90.000
10.2	877.082	1.00	P	DICVOL91/log	18May07	15:35:29	Mon__3	30.3125	3.7321	7.7525	90.000	89.979	90.000
10.1	876.748	1.00	P	DICVOL91/log	18May07	16:59:58	Mon__6	30.3539	3.7281	7.7477	90.000	90.039	90.000
10.1	876.748	1.00	P	DICVOL91/log	18May07	15:42:04	Mon__6	30.3539	3.7281	7.7477	90.000	90.039	90.000
10.1	876.748	1.00	P	DICVOL91/log	18May07	15:35:29	Mon__6	30.3539	3.7281	7.7477	90.000	90.039	90.000
9.8	876.729	1.00	P	DICVOL91/log	18May07	16:59:58	Mon_22	8.5874	30.3571	3.7304	90.000	115.638	90.000
9.8	876.729	1.00	P	DICVOL91/log	18May07	15:42:04	Mon_22	8.5874	30.3571	3.7304	90.000	115.638	90.000

Figure 1: Indexing output from CRYSFIRE for oxamic acid:isonicotinamide

Appendix K: Structure determination of oxamate:isonicotinamide

K1: Single crystal determination of oxamate:isonicotinamide

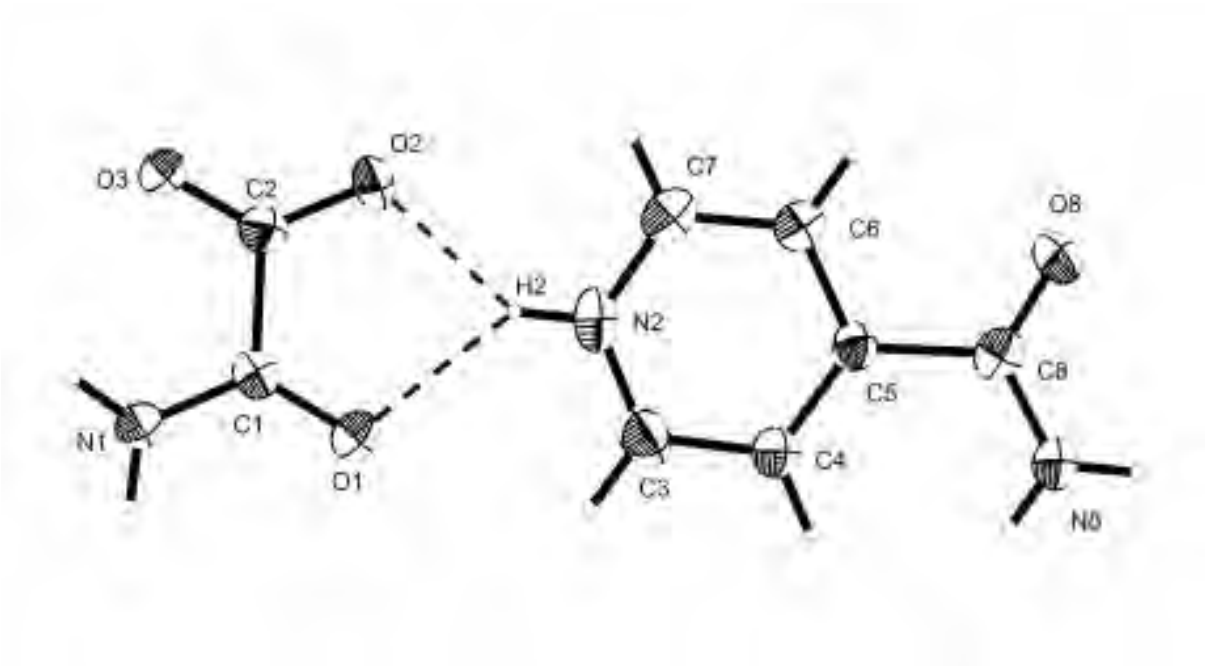

Figure K1: Atomic numbering scheme for oxamate:isonicotinamide single crystal solution

Selected intramolecular geometric parameters in oxamate:isonicotinamide (Å and °)

C1-O1 1.234(4)	C1-N1 1.325(4)	C1-C2 1.554(5)
C2-O3 1.263(4)	C3-N2 1.331(5)	C3-C4 1.383(5)
C3-H3 0.9300	C4-C5 1.386(5)	C4-H4 0.9300
C5-C6 1.388(5)	C5-C8 1.524(5)	C6-C7 1.374(5)
C6-H6 0.9300	C7-N2 1.342(5)	C7-H7 0.9300
C8-O8 1.235(4)	C8-N8 1.325(5)	N1-H1A 0.8600
N1-H1B 0.8600	N2-H2 0.8600	N8-H8A 0.8600
N8-H8B 0.8600		

O1-C1-N1 123.8(4)	O1-C1-C2 120.2(3)	N1-C1-C2 116.0(3)
O3-C2-O2 127.1(4)	O3-C2-C1 118.9(3)	O2-C2-C1 114.0(3)
N2-C3-C4 120.0(4)	N2-C3-H3 120.0	C4-C3-H3 120.0
C3-C4-C5 119.2(4)	C3-C4-H4 120.4	C5-C4-H4 120.4
C4-C5-C6 119.1(3)	C4-C5-C8 123.1(3)	C6-C5-C8 117.7(3)
C7-C6-C5 119.5(4)	C7-C6-H6 120.3	C5-C6-H6 120.3
N2-C7-C6 119.9(4)	N2-C7-H7 120.0	C6-C7-H7 120.0
O8-C8-N8 124.0(4)	O8-C8-C5 118.9(4)	N8-C8-C5 117.1(3)
C1-N1-H1A 120.0	C1-N1-H1B 120.0	H1A-N1-H1B 120.0

C3-N2-C7 122.2(3)

Table K1 : Final refined atomic positions and isotropic displacement factors for oxamate:isonicotinamide

Atom	x	y	z	U_{iso}/Å^2
C1	0.4322(12)	0.3097(5)	0.21109(11)	0.0310(11)
C2	0.5427(12)	0.4571(5)	0.17934(12)	0.0316(11)
C3	0.9173(12)	-0.0804(6)	0.14158(13)	0.0394(12)
H3	0.83230	-0.10480	0.16970	0.047
C4	1.0518(12)	-0.2115(5)	0.11562(11)	0.0322(11)
H4	1.0565	-0.3241	0.1260	0.039
C5	1.1794(11)	-0.1731(5)	0.07395(11)	0.0272(10)
C6	1.1697(12)	-0.0039(5)	0.05934(13)	0.0341(12)
H6	1.2551	0.0242	0.0315	0.041
C7	1.0330(14)	0.1217(5)	0.08629(13)	0.389
H7	1.0260	0.2355	0.0768	0.047
C8	1.3144(12)	-0.3097(5)	0.04206(13)	0.0337(11)
N1	0.2662(10)	0.3575(4)	0.24758(10)	0.0443(11)
H1A	0.1947	0.2812	0.2661	0.053
H1B	0.2299	0.4649	0.2528	0.053
N2	0.9096(9)	0.0801(4)	0.12636(10)	0.0366(10)
H2	0.8226	0.1600	0.1428	0.044
N8	1.4348(10)	-0.4553(4)	0.05931(10)	0.0403(10)
H8A	1.5119	-0.5359	0.0424	0.048
H8B	1.4359	-0.4691	0.0874	0.048
O1	0.4941(8)	0.1584(3)	0.20132(8)	0.0415(8)
O2	0.6705(8)	0.4054(3)	0.14323(8)	0.0437(9)
O3	0.4975(9)	0.6072(3)	0.19098(8)	0.0437(9)
O8	1.3038(8)	-0.2797(3)	0.00216(8)	0.0480(9)

Table K2: Experimental details – single-crystal data for oxamate:isonicotinamide

Crystal data	
Chemical formula	$C_6H_7N_2O$, $C_2H_2NO_3$
M_r	211.8
Space group, cell setting	$P2_1/_n$, Monoclinic
a , b, c	3.7386(18), 7.771(3), 30.372(13)
Beta (˚)	90.15(2)
V (Å^3)	882.4(7)
Z	4
D_x (Mg m^{-3})	1.590
Radiation type	Cu Kα
μ (mm^{-1})	1.115
Specimen form, colour	Plate, colourless
Specimen size (mm)	0.30 x 0.24 x 0.05
Data Collection	
Diffractometer	Bruker Smart 6000 CCD
Data Collection method	CCD slices
Absorption correction	Empirical (using intensity measurements)
T_{min}	0.7308
T_{max}	0.9463
No. Of measured, independent and observed reflections	4376, 1080, 898
Criterion for observed reflections	$I>2\sigma(I)$
R_{int}	0.0543
R_{max}	55.95
Refinement	
Refinement on	F^2
$R[F^2>2\sigma(F^2)]$, $wR(F^2)$, S	0.0600, 0.0971, 1.046
Reflection/profile data	1080 reflections
H-atom treatment	Constrained to parent site
Weighting Scheme	$W = 1/[\sigma^2(F^2_0) + (0.0112P)^2 + 0.6383P]$, where $P = (F^2_0 + F^2_C)/3$
(Δ/σ) max	< 0.0001
$\Delta\rho_{max}$, $\Delta\rho_{min}$(e Å^{-3})	0.213, -0.201

K2: Powder crystal determination of oxamic acid:isonicotinamide

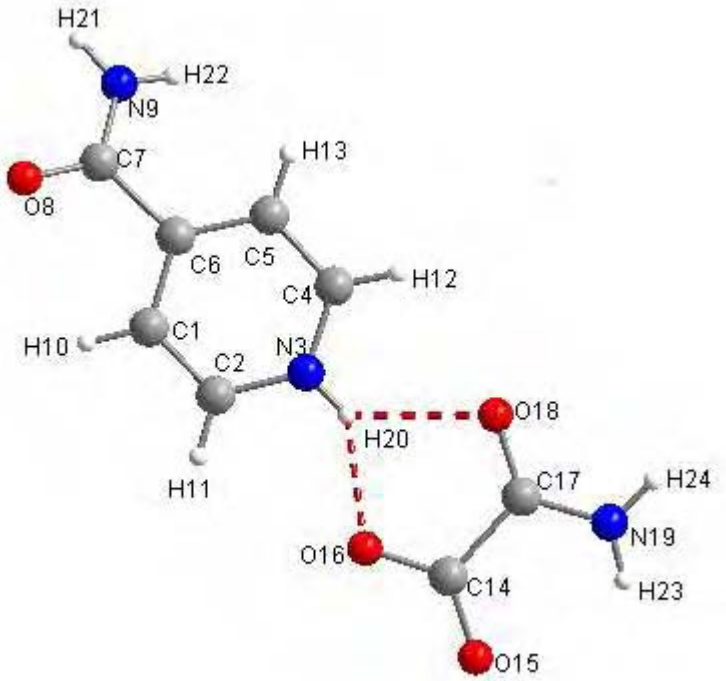

Figure K2: Atomic numbering scheme for oxamate:isonicotinamide

Selected intramolecular geometric parameters in oxamate:isonicotinamide (Å and °)

C1—C2 1.39(1)	C6 –C7 1.51(1)	C17—O18 1.25(1)
C2—N3 1.37(1)	C7—O8 1.24(1)	C17—N19 1.32(1)
N3—C4 1.38(1)	C7—N9 1.02(1)	C4—C5 1.39(1)
C17—C14 1.55(1)	C5—C6 1.40(1)	C14—O16 1.34(1)
C6—C1 1.40(1)	C14—O15 1.25(1)	
C1-C2-N3 118(1)	C6-C7-O8 118(1)	N19-C17-C14 120(1)
C2-N3-C4 122(1)	C6-C7-N9 119(1)	O18-C17-C14 120(1)
N3-C4-C5 119(1)	O8-C7-N9 120(1)	C4-C5-C6 118(1)
O15-C14-O16 118(1)	C5-C6-C1 119(1)	C6-C1-C2 119(1)
O15-C14-C17 118(1)	O16-C14-C17 120(1)	O18-C17-N19 119(1)

Table K3: Final refined atomic positions for oxamic acid:isonicotinamide

Atom	x	y	z
C1	0.115(5)	0.784(1)	0.3846(3)
C2	-0.035(4)	0.906(1)	0.3561(3)
N3	-0.112(4)	1.0687(8)	0.3718(2)
C4	-0.017(4)	1.119(1)	0.4140(3)
C5	0.117(4)	0.996(1)	0.4436(3)
C6	0.151(5)	0.824(1)	0.4296(3)
C7	0.337(5)	0.697(1)	0.4690(1)
O8	0.297(3)	0.7141(14)	0.5004(3)
N9	0.467(4)	0.5487(8)	0.44301(7)
H10	0.234(18)	0.668(4)	0.3714(5)
H11	-0.045(14)	0.880(3)	0.3209(4)
H12	-0.086(15)	1.247(2)	0.4257(7)
H13	0.143(15)	1.027(2)	0.4783(4)
C14	0.557(4)	0.4532(5)	0.3200(2)
O15	0.475(4)	0.608(14)	0.3119(5)
O16	0.643(3)	0.409(2)	0.3617(4)
C17	0.4345(6)	0.3128(12)	0.2866(4)
O18	0.481(5)	0.156(1)	0.2951(5)
N19	0.308(4)	0.357(2)	0.2473(4)
H20	-0.24(3)	1.162(6)	0.350(14)
H21	0.58(4)	0.451(8)	0.4647(4)
H22	0.49(4)	0.525(8)	0.4078(6)
H23	0.31(4)	0.281(8)	0.2379(6)
H24	0.27(4)	0.464(8)	0.2472(6)

Appendix L Structure determination of oxamate:nicotinamide

L1: Single crystal determination of oxamate:nicotinamide

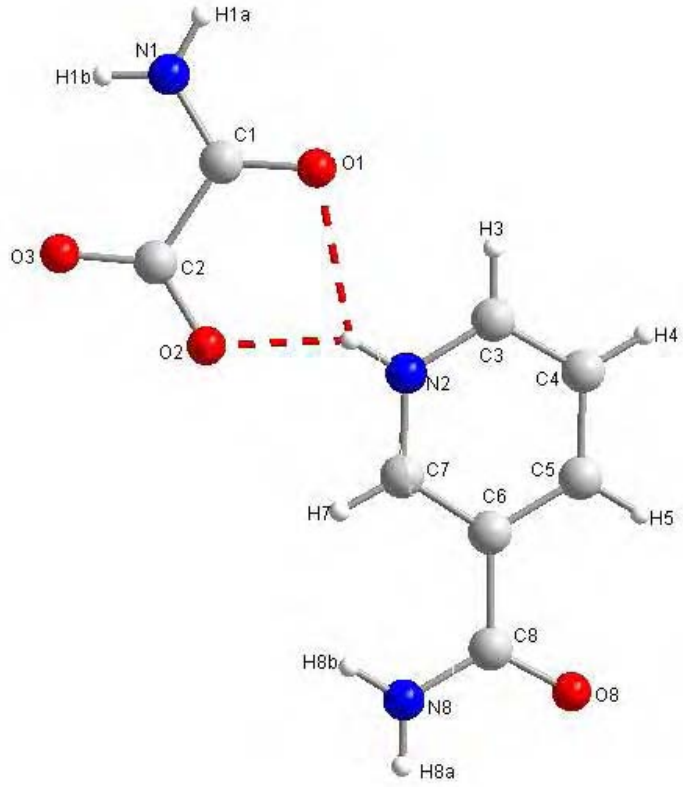

Figure L1: Atomic numbering scheme for oxamate:nicotinamide

Selected intramolecular distances (Å) and angles (°)

C1—O1 1.235(3)	C1—N1 1.318(4)	C1—C2 1.545(4)
C2—O3 1.240(3)	C2—O2 1.256(3)	C3—N2 1.330(4)
C3—C4 1.374(5)	C3—H3 0.9300	C4—C5 1.384(4)
C4—H4 0.9300	C6—H7 1.381(4)	C6—C8 1.503(4)
C7—N2 1.336(4)	C7—H7 0.9300	C8—O8 1.233(3)
C8—N8 1.321(4)	N1—H1A 0.8600	N1—H1B 0.8600
N2—H2 0.8600	N2—N8A 0.8600	N8—H8B 0.8600
O1-C1-N1 124.6(3)	O1-C1-C2 119.6(2)	N1-C1-C2 115.8(2)
O3-C2-O2 126.6(3)	O3-C2-C1 117.8(3)	O2-C2-C1 115.5(2)
N2-C3-C3 119.8(3)	N2-C3-H3 120.1	C4-C3-H3 120.1

C3-C4-C5 118.6(3)	C3-C4-H4 120.7	C5-C4-H4 120.7
C6-C5-C4 120.8(3)	C6-C5-H5 119.6	C4-C5-H5 119.6
C7-C6-C5 117.8(3)	C7-C6-C8 123.0(2)	C5-C6-C8 119.2(2)
N2-C7-C6 120.2(3)	N2-C7-H7 119.9	C6-C7-H7 119.9
O8-C8-N8 123.2(3)	O8-C8-C6 118.3(3)	N8-C8-C6 118.5(2)
C1-N1-H1A 120	C1-N1-H1B 120	H1A-N1-H1B 120
C3-N2-C7 122.7(3)	C3-N2-H2 118.7	C7-N2-H2 118.7
C8-N8-H8A 120.0	C8-N8-H8B 120.0	H8A-N8-H8B 120.0

O1-C1-C2 119.6(2)	O1-C1-N1 124.6	C1-C2-O3 117.9
C1-C2-O2 115.5	O2-C2-C3 126.6	H1A-N1-H1B 120.0
N2-C3-C4 119.8	C3-C4-C5 118.6	C4-C5-C6 120.8
C5-C6-C7 117.8	C6-C7-N2 120.2	C7-N2-C3 122.7
C6-C8-O8 118.3	C6-C8-N8 118.4	O8-C8-N8 123.2

Table L1: Final refined atomic positions and isotropic displacement factors for oxamate:nicotinamide – single crystal structure

Atom	x	y	z	U_{iso}/Å^2
C1	0.5012(4)	0.1450(3)	-0.1106(2)	0.0333(7)
C2	0.4988(4)	0.2488(3)	-0.1954(2)	0.0351(7)
C3	0.7856(5)	0.4051(3)	0.1090(2)	0.0426(8)
H3	0.7501	0.3190	0.1257	0.051
C4	0.9014(6)	0.4862(3)	0.1814(2)	0.0483(6)
H4	0.9467	0.4553	0.2472	0.058
C5	0.9492(5)	0.6147(3)	0.1544(2)	0.0420(8)
H5	1.0280	0.6705	0.2025	0.050
C6	0.8814(4)	0.6611(3)	0.0569(2)	0.0318(7)
C7	0.7676(4)	0.5742(3)	-0.0127(2)	0.0336(7)
H7	0.7208	0.6021	-0.0790	0.040
C8	0.9347(4)	0.8018(3)	0.0309(2)	0.0348(7)
N1	0.4564(4)	0.0194(2)	-0.14010(18)	0.0429(7)
H1A	0.4541	-0.0426	-0.0963	0.051
H1B	0.4294	-0.0004	-0.2031	0.051
N2	0.7247(3)	0.4503(2)	0.01590(18)	0.0357(6)
H2	0.65470	0.39770	-0.02960	0.043
N8	0.8659(4)	0.8454(3)	-0.06221(19)	0.0442(7)
H8A	0.8975	0.9247	-0.0792	0.053
H8B	0.7894	0.7946	-0.1058	0.053
O1	0.5420(3)	0.1830(2)	-0.02199(14)	0.0444(6)
O2	0.5585(4)	0.3655(2)	-0.16670(15)	0.0458(6)
O3	0.4369(4)	0.2105(2)	-0.28373(16)	0.0558(7)
O8	1.0448(3)	0.8696(2)	0.09696(16)	0.0473(6)

Table L2: Experimental details – single-crystal data for oxamate:nicotinamide

Crystal data	
Chemical formula	$C_6H_7N_2O_2$, $C_2H_2NO_3$
M_r	211.8
Space group, cell setting	$P2_1/c$, Monoclinic
a , b, c	6.9742(14), 9.8751(16), 13.676(2)
Beta	103.86(1)
V ($Å^3$)	914.5(3)
Z	4
D_x ($Mg\ m^{-3}$)	1.590
Radiation type	Cu Kα
μ (mm^{-1})	1.076
Specimen form, colour	block, colourless
Specimen size (mm)	0.12 x 0.10 x 0.08
Data Collection	
Diffractometer	Bruker Smart 6000 CCD
Data Collection method	CCD slices
Absorption correction	Empirical (using intensity measurements)
T_{min}	0.8817
T_{max}	0.9189
No. Of measured, independent and observed reflections	1530
Criterion for observed reflections	$I>2\sigma(I)$
R_{int}	0.0398
R_{max}	65.80
Refinement	
Refinement on	F^2
$R[F^2>2\sigma(F^2)]$, $wR(F^2)$, S	0.0605, 0.0719, 1.168
Reflection/profile data	
H-atom treatment	Constrained to parent site
Weighting Scheme	$W = 1/[\sigma^2(F^2_0) + (0.1016P)^2 + 0.3815P]$, where $P = (F^2_0 + F^2_C)/3$
(Δ/σ) max	< 0.0001
$\Delta\rho_{max}$, $\Delta\rho_{min}$($e\ Å^{-3}$)	0.213, -0.201

L2: Powder determination of oxamate:nicotinamide

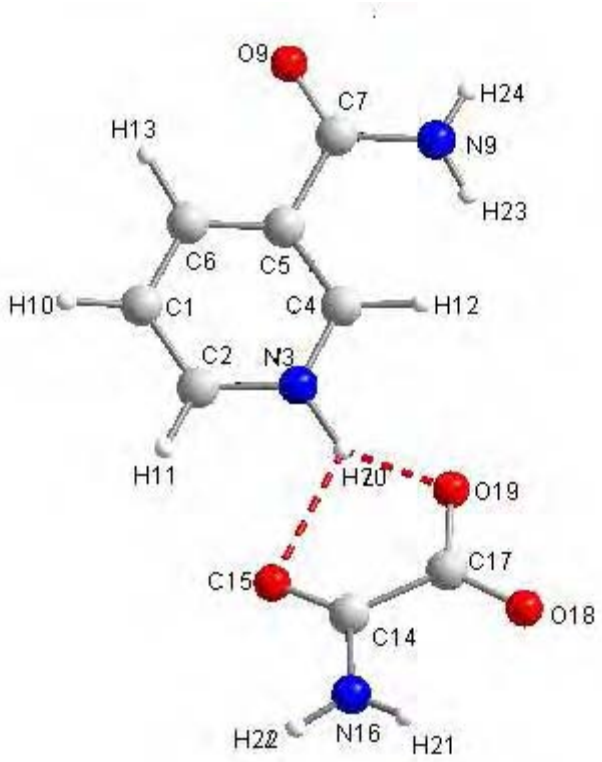

Figure L2: Atomic numbering scheme for oxamate:nicotinamide

Selected intramolecular geometric parameters in oxamate:nicotinamide (Å and °)

C1—C2 1.39(1)	C5—C6 1.34(1)	C6—C1 1.37(1)
C2—N3 1.37(1)	C5—C7 1.51(1)	C7—O9 1.21(1)
N3—C4 1.38(1)	C7—N8 1.37(1)	N8—H230.84(1)
C4—C5 1.40(1)	N8—H24 0.87(1)	C1—H10 1.08(1)
N3—H11 1.08(1)	C4—H12 1.08(1)	C6—H13 1.08(1)
N16—H21 0.89(1)	N16—H22 0.82(1)	

C1-C2-N3 120(1)	N16-C14-O15 122(1)	C2-N3-C4 120(1)
N16-C14-C17 116(1)	N3-C4-C5 120(1)	O15-C14-C17 120(1)
C4-C5-C6 120(1)	O19-C17-O18 120(1)	C5-C6-C1 119(1)
O19-C17-C14 120(1)	C6-C1-C2 119(1)	O18-C17-C14 118(1)

C5-C7-O9 119(1) C5-C7-N8 118(1)

Table L3: Final refined atomic positions in the powder solution of oxamate:nicotinamide

Atom	x	y	z
C1	0.105(6)	0.514(2)	0.821(5)
C2	0.222(5)	0.594(3)	0.8962(4)
N3	0.279(4)	0.545(2)	0.993(6)
C4	0.229(6)	0.420(2)	1.0142(6)
C5	0.217(6)	0.336(2)	0.9368(4)
C6	0.50(5)	0.386(2)	0.8448(4)
C7	0.062(5)	0.198(2)	0.965(4)
N8	0.131(4)	0.154(2)	1.0623(4)
O9	-0.037(5)	0.126(2)	0.9007(6)
H10	0.03(2)	0.560(5)	0.750(8)
H11	0.25(2)	0.699(5)	0.8815(5)
H12	0.27(2)	0.384(3)	1.090(1)
H13	-0.06(2)	0.329(3)	0.790(6)
C14	0.489(5)	0.646(2)	0.607(5)
O15	0.455(6)	0.682(2)	0.519(5)
N16	0.535(4)	0.515(2)	0.6354(4)
C17	0.506(7)	0.747(1)	0.6910(5)
O18	0.554(5)	0.706(2)	0.7809(5)
N19	0.444(5)	0.869(2)	0.6723(5)
H20	0.37(2)	0.609(5)	1.053(1)
H21	0.54(4)	0.45(1)	0.5887(10)
H22	0.57(4)	0.49(1)	0.6956(10)
H23	0.10(4)	0.08(1)	1.0792(10)
H24	0.21(4)	0.21(1)	1.1058(10)

Appendix M: Thermal expansion of monoclinic systems

In order to be able to compare the thermal expansion from one monoclinic system to the other, anisotropic nature of thermal expansion is best described in a Cartesian axis. The thermal expansion tensors of oxamic acid: nicotinamide were evaluated by the following procedure used for monoclinic systems[50]. The non-zero thermal expansivity coefficients of the tensor are first determined by evaluating the following expressions that describe the lengths of the crystallographic axes *a,b* and *c*, and the angle β as a function of temperature. The elements of the tensor are shown in Figure M.1;

$$\begin{matrix} \alpha_{11} & 0 & \alpha_{13} \\ 0 & \alpha_{22} & 0 \\ \alpha_{31} & 0 & \alpha_{33} \end{matrix}$$

Figure M1: Non-zero thermal co-efficient tensor

The tensor elements are evaluated from the following;

$$\alpha_{11} = d[\ln(a)]/dT + \cot(\beta)d\beta/dT$$

$$\alpha_{22} = d[\ln(b)]/dT$$

$$\alpha_{33} = d[\ln(c)]/dT$$

$$\alpha_{13} = \alpha_{31} = 1/2[\cot(\beta)\{d[\ln(a)]/dT - d[\ln(c)/dT\} - d(\beta)/dt].$$

Equations M.2-M.6: Tensor elements for a monoclinic system

The tensor is not diagonal when described in the monoclinic crystal axis frame, but can be made so by using the Cartesian axes c,b and a* as an orthogonal basis set and by rotating the principal axis of the tensor x by an angle φ from the a* axis in the anticlockwise sense when looking down the crystallographic b axis, where the rotation of the principal axis is shown by equation 5.7.

$$\tan 2\varphi = 2\alpha_{13} /(\alpha_{33} - \alpha_{11}).$$ [Equation M.7]

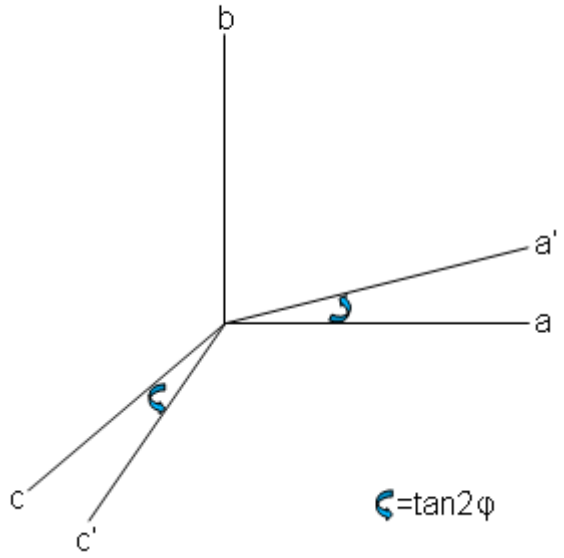

Figure M2: The anti-clockwise rotation of principal axis to Cartesian axis frame

Therefore, in this notation we have;

$$S_{11} = \alpha_{11}\cos^2\varphi + \alpha_{33}\sin^2\varphi - \alpha_{13}\sin 2\varphi$$

$$S_{22} = \alpha_{22}$$

$$S_{33} = \alpha_{11}\sin^2\varphi + \alpha_{33}\cos^2\varphi + \alpha_{13}\sin 2\varphi$$

Equations M.8-10: Diagonal elements of the thermal expansion tensor in its principal diagonalised form

All values of the derivatives were taken from the gradients of relevant graphs and the reference value of β in the cot (β) terms was taken to the measurement at 100 K.

Table M1: The thermal expansion coefficients and tensor elements of oxamic acid and nicotinamide salt

Thermal expansion coefficient (x $10^{-5}K^{-1}$)

α_{11}= 1.99249

α_{22}= -0.0003

α_{33}= 0.0007

α_{13}= α_{31}= 1.117604

Diagonalised thermal expansion tensor elements (x $10^{-5}K^{-1}$)

S_{11}=2.33137
S_{22}=0.0003
S_{33}=0.0944

The diagonalised thermal expansion tensor confirms the anisotropic nature of the salt.

Appendix N: Indexing oxamic acid:nicotinamide

Merit	Volume	V/Vi	BL	IndexProg	Date	Time	Pedig	a	b	c	alpha	beta	gamma
11.0	1839.348	1.00	P	DICVOL91/log	4Jun07	14:17:00	Mon_5	17.0613	9.8861	13.6986	90.000	127.244	90.000
11.0	1839.340	1.00	P	DICVOL91/log	4Jun07	13:57:40	Mon_5	17.0613	9.8861	13.6986	90.000	127.244	90.000
11.0	1839.173	1.00	P	DICVOL91/log	4Jun07	14:17:00	Mon_9	17.0620	9.8866	13.9940	90.000	128.820	90.000
11.0	1839.173	1.00	P	DICVOL91/log	4Jun07	14:17:00	Mon_7	17.0620	9.8866	13.9940	90.000	128.820	90.000
11.0	1839.173	1.00	P	DICVOL91/log	4Jun07	13:57:40	Mon_9	17.0620	9.8866	13.9940	90.000	128.820	90.000
11.0	1839.173	1.00	P	DICVOL91/log	4Jun07	13:57:40	Mon_7	17.0620	9.8866	13.9940	90.000	128.820	90.000
10.87	918.468	.50	P	LZONv6.23b	4Jun07	14:04:55	30016	13.7035	9.8868	6.9878	90.000	104.038	90.000
10.80	1838.144	1.00	P	KOHLv7.01b	4Jun07	13:47:54	3	13.9895	9.8854	13.6966	90.000	103.966	90.000
9.7	1837.982	1.00	P	DICVOL91/log	4Jun07	14:17:00	Mon_1	13.9861	9.8842	13.6992	90.000	103.945	90.000
9.7	1837.982	1.00	P	DICVOL91/log	4Jun07	13:57:40	Mon_1	13.9861	9.8842	13.6992	90.000	103.945	90.000
9.1	1840.370	1.00	P	DICVOL91/log	4Jun07	14:17:00	Mon_11	17.0608	9.8935	13.6967	90.000	127.246	90.000
9.1	1840.370	1.00	P	DICVOL91/log	4Jun07	13:57:40	Mon_11	17.0608	9.8935	13.6967	90.000	127.246	90.000
7.7	1837.448	1.00	P	DICVOL91/log	4Jun07	14:17:00	Mon_8	16.8178	9.8821	13.9876	90.000	127.776	90.000
7.7	1837.448	1.00	P	DICVOL91/log	4Jun07	13:57:40	Mon_8	16.8178	9.8821	13.9876	90.000	127.776	90.000
7.5	1837.792	1.00	P	DICVOL91/log	4Jun07	14:17:00	Mon_10	16.8180	9.8859	13.9860	90.000	127.783	90.000
7.5	1837.792	1.00	P	DICVOL91/log	4Jun07	13:57:40	Mon_10	16.8180	9.8859	13.9860	90.000	127.783	90.000
6.9	1838.723	1.00	P	DICVOL91/log	4Jun07	14:17:00	Mon_4	16.8271	9.8887	13.7952	90.000	126.773	90.000
6.9	1838.723	1.00	P	DICVOL91/log	4Jun07	13:57:40	Mon_4	16.8271	9.8887	13.7952	90.000	126.773	90.000
6.8	1838.145	1.00	P	DICVOL91/log	4Jun07	14:17:00	Mon_6	16.8270	9.8920	13.7951	90.000	126.780	90.000
6.8	1838.146	1.00	P	DICVOL91/log	4Jun07	13:57:40	Mon_6	16.8270	9.8920	13.7951	90.000	126.780	90.000
6.8	1836.650	1.00	P	DICVOL91/log	4Jun07	14:17:00	Mon_2	13.9840	9.8777	13.7992	90.000	105.512	90.000
6.8	1836.650	1.00	P	DICVOL91/log	4Jun07	13:57:40	Mon_2	13.9840	9.8777	13.7992	90.000	105.512	90.000
5.4	1836.207	1.00	P	DICVOL91/log	4Jun07	14:17:00	Mon_3	17.0594	9.8466	13.7193	90.000	127.255	90.000
5.4	1836.207	1.00	P	DICVOL91/log	4Jun07	13:57:40	Mon_3	17.0594	9.8466	13.7193	90.000	127.255	90.000
5.2	2195.30	1.19	P	ITO12/log	4Jun07	13:46:26	483	13.8818	14.2649	11.7939	100.696	99.052	102.226
4.81	2472.619	1.34	P	TAUPv1.1a	4Jun07	13:45:47	Ort_1	11.7398	13.2551	15.8900	90.000	90.000	90.000
14.97	918.878	.50	P	FJZNv6.22a	4Jun07	13:46:55	131	13.6993	9.8847	6.9937	90.000	104.010	90.000
14.74	918.903	.50	P	KOHLv7.01b	4Jun07	13:47:54	6	13.7000	9.8848	6.9936	90.000	104.011	90.000
11.02	1051.337	.57	P	LZONv6.23b	4Jun07	14:04:55	30003	10.0568	13.3157	8.0037	94.712	100.652	89.130
9	923.201	.50	P	TREOR90/log	4Jun07	13:47:22	Mon_10	13.6988	9.8894	7.0258	90.000	104.081	90.000
7.1	2103.03	.60	P	ITO12/log	4Jun07	13:46:26	463	8.4136	13.5761	10.3640	90.893	111.271	89.676
7	919.371	.50	P	TREOR90/log	4Jun07	13:47:22	Mon_6	16.7661	9.9204	6.9670	90.000	127.497	90.000
6	2001.682	1.09	P	TREOR90/log	4Jun07	13:47:22	Mon_3	14.8066	17.0046	7.9727	90.000	94.533	90.000
6	1287.591	.70	P	TREOR90/log	4Jun07	13:47:22	Mon_2	16.3855	11.7722	6.8941	90.000	104.480	90.000
6	1287.590	.70	P	TREOR90/log	4Jun07	13:47:22	Mon_1	16.1097	11.7722	6.8941	90.000	99.993	90.000
6	919.701	.50	P	TREOR90/log	4Jun07	13:47:22	Mon_5	13.8145	9.9265	6.9656	90.000	105.666	90.000
6	919.701	.50	P	TREOR90/log	4Jun07	13:47:22	Mon_4	13.8091	9.9265	6.9656	90.000	103.671	90.000
10.38	696.418	.38	P	LZONv6.23b	4Jun07	14:04:55	80003	8.9269	9.8809	8.3007	97.215	101.893	96.935
7	919.962	.50	P	TREOR90/log	4Jun07	13:47:22	Mon_7	16.7101	9.9149	6.9658	90.000	127.503	90.000
5.1	1142.03	.62	P	ITO12/log	4Jun07	13:46:26	583	10.1039	13.2757	8.7383	92.455	102.756	89.458
5.1	1085.04	.59	P	ITO12/log	4Jun07	13:46:26	466	8.2650	13.5048	10.1981	90.806	108.502	89.744
5	915.859	.50	P	TREOR90/log	4Jun07	13:47:22	Mon_9	13.7810	9.9157	6.9559	90.000	105.928	90.000
5	915.859	.50	P	TREOR90/log	4Jun07	13:47:22	Mon_8	13.6267	9.9157	6.9559	90.000	101.469	90.000
4	2112.355	1.15	P	TREOR90/log	4Jun07	13:47:22	Ort_1	16.7269	11.4825	10.9980	90.000	90.000	90.000
4.8	1490.51	.81	P	ITO12/log	4Jun07	13:46:26	446	14.8348	7.6497	14.2726	90.000	113.045	90.000
18.14	629.218	.34	P	LZONv6.23b	4Jun07	14:04:55	60001	7.4624	15.9635	5.1095	91.296	95.444	88.226
17.62	515.411	.28	P	KOHLv7.01b	4Jun07	13:47:54	5	9.5154	8.8114	7.9130	108.332	120.287	64.964
12.57	502.410	.27	P	KOHLv7.01b	4Jun07	13:47:54	10	8.5633	9.5016	7.8008	118.745	108.537	65.676
8.13	2656.505	1.44	P	FJZNv6.22a	4Jun07	13:46:55	331	13.2882	15.7165	12.7104	90.000	90.000	90.000
5.1	2640.64	1.44	P	ITO12/log	4Jun07	13:46:26	664	17.2244	14.4849	10.6988	90.000	97.612	90.000

Figure N1: Indexing output of oxamic acid:nicotinamide

Appendix O: Indexing fumaric acid:nicotinamide

Table O1: Indexing output for fumaric acid:nicotinamide

Merit	Volume	IndexProg	Date	a	b	c	alpha	beta	gamma
26.43	1102.851	KOHLv7.01b	18-Jun-08	14.3889	13.8156	5.5583	90	93.517	90
25.5	1102.98	DICVOL91/log	18-Jun-08	18.716	13.8163	5.5578	90	129.873	90
25.5	1102.98	DICVOL91/log	18-Jun-08	17.6359	13.8163	5.5578	90	125.465	90
25.5	1102.972	DICVOL91/log	18-Jun-08	15.7418	13.8163	5.5578	90	114.152	90
25.5	1102.971	DICVOL91/log	18-Jun-08	15.1054	13.8163	5.5578	90	108.028	90
25.4	1103.06	DICVOL91/log	18-Jun-08	14.3916	13.8159	5.5581	90	93.51	90
6.6	5085.308	DICVOL91/log	18-Jun-08	35.6472	31.166	4.5773	90	90	90
5.7	5214.102	DICVOL91/log	18-Jun-08	41.4572	14.3605	8.7581	90	90	90
5.6	4967.622	DICVOL91/log	18-Jun-08	74.5999	11.3849	5.849	90	90	90
9	3468.679	TREOR90/log	18-Jun-08	17.4869	14.3593	13.814	90	90	90
4.6	2521.75	ITO12/log	18-Jun-08	13.687	14.8747	13.4363	112.282	94.008	85.777
6.6	2576.12	ITO12/log	18-Jun-08	13.959	14.925	13.0914	106.581	99.77	87.224
17	1736.525	TREOR90/log	18-Jun-08	14.3612	13.8119	8.7546	90	90	90
10.09	3400.429	KOHLv7.01b	18-Jun-08	13.5723	22.5875	12.0058	90	112.498	90
9.8	2356.96	ITO12/log	18-Jun-08	14.8317	17.1405	10.4053	103.7	105.128	69.232
9.49	1083.336	KOHLv7.01b	18-Jun-08	10.4415	13.5506	8.6847	101.848	108.006	103.588
4.4	5748.25	ITO12/log	18-Jun-08	18.9336	21.9922	13.8049	90	90	90
15.8	996.253	KOHLv7.01b	18-Jun-08	12.9207	13.6946	6.4967	84.039	105.189	116.091
11.34	1065.486	KOHLv7.01b	18-Jun-08	13.2538	13.2086	6.6413	97.771	105.912	72.661
9.14	1014.063	KOHLv7.01b	18-Jun-08	7.8242	20.2495	6.4634	92.86	97.281	91.354
6.3	3011.75	ITO12/log	18-Jun-08	17.2691	22.142	7.8765	90	90	90
4.8	5742.57	ITO12/log	18-Jun-08	18.7379	22.2255	13.789	90	90	90

Appendix P: Structure determination of fumaric acid:nicotinamide

P1: Single crystal determination of fumaric acid:nicotinamide

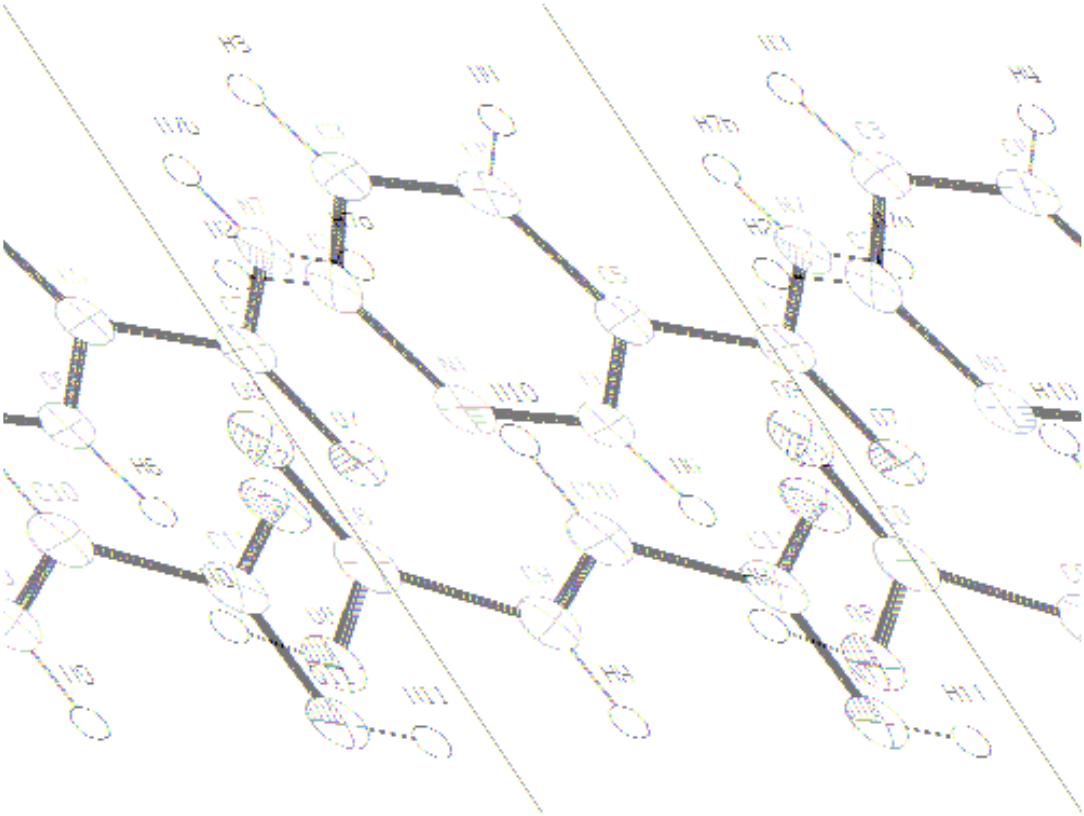

Figure P1: Atomic numbering scheme for fumaric acid:nicotinamide

Table P1 : Final refined atomic positions and isotropic displacement factors for fumaric acid:nicotinamide

Atom	x	y	z	U_{iso}/Å^2
C2	0.8233(3)	0.55975(11)	0.34373(11)	0.0352(4)
H2	0.9595	0.5832	0.3799	0.042
C3	0.6744(3)	0.62561(11)	0.29686(12)	0.0377(4)
H3	0.7079	0.6931	0.3005	0.045
C4	0.4754(3)	0.59181(11)	0.24443(11)	0.0350(4)
H4	0.3697	0.6359	0.2119	0.042
C5	0.4317(3)	0.49223(10)	0.23987(10)	0.0298(4)
C6	0.5914(3)	0.43120(10)	0.28925(11)	0.0314(4)
H6	0.5633	0.3632	0.2867	0.038
C7	0.2207(3)	0.44850(10)	0.18527(10)	0.0301(4)
N1	0.7833(2)	0.46395(9)	0.34024(9)	0.0344(3)
N7	0.0770(2)	0.50649(9)	0.13449(10)	0.0374(4)
H7A	-0.0494	0.4826	0.1027	0.045
H7B	0.1077	0.5691	0.1324	0.045
O7	0.1852(2)	0.35946(7)	0.19058(8)	0.0379(3)
C8	0.6744(3)	0.31135(11)	0.05629(11)	0.0323(4)
C9	0.4874(3)	0.24989(11)	0.00716(11)	0.0325(4)
H9	0.5047	0.1813	0.0080	0.039
C10	0.2985(3)	0.28909(11)	-0.03748(11)	0.0346(4)
H10	0.2888	0.3579	-0.0394	0.042
C11	0.0994(3)	0.23304(11)	-0.08514(10)	0.0313(4)
O8	0.8317(2)	0.26044(8)	0.10824(9)	0.0411(3)
H8	0.9376	0.2977	0.1322	0.062
O9	0.6779(2)	0.39909(8)	0.04933(9)	0.0425(3)
O11	0.1195(2)	0.13910(7)	-0.07607(8)	0.0386(3)
H11	0.003	0.1119	-0.1053	0.058
O12	-0.0689(2)	0.27372(8)	-0.12767(8)	0.0393(3)

Bond lengths [Å] and angles [°] for Fumaric acid:nicotinamide

C(2)-N(1)	1.340(2)	N(7)-H(7A)	0.8800
C(2)-C(3)	1.377(2)	N(7)-H(7B)	0.8800
C(2)-H(2)	0.9500	C(8)-O(9)	1.2138(19)
C(3)-C(4)	1.383(2)	C(8)-O(8)	1.3182(19)
C(3)-H(3)	0.9500	C(8)-C(9)	1.487(2)
C(4)-C(5)	1.395(2)	C(9)-C(10)	1.315(2)
C(4)-H(4)	0.9500	C(9)-H(9)	0.9500
C(5)-C(6)	1.388(2)	C(10)-C(11)	1.485(2)
C(5)-C(7)	1.499(2)	C(10)-H(10)	0.9500
C(6)-N(1)	1.337(2)	C(11)-O(12)	1.2238(19)
C(6)-H(6)	0.9500	C(11)-O(11)	1.3056(19)
C(7)-O(7)	1.2459(18)	O(8)-H(8)	0.8400
C(7)-N(7)	1.320(2)	O(11)-H(11)	0.8400

N(1)-C(2)-C(3)	122.51(15)	C(7)-N(7)-H(7A)	120.0
N(1)-C(2)-H(2)	118.7	C(7)-N(7)-H(7B)	120.0
C(3)-C(2)-H(2)	118.7	H(7A)-N(7)-H(7B)	120.0
C(2)-C(3)-C(4)	118.91(14)	O(9)-C(8)-O(8)	124.31(14)
C(2)-C(3)-H(3)	120.5	O(9)-C(8)-C(9)	122.86(14)
C(4)-C(3)-H(3)	120.5	O(8)-C(8)-C(9)	112.83(13)
C(3)-C(4)-C(5)	119.28(14)	C(10)-C(9)-C(8)	120.96(14)
C(3)-C(4)-H(4)	120.4	C(10)-C(9)-H(9)	119.5
C(5)-C(4)-H(4)	120.4	C(8)-C(9)-H(9)	119.5
C(6)-C(5)-C(4)	117.86(14)	C(9)-C(10)-C(11)	124.38(14)
C(6)-C(5)-C(7)	118.81(13)	C(9)-C(10)-H(10)	117.8
C(4)-C(5)-C(7)	123.32(13)	C(11)-C(10)-H(10)	117.8
N(1)-C(6)-C(5)	122.82(13)	O(12)-C(11)-O(11)	124.26(14)
N(1)-C(6)-H(6)	118.6	O(12)-C(11)-C(10)	121.35(14)
C(5)-C(6)-H(6)	118.6	O(11)-C(11)-C(10)	114.38(13)
O(7)-C(7)-N(7)	122.48(14)	C(8)-O(8)-H(8)	109.5
O(7)-C(7)-C(5)	119.09(13)	C(11)-O(11)-H(11)	109.5
N(7)-C(7)-C(5)	118.43(12)		
C(6)-N(1)-C(2)	118.61(13)		

Table P2: Experimental details – single-crystal data for fumaric acid:nicotinamide

Crystal data	
Chemical formula	C6H6N2O, C4H4O4
M_r	238.20
Space group, cell setting	$P2_1/c$, Monoclinic
a , b, c	5.5376(4), 13.7850(10), 14.2006(11)
Beta (˚)	92.54(1)
V ($Å^3$)	1082.95(14)
Z	4
D_x ($Mg\ m^{-3}$)	1.461
Radiation type	Cu Kα
μ (mm^{-1})	1.115
Specimen form, colour	Slab, colourless
Specimen size (mm)	0.34 x 0.15 x 0.06
Data Collection	
Diffractometer	Bruker Smart 6000 CCD
Data Collection method	Omega Scan
Absorption correction	Empirical (using intensity measurements)
T_{min}	0.7222
T_{max}	0.9411
No. Of measured, independent and observed reflections	6418, 1835, 1639
Criterion for observed reflections	$I>2\sigma(I)$
R_{int}	0.0543
R_{max}	
Refinement	
Refinement on	F^2
$R[F^2>2\sigma(F^2)]$, $wR(F^2)$, S	0.0471, 0.1222, 1.037
Reflection/profile data	1835 reflections
H-atom treatment	Constrained to parent site
Weighting Scheme	$W = 1/[\sigma^2(F^2_0) + (0.0812P)^2 + 0.1751P]$, where $P = (F^2_0 + F^2_C)/3$
(Δ/σ) max	< 0.0001
$\Delta\rho_{max}$, $\Delta\rho_{min}$($e\ Å^{-3}$)	0.213, -0.201
Extinction method	None
Extinction coefficient	N/A

Powder crystal determination of fumaric acid:nicotinamide

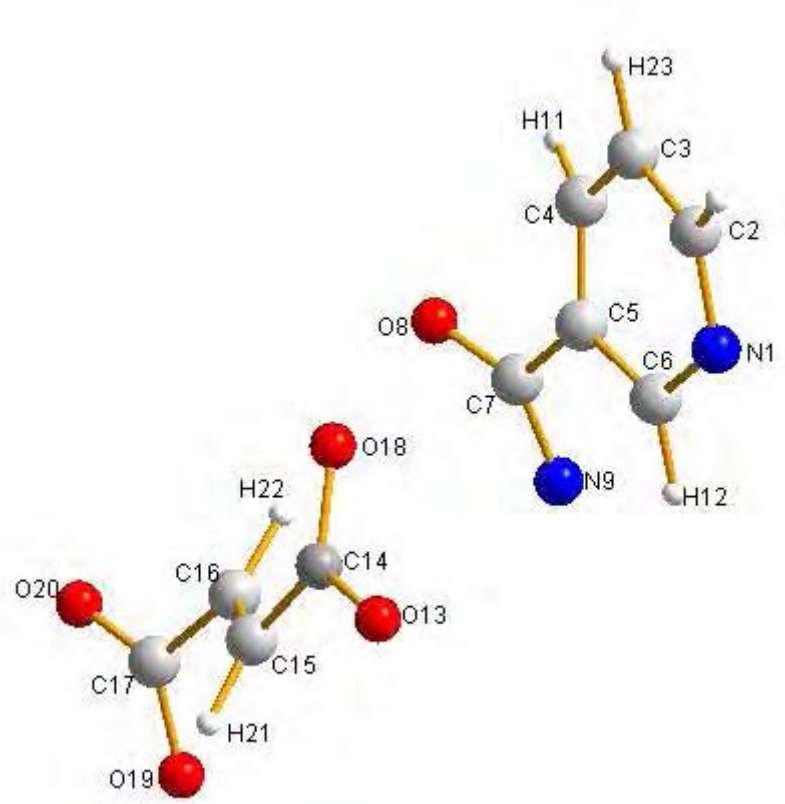

Figure P2: Atomic numbering scheme for fumaric acid:nicotinamide

N1---C2 1.33553(17)	N1---C6 1.34522(7)	C2---N11.33553(17)
C2---C3 1.39193(9)	C2---H10 1.07992(6)	C3---C2 1.39193(9)
C3---C4 1.35195(7)	C3---H23 1.08303(14)	C4---C3 1.35195(7)
C4---C51.35509(19)	C4---H11 1.07986(7)	C5---C4 1.35509(19)
C5---C6 1.38734(9)	C5---C7 1.50027(8)	C6---N1 1.34522(7)
C6---C5 1.38734(9)	C6---H12 1.08001(13)	C7---C5 1.50027(8)
C7---O8 1.23432(8)	C7---N9 1.29935(13)	O8---C71.23432(8)
N9---C7 1.29935(13)	H10---C2 1.07992(6)	H11---C4 1.07986(7)
H12---C6 1.08001(13)	O13---O14 1.23964(7)	C14---O13 1.23964(7)
C14---C15 1.48856(9)	C14---O18 1.32027(18)	C15---C14 1.48856(9)
C15---C16 1.28011(7)	C15---H21 1.05273(11)	C15---H22 2.02125(14)
C16---C15 1.28011(7)	C16---C17 1.49483(9)	C16---H21 2.02303(15)
C16---H22 1.05149(10)	C17---C16 1.49483(9)	C17---O19 1.30833(16)
C17---O20 1.21760(7)	O18---O14 1.32027(18)	O19---C17 1.30833(16)
O20---C17 1.21760(7)	H21---C15 1.05273(11)	H21---C16 2.02303(15)
H22---C15 2.02125(14)	H22---C161.05149(10)	H23---C3 1.08303(14)

Table P4: Final powder X-ray diffraction refined atomic positions and isotropic displacement factors for fumaric acid:nicotinamide

Atom	x	y	z	U_{iso}/Å^2
N1	0.16087	0.53418	0.22849	0.025
C2	0.17678	0.44215	0.16935	0.025
C3	0.22366	0.38106	0.33513	0.025
C4	0.26228	0.41818	0.54316	0.025
C5	0.26245	0.51543	0.57628	0.025
C6	0.20638	0.57339	0.42367	0.025
C7	0.31079	0.55827	0.79846	0.025
O8	0.37284	0.51224	0.91126	0.025
N9	0.27951	0.63794	0.88823	0.025
H10	0.16007	0.41747	-0.01263	0.05
H11	0.28129	0.37069	0.69262	0.05
H12	0.19218	0.64724	0.47398	0.05
C13	0.58435	0.25375	0.8442	0.025
C14	0.5402	0.29567	0.67614	0.025
C15	0.48935	0.23778	0.48408	0.025
C16	0.47664	0.27282	0.27128	0.025
C17	0.41636	0.22058	0.08476	0.025
O18	0.55064	0.38984	0.64633	0.025
O19	0.43642	0.13136	0.02782	0.025
O20	0.35956	0.26588	-0.04192	0.025
H21	0.45718	0.17214	0.52793	0.05

Appendix Q: Indexing of maleic acid:nicotinamide product A

Table Q1: Index output for maleic acid:nicotinamide product A

Merit	Volume	V/V1	IndexProg	a	b	c	alpha	beta	gamma
22.27	2040.138	1	TAUPv3.3a	6.4374	10.8654	29.1677	90	90	90
22.25	2040.078	1	KOHLv7.01b	10.8665	29.1648	6.4372	90	90	90
17.83	2038.151	1	TAUPv3.3a	6.4377	10.872	29.1201	90	90	90
15.4	2037.75	1	DICVOL91/log	29.1186	10.8685	6.4389	90	90	90
15.4	2037.75	1	DICVOL91/log	29.1186	10.8685	6.4389	90	90	90
7.2	1357.687	0.67	DICVOL91/log	19.7333	6.4397	10.8609	90	100.355	90
7.2	1357.687	0.67	DICVOL91/log	19.7333	6.4397	10.8609	90	100.355	90
7.1	1358.472	0.67	DICVOL91/log	20.7397	6.4399	10.8654	90	110.593	90
7.1	1358.472	0.67	DICVOL91/log	20.7397	6.4399	10.8654	90	110.593	90
6.8	1357.346	0.67	DICVOL91/log	24.1712	6.4403	10.8548	90	126.556	90
6.8	1357.346	0.67	DICVOL91/log	24.1712	6.4403	10.8548	90	126.556	90
12	950.223	0.47	TREOR90/log	14.4895	6.4385	10.5369	90	104.836	90
10.41	1735.598	0.85	KOHLv7.01b	10.9535	29.109	5.5018	90	98.354	90
7	1577.445	0.77	TREOR90/log	10.8345	17.0146	9.3993	90	114.44	90
5	2274.03	1.11	ITO12/log	12.0879	17.9924	11.8978	111.66	105.831	74.597
4.9	1782.78	0.87	ITO12/log	11.0106	20.8687	7.9291	94.96	100.076	93.041
4.9	1782.78	0.87	ITO12/log	11.0106	20.8687	7.9291	94.96	100.076	93.041
11.6	1025.69	0.5	ITO12/log	11.8144	11.9324	8.4614	101.007	109.084	65.763
8.5	822.36	0.4	ITO12/log	11.3126	11.8808	6.7632	98.973	98.969	109.942
8	909.069	0.45	TREOR90/log	15.3876	5.925	11.1664	90	116.755	90
6.5	2144.52	1.05	ITO12/log	19.4612	20.791	5.8238	95.079	94.412	113.001
6	1475.808	0.72	TREOR90/log	22.5702	10.15	6.4751	90	95.789	90
10	907.606	0.44	TREOR90/log	14.3505	5.9314	11.1468	90	106.945	90
9	1311.082	0.64	TREOR90/log	12.5031	11.6857	10.8228	90	123.991	90
7	1165.687	0.57	TREOR90/log	16.6255	6.4331	10.9365	90	94.746	90
6.6	1369.94	0.67	ITO12/log	10.495	19.581	6.8515	97.39	89.3	101.127
6	1426.306	0.7	TREOR90/log	12.6442	10.3618	11.04	90	99.568	90
6	1426.306	0.7	TREOR90/log	12.6442	10.3618	11.04	90	99.568	90
6	1298.104	0.64	TREOR90/log	20.3385	9.7748	6.5432	90	93.703	90
5	5925.499	2.9	TREOR90/log	16.9261	16.9261	20.6828	90	90	90
6.4	1464.86	0.72	ITO12/log	13.9531	18.1271	5.9686	93.08	97.995	100.541

Appendix R: Structure determination of maleic acid:nicotinamide product A

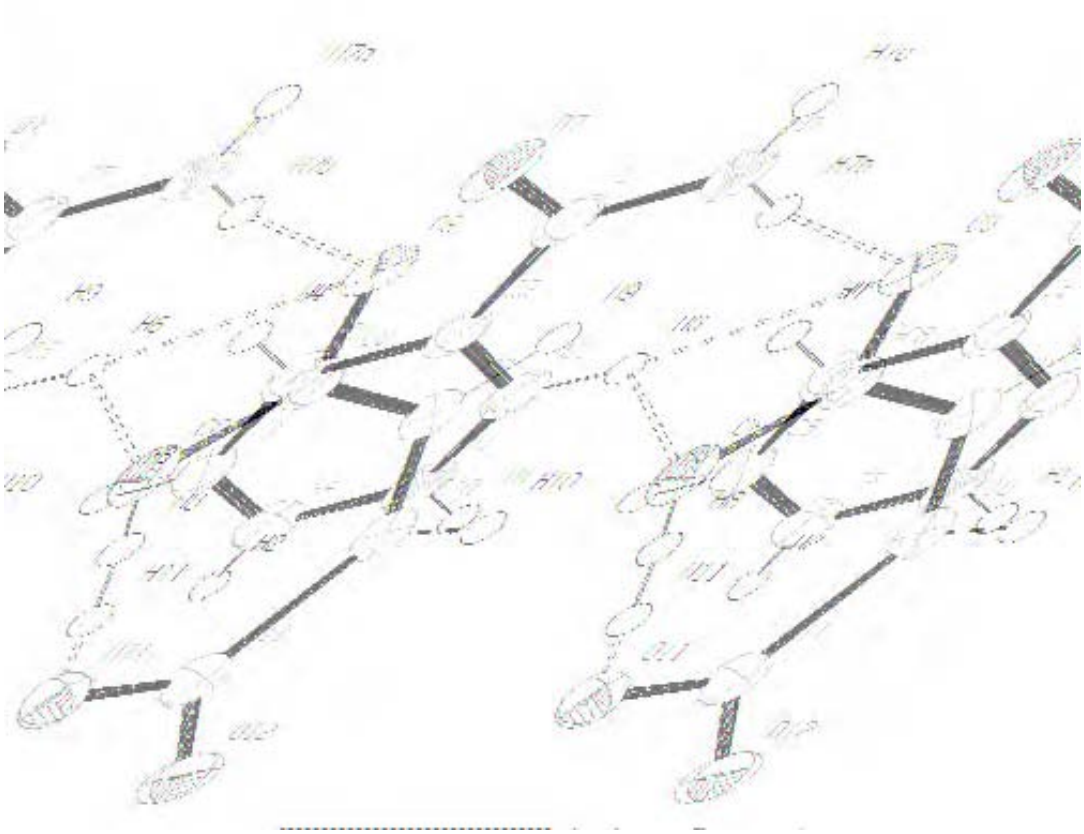

Figure R1: Atomic numbering scheme for maleate:nicotinamide product A

Selected intramolecular distances (Å) and angles (°)

C(2)-N(1)	1.341(2)	C(7)-O(7)	1.2369(17)
C(2)-C(3)	1.376(2)	C(7)-N(7)	1.3277(19)
C(2)-H(2)	0.9500	N(1)-H(1)	0.8800
C(3)-C(4)	1.381(2)	N(7)-H(7A)	0.8800
C(3)-H(3)	0.9500	N(7)-H(7B)	0.8800
C(4)-C(5)	1.392(2)	C(8)-O(9)	1.2412(18)
C(4)-H(4)	0.9500	C(8)-O(8)	1.2860(18)
C(5)-C(6)	1.3782(19)	C(8)-C(9)	1.4926(19)
C(5)-C(7)	1.506(2)	C(9)-C(10)	1.335(2)
C(6)-N(1)	1.339(2)	C(9)-H(9)	0.9500
C(6)-H(6)	0.9500	C(10)-C(11)	1.4947(19)

C(10)-H(10)	0.9500	O(8)-H(8)	0.8400
C(11)-O(12)	1.2379(17)	O(11)-H(11)	0.8400
C(11)-O(11)	1.2847(18)		

N(1)-C(2)-C(3)	118.91(14)	C(9)-C(10)-C(11)	130.14(13)
N(1)-C(2)-H(2)	120.5	C(9)-C(10)-H(10)	114.9
C(3)-C(2)-H(2)	120.5	C(11)-C(10)-H(10)	114.9
C(2)-C(3)-C(4)	119.60(14)	O(12)-C(11)-O(11)	122.03(13)
C(2)-C(3)-H(3)	120.2	O(12)-C(11)-C(10)	117.61(13)
C(4)-C(3)-H(3)	120.2	O(11)-C(11)-C(10)	120.35(12)
C(3)-C(4)-C(5)	120.39(13)	C(8)-O(8)-H(8)	109.5
C(3)-C(4)-H(4)	119.8	C(11)-O(11)-H(11)	109.5
C(5)-C(4)-H(4)	119.8		
C(6)-C(5)-C(4)	117.81(14)		
C(6)-C(5)-C(7)	122.66(13)		
C(4)-C(5)-C(7)	119.53(12)		
N(1)-C(6)-C(5)	120.43(14)		
N(1)-C(6)-H(6)	119.8		
C(5)-C(6)-H(6)	119.8		
O(7)-C(7)-N(7)	123.00(14)		
O(7)-C(7)-C(5)	118.84(13)		
N(7)-C(7)-C(5)	118.15(12)		
C(6)-N(1)-C(2)	122.86(13)		
C(6)-N(1)-H(1)	118.6		
C(2)-N(1)-H(1)	118.6		
C(7)-N(7)-H(7A)	120.0		
C(7)-N(7)-H(7B)	120.0		
H(7A)-N(7)-H(7B)	120.0		
O(9)-C(8)-O(8)	122.69(13)		
O(9)-C(8)-C(9)	117.02(13)		
O(8)-C(8)-C(9)	120.28(13)		
C(10)-C(9)-C(8)	130.25(13)		
C(10)-C(9)-H(9)	114.9		
C(8)-C(9)-H(9)	114.9		

Table R1: Final refined atomic positions and istropic displacement factors for maleate:nicotinamide

Atom	x	y	z	Uiso/Å^2
C2	0.8400(3)	0.10591(14)	0.11242(5)	0.0311(4)
H2	0.9651	-0.1204	0.1293	0.037
C3	0.7921(3)	0.17669(13)	0.07472(5)	0.0309(4)
H3	0.8841	-0.2407	0.0653	0.037
C4	0.6094(3)	0.15407(13)	0.05065(5)	0.0273(3)
H4	0.576	-0.2027	0.0246	0.033
C5	0.4739(2)	0.06052(12)	0.06440(4)	0.0236(3)
C6	0.5286(2)	0.00756(13)	0.10245(5)	0.0257(3)
H6	0.4389	0.0717	0.1128	0.031
C7	0.2761(2)	0.03699(12)	0.03755(5)	0.0256(3)
N1	0.7073(2)	0.01612(11)	0.12494(4)	0.0283(3)
H1	0.739	0.0292	0.149	0.034
N7	0.1565(2)	0.05764(11)	0.04977(4)	0.0301(3)
H7A	0.0414	0.0744	0.0343	0.036
H7B	0.1924	0.1037	0.0733	0.036
O7	0.23401(18)	0.10497(10)	0.00477(3)	0.0340(3)
C8	0.1643(2)	0.19101(13)	0.16467(5)	0.0262(3)
C9	0.1581(2)	0.28759(12)	0.20107(5)	0.0245(3)
H9	0.1567	0.37	0.1901	0.029
C10	0.1540(2)	0.27659(12)	0.24663(5)	0.0240(3)
H10	0.1516	0.3523	0.2629	0.029
C11	0.1528(2)	0.16378(13)	0.27603(5)	0.0252(3)
O8	0.13510(18)	0.07712(9)	0.17502(4)	0.0338(3)
H8	0.1143	0.0707	0.2034	0.051
O9	0.20188(18)	0.22591(10)	0.12499(3)	0.0358(3)
O11	0.12887(18)	0.05679(9)	0.25793(4)	0.0342(3)
H11	0.1166	0.0641	0.2294	0.051
O12	0.17355(18)	0.17796(10)	0.31789(3)	0.0347(3)

Appendix S: Structure determination of maleate:isonicotinamide

S1: Single crystal determination of maleate:isonicotinamide

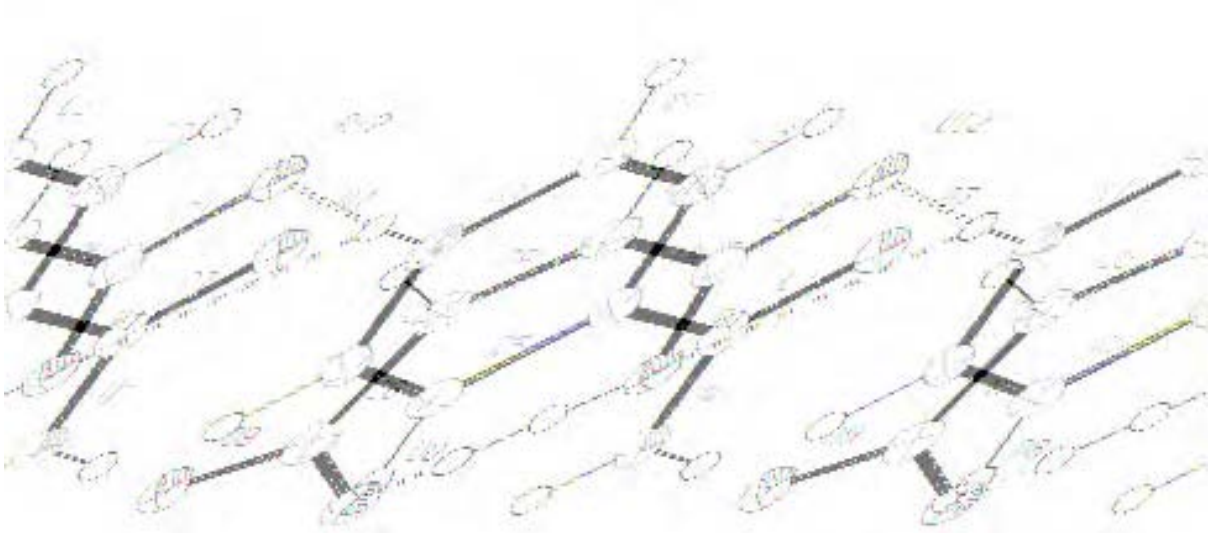

Figure S1: The atomic numbering scheme of maleate:isonicotinamide. Displacement ellipsoids are drawn at the 50 % probability level and H atoms are shown as small spheres of arbitrary radii.

Selected intramolecular distances (Å) and angles (°)

C8-O9 1.235(3)	C8-O8 1.294(3)	C8-C9 1.485(3)
C9-C10 1.338(3)	C9-H9 0.9500	C10-C11 1.499(3)
C10-H10 0.9500	C11-O12 1.246(3)	C11-O11 1.271(3)
O8-H8 0.8400	O11-H11 0.8400	C2-N1 1.334(3)
C2-C3 1.379(3)	C2-H2 0.9500	C3-H3 0.9500
C4-C5 1.388(3)	C4-C7 1.521(3)	C5-C6 1.377(3)
C5-H5 0.9500	C6-N1 1.332(3)	C6-H6 0.9500
C6-O7 1.232(3)	C7-N7 1.324(3)	N1-H1 0.8800
N7-H7A 0.8800	N7-H7B 0.8800	

O9-C8-O8 121.2(2)	O9-C8-C9 118.2(2)	O8-C8-C9 120.57(19)
C10-C9-C8 130.7(2)	C10-C9-H9 114.6	C8-C9-H9 114.6
C9-C10-C11 129.1(2)	C9-C10-H10 115.5	C11-C10-H10 115.5
O12-C11-O11 121.87(19)	O12-C11-C10 116.7(2)	O11-C11-C10 121.45(19)
C8-O8-H8 109.5	C11-O11-H11 109.5	N1-C2-C3 119.9(2)
N1-C2-H2 120.1	C3-C2-H2 120.1	C4-C3-C2 119.7(2)
C4-C3-H3 120.2	C2-C3-H3 120.2	C3-C4-C5 118.97(19)
C3-C4-C7 117.96(18)	C5-C4-C7 123.26(19)	C6-C5-H5 120.4
C4-C5-H5 120.4	N1-C6-C5 120.24(19)	N1-C6-H6 119.9
C5-C6-H6 119.9	O7-C7-N7 124.37(19)	O7-C7-C4 118.51(19)
N7-C7-C4 117.13(18)	C6-N1-C2 122.00(18)	C6-N1-H1 119.0
C2-N1-H1 119.0	C7-N7-H7A 120.0	C7-N7-H7B 120.0
H7A-N7-H7B 120.0		

Table S1: Final refined atomic positions and isotropic displacement factors for maleate:isonicotinamide - Single crystal structure.

Atom	x	y	z	U_{iso}/Å^2
N1	0.6298(5)	0.66710(17)	0.78234(13)	0.0249(4)
H1	0.5456	0.6497	0.8385	0.03
C2	0.6352(6)	0.5733(2)	0.70288(16)	0.0257(5)
H2	0.5523	0.4891	0.7078	0.031
C3	0.7613(6)	0.5988(2)	0.61361(17)	0.0256(5)
H3	0.7684	0.5321	0.5572	0.031
C4	0.8768(5)	0.7214(2)	0.60671(15)	0.0220(5)
C5	0.8748(6)	0.8165(2)	0.69162(16)	0.0255(5)
H5	0.96	0.9014	0.6893	0.031
C6	0.7479(6)	0.7863(2)	0.77926(16)	0.0260(5)
H6	0.7446	0.8507	0.8377	0.031
C7	0.9930(5)	0.7457(2)	0.50446(16)	0.0230(5)
N7	1.1759(5)	0.85725(17)	0.50537(14)	0.0267(5)
H7A	1.2481	0.8751	0.4478	0.032
H7B	1.2254	0.9135	0.5635	0.032
O7	0.9120(4)	0.66154(15)	0.42683(12)	0.0313(4)
C8	0.4825(6)	0.8785(2)	1.23913(17)	0.0265(5)
C9	0.2897(6)	0.7486(2)	1.20344(17)	0.0265(5)
H9	0.1821	0.7136	1.2555	0.032
C10	0.2422(6)	0.6727(2)	1.11010(16)	0.0260(5)
H10	0.1054	0.5926	1.1058	0.031
C11	0.3746(6)	0.6963(2)	1.01142(16)	0.0253(5)
O8	0.6318(5)	0.93794(15)	1.17473(12)	0.0347(4)
H8	0.5842	0.8941	1.1145	0.052
O9	0.4964(4)	0.92784(14)	1.33153(11)	0.0304(4)
O11	0.5467(5)	0.80175(15)	1.00597(12)	0.0334(4)
H11	0.5808	0.8489	1.0649	0.05
O12	0.3081(4)	0.60743(15)	0.93542(11)	0.0307(4)

Appendix T: ^{1}H NMR of forms I & II oxamic acid

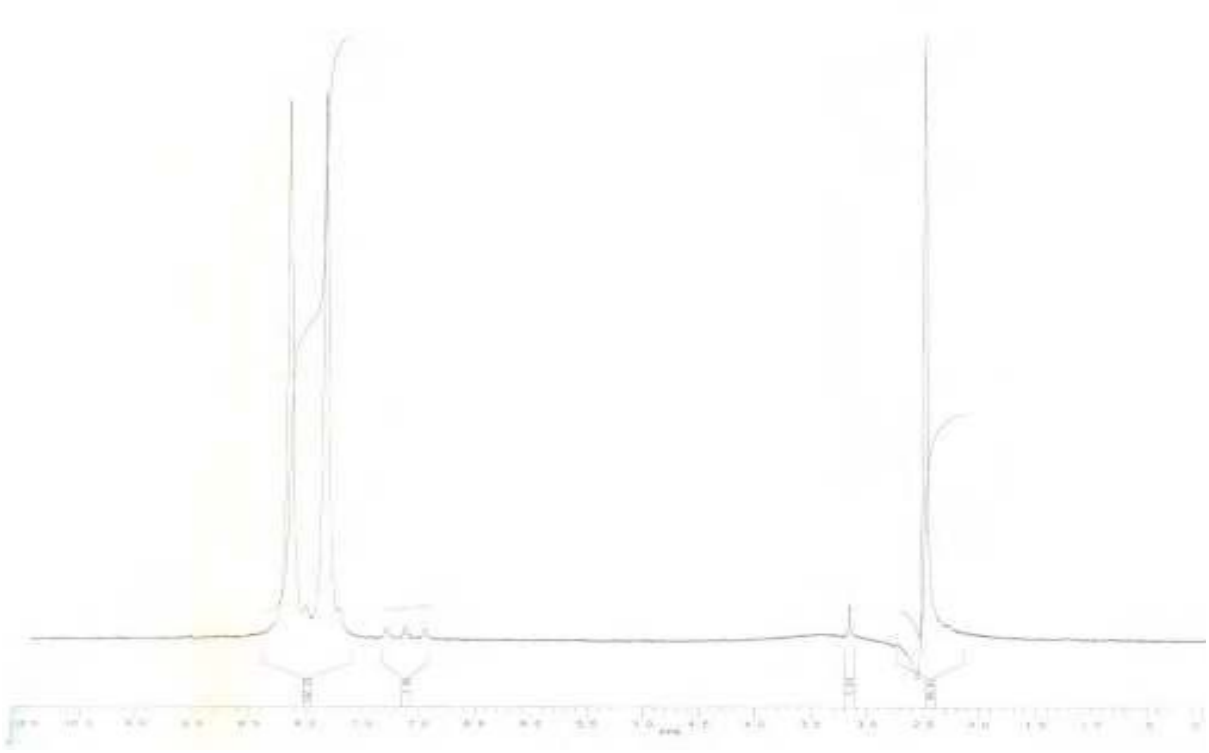

Figure T1: ^{1}H NMR of oxamic acid form I (0-10.5 ppm) in DMSO

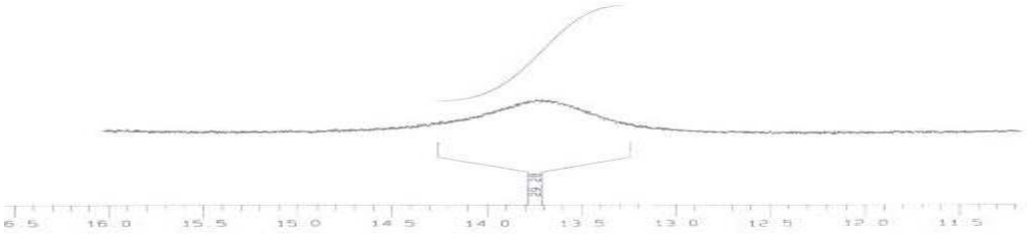

Figure T2: ^{1}H NMR of oxamic acid form I (11.5-16 ppm) in DMSO

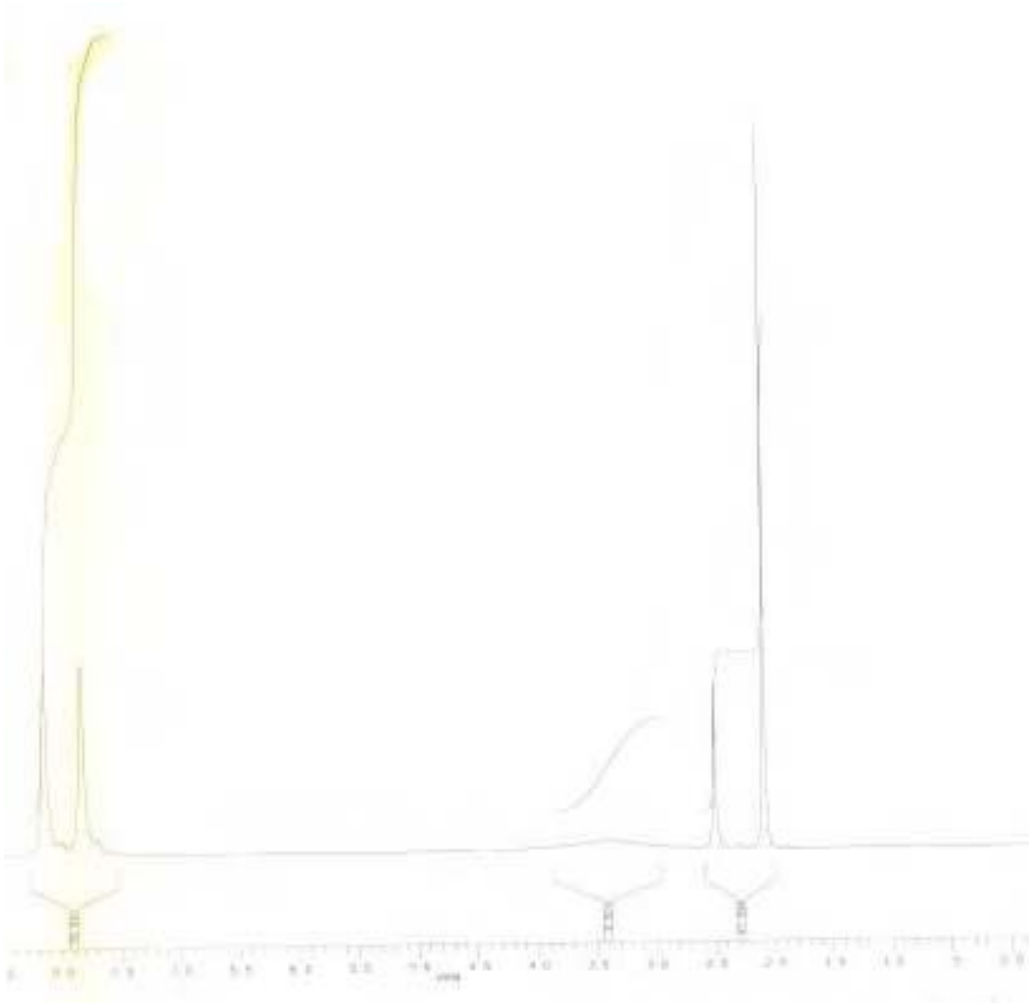

Figure T3: ^{1}H NMR of oxamic acid form II (0-8.5 ppm) in DMSO

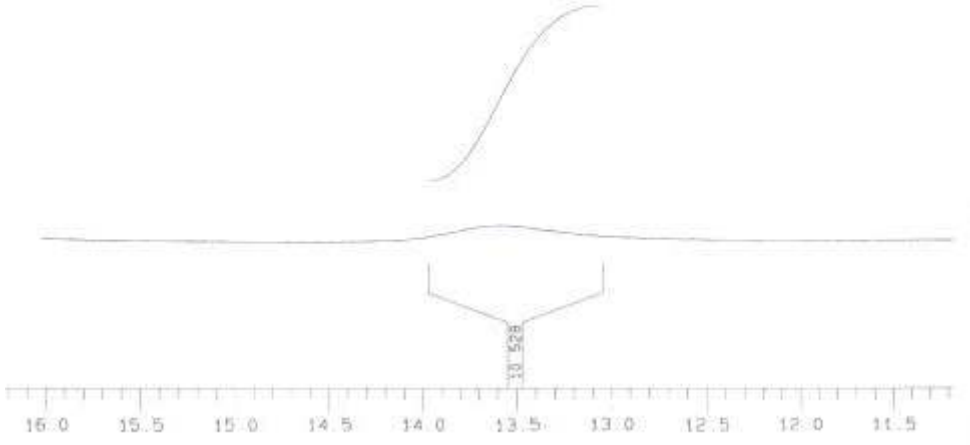

Figure T4: ^{1}H NMR of oxamic acid form II (11-16 ppm) in DMSO

In figures (T1-T4), two singlet peaks are seen for the amine protons instead of a doublet due to free rotation in the bond being hindered. This hindrance occurs as the π-system stabilizes the molecule and hence the protons are in a different environment. There is little coupling between the two hydrogens on the nitrogen as they are nearly equivalent. There is also an impurity present within the commercial sample which is seen at 7.2 ppm; this impurity is not seen in the ^{1}H NMR of oxamic acid recrystallised from ethyl acetate

Appendix U: Solid state NMR of oxamic acid (forms I and II)

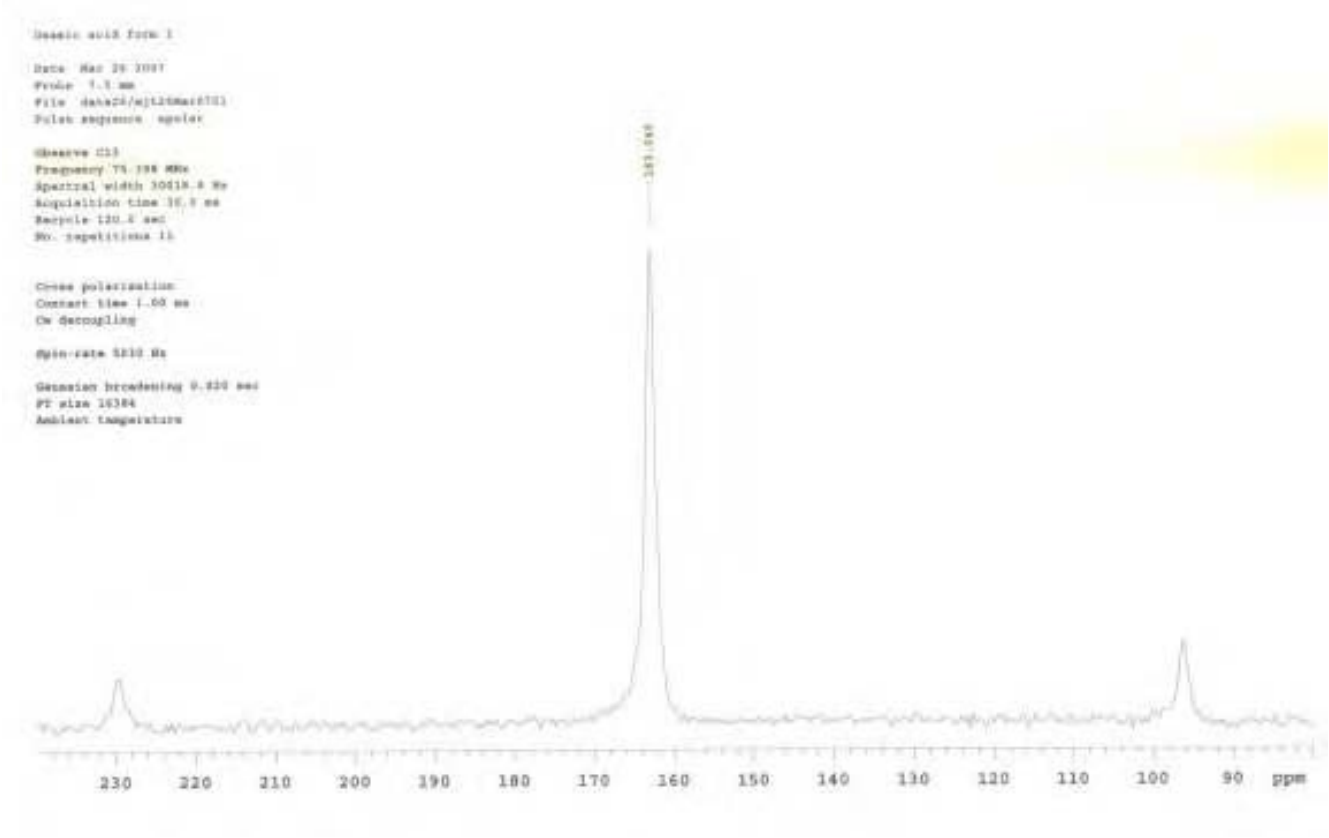

Figure U1: Solid state ^{13}C NMR of oxamic acid form I

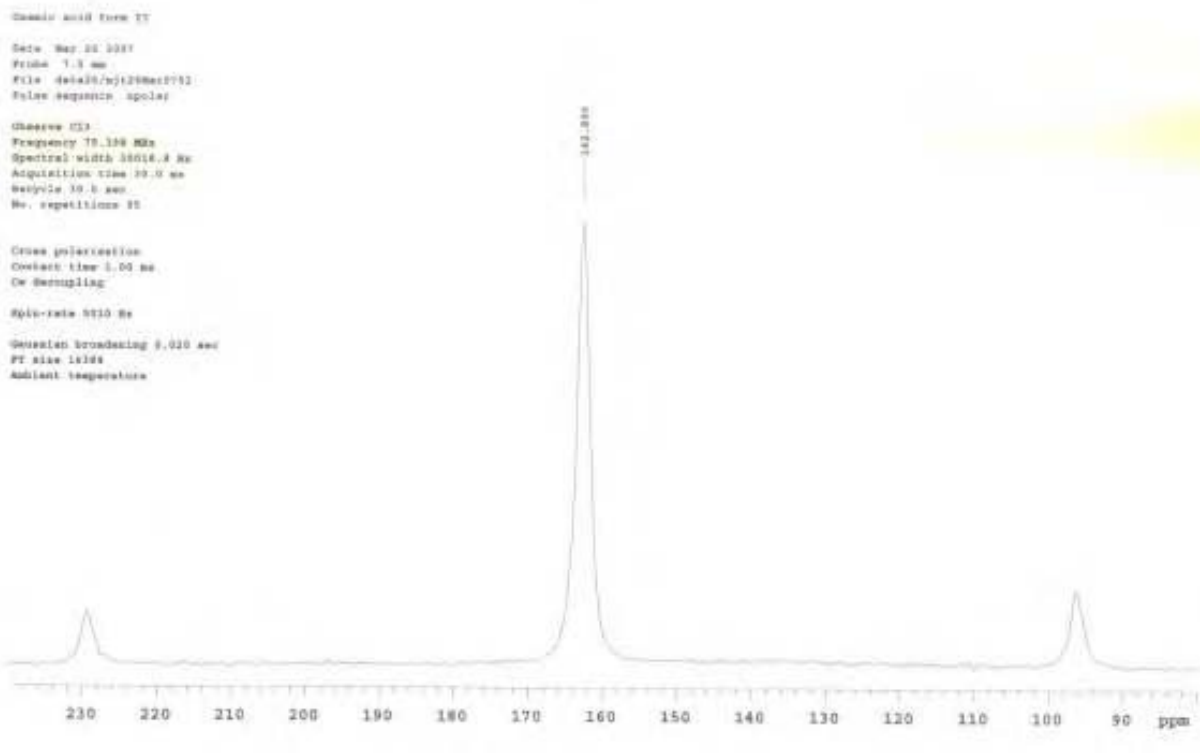

Figure U2: Solid state ^{13}C NMR of oxamic acid form II

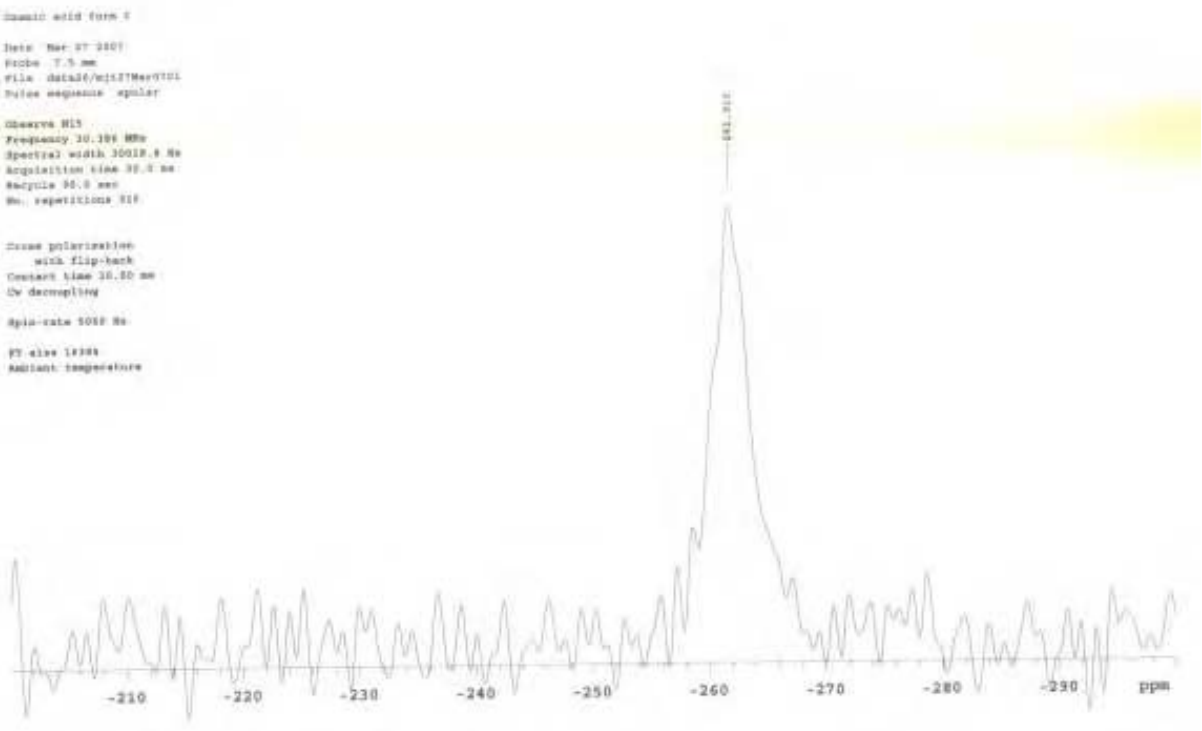

Figure U3: Solid state ^{15}N NMR of oxamic acid form I

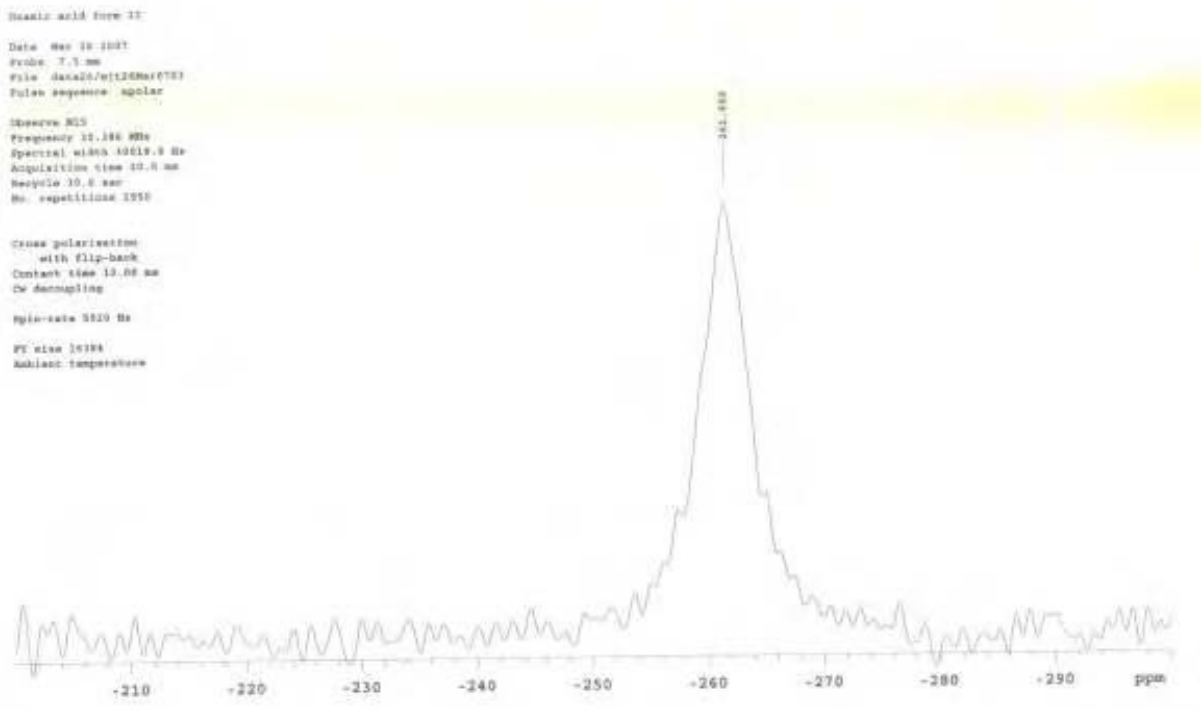

Figure U4: Solid state ^{15}N NMR of oxamic acid form II

Appendix V: The polymorphism of oxamic acid

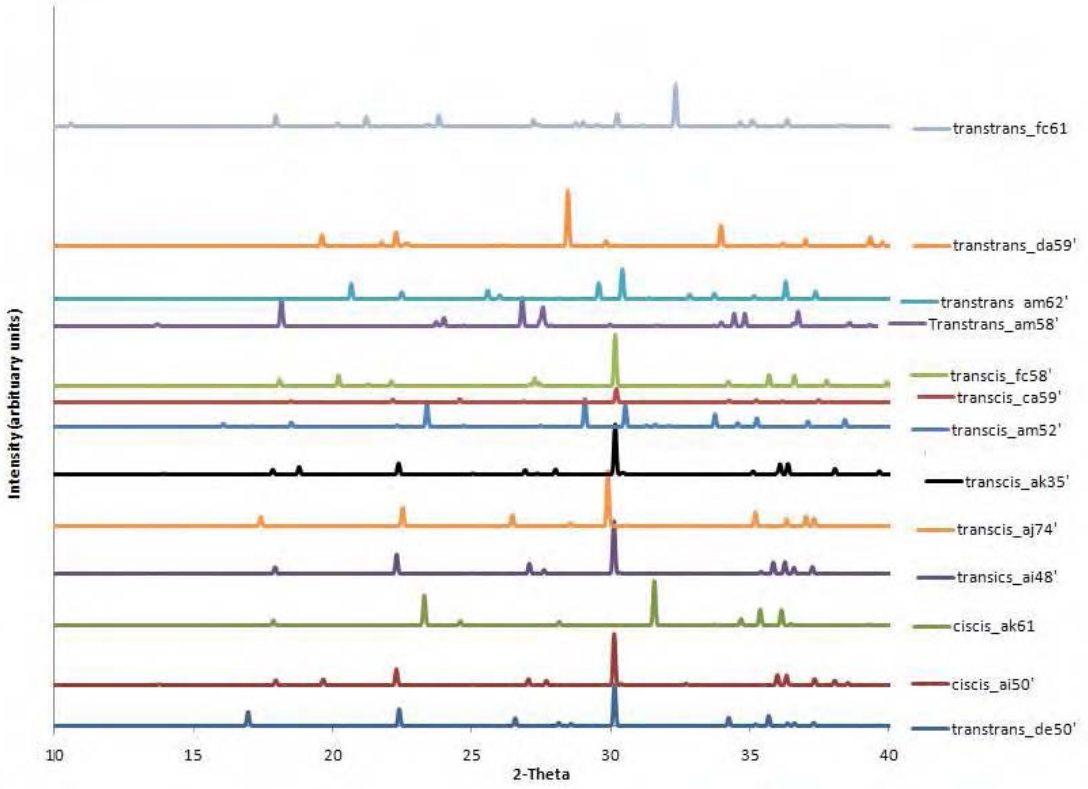

Figure V1: Powder diffraction patterns of predicted crystal structures of oxamic acid.

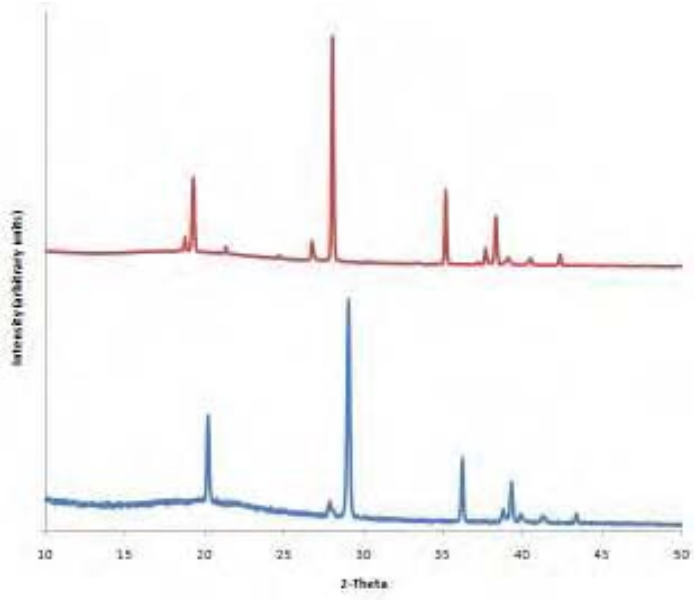

Figure V2: Diffraction pattern of oxamic acid form I (red) and form II (blue)

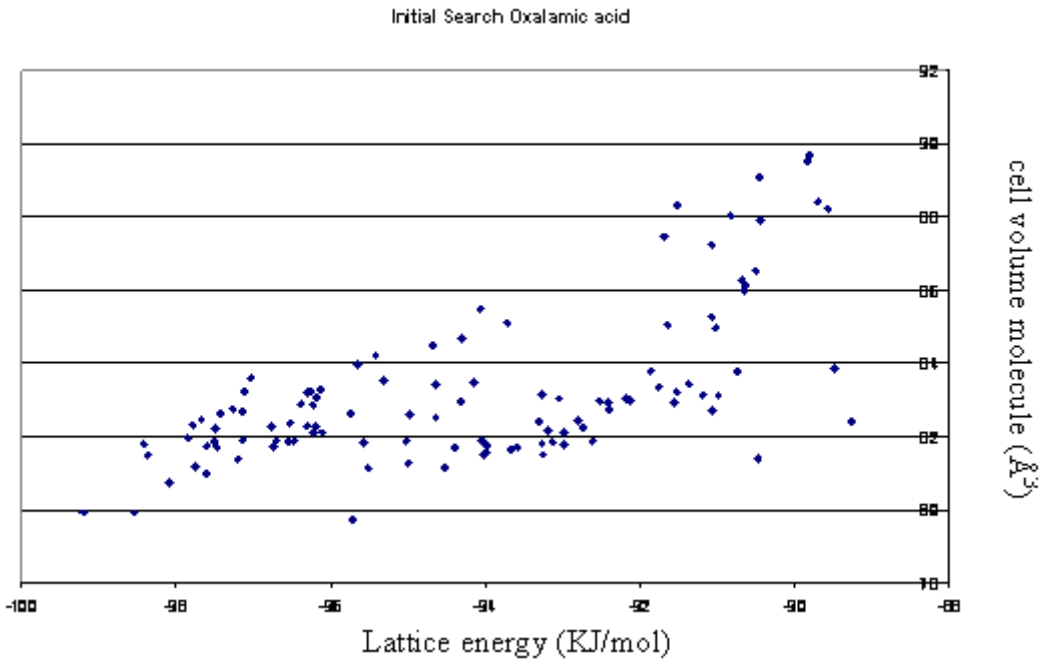

Figure V3: Energy landscape of Oxamic acid.

Appendix W: Single crystal structure of oxamic acid

Data was recorded at room temperature on a Bruker smart 6000 diffractometer equipped with a CCD detector and a Cu tube source. The structure was solved and refined using SHELXL.

Formula	$C_2H_3N_3O$
Formula weight	85.07
Temperature	293(2) K
Wavelength	1.54178 Å
Crystal system, space group	Monoclinic, Cc
a	9.530(5)Å
b	5.424(3)Å
c	6.866(4)Å
β	107.18(4)°
Volume	339.1(3) $Å^3$
Z, calculated density	3, 1.250 Mg/cm^3
Crystal size	0.20 x 0.12 x 0.08 mm
Final R indicies [I >2θ(I)]	
R1	0.2160
wR2	0.4178

Table W1: Atomic positions of oxamic acid

Atom	x	y	z	U_{eq}/ $Å^2$
O(3)	0.4527(7)	0.8718(10)	0.7305(9)	0.021(2)
O(4)	0.6696(9)	0.8769(17)	0.9767(12)	0.034(3)
O(1)	0.6856(10)	1.3607(19)	0.9763(15)	0.052(3)
O(2)	0.4573(8)	1.3766(18)	0.7417(11)	0.027(2)
C(2)	0.5520(20)	0.9803(18)	0.8390(40)	0.028(3)
C(1)	0.5540(20)	1.2669(18)	0.8390(40)	0.029(3)